UNIVERSITY OF CALIFORNIA
Los Angeles

Transverse instability and beam realignment in plasma wakefield acceleration

A dissertation submitted in partial satisfaction
of the requirements for the degree
Doctor of Philosophy in Physics

by

Lance Arthur Hildebrand

2024

ABSTRACT OF THE DISSERTATION

Transverse instability and beam realignment in plasma wakefield acceleration

by

Lance Arthur Hildebrand
Doctor of Philosophy in Physics
University of California, Los Angeles, 2024
Professor Warren B. Mori, Chair

In this dissertation, some of the major obstacles facing the design of a future multi-stage plasma-based linear collider (LC) are addressed. Plasma-based acceleration (PBA) is being considered for future LC designs because of large acceleration gradients that may dramatically reduce the size and cost. A critical challenge for PBA is ensuring the quality, i.e., the energy spread and emittance, of the witness beam is maintained. This requires transporting the witness beam in a stable manner even when there is an offset between the drive and witness beams, both in the plasma and between stages. When the tightly focused, high charge electron beams required for LCs are matched to the transverse wakefield, the space charge forces of the beam move the plasma ions significantly within the transit time of the beam. This ion motion, perturbs the wakefields which can cause degradation to the beam quality. In this dissertation, the acceleration of electron beams in nonlinear wakefields driven by electron beams is investigated using both theoretical models and particle-in-cell (PIC) simulations. Cases where there are misalignments between the drive and witness beam, both with and without ion motion are considered. Novel ideas to help address these issues are provided.

The existing theory for describing the hosing instability is extended to regimes relevant to future experiments and ultimately the LC regime. An azimuthal mode decomposition is employed to solve for the fields at the plasma sheath boundary, improving the hosing theory so that it provides better agreement with PIC simulations. Another issue, that has largely been unstudied, is beams with asymmetrical transverse sizes. The same azimuthal decomposition method can be used to characterize the wakefields created by such asymmetric beams.

Methods to mitigate the hosing instability are discussed and investigated. There have been many studies recently with different methods to detune the resonance between the beam and plasma channel and damp the instability. These are based on varying the betatron frequency (oscillation frequency of the centroid of the beam) or focusing force along the bunch. The idea of using a sufficient energy chirp on the witness beam that will eventually be corrected while accelerating because it underloads the plasma wake is discussed, as well as the idea of using an asymmetric drive beam that causes the focusing force to vary along the witness beam, both of which will cause the witness beam hosing to be damped.

The issue of plasma ion motion is addressed. The ion density distributions and resulting wakefields from tightly focused electron beams are described and a model for how the emittance evolves in these ion density profiles when the beam is asymmetric or has an offset is developed. It was found that when the drive beam induces ion motion before the witness beam, it can fully eliminate the hosing and realign the witness beam, but at the cost of large emittance growth in a uniform plasma. Using PIC simulations to study the LC regime, where ion motion is significant, it is possible to adiabatically match the beams in the presence of ion motion using plasma density ramps while essentially eliminating any transverse misalignment of the witness beam and maintaining the beam emittance, enabling stable transport of high quality electron beams for future PWFA-LCs. A single stage for which the witness electron beam is realigned, emittance growth is limited to a few percent, the energy spread is limited to less than a percent, and there is 50 percent drive-to-witness

energy transfer efficiency is presented.

The dissertation of Lance Arthur Hildebrand is approved.

George J. Morales

Chandrashekhar J. Joshi

Troy A. Carter

Warren B. Mori, Committee Chair

University of California, Los Angeles

2024

To my parents and my brother for their love, support, and inspiration.

TABLE OF CONTENTS

LIST OF FIGURES

LIST OF TABLES

ACKNOWLEDGMENTS

First, I want to thank my advisor, Warren Mori. Warren took me on as a student after hearing that the professor I had been working for previously had left UCLA. I quickly learned Warren has a strong presence in many different areas of plasma physics and had amassed a large and talented research group. Warren has been a very patient and understanding advisor and always believes in and encourages his students even when faced with difficult problems or roadblocks, of which I have faced many. Warren has been a great role model for me and I hope to live up to the standard he has set as both a physicist and mentor.

Second, I want to thank Weiming An, who was a postdoc who guided me for my first several years. Weiming inspired me to start the research in this dissertation. My graduate school trajectory would have been much different without his constant support. He has been a very kind and patient second mentor to me. After he accepted a position as a professor in China, he continued to check in on me and do zoom calls to offer his opinion and help until the end. I'm very grateful for his mentorship.

I want to thank Yujian Zhao. I spent a lot of time mentoring Yujian when he started the year after me, but soon he mentored me on many subjects. We have had many great conversations about research and life in the office and while rooming together at conferences. Many of the research in this dissertation was done in tandem with Yujian. He has been a great partner and friend through this process and I'm grateful he decided to join our group.

I am grateful for my classmate and roommate for most of graduate school, David Hamilton. We've spent countless hours discussing our careers, life in general, and having great times together. I'm also grateful for all my other classmates and friends who made this experience enjoyable and memorable: Philip Lu, Gurleen Bal, Matteo Vicino, John Gardiner, Cole Stephens, Warren Nadvornick, and Stathis Megas.

I also want to thank the other postdocs in our research group, Fei Li and Xinlu Xu, for their help and support. Fei and Xinlu are both very talented physicists who helped

spark many ideas in this dissertation. This research would not be possible without their contributions. I am grateful for all the graduate students in our group who helped me and brought happiness and laughs during this process. Kyle Miller and I started this research journey together and developed a friendship on and off campus. Thamine Dalichaouch has helped and inspired me when we worked in the office and traveled to meetings together. Sarah Chase has been a great friend and supporter during this long and arduous process. I also want to thank Qianqian Su, Adam Tableman, Roman Lee, Jacob Pierce, Asher Davidson, Ben Winjum, Frank Tsung, Paulo Alves, and Viktor Decyk.

Finally, I want to acknowledge my committee members, who have all provided me guidance during this process. Troy Carter was my professor for E&M and was a very helpful and friendly professor and role model. During my internship before coming to UCLA, a plasma physicist at APL told me George Morales' graduate plasma physics courses (222) was the best course they ever took and when I had the honor of taking it, I had the same opinion. Chan Joshi has always inspired me and challenged me in my research. Chan is one of the best scientists I've met - he is always optimistic and tenacious in the face of challenges, which has led to many great scientific feats in our field.

VITA

2011–2015	B.S. (Computational Physics) and B.S. (Applied Mathematics) University of Wisconsin, La Crosse
2014, 2015	NASA Summer Intern Johns Hopkins Applied Physics Laboratory, Laurel, Maryland
2015-2017	M.S. (Physics) University of California, Los Angeles
2017-present	Ph.D. Candidate Department of Physics and Astronomy, University of California, Los Angeles

PUBLICATIONS

Lance Hildebrand, Yujian Zhao, Weiming An, Fei Li, Qianqian Su, Xinlu Xu, Chan Joshi, and Warren B. Mori, "Beam realignment with emittance preservation in a plasma wakefield accelerator stage", submitted to Physical Review Letters (2024)

Lance Hildebrand, Weiming An, Xinlu Xu, Fei Li, Yujian Zhao, Mark J. Hogan, Vitaly Yakimenko, Sergei S. Nagaitsev, Erik Adli, Chan Joshi, and Warren B. Mori, "Mitigation techniques for witness beam hosing in plasma based acceleration", Proceedings of the IEEE Advanced Accelerator Concepts Workshop (2018)

Yujian Zhao, Lance Hildebrand, Weiming An, Xinlu Xu, Fei Li, Thamine N. Dalichaouch, Qianqian Su, Chan Joshi, and Warren B. Mori, "Emittance preservation in the presence of ion motion for low-to-high energy stages of a plasma based accelerator", Physics Review Accelerators and Beams **26**, 121301 (2023).

Yujian Zhao, Lance Hildebrand, Weiming An, Xinlu Xu, Fei Li, Thamine N. Dalichaouch, Qianqian Su, Chan Joshi, and Warren B. Mori, "Emittance preservation for the electron arm in a single PWFA-LC stage using quasi-adiabatic plasma density ramp matching sections", submitted to Physics of Plasmas (2024)

Yujian Zhao, Weiming An, Xinlu Xu, Fei Li, Lance Hildebrand, Mark J. Hogan, Vitaly Yakimenko, Chan Joshi, and Warren B. Mori, "Emittance preservation through density ramp matching sections in a plasma wakefield accelerator", Physics Review Accelerators and Beams **23**, 011302 (2020)

Qianqian Su, Fei Li, Weiming An, Viktor Decyk, Yujian Zhao, Lance Hildebrand, Thamine N. Dalichaouch, Shiyu Zhou, Eduardo Paulo Alves, Ann S. Almgren, Warren B. Mori, "Implementation of a Mesh refinement algorithm into the quasi-static PIC code QuickPIC", submitted to Journal of Computational Physics (2024)

Qianqian Su, Jeffery Larson, Thamine N. Dalichaouch, Fei Li, Weiming An, Lance Hildebrand, Yujian Zhao, Viktor Decyk, Paulo Alves, Stefan M. Wild, and Warren B. Mori, "Optimization of transformer ratio and beam loading in a plasma wakefield accelerator with a structure-exploiting algorithm", Physics of Plasmas **30**, 053108 (2023)

CHAPTER 1

Introduction

1.1 Background

One of the most exciting recent successes of physics was the discovery of the Higgs boson, validating the prediction of the Standard Model of particle physics. This discovery at the Large Hadron Collider (LHC) [1] was enabled by colliding protons at energies of 7 TeV, or 14 TeV center of mass (CM) energy. Circular accelerators such as the LHC have been primarily used over linear accelerators due to the fact that particles can orbit many times, gaining energy and having many more chances to collide, whereas in a linear collider there is only one chance to collide beams. However, synchrotron radiation can become significant in circular accelerators when using low mass particles like electrons and positrons, which is why hadrons are typically used. The loss from synchrotron radiation during each turn for a particle of rest mass m_b and energy E, in a synchrotron with circumference C scales as

$$\Delta E \text{ [TeV]} \approx 5.5 \frac{(E \text{ [100 GeV]}/(m_b/m_e))^4}{C \text{ [km]}}, \tag{1.1}$$

where m_e is the rest mass of an electron.

Linear accelerators do not suffer from synchrotron radiation and therefore collide leptons such as electrons and positrons because the collisions between them are easier to analyze and the strong force does not need to be overcome. There are thus plans to build a next generation linear collider with existing radio-frequency (RF) accelerator technology, called the International Linear Collider (ILC) [2]. The plan is for this collider to operate initially with collision energies of 500 GeV (CM), with potential plans to upgrade 1 TeV (CM) or

greater in the future, over a length of around 30 km, which is 10 times as long as the longest existing accelerator at the Stanford Linear Accelerator Center (SLAC). The ILC is meant to probe beyond the Standard Model in order to answer questions about the nature of the Higgs boson, dark matter and dark energy, and supersymmetry. The initial proposed cost estimate was around $7 billion, but the final cost is more likely to end up being closer to $20 billion. And because of these high costs, development has been delayed. For these reasons, there is also renewed interest in developing a circular lepton collider where muons collide [3]. Muons are massive enough that their synchrotron radiation is sufficiently low, however there are still many technological challenges to produce and cool muons. CERN recently announced plans for a Future Circular Collider (FCC) with a 90.7 km circumference tunnel [4]. The first phase is planned to be a precision electron-positron collider by 2040, followed by a 100 TeV hadron-hadron collider by 2070.

The cost of these accelerators is driven by their extremely large size. The reason a linear collider needs to be tens of km long is that the acceleration gradient within a conventional vacuum structure is limited due to electric breakdown of the walls of the accelerating structure, usually to around $20 \sim 150$ MeV [5]. There has thus been an active research effort in future (advanced) accelerator technology aimed at overcoming this limit, the most successful of which has been plasma-based acceleration (PBA). Plasmas of course have no breakdown limit, so they can sustain extremely large acceleration gradients and potentially reduce the cost of a future linear accelerator.

1.2 Plasma-based acceleration

The concept of plasma-based acceleration (PBA) was first proposed by Tajima and Dawson in 1979 [6]. When a laser propagates through a plasma, the ponderomotive force pushes plasma electrons away, thereby creating a charge separation between the electrons and ions. The resulting electric field pulls the electrons back after the laser passes establishing a plasma

oscillation. The oscillations are phased such that they produce an axial electric field with a phase velocity that is the same as the drive beam, $v_\phi = v_b$, and its wavelength is $\lambda_p = 2\pi v_\phi/\omega_p$, where ω_p is the plasma frequency. These phased oscillations are referred to as a wakefield. It was realized the longitudinal electric field can accelerate particles injected into this wakefield. The lasers required to effectively drive a wakefield need to have high power and short pulse lengths. This concept is referred to as laser wakefield acceleration (LWFA). Another PBA concept proposed by Chen et al. in 1985 [7] uses the space charge force of a charged particle beam to drive the wake and is referred to as plasma wakefield acceleration (PWFA). In both of these scenarios, the drive beam particles or laser beam lose energy to the wake, which in turn gives energy to the trailing (witness) beam particles inside the wakefied. This process can continue until the drive beam or laser loses all its energy and the wakefield ceases to be excited. The length over which this occurs is called the pump depletion length. In some cases, the process is limited by dephasing which occurs if the accelerated particles (moving at the speed of light, c) outrun the wave (which is moving at its phase velocity). In this dissertation, we will mainly focus on PWFA, but several of the proposed concepts may also be applied to LWFA. Fig. 1.1 shows a typical PWFA scenario, where an electron bunch excites a wake and a second bunch is loaded in the back of the wake to be accelerated.

In order to estimate the acceleration gradient that can be achieved in PBA, we can use Gauss's Law to calculate the magnitude of the plasma wave electric field. Assuming a 1D plasma wave driven by a driver traveling at the speed of light, c, that drives a density perturbation equal to the background electron density $n_1 = n_{e0}$ and using the Fourier transform of Gauss's Law, we have

$$k_{pe}|E| = 4\pi e n_{e0} = \frac{m_e \omega_p^2}{e} \rightarrow |E| = \frac{m_e c \omega_p}{e}. \tag{1.2}$$

This limit is often called the wave-breaking field, E_{WB}, and is commonly cited in an engineering form

$$E_{\mathrm{WB}} = 0.96 \text{ GeV/m}\sqrt{n_e \text{ } [10^{14} \text{ cm}^{-3}]}. \tag{1.3}$$

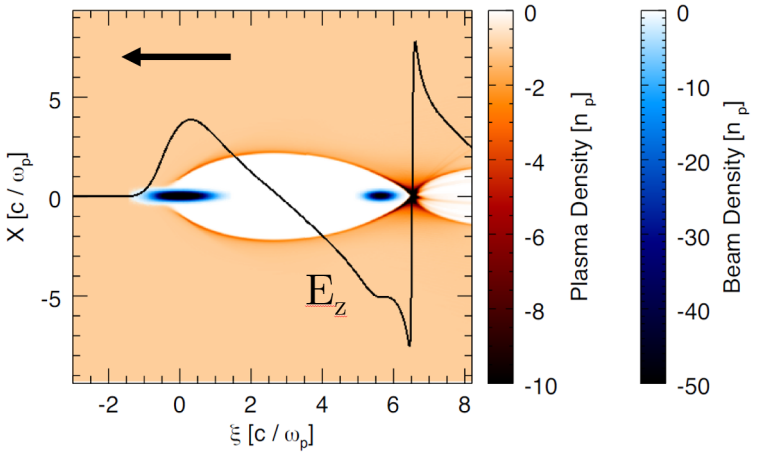

Figure 1.1: Particle-in-cell simulation of a typical PWFA two bunch scenario. The plasma is preformed. An intense drive bunch blows out the plasma electrons, which are pulled back to the axis by the ion column. The witness bunch is loaded and accelerated in the back of the wake, where the accelerating field, E_z, is large.

In reality, the wave has harmonics and the analysis is more complicated for phase velocities near the speed of light, and the wakefield is far from one-dimensional; nevertheless this estimate is very useful. Densities used in PBA are typically in the range of $10^{16} - 10^{19}$ cm^{-3}, corresponding to wavebreaking acceleration gradients of ten to hundreds of GeV/m. Therefore, PBA can be a promising path for making linear accelerators more compact and affordable.

In the last several decades there has been an extensive research campaign based around the ideas of PBA. Technology such as chirped pulse amplification [8] led to the development of short pulse laser systems that in turn led to many demonstrations of energy gain in LWFA [9, 10, 11, 12, 13, 14, 15]. The advantage of these lasers is that they can be compact (so called "table-top") systems.

Alongside the successes of LWFA, PWFA has shown great promise, starting with a series of experiments performed at SLAC [16, 17, 18, 19, 20, 21, 22]. The acceleration gradient in these experiments increased over the years: 280 MeV/m [19], 27 GeV/m [20], and 52

GeV/m [21]. The last of which demonstrated energy doubling of electrons in the tail of a single beam over only 85 cm of plasma. An acceleration gradient of 56 MeV/m [18] was achieved for positrons. Ref. [22] demonstrated that a witness beam can extract energy from the wake with high efficiency (up to 50%). High energy transfer efficiency is one advantage of PWFA over LWFA, that has struggled with this due to laser evolution and dephasing. This progress was possible due to pulse compression techniques developed for the LCLS X-ray FEL. Electron beams with tens of kA and durations less than 100 fs led to the breakthrough energy doubling results [21].

Initially theoretical development was limited to the overdense plasma case where the plasma density is larger than the beam density, also referred to as the linear regime of PWFA, where the plasma is treated as a fluid. In this regime, the wakefields are assumed to be sinusoidal and can be solved for using Green's functions. A one-dimensional linear theory was provided in the original PWFA paper [7] and expanded upon into multi-dimensions in a follow on paper [23]. A general multi-dimensional approach for linear theory was given by Katsouleas et al. [24]. However, in general the linear regime does not have ideal wakefield properties for focusing and accelerating electron beams unless the witness beam is perfectly tailored to modify (load) the wake. Rosenzweig et al. [25] instead proposed using the underdense plasma regime, where a high-intensity electron beam excites a nonlinear plasma wakefield where all the electrons are blown out of the cavity behind the drive beam. This is now called the "blowout" or "bubble" regime and is the primary regime considered for PWFA (as well as LWFA) because of the ideal wakefield properties, namely that the focusing force is transversely linear and does not vary longitudinally and the acceleration field is transversely uniform.

In 2005, Lu et al. [26], characterized the breakdown of linear theory in terms of the beams charge per unit length (also just called current), $\Lambda \equiv n_b/n_p(k_p\sigma_r)^2$ and spot size, $k_p\sigma_r$. Namely, for an electron driver with $\Lambda < 1$ and $(\Lambda/10)^{1/2} < k_p\sigma_r < 1$, fluid theory will still capture the blowout even if $n_b/n_p > 1$ because plasma electron trajectories do not

cross. However, in cases where $\Lambda > 1$, trajectories will cross and we need a particle based model to describe the nonlinear wake. This was done the following year by Lu et al. [27, 28], by assuming the blown out electrons form a thin, uniform electron sheath. If this sheath is described phenomenologically, the gauge-invariant wake pseudopotential, $\psi \equiv \phi - A_z$, where ϕ is the scalar potential and A_z is the axial vector potential, can be calculated in terms of the blowout radius, r_b, i.e., the radius in cylindrical coordinates of the innermost electron trajectory (where $\xi \equiv ct - z$ is the time-like variable). They were able to determine the total force for an electron at r_b from the electric and magnetic fields of the wakefields and use this to obtain a differential equation for r_b. The forces on a trailing beam particle (moving at c) can be obtained as gradients of ψ. This phenomenological model will be described in detail in the next chapter.

High acceleration gradients and efficiency are important features of a PBA that make it inexpensive and attractive when compared to conventional RF technology. However, when accelerating particles, it is also important to accelerate them at the same rate, i.e., keep the beam's energy spread low. Theoretical developments have shown that beam shaping and placement within the wake, referred to as beam loading, can flatten the accelerating field, which minimizes the energy spread growth during acceleration and also leads to higher efficiency. This was done in the linear regime in Ref. [24] and in the blowout regime in Ref. [29, 30]. The latter work used the nonlinear blowout theory and described beam loading in this regime as a modification to the blowout radius in the witness beam region. This work found a beam shape that is trapezoidal will flatten the wake and placed limits on the amount of charge that can be loaded. Recently, an improved model for the sheath structure has been developed which describes the fact that ψ becomes negative in the rear of the wake [31]. This predicts that the bunch shape is still trapezoidal but can be longer and have more net charge, for ideal beam loading.

Finally, it is important to maintain the quality of the beam while it is being accelerated. An important quantity that characterizes the quality of the beam is its geometrical emittance,

$\epsilon \equiv \sqrt{\langle x^2 \rangle \langle x'^2 \rangle - \langle x x' \rangle^2}$, which is related to the area in phase space. Actually, the normalized emittance defined by $\epsilon_N \equiv \bar{\gamma}\epsilon$, where $\bar{\gamma}$ is the average Lorentz factor of the beam, is what we really want to be conserved during acceleration. Given an initial emittance, there is a corresponding matched spot size such that the transverse beam envelope will not oscillate as the beam propagates. In the ideal case, with no misalignments or energy spread, the normalized emittance will be conserved while the beam is accelerating if it is matched. These matched spot sizes may be very small and they are often achieved by using plasma matching sections [32, 33, 34, 35, 36, 37], which consist of an upramp that matches the beam before the density plateau and a downramp at the end of the acceleration section. However, there are still many sources of emittance growth that must be controlled when designing a plasma-based linear accelerator. Ref. [38] summarizes many of these sources of growth both inside and outside the plasma. Outside the plasma, things such as leaking dispersion from magnetic dipole chicanes, chromatic focusing of divergent beams, or because of optics such as plasma lenses can cause emittance growth. Inside the plasma, the main sources of growth are from mismatches, misalignments, and nonlinear transverse wakefields. A main result from this dissertation is a concept, presented in Chapter 6, that can potentially address all of the sources in the plasma in one scheme.

Another thrust of PWFA research has been injection schemes. In this dissertation, we will focus on external injection, where the electron bunches are spaced properly before being sent into the plasma. However, there have been a number of promising internal or so-called self-injection schemes, where a single beam drives a wake and background plasma electrons are injected/trapped and accelerated in the back of the bubble. Such schemes include ionization injection [39, 40, 41] and downramp injection [42, 43, 44, 45].

One of the main experimental facilities currently conducting PWFA experiments for future high-energy physics applications is FACET-II (Facility for Accelerator Experiments and Tests) at SLAC [46, 47]. Experiments at its predecessor proved that high efficiency and high gradient acceleration can be simultaneously achieved through PWFA in the blowout

regime. A major scientific goal of FACET-II will be to demonstrate high efficiency and high gradient acceleration while also maintaining small witness beam emittance and energy spread, which is required for future applications, such as a plasma-based linear collider.

1.3 Plasma-based linear colliders

One of the initial concepts for a plasma acceleration stage was to place it at the end of a conventional linear accelerator (e.g., the ILC), known as an "afterburner". The high energy bunches from the accelerator would be injected into the plasma for additional acceleration and focusing before the interaction point (IP). Ideally, you could double the energy of the final output beam in a distance of ~ 10 meters. For an electron-positron (e^+e^-) collider, you would use two plasma stages, one for electrons and one for positrons. The physics of accelerating positrons in the plasma wakefields is inherently more difficult than electrons due to the transverse wakefields in the bubble being defocusing for positive charges. This dissertation does not consider the positron arm, but there has been much progress on achieving all the features we described for the electron arm [48, 49, 50, 51, 52, 53, 54, 55, 56].

More recently, designs of a full multi-stage plasma-based LC have been proposed [57, 58, 59], which would involve a witness beam getting accelerated to energies up to a TeV over a series of plasma stages. Specifically, as envisioned in Ref. [58], a conventional accelerator could provide a train of 25 GeV bunches to ~ 20 one meter long plasma cells, where a witness beam would pick up an additional 25 GeV per stage, therefore acquiring ~ 500 GeV by the IP. The positron arm would have the same design so that 1 TeV center of mass (CM) energies could be achieved. The schematic for this design is displayed in Fig. 1.2. As pointed out in Ref. [59], a first step could be a 250 Gev (CM) Higgs factory, which would be upgraded over time with the addition of more plasma cells to reach multi-TeV energies.

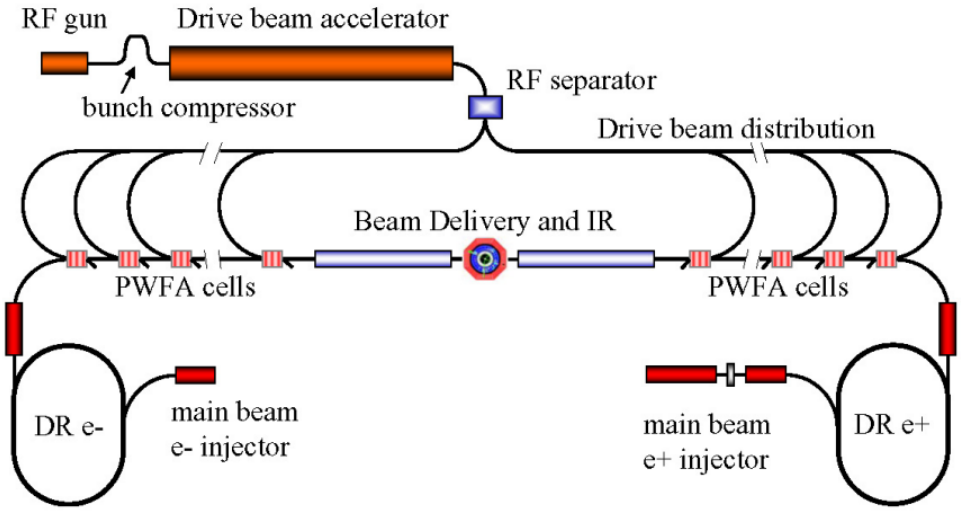

Figure 1.2: Schematic of an envisioned plasma-based linear collider [58]

Besides energy, the main figure of merit for a collider is the luminosity, given by

$$\mathcal{L} = \frac{fN^2}{4\pi\sigma_x\sigma_y}, \tag{1.4}$$

where f is the repetition rate of collisions, N is the number of particles in each beam, and σ_x and σ_y are the transverse spot sizes of the beams. Essentially the luminosity measures the ability of a collider to produce the required number of interactions, i.e., it is the proportionality constant between the events per second, dR/dt, and the cross section, σ_p. For high-energy physics applications, luminosities of $\sim 10^{34}$ cm^{-2}s^1 are desired. Thus, for a given charge per bunch, it is desirable to have small spot sizes at the collision point (CP). For given focusing elements (beam line) at the final focus, the ability to focus a beam is determined by its normalized emittance (area in transverse phase space) and energy spread. For beams around a nanocoulomb of charge, we need the beams to have ~ 100 nm normalized emittances. As we will discuss, these beams are very intense and their local space charge forces can pull plasma ions to the axis within their transit time which can have drastic consequences for emittance preservation.

Another important aspect of colliders is beam-beam interactions at the collision point.

The physics of colliding beams is complex and we will only summarize some of the main features here. When an electron and positron beam collide they will undergo a strong pinching effect from the other beams field, called disruption. The disruption parameter can be defined by

$$D_{x,y} \equiv \frac{\sigma_z}{f_{x,y}} = \frac{2Nr_e\sigma_z}{\gamma\sigma_{x,y}\left(\sigma_x + \sigma_y\right)}, \tag{1.5}$$

where $f_{x,y}$ is the focal length, r_e is the classical electron radius, and σ_z is the beam length [60]. There are many implications of disruption. The pinching effect can actually lead to luminosity enhancement but there may also be deflection, kink instabilities, and beamstrahlung. Beamstrahlung is the radiation of photons from the curved deflection of beam particles which will alter the energy and charge of the colliding beams. This can be quantified by the Lorentz-invariant beamstrahlung parameter $\chi \equiv E^*/E_{\rm cr}$, which relates the electromagnetic field in the particle's rest frame, E^*, with the QED critical field, $E_{\rm cr} = m^2c^3/(e/\hbar)$ [61, 62]. When $\chi \gtrsim 1$, QED effects become important and when $\chi \gg 1$, the QED effects become fully nonperturbative. The average beamstrahlung parameter for a Gaussian beam is given by

$$\Upsilon = \frac{5r_e^2\gamma N}{6\alpha\sigma_z\left(\sigma_x + \sigma_y\right)}, \tag{1.6}$$

where α is the fine structure constant [60]. One of the main ways to prevent strong disruption and beamstrahlung is to use flat beams ($\sigma_x \gg \sigma_y$). Most of the work in this dissertation will use round beams, but we will address the need for flat witness beams. In regimes where $\Upsilon > 1$ (likely in round beam cases), there may be significant dilution of the luminosity spectrum due to the energy loss which leads to an energy spread [63],

$$\sigma_\gamma \simeq 1.24\frac{\alpha^2\sigma_z}{r_e\gamma}\frac{\Upsilon^2}{\left(1 + (3\Upsilon/2)^{2/3}\right)^2}. \tag{1.7}$$

But this may provide interesting opportunities to study non-linear QED effects above the Schwinger limit [64, 62]. Another important consideration is beam-beam offsets at the interaction point (IP). For rigid beams with an offset in the y direction, the luminosity reduction is given by

$$\frac{\mathcal{L}}{\mathcal{L}_0} = \exp\left(-\frac{\Delta y^2}{4\sigma_y^2}\right), \tag{1.8}$$

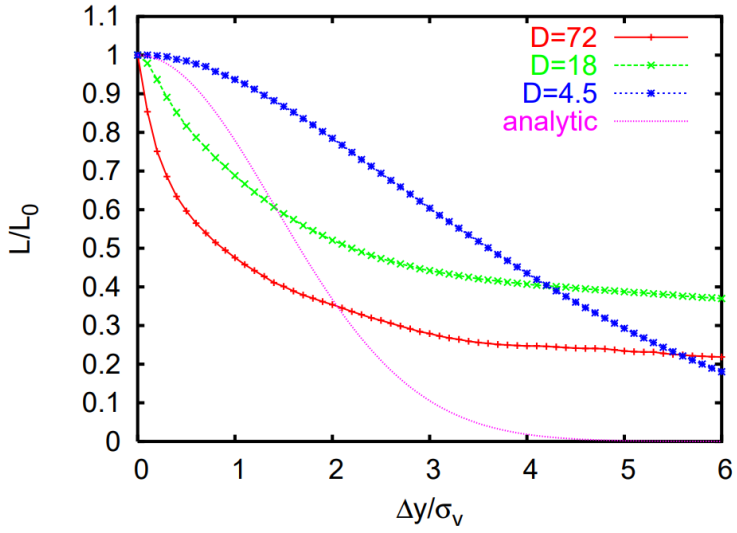

Figure 1.3: Luminosity as a function of offset for different disruption parameters [65]

however, beam-beam effects strongly affect this, as shown in Fig. 1.3. This means it will be critical, especially for higher disruption, to limit the transverse beam offset while accelerating the beam in the PWFA stages. This will be one of the main goals of this dissertation.

Besides an e^-e^+ collider, another route to pursue could be a $\gamma - \gamma$ collider [66]. Beams of hard photons (as high energy and intensity as the electron beams) could be produced by the inverse Compton scattering of laser light shone onto the electron beams. This would completely bypass the positron problem and permit the use of lower energy electron beams. Fig. 1.4 shows the schematic of a possible set up. This may also be possible without lasers, where colliding photons are instead generated from beamstrahlung [62]. Another idea is to use an XFEL to generate the gamma rays [67].

There are many different components of a multi-stage PWFA-LC, all of which must be considered together in order to minimize the beam emittance and energy spread before the final focus and maximize the luminosity at the IP. FACET-II at SLAC will undertake many such studies of both two-bunch PWFA as well as the beam delivery system and eventually beamstrahlung physics. However, the beam parameters at FACET-II are not as extreme as

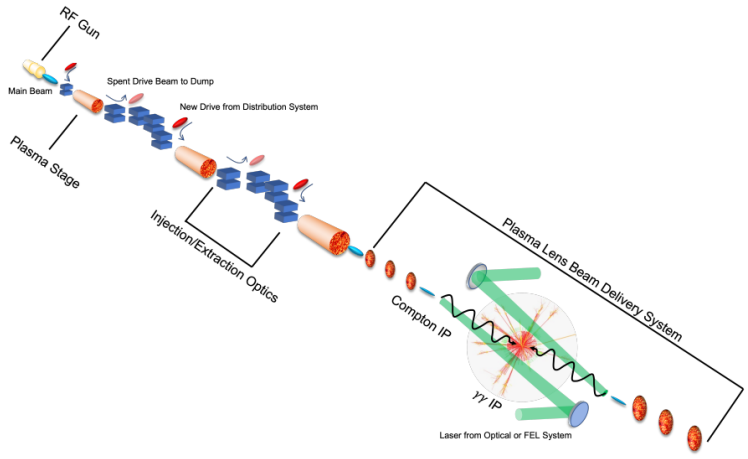

Figure 1.4: Illustration of a $\gamma - \gamma$ linear collider with plasma lens focusing elements [68]

would be needed for a PWFA-LC. Particle-in-cell simulations permit exploration of physics that will only manifest itself for LC beam parameters. Simulations have played a fundamental role in our understanding of PWFA, helped design and interpret experiments, and will help in the understanding of the complex beam interactions and non-linear QED effects that arise from them.

1.4 Particle-in-cell simulation

Computer simulations of plasmas have played a crucial role in the development of plasma theory, applications, and experiments. There are three broad categories of simulations: fluid or magnetohydrodynamics, fully kinetic (but continuum) or Vlasov, and fully kinetic (but discrete) or particle-in-cell (PIC). PIC [69, 70], as its name suggests, is a particle-based simulation where charged particles are pushed in their self-consistent electromagnetic fields. The charges and currents are deposited on a grid. Maxwell's equations are solved on the grid and then the fields (forces) are interpolated to the particle positions. The particles are then pushed using the Lorentz force. Because of the relatively few amount of assumptions, PIC typically captures complex physics most accurately but can be much more demanding than

fluid but potentially less demanding than Vlasov codes in multi-dimensions. Frequently, PIC is referred to as a numerical experiment, because all particle trajectories are calculated in their self-consistent fields. This in part explains the great successes of PWFA and LWFA, where simulations and experiments worked strongly in tandem with each other. Of course one typically cannot represent every plasma particle in a simulation, but instead we use macroparticles that represent many real particles. Interestingly, in some situations, it is possible to use one macroparticle for every beam particle. Furthermore, it is important to use small enough cell sizes to resolve the minimum length scale of the problem where important physics needs to be captured. OSIRIS [71, 72] is a fully-3D PIC code developed originally at UCLA (now co-developed with the Instituto Superior Técnico at the University of Lisbon) that has been used and benchmarked for a wide variety of plasma physics problems.

Plasma-based acceleration problems can be very expensive to simulate because often the physics is inherently three dimensional and beams must propagate long distances, so it can be beneficial to use reduced models to save computational costs. In PWFA and LWFA, one way to dramatically speed up PIC codes is to use the quasi-static approximation [73, 74]. This approximation is also widely used in the theoretical analysis of plasma wakefields, as we will discuss next chapter. QuickPIC, developed by C. Huang et al. [75] in 2006, was the first fully-3D, quasi-static PIC code. Later the code was improved by W. An et al. [76]. The quasi-static approximation assumes the beam evolves on a slower timescale than the plasma and uses the coordinates $(x, y, \xi = ct - z, s = z)$. Each 3D timestep, fixed s, the plasma is advanced on the fast timescale ξ through the beam, then the beam is pushed forward in s . By taking advantage of the quasi-static approximation, QuickPIC essentially embeds a 2D simulation with ξ being the time coordinate (and s fixed) into a 3D one with s being the time coordinate. The simulation is parallelized with a hybrid MPI domain decomposition in each 2D slab and there is also OpenMP parallelization within the MPI domain. Additional parallelization is possible because once a 2D slab has been advanced past some ξ (at a fixed s) another 2D slab can be initialized for $s + \Delta s$, before the slab at s has finished being

advanced to $\xi_{\max}$. Thus, multiple 2D slabs can be updated at the same time as long as they are synchronized. This is referred to as pipelining [77]. Because of the extra level of parallelization and the fact that the 3D timestep now just has to resolve the beams betatron wavelength ($k_\beta = k_p/\sqrt{2\gamma}$), QuickPIC has orders of magnitude speed-up over OSIRIS, while still being highly accurate for PWFA problems.

Another reduced model is the quasi-3D algorithm [78]. If a problem is completely azimuthally symmetric with respect to the propagation axis, then a cylindrical $r-z$ code will be equivalent to full 3D with the proper geometrical effects, but much faster because you have reduced the dimensionality. Quasi-3D is an extension of $r-z$, where the fields and current are expanded into azimuthal Fourier harmonics (or modes) of ϕ. It can be thought of as a hybrid approach that uses a PIC description in $r-z$ and a gridless description in ϕ. The field solve can be decomposed for each m mode, where the fields are now complex 2D arrays. Explicitly, the decomposition is

$$\begin{aligned}\mathbf{F}(r,z,\phi) &= \mathbb{R}\left\{\sum_{m=0}\mathbf{F}^m(r,z)e^{im\phi}\right\}\\ &= \mathbf{F}^0(r,z) + \mathbb{R}\left\{\mathbf{F}^1\right\}\cos\phi - \mathbb{I}\left\{\mathbf{F}^1\right\}\sin\phi\\ &+ \mathbb{R}\left\{\mathbf{F}^2\right\}\cos(2\phi) - \mathbb{I}\left\{\mathbf{F}^2\right\}\sin(2\phi)\\ &+ \ldots \end{aligned} \tag{1.9}$$

The particles are advanced in 3D Cartesian coordinates using the total fields. This algorithm has been implemented into OSIRIS [79] and recently has been implemented into the QuickPIC framework in a separate code called QPAD (QuickPIC with Azimuthal Decomposition) [80]. In QPAD, the 2D part is now 1D in r for each azimuthal mode number. QPAD has shown orders of magnitude speedup over QuickPIC for mostly azimuthally symmetric problems, where only a few modes are needed. QPAD is thus very useful for problems with moderate asymmetry. It is highly accurate even with only 3 modes (meaning $m = 0, 1, 2, 3$ were included) for problems with small beam offsets, as shown in Fig. 1.5. This example from Ref. [80] shows a witness beam undergoing transverse oscillations that are resonantly

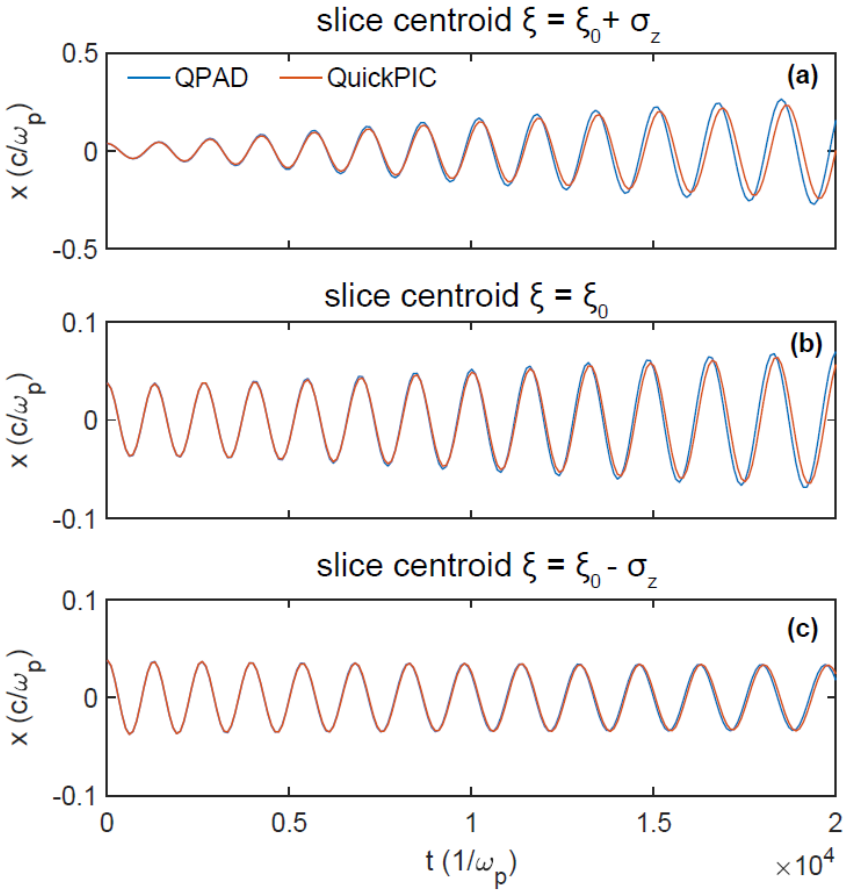

Figure 1.5: Beam centroid oscillations of slices (a) $+\sigma_z$, (b) 0, and (c) $-\sigma_z$ with respect to the beam center. Reproduced from [80].

coupled to the wake oscillations, therefore the oscillations grow in time. This is known as the hosing instability and will be described in detail in the next chapter. Because of the speedup and more highly resolved $r-z$ grid it has now become possible to simulate PWFA-LC problems fully self-consistently, which enabled much of the results in this dissertation. For high asymmetry, as many more modes are needed, eventually the speedup is lost and it is better to just use QuickPIC.

Finally, we can get substantial speedup by using mesh refinement which has recently been implemented into QuickPIC [81]. Currently, this is only available in a development branch of QuickPIC. This is particularly useful for highly asymmetric problems, such as flat

beams ($\sigma_x \gg \sigma_y$), where QPAD is not effective. When witness beams are very narrow, such as in PWFA-LC scenarios, the length scale ratio discrepancy between the witness beam spot size and blowout radius can be as large as 500. So using the same cell size throughout the simulation is a very inefficient use of computational resources. While this is still possible in QPAD since only a 1D grid in r is needed, in QuickPIC is not possible as a full 3D grid is needed. Instead, we can use a fine grid around the witness beam and any ion collapse and a larger grid around the drive beam and background plasma. This must be done in a smooth way and iterated to ensure numerical convergence and eliminate spurious signals when particles cross resolution boundaries [81].

1.5 Dissertation outline

The main goal of this dissertation is to provide theoretical analysis and high fidelity simulations of highly nonlinear beam and plasma interactions important for plasma-based accelerators. We heavily rely on quasi-static PIC simulations to verify our models and explore various ranges of parameters. Furthermore, in this dissertation we are mainly motivated by describing the electron arm of a PWFA-LC design. In Chapter 2, we review the most important theories that will be used and referenced throughout this dissertation. In Chapter 3, we begin by describing the hosing instability and asymmetric wakes by using a perturbation theory on the phenomenological model of the nonlinear blowout regime. We show that using a Fourier azimuthal decomposition of the fields can provide a more accurate hosing instability model by describing the perturbed plasma sheath fields with the $m = 1$ mode. We derive a very similar model to the hosing equation for wakes created by asymmetric (elliptical) beams using the $m = 2$ mode. In Chapter 4, we describe ways to mitigate the hosing instability. We rely on methods related to a known technique used for years in conventional accelerators called BNS damping. Many new studies have identified different mechanisms that can invoke this damping in plasma accelerators. We discuss how the drive beam may

be inherently stable and investigate two methods to mitigate witness beam hosing. The first using a direct energy chirp on the beam and the second by using asymmetric wakes. In Chapter 5, we investigate the problem of ion motion in PWFA-LCs. We describe this using a ring model and calculate the perturbation to the wakefields from this. We then show that drive beam induced ion motion can eliminate hosing and realign the witness beam with the drive beam axis, which is important when colliding beams. In Chapter 6, we discuss the need for plasma matching sections for PWFA-LCs when there is ion motion. We show that quasi-adiabatic plasma density ramps can simultaneously match the beams to the plasma in the presence of ion motion and realign the witness beam with the emittance growth limited to a couple percent. Finally, in Chapter 7, we will summarize our results and provide directions for future work.

CHAPTER 2

Review of the nonlinear theory of plasma wakefields and hosing

This chapter will consist of a review of existing theories to describe plasma wakefields in the blowout regime. We cover some of the fundamental equations and approximations commonly used. Then we review the foundational work of Lu et al. [27, 28] that calculated the fields in the blowout regime, as well as the theories for beam loading and hosing that employed this model. Finally, we discuss a more recent approach to calculate the equations that describe hosing. This will set the stage for the following chapter, where we discuss our approach to modeling hosing in regimes with highly intense beams.

2.1 Betatron motion of electrons in a pure ion column

When the drive beam has a high current, $\Lambda \equiv n_b/n_p(k_p\sigma_r)^2 \gtrapprox 1$, the plasma electrons are completely blown out, leaving a pure ion column behind the drive beam. The transverse (focusing) force an electron will feel in this ion column is given by Gauss's Law (the focusing field is actually electromagnetic),

$$\mathbf{F}_\perp = -\frac{\mathbf{r}}{2}\, m\omega_p^2, \tag{2.1}$$

where ω_p is the electron plasma frequency. We have assumed azimuthal symmetry so the x and y directions are the same, and so the force is proportional to $\mathbf{r}$. Looking at just the x direction, we have

$$F_x = \frac{dp_x}{dt} = \frac{d(\gamma m v_x)}{dt} = -\frac{x}{2}\, m\omega_p^2. \tag{2.2}$$

Assuming the particle moves at the speed of light, we have $cdt = dz$, and thus

$$\frac{d}{dz}(\gamma x') = -k_p^2 \frac{x}{2}, \tag{2.3}$$

where $' \equiv \frac{d}{dz}$ and k_p is the plasma wavenumber. So the electron equation of motion in the ion column is

$$x'' + \frac{\gamma'}{\gamma} x' + k_\beta^2 x = 0, \tag{2.4}$$

where $k_\beta \equiv k_p/\sqrt{2\gamma}$ is the betatron wavenumber. With no acceleration ($\gamma' = 0$), the beam electrons will exhibit simple harmonic oscillations at the betatron frequency as they propagate in the wake, known as betatron motion. If γ' is not a function of x or y, then the motion in the two transverse planes is decoupled. The acceleration and energy changes of the beam typically evolve on a timescale slower than the betatron frequency, so this is the smallest timescale we need to resolve. Explicitly,

$$\frac{\gamma'}{\gamma k_\beta} = E_z \sqrt{\frac{2}{\gamma}}, \tag{2.5}$$

where E_z is the normalized accelerating field, which is typically on the order of unity, so the second term in Eq. 2.4 is usually small, but its effect cannot be neglected. In Sec. 2.5, we discuss collective effects when the beam has an offset.

2.2 Quasi-static approximation and co-moving coordinates

As we mentioned in the introduction chapter, one of the fundamental approximations used in PBA is the quasi-static approximation (QSA) [73] which was developed to study short pulse laser-plasma interactions. Whittum et al. [82] also used similar approximations for describing particle beam-plasma interactions. This approximation is based on the assumption that the drive beam (moving at near the speed of light) evolves on a timescale (spatial scale) much slower (longer) than the plasma wake period (wavelength). It can thus be viewed as a sort of frozen field approximation, where the drive beam is "frozen" while the plasma evolves around it. It is helpful to make a mathematical transformation to a frame described by the

co-moving coordinates $(x, y, \xi = ct - z, s = z)$, where we take the speed of the driver and also the phase velocity of the wake to be the speed of light, c. Then, the QSA implies $\frac{\partial}{\partial s} \ll \frac{\partial}{\partial \xi}$. Since the beams evolves on the length scale of their betatron wavelength, $\lambda_\beta = 2\pi\sqrt{2\gamma_b}/k_p$, the approximation is valid when $\gamma_b \gg 1$.

Now we can write down Maxwell's equations in these co-moving coordinates and apply the quasi-static approximation. We start from the equations for the vector and scalar potentials, $\mathbf{A}$ and ϕ in the Lorenz gauge. In cgs units, we have

$$\left(\frac{1}{c^2}\frac{\partial^2}{\partial t^2} - \nabla^2\right)\begin{pmatrix}\mathbf{A}\\ \phi\end{pmatrix} = 4\pi\begin{pmatrix}\mathbf{J}/c\\ \rho\end{pmatrix}, \tag{2.6}$$

where the Lorenz gauge condition is

$$\frac{1}{c}\frac{\partial \phi}{\partial t} + \nabla\cdot\mathbf{A} = 0. \tag{2.7}$$

These equations are also accompanied by the continuity equation

$$\frac{\partial \rho}{\partial t} + \nabla\cdot\mathbf{J} = 0. \tag{2.8}$$

Now, our coordinate transformation implies

$$\frac{\partial}{\partial t} = \frac{\partial}{\partial \xi}\frac{\partial \xi}{\partial t} + \frac{\partial}{\partial s}\frac{\partial s}{\partial t} = c\frac{\partial}{\partial \xi} \tag{2.9}$$

$$\frac{\partial}{\partial z} = \frac{\partial}{\partial s}\frac{\partial s}{\partial z} + \frac{\partial}{\partial \xi}\frac{\partial \xi}{\partial z} = \frac{\partial}{\partial s} - \frac{\partial}{\partial \xi} \approx -\frac{\partial}{\partial \xi}, \tag{2.10}$$

where we applied the quasi-static approximation in the very last step. Upon substituting these into Eq. 2.6, we have

$$\begin{aligned}\left(\frac{\partial^2}{\partial \xi^2} - \nabla_\perp^2 - \frac{\partial^2}{\partial \xi^2}\right)\begin{pmatrix}\mathbf{A}\\ \phi\end{pmatrix} &= 4\pi\begin{pmatrix}\mathbf{J}/c\\ \rho\end{pmatrix}\\ -\nabla_\perp^2\begin{pmatrix}\mathbf{A}\\ \phi\end{pmatrix} &= 4\pi\begin{pmatrix}\mathbf{J}/c\\ \rho\end{pmatrix},\end{aligned} \tag{2.11}$$

where $\nabla_\perp = \hat{x}\frac{\partial}{\partial x} + \hat{y}\frac{\partial}{\partial y}$. The field equations are now two-dimensional Poisson equations such that intuition built from electrostatics and magnetostatics for infinitely long lines of charge and currents can be utilized. The gauge condition and continuity equations reduce to

$$\frac{\partial}{\partial \xi}\left(\phi - A_z\right) = -\nabla_\perp \cdot \mathbf{A}_\perp, \tag{2.12}$$

$$\frac{\partial}{\partial \xi}\left(\rho - J_z/c\right) = -\nabla_\perp \cdot \mathbf{J}_\perp/c, \tag{2.13}$$

respectively. We can rewrite Eq. 2.11 as

$$-\nabla_\perp^2(\phi - A_z) = 4\pi(\rho - J_z/c), \tag{2.14}$$

$$-\nabla_\perp^2 \mathbf{A}_\perp = 4\pi \mathbf{J}_\perp/c. \tag{2.15}$$

Now we can define a gauge-invariant pseudopotential, $\psi \equiv \phi - A_z$, and source term, $S \equiv -(\rho - J_z/c)$. Then, we have

$$\frac{\partial \psi}{\partial \xi} = -\nabla_\perp \cdot \mathbf{A}_\perp, \tag{2.16}$$

$$\nabla_\perp^2 \psi = 4\pi S, \tag{2.17}$$

$$\frac{\partial S}{\partial \xi} = \nabla_\perp \cdot \mathbf{J}_\perp/c. \tag{2.18}$$

The continuity equation now implies that the source term (which is an effective quasi-charge density) is conserved locally on a two dimensional grid where time is replaced with ξ. We can integrate the continuity equation over a transverse slice

$$\begin{aligned} \frac{d}{d\xi}\int r dr\, S(r,\xi) &= \int r dr\, \nabla_\perp \cdot \mathbf{J}_\perp/c \\ &= \oint_{\mathrm{bd}} \mathbf{J}_\perp/c \cdot d\mathbf{l}_\perp \\ &= 0, \end{aligned} \tag{2.19}$$

to find that the total quasi-charge is conserved within each slice. Thus, the continuity equation under the quasi-static assumption tells us for each transverse plasma slice, the

total quasi (or source) charge is conserved as the wake forms behind the driver. Before the driver arrives $S(r,\xi) = 0$, so we have

$$\int r dr\, S(r,\xi) = 0 \tag{2.20}$$

for all slices. This constraint will be used later. Now, we can express the full fields as

$$E_z = -\frac{\partial \phi}{\partial z} - \frac{1}{c}\frac{\partial A_z}{\partial t} = \frac{\partial \psi}{\partial \xi}, \tag{2.21}$$

$$B_z = \hat{z} \cdot (\nabla_\perp \times \mathbf{A}_\perp), \tag{2.22}$$

$$\mathbf{E}_\perp = -\nabla_\perp \phi - \frac{\partial \mathbf{A}_\perp}{\partial \xi}, \tag{2.23}$$

$$\mathbf{B}_\perp = \nabla_\perp \times (A_z \hat{z}) + \nabla_z \times \mathbf{A}_\perp. \tag{2.24}$$

Finally, the QSA implies a conserved quantity for particle trajectories [74]. This follows from the translational invariance in $s = z$. In the framework of Hamiltonian mechanics, the QSA leads to

$$\frac{dH}{dt} = \frac{\partial H}{\partial t} = c\frac{\partial H}{\partial \xi} = -c\frac{\partial H}{\partial z} = c\frac{dP_z}{dt}, \tag{2.25}$$

where H is the Hamiltonian and $P_z = p_z - e/cA_z$ is the canonical momentum. This leads to the conserved quantity

$$H - cP_z = \gamma mc^2 - e\phi - cp_z - eA_z = \gamma mc^2 - cp_z - e\psi. \tag{2.26}$$

We can again assume that the plasma is unperturbed in front of the driver, which leads to

$$\begin{aligned} \gamma mc^2 - cp_z - e\psi &= mc^2 \\ (\gamma - p_z/mc) &= 1 + e\psi/mc^2., \end{aligned} \tag{2.27}$$

In plasma-based acceleration, it is common to use normalized units to simplify the form of the equations. We normalize charge to the elementary charge e, mass to the electron mass m, lengths to c/ω_p, time to ω_p^{-1}, velocities to the speed of light c, charge densities to en_p, current densities to $en_p c$, electric and magnetic fields to $mc\omega_p/e$, potentials to mc^2/e, and forces to

$mc\omega_p$. These dimensionless units are also employed in our simulations. Using normalized units, the conserved quantity becomes $\gamma - p_z = 1 + \psi$, and we also have $\gamma^2 = 1 + p_\perp^2 + p_z^2$. We can combine these and solve for p_z to obtain

$$p_z = \frac{1 + p_\perp^2 - (1+\psi)^2}{2(1+\psi)}. \tag{2.28}$$

Thus, once ψ and $p_\perp$ are known, p_z will also be known.

2.3 Nonlinear wakefields in the blowout regime

We are now in a position to calculate the trajectory for an electron at the boundary of the plasma sheath and the ion column in the blowout regime as done in Refs. [27, 28]. We assume that the same electron remains at the innermost location, $r = r_b(\xi)$, which is not rigorously valid in the front of the bubble, but is a good approximation elsewhere. This leads to a differential equation for $r_b(\xi)$ in terms of ψ. Therefore, we will first need to calculate ψ using a phenomenological model for the source charge density in the sheath utilizing the fact that the total source charge, $S \equiv -(\rho - J_z)$, within each slice vanishes.

We assume azimuthal symmetry and so the forms of the potentials are solutions to the Poisson equations derived above. If we consider locations inside the bubble but outside the beam, these solutions can be written as

$$\phi(r,\xi) = \phi_0(\xi) - \frac{r^2}{4} + \Lambda(\xi)\ln r, \tag{2.29}$$

$$A_z(r,\xi) = A_{z0}(\xi) + \Lambda(\xi)\ln r, \tag{2.30}$$

where $\Lambda(\xi) = \int_0^\infty r dr\, n_b(\xi)$, $\phi_0(\xi) = \phi(r=0,\xi)$, $A_{z0}(\xi) = A_z(r=0,\xi)$, and $\phi(r=\infty) = A_z(r=\infty) = 0$. Both ϕ_0 and A_{z0} vary from slice to slice and neither are well-defined globally since the integral over their source terms also varies from slice to slice. However, a key point is that neither ϕ_0 and A_{z0} need to be known independently. Subtracting Eq. 2.30 from Eq. 2.29, we get

$$\psi(r,\xi) = \psi_0(\xi) - \frac{r^2}{4}. \tag{2.31}$$

The source term for ψ is the source charge, which is conserved slice to slice. The above expression is valid inside the beam since $\rho - J_z$ for the beam essentially vanishes. We also have the solution to Eq. 2.16,

$$A_r(r,\xi) = -\frac{r}{2}\frac{\partial \psi_0}{\partial \xi}. \tag{2.32}$$

The transverse force on an electron is

$$\begin{aligned} F_\perp &= -(E_r - v_z B_\theta) = \frac{\partial \phi}{\partial r} - v_z \frac{\partial A_z}{\partial r} + (1-v_z)\frac{\partial A_r}{\partial \xi} \\ &= -\frac{r}{2} + (1-v_z)\frac{\Lambda(\xi)}{r} - \frac{1}{2}(1-v_z)\frac{d^2\psi_0}{d\xi^2} r, \end{aligned} \tag{2.33}$$

where the first term is due to the uniform ion column, the second is due to the beam, and the third is due to the plasma radial currents. We can see that for electrons with $v_z = 1$, such as beam electrons, the last two terms vanish and we are left with a linear, radially inward focusing force. This is often stated as arising from space charge forces in the ion column. However, those arguments assume translational invariance. This description which describes the full electromagnetic character of the wake is more rigorous. Using the fact that $\frac{d\xi}{dt} = 1 - v_z$, we have

$$\frac{dp_\perp}{d\xi} = F_\perp/(1-v_z). \tag{2.34}$$

The LHS can be rewritten as

$$\frac{dp_\perp}{d\xi} = \frac{d(\gamma v_\perp)}{d\xi} = \frac{d}{d\xi}\left(\gamma(1-v_z)\frac{dr_\perp}{d\xi}\right) = \frac{d}{d\xi}\left((1+\psi)\frac{dr_\perp}{d\xi}\right) \tag{2.35}$$

and the RHS as

$$F_\perp/(1-v_z) = -\frac{r}{2(1-v_z)} + \frac{\Lambda(\xi)}{r} - \frac{1}{2}\frac{d^2\psi_0}{d\xi^2} r. \tag{2.36}$$

Using the constant of motion, Eq. 2.27, we have

$$\frac{1}{1-v_z} = \frac{\gamma}{1+\psi} = 1 + \frac{p_z}{1+\psi}, \tag{2.37}$$

and substituting in Eq. 2.28 leads to

$$\frac{1}{1-v_z} = \frac{1 + p_\perp^2 + (1+\psi)^2}{2(1+\psi)^2} = \frac{1}{2}\left(1 + \frac{1+p_\perp^2}{(1+\psi)^2}\right). \tag{2.38}$$

Using $p_\perp = (1+\psi)dr_\perp/d\xi$, we can write out the full equation of motion for an electron at $r = r_b(\xi)$,

$$\frac{d}{d\xi}\left((1+\psi)\frac{dr_b}{d\xi}\right) = r_b\left(-\frac{1}{4}\left[1+\frac{1}{(1+\psi)^2}+\left(\frac{dr_b}{d\xi}\right)^2\right]+\frac{\Lambda}{r_b^2}-\frac{1}{2}\frac{d^2\psi_0}{d\xi^2}\right), \tag{2.39}$$

where ψ is evaluated at r_b.

So to close the above equation we need to calculate $\psi_0(\xi)$ as a function of $r_b(\xi)$. To calculate this, we need a model for the source term to use in Eq. 2.17. Lu et al. [27, 28] used a simple constant density for the thin electron sheath given by

$$S(r,\xi) = \begin{cases} -1 & r < r_b \\ n_\Delta & r_b \le r \le r_b + \Delta \\ 0 & r > r_b + \Delta, \end{cases} \tag{2.40}$$

where Δ is the width of the sheath, which is a free parameter, and n_Δ is the electron density in the sheath. Using the fact that the total source charge within a given slice must vanish (Eq. 2.20), a relationship between Δ, n_Δ, and r_b can be found, namely

$$n_\Delta = \frac{r_b^2}{(r_b+\Delta)^2 - r_b^2}. \tag{2.41}$$

This model is illustrated in Fig. 2.1. There have been other models for the sheath that try to capture the fields outside the bubble more accurately [83] or to more accurately model the fields at the very rear of the bubble including capturing the negativity of ψ [31]. These more complicated models are generally necessary to describe important physical effects in the very rear of the bubble, such as self-injection or optimal beam loading.

Using the simple profile, Lu et al. [27, 28] showed that the solution to the Poisson equation for ψ gives, $\psi_0(\xi) = \frac{r_b^2(\xi)}{4}(1+\beta)$ for $r \le r_b$, where $\beta \equiv \frac{(1+\alpha)^2\ln(1+\alpha)^2}{(1+\alpha)^2-1} - 1$ and $\alpha \equiv \Delta/r_b$. We can then rewrite Eq. 2.39 and collect terms to obtain

$$A(r_b)\frac{d^2r_b}{d\xi^2} + B(r_b)r_b\left(\frac{dr_b}{d\xi}\right)^2 + C(r_b)r_b = \frac{\Lambda}{r_b}, \tag{2.42}$$

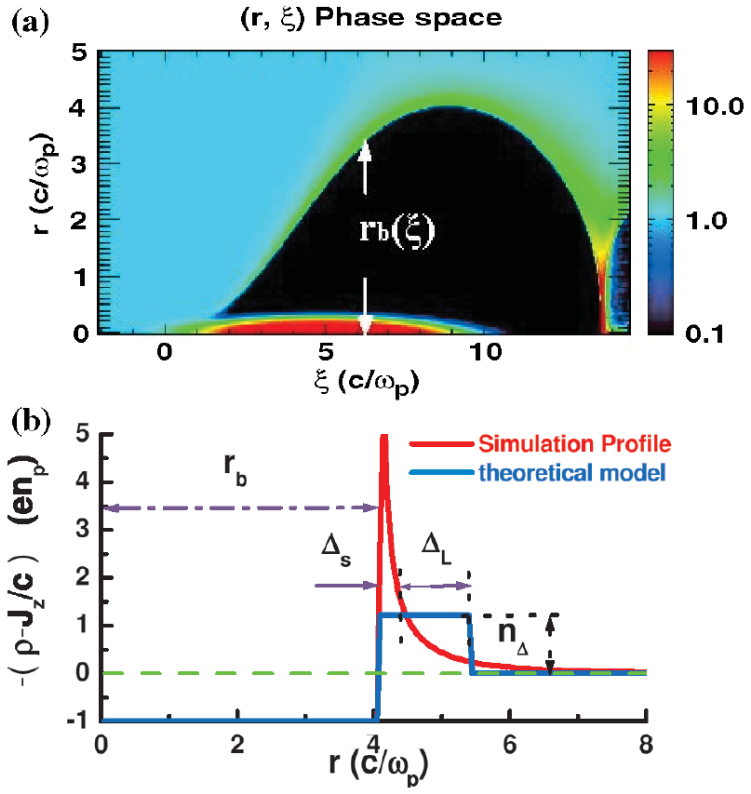

Figure 2.1: (a) Electron density with the defined blowout radius $r_b(\xi)$ and (b) $-(\rho - J_z/c)$ profile from a PIC simulation. Reproduced from [27].

where

$$A(r_b) = 1 + \left(\frac{1}{4} + \frac{\beta}{2} + \frac{1}{8} r_b \frac{d\beta}{dr_b}\right) r_b^2 \tag{2.43}$$

$$B(r_b) = \frac{1}{2} + \frac{3}{4}\beta + \frac{3}{4} r_b \frac{d\beta}{dr_b} + \frac{1}{8} r_b^2 \frac{d^2\beta}{dr_b^2} \tag{2.44}$$

$$C(r_b) = \frac{1}{4}\left(1 + \frac{1}{\left(1 + \frac{\beta}{4} r_b^2\right)^2}\right). \tag{2.45}$$

In the ultra-relativistic regime, where $r_{b,\max} \gg 1$ and therefore $\beta \ll 1$, Eq. 2.42 simplifies to

$$r_b \frac{d^2 r_b}{d\xi^2} + 2\left(\frac{dr_b}{d\xi}\right)^2 + 1 = \frac{4\Lambda}{r_b^2}. \tag{2.46}$$

This simplified version is similar to the equation for a circle for most of the trajectory when $\Lambda(\xi) = 0$. So we choose an appropriate Δ and solve Eq. 2.42, or just solve 2.46, to get $r_b(\xi)$ and then calculate $\psi(r, \xi)$, which fully characterizes the fields inside the wake.

2.4 Beam loading in the blowout regime

One important consequence of having a phenomenological model of the wakefields in the blowout regime is the development of a beam loading theory for nonlinear wakes. As mentioned in the last chapter, beam loading is essential to maintain low energy spread which will be crucial in order to focus beams at the interaction point for linear colliders. Energy spread may also cause larger emittance growth during acceleration. Beam loading is also important to absorb as much of the wake energy as possible, both to maximize efficiency and also to prevent heat escaping and damaging the walls of the plasma chamber.

In this dissertation, we will use existing beam loading theory to determine how to properly load the witness beam. The first theory of beam loading was developed for the linear regime [24], where the wakes are sinusoidal and superposition is valid. By placing a second bunch in the negative phase of E_z, we can flatten it using superposition by using a bunch with triangular density $\rho(\xi) = \rho_0(\xi_f - \xi)/(\xi_f - \xi_0)$, where ξ_0 is the head of the beam and ξ_f is the tail.

In the blowout regime, the wakefield E_z is a function of the blowout radius and its slope, as discussed in the previous section. Therefore, in order to flatten the wakefield with a witness beam, we will need to calculate how the witness beam alters the wake shape. This was done in Refs. [29, 30], and we review the main results from these papers next.

In order to make the analysis tractable, we use the ultra-relativistic limit where $\psi \approx \frac{r_b^2 - r^2}{4}$ and therefore

$$E_z = \frac{\partial \psi}{\partial \xi} = \frac{1}{2} r_b \frac{dr_b}{d\xi}. \tag{2.47}$$

We first write Eq. 2.46 in terms r_b only,

$$\frac{dr_b'}{dr_b} = \frac{4\lambda(r_b) - r_b^2\left(2(r_b')^2 + 1\right)}{r_b^3 r_b'}, \tag{2.48}$$

where $\lambda(r_b) = \Lambda(\xi)$. We can then integrate this and substitute the result into Eq. 2.47 to obtain

$$E_z = -\frac{r_b}{2\sqrt{2}}\sqrt{\frac{16\int_{r_b}\lambda(\zeta)\zeta d\zeta + C}{r_b^4} - 1}. \tag{2.49}$$

We can evaluate the constant C by using the condition $E_z(r_b = R_b) = 0$, where $R_b = \max(r_b)$, and the fact that $\lambda = 0$ in this region. We obtain $C = R_b^4$. Also, we note that R_b can be shown to roughly scale as $R_b \approx 2\sqrt{\Lambda_0}$ [26]. We would like E_z to be a constant, $-E_s$, within the witness beam, i.e., starting at $\xi = \xi_s$. Therefore, we have

$$E_s = \frac{r_b}{2\sqrt{2}}\sqrt{\frac{16\int_{r_s}^{r_b}\lambda(\zeta)\zeta d\zeta + R_b^4 - r_b^4}{r_b^4}}, \tag{2.50}$$

where $r_s \equiv r_b(\xi_s)$. The resulting current profile that achieves this is therefore,

$$\lambda(r_b) = E_s^2 + \frac{r_b^2}{4} \tag{2.51}$$

and the magnitude of the loaded wakefield is

$$E_s = \frac{r_s}{2\sqrt{2}}\sqrt{\frac{R_b^4}{r_s^4} - 1}. \tag{2.52}$$

To find how the wake's shape ($r_b(\xi)$ trajectory) is perturbed by the witness beam, we can integrate Eq. 2.47,

$$-E_s = \frac{1}{2} r_b r_b' = \frac{1}{4}(r_b^2)' \tag{2.53}$$

starting from ξ_s to obtain $r_b^2 = r_s^2 - 4E_s(\xi - \xi_s)$. Thus, when $r_b = 0$, it follows that $\xi = \xi_s + r_s^2/(4E_s)$, which determines the end of the loaded wake. The value of blowout radius at the front of the beam, r_s, can be expressed in terms of E_s as $r_s^2 = \sqrt{16E_s^4 + R_b^4} - 4E_s^2$. Next, substituting the expression for r_b within the witness beam region into Eq. 2.51, we arrive at

$$\Lambda(\xi) = \sqrt{E_s^4 + \frac{R_b^4}{16}} - E_s(\xi - \xi_s). \tag{2.54}$$

This is the well known trapezoidal shape, which is similar in form to the linear wakefield result. Fig. 2.2 shows the loaded wake from a beam with this profile from a PIC simulation. This can be integrated to get the total charge that can be loaded into the wake,

$$Q_s = 2\pi \int_{\xi_s}^{r_s^2/(4E_s)} \Lambda(\xi) d\xi = \frac{\pi R_b^4}{16 E_s}. \tag{2.55}$$

This has important implications for the acceleration gradient and energy transfer efficiency. $Q_s E_s$ is the energy absorbed per unit length and because it is a constant there is a trade-off between the amount of charge that can be accelerated and the gradient with which it can be accelerated.

An improved beam loading theory was recently developed by Dalichaouch et al. [31] which better models the rear of the wake using a multisheath model for ψ, which also explains the negativity of ψ. It provides an improved estimate for the transfer efficiency and amount of charge that can be loaded. The current profile is only slightly modified; it remains approximately trapezoidal.

2.5 Hosing theory

The hosing instability and its consequences remains a major obstacle to the development of a future plasma-based LC and it is one one of the major topics of this dissertation. In this section we review the existing theories for this instability. Transverse wakefield instabilities have been studied for decades in conventional RF linear accelerators. Offset beams which

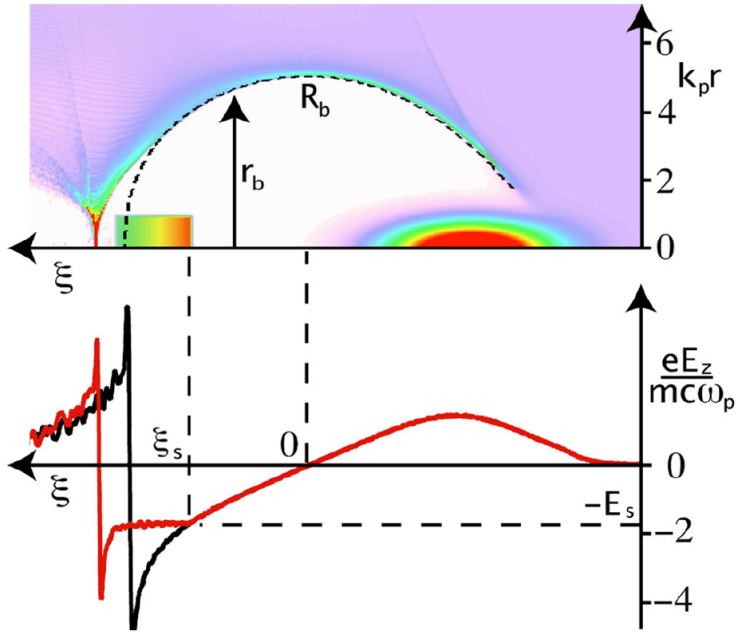

Figure 2.2: The electron density from a PIC simulation with OSIRIS for $k_p R_b = 5$ is presented. The beams move to the right. The broken black line traces the blowout radius in the absence of the load. On the bottom, the red (black) line is the lineout of the wakefield $E_z(\xi, r_b = 0)$ when the beam load is present (absent). Reproduced from [29].

create dipole EM modes in the cavity can result in amplification of the beam oscillation and eventually beam breakup. The mode is excited at the beam head and results in strong deflection at the tail. These modes can also excite the instability in subsequent bunches. In general, there is more deflection with higher current and less with higher energy. The cure for this instability is called Balakin-Novokhatski-Smirnov (BNS) damping, which in simple terms breaks the resonance of the instability by introducing a variation in energy or focusing along the bunch. This phase mixing method can also be applied in the blowout regime of PWFA, as we will discuss in Chapter 4. Next, we will discuss general transverse beam dynamics and the theories of hosing for plasma-based accelerators.

2.5.1 Transverse dynamics of a beam slice

We start by considering a beam slice consisting of N particles. The centroid is defined by

$$x_b \equiv \langle x \rangle = \frac{1}{N}\sum_i^N x_i, \tag{2.56}$$

where x_i is the transverse position of each particle. We assume linear focusing forces so that the transverse planes are decoupled. The spot size of the slice is defined by

$$\sigma_x = \sqrt{\langle (x - x_b)^2 \rangle}. \tag{2.57}$$

The dynamics of the centroid and spot size can be solved for using the equation of motion derived above, Eq. 2.4, except we now include the resulting plasma channel centroid, x_c, resulting from the offset beam,

$$x'' + \frac{\gamma'}{\gamma}x' = -\frac{k_p^2}{2\gamma}(x - x_c), \tag{2.58}$$

where $' \equiv \frac{d}{ds}$. The centroid equation is therefore

$$x_b'' = \left\langle -\frac{\gamma'}{\gamma}x' - \frac{k_p^2}{2\gamma}(x - x_c) \right\rangle = -\left\langle \frac{\gamma'}{\gamma}x' \right\rangle - \left\langle \frac{k_p^2}{2\gamma}(x - x_c) \right\rangle. \tag{2.59}$$

Next, we assume there is an uncorrelated energy spread and energy change, i.e., $\gamma = \overline{\gamma} + \Delta\gamma$ and $\gamma' = \overline{\gamma'} + \Delta\gamma'$, where the bar represents the slice average. We have

$$\begin{aligned}\left\langle \frac{\gamma'}{\gamma} x' \right\rangle &= \frac{\overline{\gamma'} + \Delta\gamma'}{\overline{\gamma} + \Delta\gamma} x'_b \\ &\approx \frac{\overline{\gamma'} + \Delta\gamma'}{\overline{\gamma}} \left(1 - \frac{\Delta\gamma}{\overline{\gamma}}\right) x'_b \\ &\approx \frac{\overline{\gamma'} + \Delta\gamma'}{\overline{\gamma}} x'_b - \frac{\overline{\gamma'}\Delta\gamma}{\overline{\gamma}} x'_b, \end{aligned} \tag{2.60}$$

where we assumed $\Delta\gamma \ll \overline{\gamma}$ and $\Delta\gamma\Delta\gamma' \ll \overline{\gamma}\,\overline{\gamma'}$, and

$$\left\langle \frac{k_p^2}{2\gamma}(x - x_c) \right\rangle \approx \overline{k_\beta}^2 \left(1 - \frac{\Delta\gamma}{\overline{\gamma}}\right)(x_b - x_c), \tag{2.61}$$

where $\overline{k_\beta} = k_p/\sqrt{2\overline{\gamma}}$. The equation for the beam centroid becomes

$$x''_b + \frac{\overline{\gamma'} + \Delta\gamma'}{\overline{\gamma}} x'_b + \frac{\overline{\gamma'}\Delta\gamma}{\overline{\gamma}} x'_b + \overline{k_\beta}^2 \left(1 - \frac{\Delta\gamma}{\overline{\gamma}}\right)(x_b - x_c) = 0. \tag{2.62}$$

With no energy spread and assuming all particles are accelerated equally, we have

$$x''_b + \frac{\overline{\gamma'}}{\overline{\gamma}} x'_b + \overline{k_\beta}^2 (x_b - x_c) = 0. \tag{2.63}$$

The spot size evolution can be calculated by taking derivatives of the spot size definition, Eq. 2.57 (assuming $\Delta\gamma = \Delta\gamma' = 0$). We define $\tilde{x} \equiv x - x_b$. The first derivative is $\sigma'_x = \langle \tilde{x}\tilde{x}' \rangle / \sigma_x$. The second derivative is

$$\begin{aligned}\sigma''_x &= \frac{\langle \tilde{x}\tilde{x}'' \rangle + \langle \tilde{x}'^2 \rangle}{\sigma_x} - \sigma'^2_x \\ &= \frac{\langle \tilde{x}^2 \rangle \langle \tilde{x}'^2 \rangle - \langle \tilde{x}\tilde{x}' \rangle}{\sigma_x^3} + \frac{\langle \tilde{x}\tilde{x}'' \rangle}{\sigma_x} \\ &= \frac{\epsilon_x^2}{\sigma_x^3} + \frac{\langle \tilde{x}\tilde{x}'' \rangle}{\sigma_x}, \end{aligned} \tag{2.64}$$

where $\epsilon_x \equiv \sqrt{\langle \tilde{x}^2 \rangle \langle \tilde{x}'^2 \rangle - \langle \tilde{x}\tilde{x}' \rangle}$ is the geometric slice emittance. We can evaluate the last term in Eq. 2.64,

$$\begin{aligned}\langle \tilde{x}\tilde{x}'' \rangle &= \left\langle (x - x_b) \left[-\frac{\gamma'}{\gamma}(x' - x'_b) - k_\beta^2 (x - x_b) \right] \right\rangle \\ &= -\frac{\gamma'}{\gamma} \sigma_x \sigma'_x - k_\beta^2 \sigma_x^2. \end{aligned} \tag{2.65}$$

The evolution of the spot size is therefore given by

$$\sigma_x'' + \frac{\gamma'}{\gamma}\sigma_x' = \frac{\epsilon_x^2}{\sigma_x^3} - k_\beta^2 \sigma_x. \tag{2.66}$$

The spot size will be constant if each side equals zero, which means the matched spot size is given by

$$\sigma_m^2 = \epsilon_x / k_\beta. \tag{2.67}$$

So we have described the dynamics of the centroid and spot size of beam slice given the plasma channel offset. The spot size, centroid, and energy are all functions of the longitudinal coordinate ξ. The challenging part about modeling hosing is predicting the channel centroid given the beam centroid, i.e., obtaining the equation for $x_c(\xi)$ given an $x_b(\xi)$. In the next section, we will take a brief digression to explore beam matching and energy spread in more detail.

2.5.2 Beam matching with energy spread and offsets

In this section, we describe beam matching when the beam has a finite energy spread and the emittance evolution when the beam has an energy spread and offset.

In general, when a beam has an energy spread, the particles will orbit with different phases in trace space, (x, x'), hence leading to a larger area in trace space and thus emittance growth. However, following Ref. [84], we can show that if the beam starts initially matched, the emittance will not grow for small energy spreads. We start with the solution to $x'' + k_\beta^2 x = 0$, where k_β^2 is constant for an individual particle (Eq. 2.63 in the absence of acceleration),

$$x(z) = x(0)\cos(k_\beta z) + \frac{x'(0)}{k_\beta}\sin(k_\beta z). \tag{2.68}$$

Taking the derivative gives

$$x'(z) = -x(0)k_\beta \sin(k_\beta z) + x'(0)\cos(k_\beta z). \tag{2.69}$$

We define the betatron phase $\phi \equiv k_\beta z$ and calculate the second order moment

$$\begin{aligned}\langle x^2 \rangle &= \langle x_i^2 \rangle \langle \cos^2 \phi \rangle + \langle x_i'^2 \rangle \left\langle \frac{\sin^2 \phi}{k_\beta} \right\rangle + \langle x_i x_i' \rangle \left\langle \frac{\sin(2\phi)}{k_\beta} \right\rangle \\ &\approx \langle x_i^2 \rangle \langle \cos^2 \phi \rangle + \langle x_i'^2 \rangle \frac{\langle \sin^2 \phi \rangle}{\overline{k_\beta}} + \langle x_i x_i' \rangle \frac{\langle \sin(2\phi) \rangle}{\overline{k_\beta}},\end{aligned} \tag{2.70}$$

where we assume the energy spread is small so we can use the average k_β and take it out of the average. After the beam phase mixing is complete, we will have

$$\langle \cos^2 \phi \rangle = \frac{1}{2}, \quad \langle \sin^2 \phi \rangle = \frac{1}{2}, \quad \langle \sin(2\phi) \rangle = 0, \tag{2.71}$$

because the particle's ϕ coordinate will be uniformly distributed. We therefore have

$$\langle x^2 \rangle = \frac{1}{2} \left(\langle x_i^2 \rangle + \frac{\langle x_i'^2 \rangle}{\overline{k_\beta}^2} \right). \tag{2.72}$$

Using the same reasoning for x', we have

$$\langle x'^2 \rangle = \frac{1}{2} \left(\overline{k_\beta}^2 \langle x_i^2 \rangle + \langle x_i'^2 \rangle \right), \tag{2.73}$$

and finally $\langle x x' \rangle = 0$. So the final geometric emittance is

$$\epsilon = \sqrt{\langle x^2 \rangle \langle x'^2 \rangle} = \frac{1}{2} \left(\overline{k_\beta} \langle x_i^2 \rangle + \frac{\langle x_i'^2 \rangle}{\overline{k_\beta}} \right) = \frac{1}{2} \left(\overline{k_\beta} \sigma_{x_i}^2 + \frac{\sigma_{x_i'}}{\overline{k_\beta}} \right) \tag{2.74}$$

The initial (matched) emittance is given by

$$\epsilon_i = \sigma_{x_i} \sigma_{x_i'} = \overline{k_\beta} \sigma_{x_i}^2, \tag{2.75}$$

where in the last equality, we used the matching condition given by Eq. 2.67. Then, we can solve for $\sigma_{x_i'}$ and substitute this into Eq. 2.74 to arrive at $\epsilon = \epsilon_i$. Thus, we have shown that for a small energy spread, if the beam is initially matched it will remain matched.

When the beam accelerates, its geometric emittance is no longer conserved, it decreases with increasing γ. Instead, we care about the normalized emittance, $\epsilon_N \equiv \sqrt{\langle x^2 \rangle \langle p_x^2 \rangle - \langle x p_x \rangle}$. When the energy spread is small, we have $\epsilon_N \approx \overline{\gamma} \epsilon$. Next, we show when the beam is accelerated without energy spread, the normalized emittance is conserved in a linear focusing

force ($p'_x = F_x = Kx$). We start by taking the derivative of ϵ_N^2 to obtain

$$\begin{aligned} 2\epsilon_N\epsilon'_N &= 2\langle xx'\rangle\langle p_x^2\rangle + \langle x^2\rangle\langle 2p_xp'_x\rangle - 2\langle xp_x\rangle\left(\langle xp'_x\rangle + \langle x'p_x\rangle\right) \\ &= \frac{2}{\gamma}\langle xp_x\rangle\langle p_x^2\rangle + 2K\langle x^2\rangle\langle xp_x\rangle - 2\langle xp_x\rangle\left(K\langle x^2\rangle + \frac{1}{\gamma}\langle p_x^2\rangle\right). \\ &= 0. \end{aligned} \tag{2.76}$$

We thus have $\epsilon'_N = 0$, which means the normalized emittance is conserved when the beam is accelerating in a linear focusing force. It can be shown analytically that the normalized emittance of a matched beam with a small energy spread, but no acceleration, does not grow. Finally, we can see from simulations that if the beam is initially matched, is accelerating, and has a small energy spread, the normalized emittance is still conserved [85].

We have shown the importance of matching the beam to the plasma, but what happens when the beam is offset? It is easy to recalculate the emittance growth when there is energy spread and offsets. Starting from Eq. 2.74, we add offsets $x_i = \tilde{x}_i + \Delta x$ and $x'_i = \tilde{x}'_i + \Delta x'$, where $\langle\tilde{x}_i\rangle = \langle\tilde{x'_i}\rangle = 0$. We have

$$\begin{aligned} \epsilon_{sat} &= \frac{1}{2}\left[\overline{k_\beta}\langle(\tilde{x}_i + \Delta x)^2\rangle + \frac{1}{\overline{k_\beta}}\langle(\tilde{x}'_i + \Delta x')^2\rangle\right] \\ &= \frac{1}{2}\left[\overline{k_\beta}(\sigma_{x_i}^2 + \Delta x^2) + \frac{1}{\overline{k_\beta}}(\sigma_{x'_i}^2 + \Delta x'^2)\right] \\ &= \frac{1}{2}\left[\overline{k_\beta}\sigma_{x_i}^2\left(1 + \frac{\Delta x^2}{\sigma_{x_i}^2}\right) + \frac{\sigma_{x'_i}^2}{\overline{k_\beta}}\left(1 + \frac{\Delta x'^2}{\sigma_{x'_i}^2}\right)\right] \\ &= \frac{1}{2}\left[\epsilon_i\left(1 + \frac{\Delta x^2}{\sigma_{x_i}^2}\right) + \epsilon_i\left(1 + \frac{\Delta x'^2}{\sigma_{x'_i}^2}\right)\right]. \end{aligned} \tag{2.77}$$

Thus, we obtain

$$\frac{\epsilon_{sat}}{\epsilon_i} = 1 + \frac{\Delta x^2}{2\sigma_{x_i}^2} + \frac{\Delta x'^2}{2\sigma_{x'_i}^2}, \tag{2.78}$$

and because $\epsilon_N \approx \bar{\gamma}\epsilon$, we have $\epsilon_{Nsat}/\epsilon_{Ni} \approx \epsilon_{sat}/\epsilon_i$. This result intuitively makes sense, when we think about the beam phase mixing. The beam spreads out in phase space according to how large the offset is with respect to the initial spot size. So when the beam is oscillating

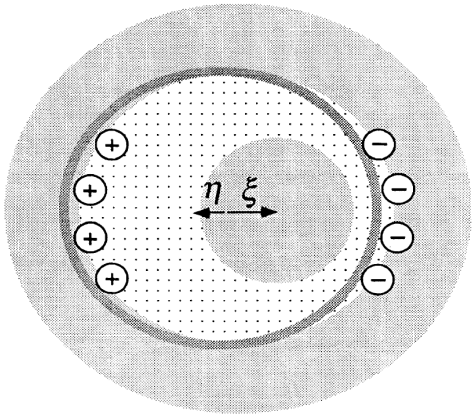

Figure 2.3: A beam slice in the ion channel, displaced by an amount ξ [denoted x_b in the text] in the x direction, induces a displacement η [denoted x_c in the text] of the channel wall, which responds as a simple harmonic oscillator with angular frequency ω_0, deflecting follow-on portions of the beam. Reproduced from [86].

with energy spread, the offset decays but at the cost of emittance growth. This will be examined in more detail in later chapters. We will now return to describing theories for describing the hosing instability.

2.5.3 Linear fluid theory in a long, adiabatic plasma channel

Before we address the nonlinear theory for the blowout regime, we review the seminal work by Whittum et al. [86]. This paper derives the equations that describe the hosing instability for an electron beam in an underdense plasma. It assumes a cold, fluid plasma channel and a rigid, round beam with a small offset, x_b, inside the ion channel, where the electrons have been adiabatically expelled, i.e., the blowout radius is a constant. Fig. 2.3 shows a diagram of this setup.

The equilibrium plasma electron density is $\rho_{e0} = -en_eH(r-b)$, where b is the channel radius and H is the Heaviside function. The beam density is assumed to be transversely uniform with radius a, given by $\rho_{b0} = -en_b(1-H(r-a))$. We can determine the perturbed

plasma from the cold fluid equations (assuming the motion in z is negligible)

$$\frac{\partial \rho_{e1}}{\partial \xi} + \nabla_\perp \cdot (\rho_{e0} \mathbf{v}_{e1}) \approx 0 \tag{2.79}$$

$$\frac{\partial \mathbf{v}_{e1}}{\partial \xi} \approx \frac{e}{m} \nabla_\perp \phi_1, \tag{2.80}$$

where $\mathbf{v}_{e1}$ is the plasma electron velocity. We let the shift in the channel be in the x direction and denote it as x_c, from which it follows that $\mathbf{v}_{e1} = \partial_\xi x_c \hat{\mathbf{x}}$. From Eq. 2.79, we have

$$\begin{aligned}
\partial_\xi \rho_{e1} &= -\rho_{e0} \nabla_\perp \cdot (\partial_\xi x_c \hat{\mathbf{x}}) - (\nabla_\perp \rho_{e0}) \cdot (\partial_\xi x_c \hat{\mathbf{x}}) \\
&= -\rho_{e0} \partial_x \partial_\xi x_c + e n_e \delta(r-b) \partial_\xi x_c \hat{\mathbf{r}} \cdot \hat{\mathbf{x}} \\
&= e n_e \delta(r-b) \partial_\xi x_c \cos\theta,
\end{aligned} \tag{2.81}$$

where $\nabla_\perp x_c = 0$ and δ is the Dirac delta function. We can thus see that ρ_{e1} is described as a surface charge at $r = b$, given by $\rho_{e1} = e n_e \delta(r-b) x_c \cos\theta$. Similarly, the beam is rigidly displaced in x by x_b, therefore $\rho_{b1} = -e n_b x_b \delta(r-a) \cos\theta$. We can then solve the Poisson equations to get

$$\psi_1 = 2\pi e n_e x_c \cos\theta \left(\frac{b^2 - r^2}{r} H(r-b) + r \right) \tag{2.82}$$

$$A_{z1} = -2\pi e n_b x_b \cos\theta \left(\frac{a^2 - r^2}{r} H(r-a) + r \right), \tag{2.83}$$

where the source term for ψ_1 is from the plasma, $\rho - J_z \approx \rho_{e1}$, and the source term for A_{z1} is from the beam, ρ_{b1}.

We can add Eq. 2.82 and Eq. 2.83 to obtain $\phi_1 = \psi_1 + A_{z1}$ (note we could have solved for ϕ_1 directly using the charge densities for both the plasma and beam) and then solve Eq. 2.79 and Eq. 2.80 for the channel response

$$\frac{\partial^2}{\partial \xi^2} x_c(\xi, s) + \omega_0^2 x_c(\xi, s) = \left(\frac{n_b a^2}{n_e b^2} \right) \omega_0^2 x_b(\xi, s) = \omega_0^2 x_b(\xi, s), \tag{2.84}$$

where $\omega_0^2 = \omega_p^2/2$. Using the Lorentz force on the beam, we can solve for the beam response,

$$\frac{\partial^2}{\partial s^2} x_b(\xi, s) + \frac{1}{\gamma} \frac{\partial \gamma}{\partial s} \frac{\partial}{\partial s} x_b(\xi, s) + k_\beta^2 x_b(\xi, s) = k_\beta^2 x_c(\xi, s). \tag{2.85}$$

This is the same equation we derived above, Eq. 2.63. Ignoring the change in energy term for now and denoting $' \equiv \frac{d}{d\xi}$ and $\dot{} \equiv \frac{d}{ds}$, we can write the above equations in the compact form

$$\begin{cases} x_c'' + \omega_0^2 x_c = \omega_0^2 x_b \\ \ddot{x_b} + k_\beta^2 x_b = k_\beta^2 x_c. \end{cases} \tag{2.86}$$

These are the equations for two coupled harmonic oscillators. Given an initial beam offset x_{b0}, we can solve for the channel centroid x_c along the beam, then we can evolve the beam centroid x_b given the solution for x_c, and so forth. These equations predict a resonant phenomena where the centroid amplitudes grow exponentially until the beam is lost or other nonlinearities arise.

Assuming an infinitely long beam and channel, perturbations will vary as $\exp(iks - i\omega\xi)$ and we get the dispersion relation

$$\left(1 - \frac{k^2}{k_\beta^2}\right)\left(1 - \frac{\omega^2}{\omega_0^2}\right) = 1, \tag{2.87}$$

which is the same as the two-stream instability dispersion relation if we let $\omega \to \omega - kV_b$ and $\omega_0 \to \omega_{pi}$, $\omega_\beta \to \omega_{pe}$. A solution for the beam centroid evolution can be found in the strong focusing and short bunch/long plasma limit, $k_\beta s \gg \omega_0 \xi$, assuming a uniform offset,

$$\frac{x_b(\xi)}{x_{b0}} \approx 0.263 \frac{e^A}{\sqrt{A}} \cos\left(k_\beta s - \frac{A}{\sqrt{3}} + \frac{\pi}{12}\right), \tag{2.88}$$

where $A = 1.3(k_\beta s)^{1/3}(\omega_0 \xi)^{2/3}$ [87]. Note that A is related to both the exponential growth as well as a shift in the betatron wavenumber. In the long bunch/short plasma limit, one interchanges s and ξ in the expression for A. For stronger beams and wakes with varying blowout radius, these results overestimate the hosing growth. Next, we address the theory developed for this regime.

2.5.4 Hosing theory in the blowout regime

Hosing theory in the blowout regime was first developed by Huang et al. [88] in 2007, based on the nonlinear theory for the blowout regime of Lu et al. [28, 27], discussed earlier. This

theory modifies the plasma centroid equation but not the beam centroid equation. In the linear fluid model, the electrons in the unperturbed sheath are assumed to be at rest. Here, we use the zeroth order trajectory from Ref. [27, 28] and apply a linear perturbation (assuming a small hosing amplitude). One major assumption of this model is that the channel is rigidly displaced to a new location and is not deformed (this assumption was also used in Whittum et al. [86]). So the channel centroid can be defined as $x_c(\xi) = (r_+(\xi) - r_-(\xi))/2$, where $r_+(\xi)$ and $r_-(\xi)$ are the perturbed blowout radii for the top and bottom electron trajectories, respectively.

We start with the equation of motion for a plasma electron trajectory

$$\frac{dp_\perp}{dt} = -(E_r + v_z B_\theta), \tag{2.89}$$

and on the LHS we use the same simplification we used in the previous section, leading to

$$2(1+\psi)^2 \frac{d}{d\xi}\left((1+\psi)\frac{dr}{d\xi}\right) = -(E_r + v_z B_\theta)\left(1 + (1+\psi)^2\left(\frac{dr}{d\xi}\right)^2 + (1+\psi)^2\right). \tag{2.90}$$

Next, we apply linear perturbation theory as follows

$$r = r_0 + r_1$$

$$E_r(r_0 + r_1) = E_0 + E_1$$

$$B_\theta(r_0 + r_1) = B_0 + B_1$$

$$v_z = v_0 + v_1$$

$$\psi(r_0 + r_1) = \psi_0 + \psi_1 \approx \psi_0, \tag{2.91}$$

where the last approximation comes from the rigid channel assumption. Using the convention $' \equiv \frac{d}{d\xi}$, the first order equation is

$$\begin{aligned} 2(1+\psi_0)^2\psi_0' r_1' + 2(1+\psi_0)^3 r_1'' = &-2(E_0 - v_0 B_0)(1+\psi_0)^2 r_0' r_1' \\ &- (E_1 - v_0 B_1 - v_1 B_0)\left(1 + (1+\psi_0)^2 r_0'^2 + (1+\psi_0)^2\right). \end{aligned} \tag{2.92}$$

The zeroth order equation is of course equivalent to the Lu et al. result (Eq. 2.39), and we can use this to simplify the first order equation to

$$r_1'' + \left[\frac{\psi_0'}{1+\psi_0} - \frac{1}{\gamma_0}\left((1+\psi_0)r_0'' + \psi_0' r_0'\right) r_0'\right] r_1' = -\frac{\gamma_0}{(1+\psi_0)^2}\left(E_1 - v_0 B_1 - v_1 B_0\right). \quad (2.93)$$

In the Huang et al. treatment of this problem, the short-pulse limit was considered where ψ_0'/ψ_0, r_0'', $r_0'\psi_0' \ll r_1''/r_1'$, so the r_1' term in the above equation was dropped.

The self-consistent perturbed force on the boundary electron, $-(E_1 - v_0 B_1 - v_1 B_0)$, is the sum of the perturbation from the beam fields and plasma fields in the sheath. In Huang's dissertation [89], this is quantified through the parameter $c_1(\xi)$ (here we will call it $c_p(\xi)$) that is calculated with simulation data (in the paper this is set to one). In the next chapter, we will rederive this equation without dropping terms by calculating the self-consistent plasma sheath fields. We define $c_p(\xi)$ as

$$-(E_1 - v_0 B_1 - v_1 B_0) = F_{b1} + F_{p1} \equiv F_{b1} c_p(\xi), \quad (2.94)$$

where F_{b1} is the perturbed beam force and F_{p1} is the perturbed plasma force. The fields of a transversely bi-Gaussian beam can be quickly derived when the beam is displaced by x_b,

$$E_{b1} = B_{b1} = -\frac{n_b \sigma_r^2}{(r_0 + r_1 - x_b) - r_0}, \quad (2.95)$$

and therefore, using $|r_1 - x_b| \ll r_0$ and $\Lambda = n_b \sigma_r^2$,

$$F_{b1} \approx (1 - v_0)\frac{\Lambda}{r_0^2}(x_b - r_1). \quad (2.96)$$

We can now rewrite the first order equation as

$$r_1'' = c_p c_r c_\psi (x_b - r_1), \quad (2.97)$$

where $c_r \equiv \Lambda/r_0^2$ and $c_\psi \equiv 1/(1+\psi_0)$. The bottom trajectory will be perturbed in a similar way, so we can write the equation for the channel centroid, $x_c = (r_+ - r_-)/2$, as

$$x_c'' = c_p c_r c_\psi (x_b - x_c). \quad (2.98)$$

This result is of the same form as linear theory (Eq. 2.86) but with the centroid frequency now the product of three terms, all of which (in normalized units) are less than unity (c_p, c_r, $c_\psi < 1$), resulting in a smaller growth of the channel centroid and therefore hosing growth. Furthermore, the coefficients can depend on longitudinal position in the wake, ξ. These coefficients are typically calculated through simulation data (one 3D timestep), but can be calculated as a function of the sheath thickness, Δ, using the Lu et al. model. The c_ψ term captures how the relativistic mass changes the resonant frequency and the fact that plasma electrons gain substantial longitudinal momentum. The c_r coefficient captures the difference in charge neutralization radius and the blowout (and variation along the bunch). Larger beam currents and smaller blowout radii lead to stronger hosing, due to the larger c_r coefficient. Thus, hosing is most severe for high current electron beams loaded in the back of the wake (which is what we want for beam loading). This leads us to explore methods to mitigate hosing, discussed later in this dissertation.

Four regimes were identified in Huang et al., namely adiabatic non-relativistic (linear theory applies), adiabatic relativistic, non-adiabatic non-relativistic, and non-adiabatic relativistic (the regime of relevance to a LC and future experiments). The simulation setups are shown in Fig. 2.4 and the results are shown in Fig. 2.5. We can see for the non-adiabatic relativistic regime there is moderate disagreement between theory and simulation, which is where we focus on improving the theory in the next chapter.

2.5.5 An approach using moments of the Vlasov equation

In this section, we briefly review another approach for deriving the equation for the plasma channel centroid in the blowout regime from Mehrling et al. [90]. The aim of this approach was to provide better agreement with simulations for the non-adiabatic, relativistic regime. In the next chapter, we will compare our approach, which is a modification of the Huang

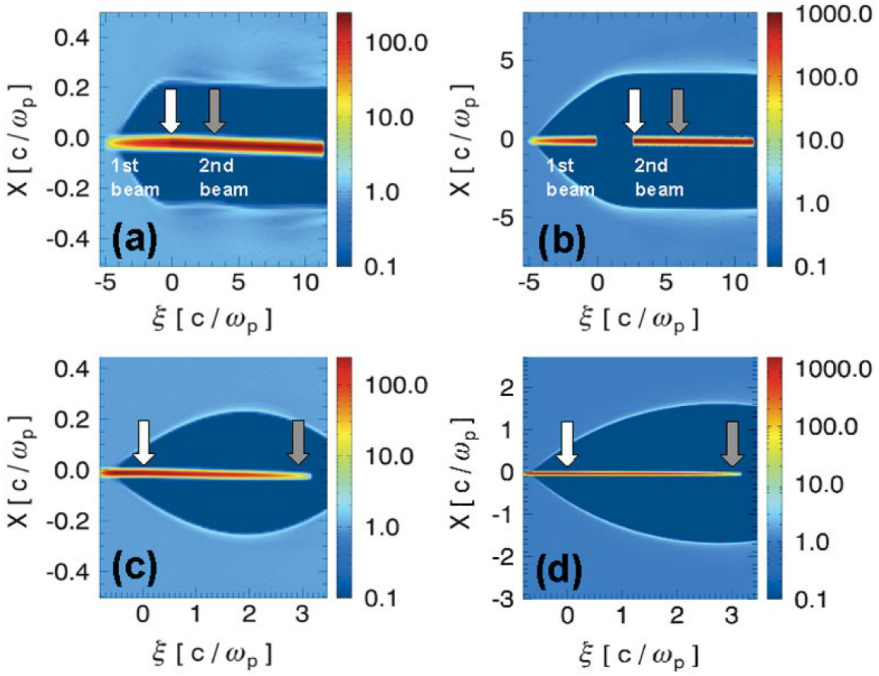

Figure 2.4: The beams (red, moving to the left) and the plasma (blue) in (a) the adiabatic non-relativistic regime, (b) the adiabatic relativistic regime, (c) the non-adiabatic non-relativistic regime, (d) the non-adiabatic relativistic regime. Left-hand (white) and right-hand (gray) arrows denote where tilts are added and the centroids are measured. Reproduced from [88].

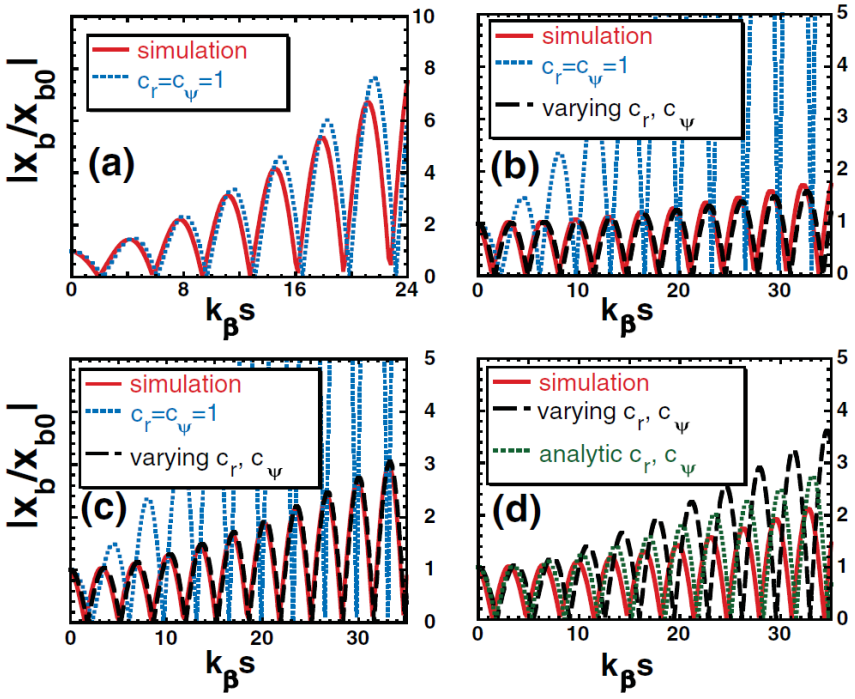

Figure 2.5: Hosing growth in four regimes. x_{b0} is the initial displacement of the beam centroid. We assume $\Delta_s = 0.1r_0$, $\Delta_L = c/\omega_p$ for the analytic curve in case (d). The slightly slower hosing growth in simulation (d) is caused by nonlinearity in beam-channel centroid coupling. Reproduced from [88].

et al. [88] framework, to this one[1]. As we will show, our improved theory provides better agreement with simulations for the regimes we explore in the next chapter.

In the Vlasov approach, the fields outside the bubble also need to be known. They assumed an exponential model of the plasma sheath of the form

$$S(r,\xi) = \begin{cases} -1 & r < r_b(\xi) \\ S_0(\xi) e^{-(r-r_b(\xi))/\Delta_\rho} & r \geq r_b(\xi), \end{cases} \tag{2.99}$$

where the sheath thickness is Δ_ρ. The wakefields and the equation for $r_b(\xi)$ for this model were derived in Ref. [83], where J_z was treated separately from S, i.e., J_z has a separate exponential profile from S, with thickness Δ_J. This implies $\rho = J_z - S$ is made up of two exponentials with different length scales. We note that neither the profile for ρ nor the assumption made in the reference that $\rho - J_z \approx \rho$ are needed to calculate the wakefields because the force on the plasma electrons, given in Eq. 2.33, only depends on the source terms S and J_z, not on ρ. Thus, Δ_ρ should represent the thickness of S not the electron density ρ. The fields outside the bubble could also be found using the Lu et al. [27, 28] model with an assumed profile for J_z. Finally, we note the model for J_z and the fields outside the bubble are not needed for the Huang et al. treatment of hosing.

Hosing is a challenging problem because it breaks azimuthal symmetry. In the Vlasov approach, phase space averages of the quasi-static plasma electron distribution are calculated. From here, we follow Mehrling et al. [90]. The plasma is described by a quasi-static form for the Vlasov equation,

$$\partial_\xi f_p + \left(\frac{\mathbf{p}_\perp \cdot \boldsymbol{\nabla}_\perp}{1+\psi} + \frac{d\mathbf{p}_\perp}{d\xi} \cdot \boldsymbol{\nabla}_{p_\perp} + \frac{d\psi}{d\xi}\partial_\psi \right) f_p = 0 \tag{2.100}$$

where $f_p(\mathbf{x}_\perp, \mathbf{p}_\perp, \psi; \xi)$ is the plasma electron distribution and ψ is written as a phase space variable through the relation $\psi = \gamma - p_z - 1$, derived earlier. Recall $\xi = ct - z$ is the time-like, co-moving longitudinal coordinate. For the zeroth order distribution, $f_{p,0}$, we assume

[1]These theories were developed around the same time, although our work has yet to be published, but has been presented at conferences.

azimuthal symmetry, so it obeys

$$\partial_\xi f_{p,0} = -\frac{\gamma}{1+\psi}\left(\frac{p_r}{\gamma}\partial_r + F_r\partial_{p_r} + F_\psi\partial_\psi\right) f_{p,0}, \tag{2.101}$$

where we have defined $F_r \equiv \frac{dp_r}{dt}$ and $F_\psi \equiv \frac{d\psi}{dt}$. The total distribution function is expanded for small moments $\langle x\rangle$ and $\langle p_x\rangle$ about the zeroth order symmetric distribution function. If the perturbation is a rigid displacement then the perturbed distribution function can be written as follows,

$$f_{p,1} \approx -\cos\theta(\langle x\rangle\partial_r + \langle p_x\rangle\partial_{p_r}) f_{p,0}. \tag{2.102}$$

Then for a general moment of a quantity Φ, we can write the evolution as

$$\partial_\xi\langle\Phi\rangle = \left\langle\frac{p_r}{1+\psi}\partial_r\Phi\right\rangle + \left\langle\frac{\gamma\dot{\theta}}{1+\psi}\partial_\theta\Phi\right\rangle + \left\langle\frac{\gamma F_r}{1+\psi}\partial_{p_r}\Phi\right\rangle + \left\langle\frac{\gamma F_\psi}{1+\psi}\partial_\psi\Phi\right\rangle. \tag{2.103}$$

What we want is the plasma centroid $\langle x\rangle$. Using the above equation gives

$$\partial_\xi\langle x\rangle = \partial_\xi\langle r\cos\theta\rangle = \left\langle\frac{p_r\cos\theta}{1+\psi}\right\rangle = \frac{\langle p_r\cos\theta\rangle}{\langle 1+\psi\rangle} + \mathcal{O}\left[(\Delta_\rho r_b)^2\right], \tag{2.104}$$

where in the last equality a series expansion of $1/(1+\psi)$ around $\langle\psi\rangle$ was used (and only the zeroth order terms were kept), which will be essential to obtain a closed form solution. We can use the moment equation again to get

$$\begin{aligned}\partial_\xi^2\langle x\rangle &= \frac{\left\langle\frac{\gamma}{1+\psi}F_r\cos\theta\right\rangle}{\langle 1+\psi\rangle} - \frac{\langle p_r\cos\theta\rangle}{\langle 1+\psi\rangle^2}\left\langle\frac{\gamma F_\psi}{1+\psi}\right\rangle \\ &= \frac{\left\langle\frac{\gamma}{1+\psi}F_r\cos\theta\right\rangle}{\langle 1+\psi\rangle} - \frac{\partial_\xi\langle x\rangle}{\langle 1+\psi\rangle}\left\langle\frac{\gamma F_\psi}{1+\psi}\right\rangle.\end{aligned} \tag{2.105}$$

Next, we expand the forces as

$$F_{r,b} \approx -\cos\theta x_b\partial_r F_{r,b,0} \tag{2.106}$$

$$F_{r,p} \approx -\cos\theta\langle x\rangle\partial_r F_{r,p,0}, \tag{2.107}$$

where x_b is the beam centroid. Finally, using the expansions and truncating to first order in

x_b, $\langle x\rangle$, and $\langle p_x\rangle$ we have

$$\begin{aligned}\partial_\xi^2\langle x\rangle = &-\frac{\langle x\rangle}{2\langle 1+\psi\rangle}\left\langle\frac{\gamma}{1+\psi}\partial_r F_{r,p,0}\right\rangle - \frac{x_b}{2\langle 1+\psi\rangle}\left\langle\frac{\gamma}{1+\psi}\partial_r F_{r,b,0}\right\rangle\\ &+\frac{\langle x\rangle}{2\langle 1+\psi\rangle}\left\langle\frac{\gamma}{1+\psi}(\partial_r + r^{-1})F_{r,p,0}\right\rangle + \frac{\langle x\rangle}{2\langle 1+\psi\rangle}\left\langle\frac{\gamma}{1+\psi}(\partial_r + r^{-1})F_{r,b,0}\right\rangle\\ &+\partial_\xi\langle x\rangle\left\langle\frac{p_r F_{r,0}}{(1+\psi)^2}\right\rangle - \frac{\partial_\xi\langle x\rangle}{\langle 1+\psi\rangle}\left\langle\frac{\gamma F_\psi}{1+\psi}\right\rangle. \end{aligned} \tag{2.108}$$

This can be rearranged to an equation of the form we have seen before,

$$\partial_\xi^2 x_c + C_d(\xi)\partial_\xi x_c + \frac{C_p(\xi)}{2}x_c = \frac{C_b(\xi)}{2}x_b, \tag{2.109}$$

where $x_c \equiv \langle x\rangle$. We can write the coefficients in terms of the wake potentials as follows,

$$C_p = -\frac{1}{\langle 1+\psi\rangle}\left(\left\langle\frac{\gamma}{1+\psi}\frac{\partial_r\Psi}{r}\right\rangle + \left\langle\frac{\partial_\xi A_r}{r}\right\rangle + \left\langle\frac{\partial_r A_{z,p}}{r}\right\rangle - \langle J_{z,b}\rangle\right) \tag{2.110}$$

$$C_b = \frac{1}{1+\psi}\left\langle\frac{\partial_r A_{z,b}}{r} + J_{z,b}\right\rangle \tag{2.111}$$

$$C_d = \frac{\langle\partial_\xi\Psi\rangle}{\langle 1+\psi\rangle}, \tag{2.112}$$

where Ψ is the pseudopotential. Without going through the details, these can be turned into radial moments using the cold fluid assumption for the zeroth order distribution. Assuming the beam is "narrow" such that there is no beam current overlap with the sheath so that $\langle J_{z,b}\rangle_r \approx 0$ and the plasma current sheath thickness is $\Delta_J \approx 1$, the coefficients are

$$C_p = \frac{1-r_b'^2}{4} - \frac{\Delta_\rho}{4}\left(\frac{1+\Lambda}{r_b} + \frac{r_b(r_b'^2 - r_b^2 - 1)}{4} - \frac{r_b^2 r_b'}{2}\right) + \mathcal{O}\left(\frac{\Delta_\rho^2}{r_b^2}\right) \tag{2.113}$$

$$C_b = \frac{\Lambda}{r_b^2}\left[1 - \Delta_\rho\left(\frac{2}{r_b} + \frac{r_b}{4}\right)\right] + \mathcal{O}\left(\frac{\Delta_\rho^2}{r_b^2}\right) \tag{2.114}$$

$$C_d = \frac{r_b'}{4}\left[r_b - \frac{\Delta_\rho}{2}\left(\frac{r_b^2}{2} - 1\right)\right] + \mathcal{O}\left(\frac{\Delta_\rho^2}{r_b^2}\right). \tag{2.115}$$

This model will be compared to our model in the next chapter.

2.6 Summary

In this chapter, we have reviewed several key concepts in plasma-based acceleration theory. We first discussed the betatron motion of beam particles in the ion column of a nonlinear wake. We described the quasi-static approximation and Maxwell's equations under this approximation in co-moving coordinates. This set the stage for reviewing the seminal work of Lu et al. [27, 28]. This work assumed a step function profile for the source $S = -(\rho - J_z)$, in order to calculate the pseudopotential, ψ, to characterize the nonlinear wakefields inside the bubble. Then, a differential equation for the blowout radius was derived.

We then reviewed the beam loading theory in the blowout regime based on the Lu et al. model. This theory predicts a trapezoidal current profile for the witness beam can flatten the accelerating field so that the witness beam energy spread can be preserved and the energy transfer efficiency can be maximized.

Next, we reviewed the basic transverse physics of a beam slice to introduce several important concepts. We derived the equation for the evolution of the slice centroid including when the slice has energy spread. We also derived the matching condition for the spot size so that it does not undergo oscillation as it is accelerated. Lastly, we discussed beam matching when the beam slice if offset or has an energy spread. We showed that the normalized emittance will not grow when the beam is accelerating in a linear focusing force and derived the saturated normalized emittance if the beam has an initial offset.

We then reviewed the linear fluid theory for hosing in the blowout regime, which predicted an exponential growth of the beam centroid due to its coupling to the plasma channel centroid. Next, we reviewed the model for hosing in the blowout regime by Huang et al. [88]. This framework uses a first order perturbation theory for the innermost electron trajectory that defines the blowout radius. This model predicts a much smaller hosing growth rate that is more in line with PIC simulations. Finally, we discussed another recent approach using moments of the quasi-static Vlasov equation. This model was intended to improve the

Huang et al. model. In the next chapter, we will compare this theory to an improved hosing theory using the Huang et al. framework.

CHAPTER 3

Hosing and asymmetric beam theory and simulation

In the previous chapter, we reviewed the existing theories of nonlinear wakefields and electron beam hosing. In this chapter, we describe an approach to amend the theory of Huang et al. [88] described in the last chapter. In Huang et al., the perturbed plasma fields were acknowledged but not calculated, but we will show these are essential to obtain accurate results for the plasma channel centroid equation that is required to describe the hosing instability. The beam centroid equation does not need to be amended. We use an $m = 1$ azimuthal decomposition description to calculate these fields. We compare the predictions of the improved theory to the analyses of Huang et al. and the Vlasov approach of Mehrling et al. [90]. We also show how this same formalism can be used for higher modes, such as the $m = 2$ mode to describe wakes formed by beams with different transverse spot sizes.

3.1 Correction to the hosing theory in the blowout regime

In the previous chapter, we reviewed two methods for describing hosing in the blowout regime. The first (Ref. [88]) used a perturbation method of the symmetric blowout of the innermost electron trajectory described by the equation of motion derived in Ref. [27, 28] (also reviewed in the previous chapter), and the second [90] used a Vlasov-based moment method by averaging the fields over all space. The latter was motivated by the deficiency of the former in the non-adiabatic, relativistic regime. In this section, we will show how the first method can be amended to be more accurate in this regime. This is done by including terms

that were originally dropped[1], as well as deriving perturbations of the sheath fields based on an azimuthal mode decomposition. As such, we will be making some similar assumptions, such as the rigid displacement of the plasma sheath, but also relaxing others, such as the short beam approximation.

3.1.1 Higher order mode source terms

We employ an azimuthal decomposition in the same way as QPAD or Quasi-3D OSIRIS, where the fields and charge and current densities are decomposed into azimuthal modes. This decomposition for a field quantity is explicitly given by

$$\begin{aligned}\mathbf{F}(r,\theta) &= \sum_{m=-\infty}^{+\infty} \mathbf{F}^m(r) e^{im\theta} \\ &= \mathbf{F}^0(r) + 2\sum_{m=1} \mathbb{R}\left\{\mathbf{F}^m\right\}\cos(m\theta) - 2\sum_{m=1} \mathbb{I}\left\{\mathbf{F}^m\right\}\sin(m\theta),\end{aligned} \tag{3.1}$$

where $\mathbf{F}$ is an arbitrary vector or scalar field [80]. Because $\mathbf{F}(r,\theta)$ is real, $\mathbf{F}^{-m} = (\mathbf{F}^m)^*$, so only positive modes need to be considered.

We can describe a beam with a small offset with the $m = 1$ (and $m = 0$) mode. To see this, we can write down the azimuthal expansion of a Gaussian beam with an offset $\langle x\rangle = x_b$. The charge distribution is

$$\rho_b(x,y) = \rho_{b0}\exp\left(-\frac{(x-x_b)^2+y^2}{2\sigma^2}\right). \tag{3.2}$$

Such a charge distribution provides an asymmetric force (in θ) which leads to a wakefield (including the blowout radius and electron sheath) that is also asymmetric. It is useful to decompose the fields from the drive beam and wakefield into azimuthal harmonics, where the source terms are the charge and current densities of the drive beam and wakefield, respectively. Under the quasi-static approximation (QSA), these fields are solutions to the

[1]We note that Ref. [90] stated the model of Huang et al. was unphysical because it did not include these terms ($\partial_\xi x_c$ terms), but these were simply dropped in the short-pulse limit.

2D scalar Poisson equations of the form

$$-\nabla_\perp^2 f = h, \tag{3.3}$$

which can be solved through a convolution integral of the Green's function, G, over the source term, where

$$-\nabla_\perp^2 G = \delta(\mathbf{x}_\perp - \mathbf{x}'_\perp). \tag{3.4}$$

It can be shown that [91]

$$G(\mathbf{x}_\perp - \mathbf{x}'_\perp) = \int_0^\infty \frac{dk}{2\pi k} \sum_m J_m(kr) J_m(kr') e^{im(\theta-\theta')}, \tag{3.5}$$

where $J_m(kr)$ is the Bessel function of the first kind. Therefore,

$$f = \int r' dr' d\theta'\, h(r', \theta') \int_0^\infty \frac{dk}{2\pi k} \sum_m J_m(kr) J_m(kr') e^{im(\theta-\theta')}. \tag{3.6}$$

If the source, h, is also decomposed as

$$h(r', \theta') = \sum_m h_m(r') e^{im\theta'}, \tag{3.7}$$

it follows that

$$f = \sum_m \left[e^{im\theta} \int_0^\infty r' dr'\, h_m(r') \int_0^\infty \frac{dk}{k} J_m(kr) J_m(kr') \right]. \tag{3.8}$$

We find using Mathematica [92], this can be rewritten as

$$f = f_0(r) + \sum_{m\neq 0,\, m=-\infty}^{m=\infty} \frac{e^{im\theta}}{2|m|} \int_0^\infty r' dr'\, h_m(r') \times \begin{cases} \left(\dfrac{r}{r'}\right)^{|m|} & r < r' \\ \left(\dfrac{r'}{r}\right)^{|m|} & r > r' \end{cases} \tag{3.9}$$

Thus, the transverse electric field from an electron beam can be obtained by using $h \to \rho_b/\epsilon_0$ (from Eq. 3.2) and $f \to \phi$. In what follows, we truncate the azimuthal expansion to lowest order, so we just keep $m = 0, 1$. Another way to derive this electric field is by using the multipole expansion in 2D [93], similar to the standard technique used in electromagnetism (c.f. Griffiths' textbook [94]). In 2D, the potential at $\mathbf{r}$ for charge distribution $\rho(r')$ is

$$\phi(\mathbf{r}) = -\frac{1}{2\pi\epsilon_0} \int \rho(r') \ln|\mathbf{r} - \mathbf{r}'| ds', \tag{3.10}$$

where the integral is over the source coordinates. We can write the log term as

$$\begin{aligned}\ln|\mathbf{r}-\mathbf{r}'| &= \ln\sqrt{r^2-2rr'\cos(\theta'-\theta)+r'^2} \\ &= \ln r + \frac{1}{2}\ln\left(1-\frac{2r'\cos(\theta'-\theta)}{r}+\frac{r'^2}{r^2}\right)\end{aligned} \tag{3.11}$$

and expand in powers of r'/r, as we are interested in the far field where $r \gg \sigma_{x,y}$ (one could expand in powers of r/r' in the opposite limit) to obtain

$$\begin{aligned}\ln|\mathbf{r}-\mathbf{r}'| &= \ln r + \sum_{m=1}^{\infty}\frac{1}{m!}(-\mathbf{r}'\cdot\nabla_\perp)^m \ln r \\ &= \ln r - \sum_{m=1}^{\infty}\frac{1}{m}\cos[m(\theta'-\theta)]\left(\frac{r'}{r}\right)^m \\ &= \ln r - \frac{r'}{r}\cos(\theta'-\theta) - \frac{r'^2}{2r^2}\cos(2(\theta'-\theta)) + \mathcal{O}\left(\frac{r'}{r}\right)^3.\end{aligned} \tag{3.12}$$

Note this gives the same result as Eq. 3.9 when substitued into Eq. 3.10. We then calculate the first order ($m=1$) potential as follows,

$$\begin{aligned}\phi_{m=1}(\mathbf{r}) &= \frac{1}{2\pi\epsilon_0 r}\int \rho(\mathbf{r}')r'\cos(\theta-\theta')r'dr'd\theta' \\ &= \frac{\cos\theta}{2\pi\epsilon_0 r}\int \rho(\mathbf{r}')r'\cos\theta'\,r'dr'd\theta' + \frac{\sin\theta}{2\pi\epsilon_0 r}\int \rho(\mathbf{r}')r'\sin\theta'\,r'dr'd\theta' \\ &= \frac{\cos\theta}{2\pi\epsilon_0 r}\int_{-\infty}^{\infty}\int_{-\infty}^{\infty}\rho_{b0}\exp\left(-\frac{(x'-x_b)^2}{2\sigma^2}-\frac{y'^2}{2\sigma^2}\right)x'dx'dy' \\ &\quad + \frac{\sin\theta}{2\pi\epsilon_0 r}\int_{-\infty}^{\infty}\int_{-\infty}^{\infty}\rho_{b0}\exp\left(-\frac{(x'-x_b)^2}{2\sigma^2}-\frac{y'^2}{2\sigma^2}\right)y'dx'dy'.\end{aligned} \tag{3.13}$$

We note that the second term will vanish because the integrand is odd. In the first term, we can easily integrate the two separate Gaussian integrals to obtain

$$\phi_{m=1}(r,\theta) = \frac{\rho_{b0}\sigma^2}{\epsilon_0 r}x_b\cos\theta \tag{3.14}$$

which, upon using $\rho_{b0} = -en_{b0}$ and $\Lambda = n_{b0}/n_p(k_p\sigma)^2$, and switching to normalized units, can be rewritten as

$$\phi_{m=1}(r,\theta) = -\frac{\Lambda}{r}x_b\cos\theta. \tag{3.15}$$

The $m = 1$ term for the electric field is therefore

$$\mathbf{E}_{m=1}(r,\theta) = -\frac{\partial \phi_{m=1}}{\partial r}\hat{r} - \frac{1}{r}\frac{\partial \phi_{m=1}}{\partial \theta}\hat{\theta} = \frac{\Lambda}{r^2}x_b\left(\cos\theta\hat{r} + \sin\theta\hat{\theta}\right). \tag{3.16}$$

Moreover, using this analysis, it can be shown that $\phi_{m=2,4,6,\ldots} = 0$ and $\phi_{m=1,3,5,\ldots} \propto x_b^m$. We can thus describe the beam fields in terms of only the $m = 1$ mode in an azimuthal decomposition for small, rigid offsets.

In order to describe the wakefield, we need to calculate the pseudopotential, ψ, for non-azimuthally symmetric source terms, $S \equiv -(\rho - J_z)$. We use the Lu et al. model [27, 28] for the plasma sheath, where the thin sheath is described by an inner and outer radial boundary, $r_{bi} = r_{b0}$ and $r_{bo} = r_{b0} + \Delta$, respectively, and $S = n_\Delta$ is a constant within the sheath. In a general (non-azimuthally symmetric) description, the boundaries, r_{bi} and r_{bo}, and the value of S in the sheath would be functions of θ. In order to calculate the source, S, and hence the pseudopotential, ψ, that results from beam asymmetries we need to make some assumptions. Thus, we do not attempt a fully general analysis. Rather, we separately consider only the $m = 1$ and $m = 2$ perturbations to the sheath. Although investigations into higher mode perturbations could be done using this framework.

For each mode, it is important to consider the physical situation that leads to the blowout perturbation. For example, the $m = 1$ case describes the displacement of the sheath caused an offset beam slice. As in Huang et al. [88], we assume that the entire wakefield, i.e., the ion column and inner and outer sheath boundaries, is displaced rigidly in the x direction (without loss of generality). Assuming the sheath is not distorted in this displacement, ψ in the new displaced frame is unchanged. Using this assumption, it is possible to find the perturbed ψ as follows. In Fig. 3.1, we show the general diagram for a rigidly displaced channel. We assume the channel is displaced by $\delta\mathbf{r_1} = \delta r_1\hat{\mathbf{x}}$. $\mathbf{r_1} = \mathbf{r_0} + \delta\mathbf{r_1}$ is the vector from the origin to the new blowout radius, where $\mathbf{r_0} = r_{b0}\hat{\mathbf{r}}$ is the vector to the unperturbed blowout radius. Assuming ψ remains unchanged, we have

$$\psi(\mathbf{r_1}) = \psi_0(\mathbf{r_0}) = \psi_0(\mathbf{r_1} - \delta\mathbf{r_1}), \tag{3.17}$$

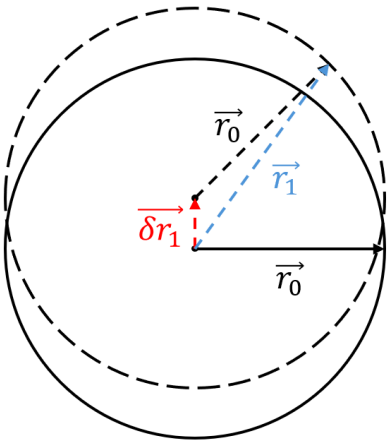

Figure 3.1: Diagram (not to scale) of a transverse slice of a rigidly displaced plasma channel. The unperturbed channel (solid black) is shifted upwards by $\delta\mathbf{r_1}$. $\mathbf{r_1}$ is the vector to the new blowout radius (dashed black) from the origin.

where ψ_0 is the unperturbed ψ inside the bubble given by Lu et al. [27, 28],

$$\psi_0(r) = \psi_0(r=0) - \frac{r^2}{4}. \tag{3.18}$$

We can Taylor expand this around the displacement $\delta\mathbf{r_1}$,

$$\psi(\mathbf{r_1}) = \psi_0(\mathbf{r_1}) - (\delta\mathbf{r_1}\cdot\nabla_\perp)\psi_0(\mathbf{r_1}) + \frac{1}{2}(\delta\mathbf{r_1}\cdot\nabla_\perp)^2\psi_0(\mathbf{r_1}) + ..., \tag{3.19}$$

which leads to

$$\psi(\mathbf{r_1}) = \psi_0(\mathbf{r_1}) + \frac{r}{2}(\delta\mathbf{r_1}\cdot\hat{\mathbf{r}}) - \frac{1}{4}(\delta\mathbf{r_1}\cdot\hat{\mathbf{r}})^2 \tag{3.20}$$

and thus the first order perturbed ψ due to the rigid displacement is

$$\psi_1(\mathbf{r_1}) = \frac{r}{2}(\delta\mathbf{r_1}\cdot\hat{\mathbf{r}}) = \frac{r}{2}\delta r_1\cos\theta. \tag{3.21}$$

Next, we give an alternative description where the sheath (both inner and outer boundaries) is displaced purely radially, i.e., $\delta\mathbf{r}_m = (\delta r_{m,c}\cos(m\theta) + \delta r_{m,s}\sin(m\theta))\hat{\mathbf{r}}$. We will show that this gives the same result for ψ_1 to first order. Using this assumption, it is possible to model the perturbed source as a function of r. This can be used to solve for the perturbed

pseudopotential coefficient for each azimuthal mode. This is similar to the way the original hosing equations were derived in Whittum et al. [86]. We note that a purely radial sheath displacement implies there is no perturbation to the azimuthal current J_θ, unlike the case of rigid displacement. This approach should apply for a perturbation with general azimuthal mode m, but here we just study the $m = 1$ and $m = 2$ cases, which we cover in Sec. 4.3, in detail. In both cases, we will ultimately assume both the value of S in the sheath, n_Δ, and the sheath thickness, Δ, remain constant. More accurate descriptions could be obtained if n_Δ and Δ vary as functions of θ.

We begin by Taylor expanding the source profile to first order in the radial displacement $\delta\mathbf{r}_m = \delta r_m \cos(m\theta)\hat{\mathbf{r}}$ (this would correspond to an offset in x for $m = 1$), as follows,

$$\begin{aligned} S(\mathbf{r}) &= S_0(\mathbf{r} - \delta\mathbf{r}) \\ &\approx S_0(\mathbf{r}) - \delta r_m \cos(m\theta)\partial_r S_0(\mathbf{r}) \\ &= S_0(\mathbf{r}) - \delta r_m \cos(m\theta)\left[(1 + n_\Delta)\delta(r - r_b) - n_\Delta\delta(r - r_b - \Delta)\right], \end{aligned} \tag{3.22}$$

where S_0 is given by the Lu et al. [27, 28] profile and δ is the Dirac delta function (not to be confused with δr). Thus, the perturbed source density is given by

$$S_m(r, \theta) = -\delta r_m \cos(m\theta)\left[(1 + n_\Delta)\delta(r - r_b) - n_\Delta\delta(r - r_b - \Delta)\right]. \tag{3.23}$$

Now we have to solve the 2D Poisson equation, $\nabla_\perp^2\psi_m = S_m$, to get the pseudopotential. The general (homogeneous) solution is given by

$$\psi_m(r) = C_1 r^m + \frac{C_2}{r^m}, \tag{3.24}$$

so we can write pseudopotential as

$$\psi_m(r) = \begin{cases} c_{m,0} r^m & r \le r_{b0} \\ c_{m,1} r^m + \dfrac{c_{m,2}}{r^m} & r_{b0} < r \le r_{b0} + \Delta \\ c_{m,3} r^m & r \ge r_{b0} + \Delta \end{cases} \tag{3.25}$$

Enforcing the continuity of ψ_m at $r = r_{b0}$ and $r = r_{b0} + \Delta$ gives use the conditions

$$\psi_m(r = r_{b0}^+) = \psi_m(r = r_{b0}^-) \tag{3.26}$$

$$\psi_m(r = (r_{b0} + \Delta)^+) = \psi_m(r = (r_{b0} + \Delta)^-). \tag{3.27}$$

We integrate over the boundaries at $r = r_{b0}$ and $r = r_{b0} + \Delta$ to get the jump conditions

$$\partial_r \psi_m(r = r_{b0}^+) - \partial_r \psi_m(r = r_{b0}^-) = -(1 + n_\Delta)\delta r_m \tag{3.28}$$

$$\partial_r \psi_m(r_{b0} + \Delta)^+) - \partial_r \psi_m(r = (r_{b0} + \Delta)^-) = n_\Delta \delta r_m. \tag{3.29}$$

These four conditions allow us to solve for the coefficients in Eq. 3.25. The solution for the first coefficient, which gives the field inside the bubble

$$c_{m,0} = \frac{\delta r_m}{2m}\left[(1 + n_\Delta) r_b^{1-m} - n_\Delta (r_b + \Delta)^{1-m}\right]. \tag{3.30}$$

Thus, the $m = 1$ field inside the wake is

$$\psi_{m=1}(r) = \frac{\delta r_{m=1}}{2} r, \tag{3.31}$$

which is important for describing the perturbed plasma fields at the blowout radius. Assuming the beam is offset in the x direction, this will be the cosine coefficient, so this result is the same as the rigid displacement result, Eq. 3.21. It is possible to use other profiles for the source term, such as an exponential profile, but this does not modify the field inside the wake. However, this may give more accurate results for the fields outside the wake, which we will discuss later. We note that in the limit that $n_\Delta = \Delta = 0$, one recovers the Whittum et al. [86] result.

3.1.2 Perturbed plasma fields

In order to determine the modified trajectory of sheath electrons, all of the perturbed plasma fields need to be determined. For radial displacements, we cannot make the same rigid displacement assumptions for ψ. Instead, we want to evaluate the total pseudopotential

at the new blowout radius, as this will be what we mainly care about when deriving the equation for the plasma channel to describe hosing. We will now use the subscript 1 instead of $m = 1$ for brevity. For the azimuthal decomposition, we assumed the channel displacement is purely radial, so we have $\delta\mathbf{r_1} = \delta r_1 \hat{\mathbf{r}}$. And thus, $\mathbf{r_1} = (r_{b0} + \delta r_1 \cos\theta)\hat{\mathbf{r}}$. Evaluating the total pseudopotential at the new radius we have

$$\begin{aligned}
\psi(\mathbf{r_1}, \xi) &= \psi_0(\mathbf{r_1}, \xi) + \psi_1(\mathbf{r_1}, \xi) \\
&= \psi_0(r = 0, \xi) - \frac{\mathbf{r_1} \cdot \mathbf{r_1}}{4} + \frac{\delta\mathbf{r_1} \cdot \mathbf{r_1}}{2} \\
&= \psi_0(r = 0, \xi) - \frac{(r_{b0} + \delta r_1 \cos\theta)^2}{4} + \frac{\delta r_1}{2}(r_{b0} + \delta r_1 \cos\theta)\cos\theta \\
&= \psi_0(r = 0, \xi) - \frac{r_{b0}^2}{4} - \frac{r_{b0}\delta r_1 \cos\theta}{2} + \frac{\delta r_1 r_{b0}\cos\theta}{2} + \mathcal{O}\left(\frac{\delta r_1^2}{r_{b0}^2}\right) \\
&= \psi_0(\mathbf{r_0}, \xi) + \mathcal{O}\left(\frac{\delta r_1^2}{r_{b0}^2}\right),
\end{aligned} \tag{3.32}$$

where, again, ψ_0 is given in Lu et al. [27, 28] and ψ_1 is given in Eq. 3.31. Thus, we have shown that to first order, ψ is unchanged as the channel is rigidly displaced. In other words, the azimuthal decomposition (with radial displacement) gives the same result as a rigid displacement to first order. This assumption is validated by simulations, meaning $\psi_{m=1}$ has the form we derived (you can also explicitly check the top and bottom blowout trajectory, although this can be tricky to compare for small displacements).

One important effect that was neglected in the initial theory of Huang et al. [88] was the perturbed plasma sheath fields because these are difficult to calculate. Now that we have the expression for ψ_1, we can derive the vector potentials through the Lorenz gauge condition

$$\nabla_\perp \cdot \mathbf{A}_\perp = -\frac{\partial\psi}{\partial\xi}. \tag{3.33}$$

We expand this into azimuthal modes in the typical way - we expand all quantities in terms of $\cos(m\theta)$ and $\sin(m\theta)$, e.g., $A_{r,m} = A_{r,m,c}\cos(m\theta) + A_{r,m,s}\sin(m\theta)$. If we assume an offset in the x direction, the perturbation δr_1 will be a $\cos\theta$ term. Taking $m = 1$ and separating

into the $\cos\theta$ and $\sin\theta$ terms (using subscripts c and s, respectively), we have

$$\frac{1}{r}\partial_r\left(rA_{r,1,c}\right) + \frac{1}{r}A_{\theta,1,s} = -\partial_\xi\psi_{1,c} = -\frac{\delta r'_{1,c}}{2}r \tag{3.34}$$

$$\frac{1}{r}\partial_r\left(rA_{r,1,s}\right) - \frac{1}{r}A_{\theta,1,c} = -\partial_\xi\psi_{1,s} = 0. \tag{3.35}$$

To solve these, we make the ansatz

$$A_{r,1} = f(\xi)r^2\cos\theta + g(\xi)\cos\theta \tag{3.36}$$

$$A_{\theta,1} = f(\xi)r^2\sin\theta - g(\xi)\sin\theta, \tag{3.37}$$

which is consistent with what is seen in simulations. Substituting these forms in, we get the solution

$$f(\xi) = -\frac{\delta r'_{1,c}}{8}, \tag{3.38}$$

while $g(\xi)$ is not able to be solved for from these equations. Inside the bubble, because we have no J_z (and no perturbation), we have $\nabla_\perp^2 A_{z,1} = -J_{z,1} = 0$, and so $A_{z,1} = a_1(\xi)r$. Similar reasoning leads to $\phi_1 = b_1(\xi)r$, thus we have $(b_1 - a_1) = \delta r_1/2$. Because of the nature of the quasi-static equations we cannot solve for a_1 or b_1 individually with the local equations. Instead, it requires knowledge of the source outside the bubble. This is similar to the offset term for the potentials, $g(\xi)$. In simulations, both these terms seem to be first order in $\delta r_1/r_0$ so they cannot be ignored, although the effect on the hosing equations seem to be small for many scenarios. Using the expressions for $\mathbf{A}_\perp$ and A_z, we can calculate the magnetic field using $\mathbf{B}_\perp = \nabla_\perp \times (A_z\hat{z}) + \nabla_z \times \mathbf{A}_\perp$. We have

$$B_\theta = -\partial_\xi A_r - \partial_r A_z \tag{3.39}$$

$$B_r = \partial_\xi A_\theta + \frac{1}{r}\partial_\theta A_z, \tag{3.40}$$

which for $m = 1$ gives

$$B_{\theta,1} = \left(\frac{\delta r''_{1,c}}{8}r^2 - \tilde{g}(\xi)\right)\cos\theta \tag{3.41}$$

$$B_{r,1} = \left(-\frac{\delta r''_{1,c}}{8}r^2 - \tilde{g}(\xi)\right)\sin\theta, \tag{3.42}$$

where we have defined $\tilde{g} \equiv g' + a_1$. B_θ explicitly appears in the plasma channel equation when we consider displacements in the x direction. So in the same way as with the pseudopotential, we can write the total B_θ (the cosine term) from the plasma evaluated at the perturbed blowout radius as

$$\begin{aligned} B_\theta(r_{b0} + \delta r_1) &= \frac{1}{2}\psi_0''(r=0,\xi)(r_{b0} + \delta r_1) + \frac{\delta r_1''}{8}(r_{b0} + \delta r_1)^2 - \tilde{g}(\xi) \\ &= \frac{1}{2}\psi_0''(r=0,\xi)(r_{b0} + \delta r_1) + \frac{\delta r_1''}{8} r_{b0}^2 - \tilde{g}(\xi) + \mathcal{O}\left(\frac{\delta r_1^2}{r_{b0}^2}\right). \end{aligned} \tag{3.43}$$

From simulations, we find that for some scenarios, the $\tilde{g}(\xi)$ term cancels with the term $\frac{1}{2}\psi_0''(r=0,\xi)\delta r_1$ (see Fig. 3.4). However, for other cases there seems to be other dominant terms.

3.1.3 Perturbed fields outside the bubble

Although in this dissertation we do not use these in the hosing equation, in this section we calculate the perturbed fields outside the bubble. We cannot solve for these without introducing another constant due to the fact that we do not have the full profiles for the perturbed currents outside the bubble. We use an exponential profile for the source profile because they are more qualitatively similar to those seen in simulations, as we mentioned before, but one could also use the Lu et al. profile. This gives different results for the fields outside the bubble, but the fields inside are the same as the Lu et al. profile. The unperturbed ψ outside the bubble is [83]

$$\begin{aligned} \psi_0(r > r_{b0}) &= \frac{\Delta r_{b0}^2}{2(r_{b0}+\Delta)}\left(1 + e^{r/\Delta}\mathrm{Ei}\left(\frac{r}{\Delta}\right)\right)\exp\left(-\frac{r - r_{b0}}{\Delta}\right) \\ &\approx \frac{\Delta r_{b0}^2}{2(r_{b0}+\Delta)}\left(1 + \frac{\Delta}{r}\right)\exp\left(-\frac{r - r_{b0}}{\Delta}\right), \end{aligned} \tag{3.44}$$

where $\mathrm{Ei}(x)$ is the exponential integral. The expression for the perturbed pseudopotential outside the bubble can be obtained using the Taylor expansion method (see Eq. 3.19). We have

$$\psi_1(r > r_{b0}, \xi) = \frac{\delta r_1 r_{b0}^2}{2(r_{b0}+\Delta)}\left(1 + \frac{\Delta}{r}\right)\exp\left(-\frac{r - r_{b0}}{\Delta}\right). \tag{3.45}$$

Next, we make a similar ansatz as before

$$A_{r,1}(r,\xi) = A(r,\xi)\cos\theta \tag{3.46}$$

$$A_{\theta,1}(r,\xi) = A(r,\xi)\sin\theta. \tag{3.47}$$

Substituting this into the gauge condition, we obtain

$$\frac{\partial}{\partial r}A(r,\xi) + \frac{2}{r}A(r,\xi) = -b'(\xi)\left(1+\frac{\Delta}{r}\right)e^{-r/\Delta}, \tag{3.48}$$

where $b(\xi) \equiv \frac{\delta r_1 r_{b0}^2}{2(r_{b0}+\Delta)} e^{r_{b0}/\Delta}$ and we have assumed $\partial_\xi \Delta \approx 0$. The solution to this ODE is

$$A(r,\xi) = b'(\xi)\Delta\left(1+\frac{3\Delta}{r}+\frac{3\Delta^2}{r^2}\right)e^{-r/\Delta} + \frac{c(\xi)}{r^2}. \tag{3.49}$$

We can solve for $c(\xi)$ by matching with the solution inside the bubble, $A(r = r_{b0},\xi) = -\delta r_1' r_{b0}^2/8 + g(\xi)$ [2]. Technically, we have ignored the small region between $r_{b0} < r < r_{b0}+\delta r_1$, but this is a reasonable assumption for small δr_1 according to simulation. We can now calculate $B_{\theta,1}$ outside the bubble

$$\begin{aligned} B_{\theta,1} = -\partial_\xi A_{r,1} - \partial_r A_{z,1} &= -\partial_\xi A(r,\xi)\cos\theta \\ &= \left[-\Delta b''(\xi)\left(1+\frac{3\Delta}{r}+\frac{3\Delta^2}{r^2}\right)e^{-r/\Delta} - \frac{c'(\xi)}{r^2}\right]\cos\theta, \end{aligned} \tag{3.50}$$

where we ignored the contribution from $A_{z,1}$ outside, which again seems reasonable for small δr_1, but should be included for larger δr_1, such as in the rear of the bubble. As we mentioned earlier, calculating $A_{z,1}$ for non-zero $J_{z,1}$ is not trivial in our formalism. The calculation of these coefficients in the expression for $B_{\theta,1}$ can be quite complex, so we use Mathematica [92] to compute them.

We can compare these expressions for the perturbed fields with results from QPAD simulations. We compare two of the four scenarios from Huang et al. [88]: case (b), which

[2] It seems matching $A_{\theta,1}$ at the boundary gives the opposite sign of $g(\xi)$ than matching $A_{r,1}$, so this is implies it must be zero (or a higher order term). But this does not seem to be borne out in the simulations. This could be a problem with the ansatz.

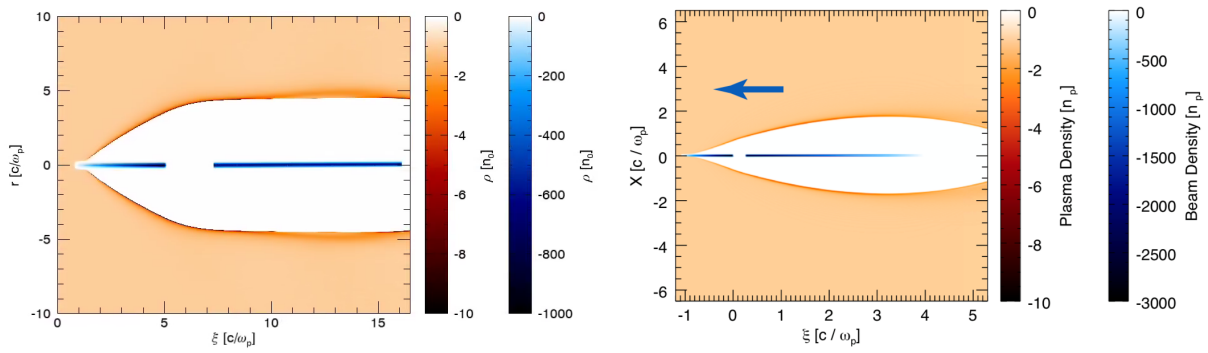

(a) (b)

Figure 3.2: Beam and plasma density for (a) case (b) and (b) case (d) in Table 3.1.

represents the adiabatic, relativistic regime, and case (d), which represents the non-adiabatic, relativistic regime. The parameters are listed in Table 3.1, and the corresponding wakes are shown in Fig. 3.2. In Fig. 3.3, we can see broad agreement for the fields inside the bubble (we have used the on-axis value from the simulation because we have not solved for the quantity $\tilde{g}(\xi)$). The fields outside roughly agree with simulation for case (b) except for $B_{\theta,1}$ at $\xi = 5.0$, which is further back in the bubble where the sheath structure becomes more complicated and the assumptions are not as good. In case (d), the fields outside do not agree as well and we see large spikes in the $B_{\theta,1}$ just outside the bubble. Finally, in Fig. 3.4, we test the rigid displacement term for the on-axis $B_{\theta,1}$ against the simulation for case (b). In this case, the E_z in the beam region is close to zero because the blowout radius is constant. We see very close agreement with the rigid displacement term, so we believe this is a dominant term, but in other scenarios there seem to be other dominant terms. Going forward we will use this term in our derivation of the hosing equation. Future work may calculate the other terms in $B_{\theta,1}(r = 0)$ and investigate its effect on the plasma channel equation.

3.1.4 Derivation of the plasma channel equation

As mentioned before, we will be using the same formalism as Huang et al. [88], where we apply a first order perturbation theory around the symmetric blowout described in Lu et al.

Parameter	(b)	(d)
n_p (cm^{-3})	5.66	2.0
$\Delta\xi$ (k_p^{-1})	2.3	0.27
γ	55,773	20,000
n_b (n_p)	800/650	4293
σ_r (10^{-3} k_p^{-1})	89.8	13
L (k_p^{-1})	4.2/8.8	1.06/3.73
Θ (10^{-3} rad)	0/7.69	0/4.17

Table 3.1: Simulation parameters similar to case (b) and (d) from Huang et al. For both cases, we use an initial untilted beam for the blowout, the tilted beam is tilted by Θ with respect to its head, which is $\Delta\xi$ behind the end of the initial beam. In both cases, the initial beam is triangular, ramping up to its maximum density. In case (b) the tilted beam is uniform and in case (d) the tilted beam is triangular starting at its maximum density and ramping down to zero. The parameters are listed in the form Beam1/Beam2, or as is if they are the same.

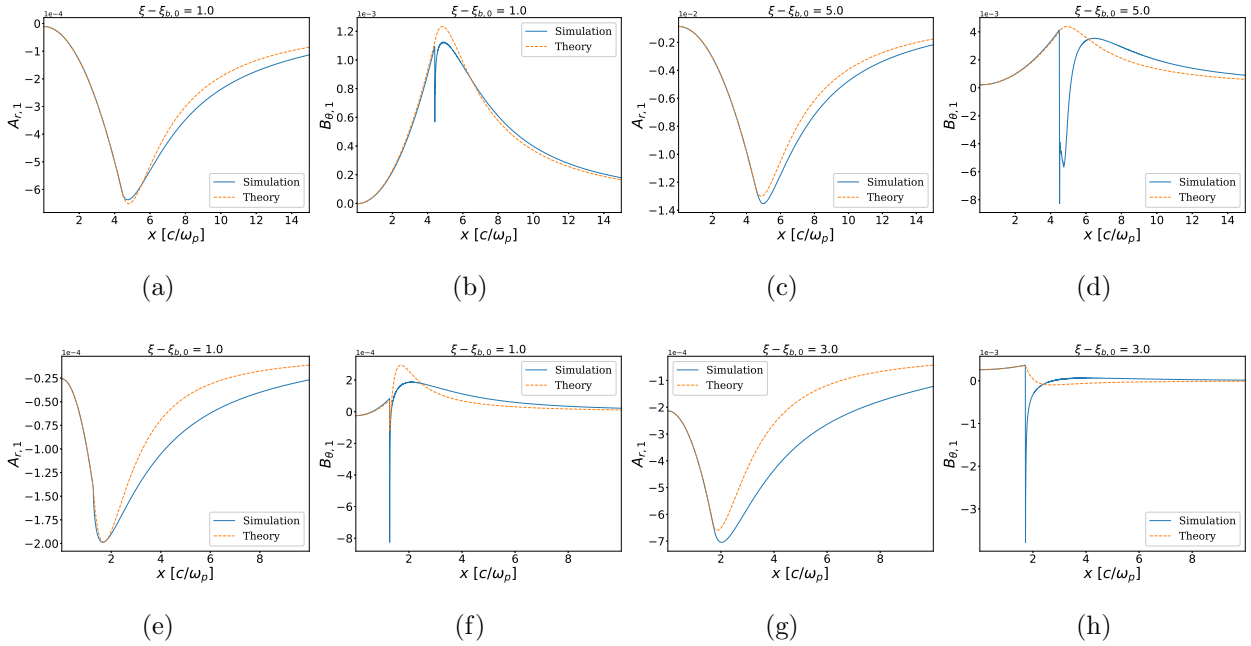

Figure 3.3: (a)-(d) $m = 1$ A_r and B_θ fields (in normalized units) for case (b) in Table 3.1. (a) $A_{r,1}$ and (b) $B_{\theta,1}$ at $k_p\xi = 1$ behind the head of the beam. (c) $A_{r,1}$ and (d) $B_{\theta,1}$ at $k_p\xi = 5$ behind the head of the beam. (e)-(h) $m = 1$ A_r and B_θ fields (in normalized units) for case (d) in Table 3.1. (e) $A_{r,1}$ and (f) $B_{\theta,1}$ at $k_p\xi = 1$ behind the head of the beam. (g) $A_{r,1}$ and (h) $B_{\theta,1}$ at $k_p\xi = 3$ behind the head of the beam. In all cases, the on-axis value for the theory line is taken from the simulation.

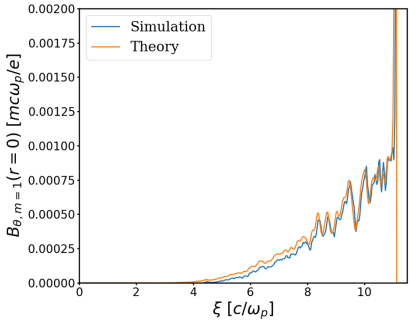

Figure 3.4: On-axis value of $B_{\theta,m=1}$ (shift of parabola) from simulation. The theory line is the rigid displacement term $B_{\theta,m=1}(r = 0) = -\frac{r_1}{2}\psi_0''(r = 0)$.

[27]. However, we will use the potentials $\psi \equiv \phi - A_z$, A_z, and A_r, instead of the electric and magnetic fields. We start with the relativistic equation motion for a plasma electron in the radial direction,

$$\frac{dP_\perp}{dt} = \frac{d}{dt}\left(\gamma \frac{dr}{dt}\right), \tag{3.51}$$

where $P_\perp$ is the perpendicular momentum and γ is the Lorentz factor. We normalize mass to the electron mass m, charge to the elementary charge e, velocities to the speed of light c, densities to the background plasma density n_p, and potentials to mc^2/e. We employ the quasi-static approximation [73]. Under this assumption, we have the constant of motion $\gamma(1 - v_z) = 1 + \psi$ and thus $d/dt = ((1+\psi)/\gamma)d/d\xi$ [74]. So we can write

$$\frac{dP_\perp}{dt} = \frac{1+\psi}{\gamma}\left[(1+\psi)\, r'\right]', \tag{3.52}$$

where the prime refers to the derivative in ξ. From [27], we also have

$$\begin{aligned}\frac{dP_\perp}{dt} &= \frac{\partial \phi}{\partial r} - v_z \frac{\partial A_z}{\partial r} + (1 - v_z)\frac{\partial A_r}{\partial \xi} \\ &= \frac{\partial \psi}{\partial r} + (1 - v_z)\frac{\partial A_z}{\partial r} + (1 - v_z)\frac{\partial A_r}{\partial \xi}.\end{aligned} \tag{3.53}$$

So we now have the equation of motion in terms of just the radial coordinate and the potentials,

$$\left[(1+\psi)\, r'\right]' = \frac{\gamma}{1+\psi}\frac{\partial \psi}{\partial r} + \frac{\partial A_z}{\partial r} + \frac{\partial A_r}{\partial \xi}, \tag{3.54}$$

where

$$\begin{aligned}\gamma &= \frac{1}{2}\left(\frac{P_\perp^2 + 1}{1+\psi} + 1 + \psi\right) \\ &= \frac{1}{2}\left(\frac{(1+\psi)^2\, r'^2 + 1}{1+\psi} + 1 + \psi\right).\end{aligned} \tag{3.55}$$

We use the potentials in the Lorenz gauge as in [27],

$$\psi = \psi(r=0) - \frac{r^2}{4}, \tag{3.56}$$

$$A_z = A_z(r=0) + \Lambda \ln r, \tag{3.57}$$

$$A_r = -\frac{r}{2}\psi'(r=0), \tag{3.58}$$

where $\Lambda(\xi) = \int_0^\infty n_b\, r dr$ is the charge per unit length of the beam. In the case of a Gaussian electron beam, we have $n_b = \left(N/((2\pi)^{3/2}\sigma_r^2\sigma_z)\right) \times e^{-r^2/2\sigma_r^2} e^{-\xi^2/2\sigma_z^2}$, where N is the number of beam electrons, σ_r is the beam spot size, and σ_z is the beam length. In this case, we have $\Lambda = n_b/n_p(k_p\sigma_r)^2 = 2I_b/I_A$, where I_b is the beam current and $I_A \approx 17$ kA is the Alfvén current.

We use the $m = 0$ potentials along with the $m = 1$ expression for A_r in the equation of motion Eq. 3.54, and following Huang et al. [88], use a perturbation approximation where we label the unperturbed (symmetric) solution with a 0 subscript and the first order quantities with a 1 subscript (these will generally correspond to the mode number)

$$r = r_0 + r_1, \tag{3.59}$$

$$\gamma = \gamma_0 + \gamma_1 = \gamma_0 + (1 + \psi_0)\, r_0' r_1', \tag{3.60}$$

$$A_r = A_{r,0} + A_{r,1}, \tag{3.61}$$

$$A_z = A_{z,0} + A_{z,1}. \tag{3.62}$$

Keeping the first order terms, we arrive at

$$(1 + \psi_0) r_1'' + \frac{r_0^2}{8} r_1'' + \left(\psi_0' + \frac{r_0 r_0'}{2}\right) r_1' + \frac{\Lambda}{r_0^2}\,(r_1 - x_b) = 0. \tag{3.63}$$

We introduce the coefficients defined in Huang et al. [88], $c_\psi \equiv 1/(1+\psi_0)$ and $c_r \equiv \Lambda/r_0^2$, and note $\psi_0' = E_{z,0}$. Assuming a rigid channel displacement, and because none of the coefficients in Eq. 3.63 change sign from the top to bottom trajectory, we replace r_1 with the channel centroid x_c. We arrive at

$$\left(1 + c_\psi \frac{r_0^2}{8}\right) x_c'' + c_\psi \left(E_{z,0} + \frac{r_0 r_0'}{2}\right) x_c' + c_r c_\psi (x_c - x_b) = 0. \tag{3.64}$$

We now make several observations about this equation. First, we see it reduces to the equation in Huang et al. [88] (note the difference in the definition of Λ), in the limit that $E_{z,0}$, $r_0 r_0' \ll r_1''/r_1'$ and $c_\psi r_0^2 \ll 8$. The dropped terms are important when you have large bubbles and accelerating fields, i.e., in the relativistic, non-adiabatic regime. Moreover, these

additional terms will be non-zero for regions in which $\Lambda = 0$, and therefore $c_r = 0$, whereas the previous model predicted a linear response in those regions.

We can use the values from simulation for zeroth order quantities in order to verify this equation. But in principle we can calculate these quantities using the Lu et al. [27, 28] model to first order in Δ/r_0. The model for ψ is

$$\psi(r,\xi) = \frac{r_0^2}{4}(1+\beta) - \frac{r^2}{4}, \tag{3.65}$$

where

$$\begin{aligned}\beta &= \frac{(1+\alpha)^2 \ln\left[(1+\alpha)^2\right]}{(1+\alpha)^2 - 1} - 1 \\ &= \alpha - \frac{\alpha^2}{6} + \mathcal{O}(\alpha^4),\end{aligned} \tag{3.66}$$

and $\alpha \equiv \Delta/r_0 = (\Delta_s + \Delta_L)/r_0$, where Δ_s corresponds to the sharp peak in the source $\rho - J_z$ and Δ_L corresponds to the region where the electrons act nearly as they would in a linear wake. We get Δ_s values by matching with simulation measurements (where the density falls off to $1/e$ of its max value). For the cases presented here, Δ_s can be assumed to be roughly constant but it can get wider as you approach the rear of the bubble. In addition, the sheath can become multi-valued in the rear of the bubble [31]. Using the Lu et al. model, we compute the coefficients from Eq. 3.64 to first order in Δ/r_0,

$$\frac{c_r c_\psi}{1 + c_\psi r_0^2/8} = \frac{\Lambda/r_0^2}{1 + r_0\Delta/4 + r_0^2/8} + \mathcal{O}\left(\frac{\Delta}{r_0}\right)^2 \tag{3.67}$$

$$\frac{c_\psi\left(E_{z,0} + r_0 r_0'/2\right)}{1 + c_\psi r_0^2/8} = \frac{r_0'\left(r_0 + \Delta/4\right)}{1 + r_0\Delta/4 + r_0^2/8} + \mathcal{O}\left(\frac{\Delta}{r_0}\right)^2. \tag{3.68}$$

These expressions can roughly be compared to the ones from the Mehrling et al. [90], except it should be noted the Δ here is technically different than the one in Mehrling et al. because it uses an exponential source to derive the fields (from Yi et al. [83]). The Δ_ρ in that reference should roughly be the same as the Δ_s used here.

3.1.5 Comparison to PIC simulations

We can now compare our model with previous models and PIC simulations, testing both the plasma channel equation with one 3D timestep simulations and full length simulations to compare the beam centroid evolution.

First, we compare results for the new equation for the two cases from Huang et al. [88] described in the previous section. The parameters are listed in Table 3.1. In Fig. 3.5, we see the results for a single ξ timestep indicate the new model provides much more accurate results than the Huang et al model (with dropped terms). First, we wish to note an apparent mistake in the Huang et al. publication [88]. In the paper, Λ was defined as $4I_b/I_A$ instead of the conventional $2I_b/I_A$ and the term ω_0^2 was inserted in a similar fashion to Whittum et al. [86] so that the equation is the same as we derive (without the extra terms of course). However, it appears Huang et al. uses $\Lambda = 2I_b/I_A$ when computing x_c, so they get a result much closer to simulation than what is shown in Fig. 3.5a. However, in this case the factor of 2 is coincidentally very close to the term $(1 + c_\psi r_0^2/8)$ (the other term is close to zero because $r_0' \approx 0$ and so $E_{z,0} \approx 0$ too). In case (d) (shown in Fig. 3.5b), we see moderately good agreement. We also ran a case with four times the beam density for both beams so that the blowout radius is about twice as large ($r_0 \sim \sqrt{\Lambda}$). In this case, we see much more accurate results because our approximations become better as the blowout radius is doubled but the perturbation is similar to the previous case, i.e., r_1/r_0 becomes smaller. In case (d) (shown in Fig. 3.5b), we see the Mehrling et al. model result is similar to what was presented in their paper, which is similar in magnitude to the simulations result but qualitatively different (more curvature). With twice the blowout radius, we see a more exaggerated curve. We note the results are sensitive to the chosen value of Δ_ρ, e.g., if we use $\Delta_\rho = 0.5$ we see large disagreement, which is not the case in our model with analytic coefficients. This is evident in case (b) (shown in Fig. 3.5a) where the Mehrling et al. model seems to break down.

We also simulate beam hosing over several betatron oscillations and the results are shown

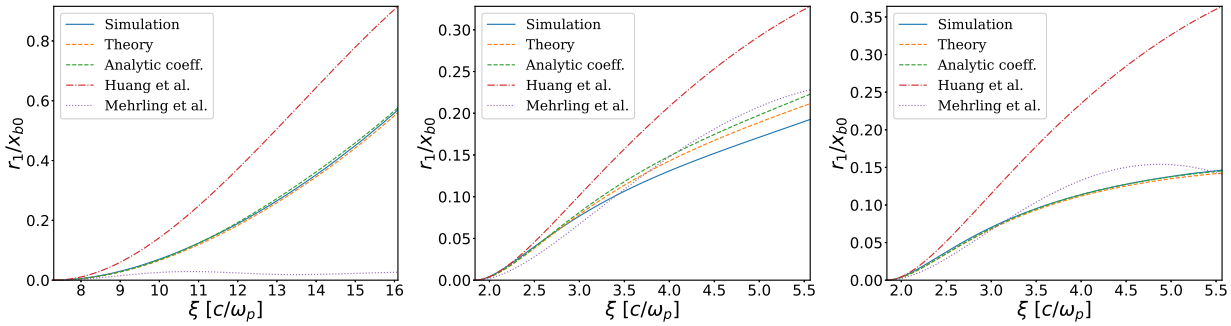

(a) (b) (c)

Figure 3.5: Plasma channel centroid comparison. (a) Case (b) in Table 3.1. In our model with analytic coefficients, $\Delta = 0.55 + 0.5$ was used and for Mehrling et al., $\Delta_\rho = 0.55$ was used. (b) Case (d) in Table 3.1. In our model with analytic coefficients, $\Delta = 0.2 + 0.5$ was used and for Mehrling et al., $\Delta_\rho = 0.2$ was used. (c) Case (d) with four times the beam density (both beams) and therefore twice the blowout radius. In our model with analytic coefficients, $\Delta = 0.35 + 0.5$ was used and for Mehrling et al., $\Delta_\rho = 0.35$ was used. The simulation line is measured using the x-crossing of the focusing force.

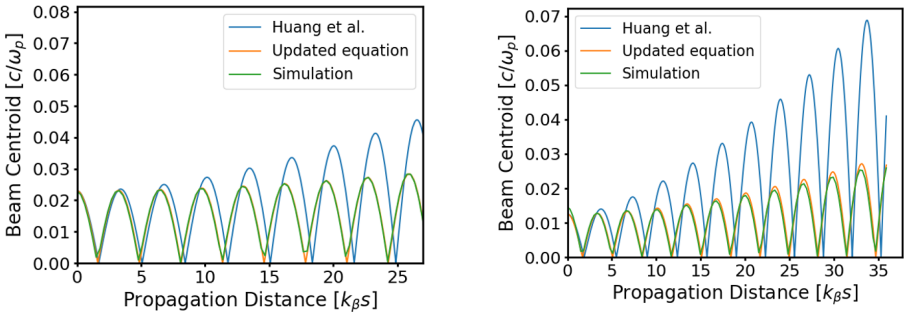

(a) (b)

Figure 3.6: Beam centroid comparison. (a) Case (b) in Table 3.1. (b) Case (d) in Table 3.1. In both cases, the centroid is measured $k_p\xi = 3$ behind the head of the tilted beam. We turn off longitudinal acceleration in the simulation to isolate the transverse physics.

in Fig. 3.6. The evolution for the beam centroid is given by

$$\ddot{x_b} + k_\beta^2 x_b = k_\beta^2 x_c, \tag{3.69}$$

where at each timestep in s, x_c is solved for along ξ using the previous x_b via Eq. 3.64. In general, we find a strong correlation between the accuracy of the plasma channel centroid and the accuracy of the full beam centroid evolution.

Next, we consider the FACET-II like parameters listed in Table 3.2. These parameters correspond to two short tri-Gaussian bunches with the witness beam loaded in the very back of the wake where the acceleration gradient is large. The results are shown in Fig. 3.7. We see decent agreement for the shorter beam separation, although this is not changed from the Huang et al. model. For the ideal beam separation, we see large disagreement between the updated model and simulation. This may be due to the small blowout radius and larger perturbation at the back of the bubble and/or a more complicated sheath structure that may need to be described with a different model (such as in Ref. [31]).

Finally, we test our model with the beam loading parameters from Tzoufras et al. [29], listed in Table 3.3. The witness beam is trapezoidally shaped to flatten the accelerating field. The results are shown in Fig. 3.8a. The witness beam is loaded in a region that still

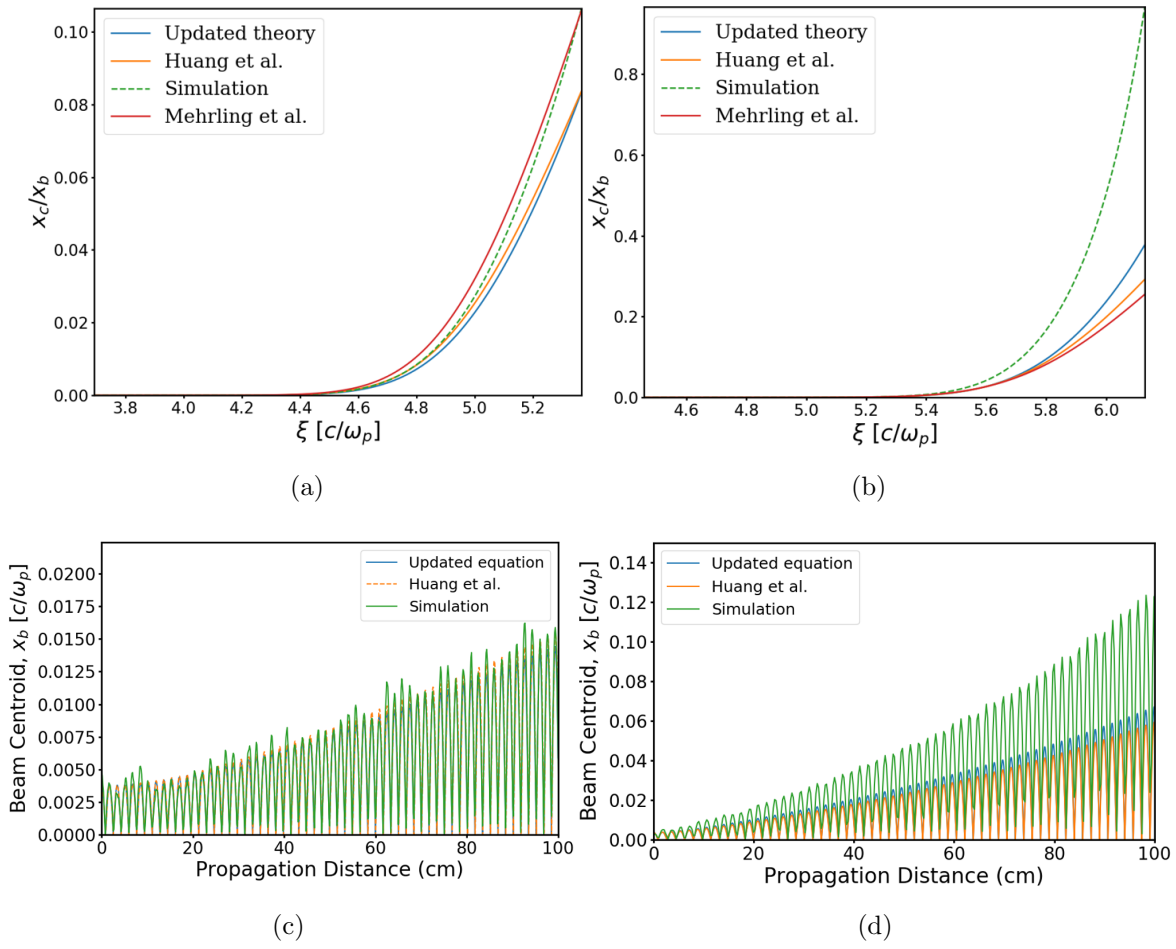

Figure 3.7: FACET-II hosing with a $\Delta x = 0.1$ μm offset witness beam. Plasma channel centroid for a beam spacing of (a) $\Delta\xi = 4.89\,k_p^{-1}$ and (b) $\Delta\xi = 5.65\,k_p^{-1}$. Full beam centroid evolution for a beam spacing of (c) $\Delta\xi = 4.89\,k_p^{-1}$ and (d) $\Delta\xi = 5.65\,k_p^{-1}$. We turn off longitudinal acceleration in the simulation to isolate the transverse physics.

$n_p = 4 \times 10^{16}$ cm^{-3} $\Delta\xi = 5.65/4.89\ k_p^{-1}$		
Parameter	Drive Beam	Witness Beam
γ	20,000	20,000
n_b (n_p)	93.93	75.15
σ_r (k_p^{-1})	0.137	0.137
σ_z (k_p^{-1})	0.48	0.24
x_{b0} ($10^{-2}\ k_p^{-1}$)	0	3.76

Table 3.2: Simulation parameters for FACET-II. We list two different spacings, $\Delta\xi = 5.65\, k_p^{-1}$ is the designed spacing for optimal beam loading.

has large blowout radius, so we see very good agreement with our model.

Additionally, we wish to test the effects of acceleration and energy spread with our model. Our equation for the plasma channel centroid will not change but the full expression for the beam centroid allowing for energy evolution is

$$\ddot{x_b} + \frac{\dot{\gamma}}{\gamma}\dot{x_b} + k_\beta^2 x_b = k_\beta^2 x_c. \tag{3.70}$$

The beam gains energy according to

$$\gamma(\xi, s) = \gamma(\xi, s = 0) - E_z(\xi) k_p s. \tag{3.71}$$

over the propagation distance, s. If the E_z is flattened all the beam particles will gain the same amount of energy. We again simulate the ideal beam loading parameters but with a 10% head-to-tail energy chirp and acceleration of the witness beam turned on. The result is shown in Fig. 3.8b. Again, we see close agreement, but the disagreement becomes larger for large propagation distances. In this case, we see a much smaller hosing growth over half a meter ($\sim 67\%$ reduced growth). We will explore these effects further in the next chapter.

$n_p = 1 \times 10^{17}$ cm^{-3} $\Delta\xi = 8.2\ k_p^{-1}$		
Parameter	Drive Beam	Witness Beam
γ	55,773	55,773
n_b (n_p)	30	30→15
σ_r (k_p^{-1})	0.5	0.5
σ_z/L (k_p^{-1})	1.417	2
x_{b0} (k_p^{-1})	0	0.05

Table 3.3: Beam loading simulation parameters, similar to the ones used in Tzoufras et al.

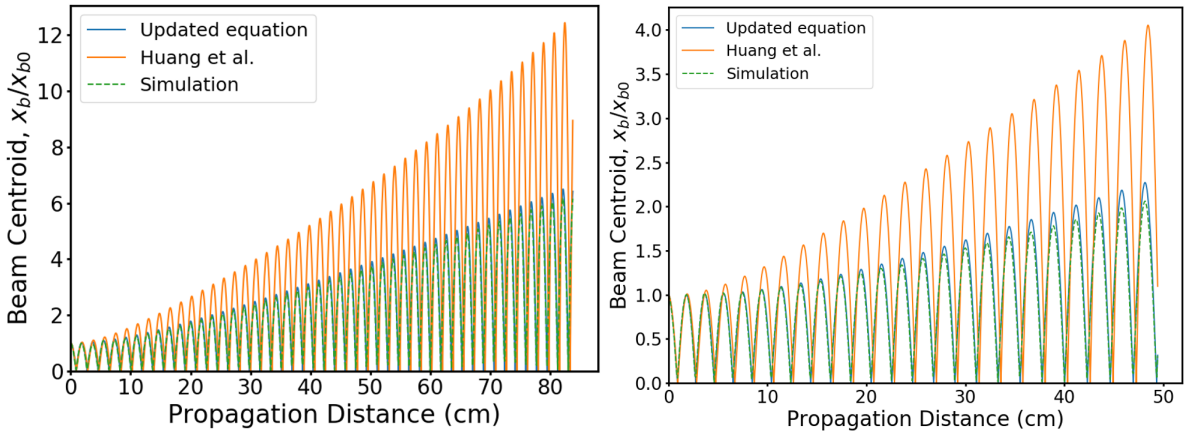

(a) (b)

Figure 3.8: Beam loading with hosing. (a) Beam centroid evolution with parameters from Table 3.3, with acceleration turned off. (b) Beam centroid evolution with a 10% head-to-tail energy chirp on the witness beam (and acceleration turned on).

3.2 Asymmetric beam theory

This section will follow the same procedures described above, but this time instead of looking at the $m = 1$ instability that describes hosing, we will look at the $m = 2$ (sometimes called the quadrupole mode) that describes asymmetric wakes. By an asymmetric beam, we mean a beam with different spot sizes in the x and y directions (sometimes also called elliptical). As long as the aspect ratio, σ_x/σ_y, is small, we only need to use the $m = 2$ mode to describe the beam and resulting wakefield. Again, we will use a Fourier azimuthal decomposition to make this explicit. Then we can use a similar perturbation method to describe the blowout perturbation and therefore wakefields inside the bubble for an asymmetric beam.

3.2.1 $m = 2$ source term and pseudopotential

We will again begin by describing the beam density in terms of the azimuthal mode decomposition. The beam density is

$$\rho_b = \rho_{b,0} \exp\left(-\frac{x^2}{2\sigma_x^2} - \frac{y^2}{2\sigma_y^2}\right), \tag{3.72}$$

which can be expanded into

$$\begin{aligned}\rho_b &= \rho_{b,0} \exp\left(-\frac{r^2\left(1+\cos(2\theta)\right)}{4\sigma_x^2} - \frac{r^2\left(1-\cos(2\theta)\right)}{4\sigma_y^2}\right) \\ &= \rho_{b,0} \exp\left(-\frac{r^2}{4\sigma_x^2} - \frac{r^2}{4\sigma_y^2}\right) \exp\left\{\left(-\frac{r^2}{4\sigma_x^2} + \frac{r^2}{4\sigma_y^2}\right)\cos(2\theta)\right\}.\end{aligned} \tag{3.73}$$

For brevity, we define

$$\frac{1}{\sigma^2} \equiv \frac{1}{2\sigma_x^2} + \frac{1}{2\sigma_y^2}, \quad \frac{1}{\Delta^2} \equiv -\frac{1}{2\sigma_x^2} + \frac{1}{2\sigma_y^2}. \tag{3.74}$$

Using the multipole expanion for the potential from the previous section, Eq. 3.12, we have

$$\begin{aligned}
\phi_{m=2}(r,\theta) &= \frac{1}{4\pi\epsilon_0 r^2}\int dr' d\theta' \rho(r') r'^3 \cos(2(\theta'-\theta)) \\
&= \frac{\cos(2\theta)}{4\pi\epsilon_0 r^2}\int dr' d\theta' \rho(r') r'^3 \cos(2\theta') + \frac{\sin(2\theta)}{4\pi\epsilon_0 r^2}\int dr' d\theta' \rho(r') r'^3 \sin(2\theta') \\
&= \frac{\rho_{b,0}\cos(2\theta)}{4\pi\epsilon_0 r^2}\int_0^\infty \int_0^{2\pi} dr' d\theta' r'^3 \cos(2\theta') e^{-r'^2/2\sigma^2} e^{-r'^2/2\Delta^2\cos(2\theta')} \\
&= \frac{\rho_{b,0}\cos(2\theta)}{4\pi\epsilon_0 r^2}\int_0^\infty dr' r'^3 I_1\left(-\frac{r'^2}{2\Delta^2}\right) e^{-r'^2/2\sigma^2} \\
&= \frac{\rho_{b,0}\cos(2\theta)}{4\pi\epsilon_0 r^2}\frac{2\Delta^4}{\left(\Delta^4/\sigma^4-1\right)^{3/2}} \\
&= \frac{\rho_{b,0}\cos(2\theta)}{4\pi\epsilon_0 r^2}\sigma_x\sigma_y\left(\sigma_x^2-\sigma_y^2\right),
\end{aligned} \tag{3.75}$$

where I_1 is the modified Bessel function of the first kind. We define $\Lambda \equiv \rho_{b,0}\sigma_x\sigma_y$, switch to normalized units, and take the gradient to obtain

$$\begin{aligned}
\mathbf{E}_{m=2} &= -\nabla\phi_{m=2} \\
&= \frac{\Lambda}{r^3}(\sigma_x^2-\sigma_y^2)\left(\cos(2\theta)\hat{\mathbf{r}} + \sin(2\theta)\hat{\theta}\right).
\end{aligned} \tag{3.76}$$

In this analysis, we are interested in the $\hat{\mathbf{r}}$ direction and the $\cos(2\theta)$ terms (we take the $y=0$ slice without loss of generality). Moreover, we note that we are in the far field for a beam traveling at the speed of light so

$$E_{r,m=2}(r,\theta) - v_z B_{\theta,m=2}(r,\theta) = (1-v_z)\frac{\Lambda}{r^3}(\sigma_x^2-\sigma_y^2)\cos(2\theta), \tag{3.77}$$

which is what we will eventually need to describe the wake shape.

In Sec. 3.1.1, we showed the general Poisson solution for an azimuthal mode m. The solution for the pseudopotential inside the bubble was

$$\psi_m(r)\cos(m\theta) = \frac{\delta r_m \cos(m\theta)}{2m}\left[(1+n_\Delta)r_b^{1-m} - n_\Delta(r_b+\Delta)^{1-m}\right] r^m. \tag{3.78}$$

We again only consider the cosine term by assuming $\sigma_x > \sigma_y$. For $m=2$, we have

$$\psi_{m=2}(r) = \frac{\delta r_{m=2}}{4}\left[\frac{1+n_\Delta}{r_b} - \frac{n_\Delta}{r_b+\Delta}\right] r^2. \tag{3.79}$$

Using $n_\Delta = \frac{r_b^2}{(r_b+\Delta)^2 - r_b^2}$ and simplifying, we obtain

$$\psi_{m=2}(r) = \frac{\delta r_{m=2}}{4}\left[\frac{3r_b^2 + 3r_b\Delta + \Delta^2}{r_b(r_b+\Delta)(2r_b+\Delta)}\right] r^2 \approx \frac{3\delta r_{m=2}}{8r_b}\left(1 - \frac{\Delta}{2r_b}\right) r^2, \tag{3.80}$$

where, in the last step, we expanded to first order in Δ/r_b.

3.2.2 $m = 2$ perturbed plasma fields and wake shape

We use the same method as we did with $m = 1$ to calculate the vector potentials. We use the Lorenz gauge condition (Eq. 3.33) for the $m = 2$ mode,

$$\frac{1}{r}\partial_r\left(rA_{r,2,c}\right) + \frac{2}{r}A_{\theta,2,s} = -\partial_\xi \psi_{2,c}. \tag{3.81}$$

We use a similar ansatz as the $m = 1$ case but with one higher degree of r (this again matches what we see in simulation)

$$A_{r,2} = \left(f_2(\xi)r^3 + g_2(\xi)r\right)\cos(2\theta) \tag{3.82}$$

$$A_{\theta,2} = \left(f_2(\xi)r^3 - g_2(\xi)r\right)\sin(2\theta), \tag{3.83}$$

and upon substituting this into Eq. 3.81, we obtain

$$f_2(\xi) = \frac{1}{16r_0^2}\left[\delta r_2 r_0'\left(1 - \frac{\Delta}{r_0}\right) - \delta r' r_0\left(1 - \frac{\Delta}{2r_0}\right)\right]. \tag{3.84}$$

Similarly to the $m = 1$ case, we cannot solve for $g_2(\xi)$, and we have $A_{z,2} = a_2(\xi)r^2$ and $\phi_2 = b_2 r^2$, where $b_2 - a_2 = \frac{3\delta r_2}{8r_0}\left(1 - \frac{\Delta}{2r_0}\right)$. We can calculate the azimuthal magnetic field as follows,

$$\begin{aligned} B_{\theta,2,c} &= -\partial_\xi A_{r,2,c} - \partial_r A_{z,2,c} \\ &= \frac{r^3}{16r_0^3}\Bigg[\delta r_2'' r_0^2\left(1 - \frac{\Delta}{2r_0}\right) - 2\delta r_2' r_0 r_0'\left(1 - \frac{\Delta}{r_0}\right) \\ &\quad + \delta r_2\left(r_0'^2\left(2 - \frac{3\Delta}{r_0}\right) - r_0'' r_0\left(1 - \frac{\Delta}{r_0}\right)\right)\Bigg] - \tilde{g}r, \end{aligned} \tag{3.85}$$

where we defined $\tilde{g} \equiv g' + 2a_2$. Again, we cannot solve for this term but we can guess it is similar to the $m = 0$ perturbed value, thus we take $\tilde{g} \approx \delta r_2 \psi_0''(r = 0)/r_0$.

We can use the azimuthal magnetic field to derive a differential equation for δr_2 in a similar way as we did for hosing. Firstly, the driving term is now $(\sigma_x^2 - \sigma_y^2)/r_0$ (see Eq. 3.77). However, unlike with hosing, the pseudopotential does not cancel out because there is no change in coordinates. Therefore, we will now have a non-zero term for it in the perturbation theory, namely $\psi = \psi_0 + \psi_1$ (where ψ_1 corresponds to $\psi_{m=2}$). So we perturb the equation of motion for a boundary electron given by Eq. 3.54 and take the first order terms to arrive at

$$\begin{aligned}(1+\psi_0)r_1'' + \left(\psi_0' + \frac{r_0 r_0'}{2}\right) r_1' + \frac{r_1}{2}\psi_0''(r=0) + B_{\theta,2} \\ - \frac{r_0}{2(1+\psi_0)^3}\psi_1 - \frac{2\gamma_0}{1+\psi_0}\left(r_0\tilde{\psi}_1 - \frac{r_1}{4}\right) = \frac{\Lambda}{r_0^2}\left(\frac{\sigma_x^2 - \sigma_y^2}{r_0} - x_b\right),\end{aligned} \tag{3.86}$$

where we define $\tilde{\psi} \equiv \psi_1/r^2$. We again use the coefficients $c_\psi \equiv 1/(1+\psi_0)$ and $c_r \equiv \Lambda/r_0^2$, substitute in the expression for $\psi_1 = \psi_{m=2}$ and $B_{\theta,2}$, and denote $r_1 = \delta r_2$ to obtain

$$\begin{aligned}&\left(1 + c_\psi \frac{r_0^2}{16}\left(1 - \frac{\Delta}{2r_0}\right)\right)\delta r_2'' + c_\psi\left(E_{z,0} + \frac{3}{8}r_0 r_0' + \frac{1}{8}\Delta r_0'\right)\delta r_2' \\ &- \frac{c_\psi}{16}\left(\frac{3\Delta}{r_0}r_0'^2 + r_0 r_0''\left(1 - \frac{\Delta}{r_0}\right) + 2(1+c_\psi^2)\left(1 - \frac{3\Delta}{2r_0}\right) + 3c_\psi^3\left(1 - \frac{\Delta}{2r_0}\right)r_0^2\right)\delta r_2 \\ &= c_r c_\psi\left(\frac{\sigma_x^2 - \sigma_y^2}{r_0} - \delta r_2\right).\end{aligned} \tag{3.87}$$

Once this differential equation is solved, we know the perturbed wake shape, δr_2, and then can compute the perturbed fields of the asymmetric wake. As we will explore in the next chapter, the focusing force strength will vary longitudinally which can cause the beam slices to resonate at different betatron frequencies. And, in accordance with the Panofsky-Wenzel theorem [95], the accelerating field will vary transversely, which can cause an increase in energy spread.

3.2.3 Comparison to PIC simulations

We compare both the field expressions and the wake shape perturbation for asymmetric witness beam with QPAD simulations. We simulate both case (b) and (d) from Table 3.1, except instead of the second beam being tilted, it is instead made asymmetric by doubling its spot size in the x direction and halving its density so that the current stays the same.

First, we compare the fields inside the wake with QPAD simulations, shown in Fig. 3.9. We have not shown the expressions for the fields outside for $m = 2$, but they could be computed in the same way as $m = 1$. Just as for the $m = 1$ case, we see essentially perfect agreement for the fields inside given the linear term gr or $\tilde{g}r$ taken from simulation.

Next we compare the wake shape perturbation δr_2 from a single 3D timestep simulation with the value obtained from integrating Eq. 3.87, shown in Fig. 3.10. The simulation value is measured using $\delta r_2(\xi) = 4F_{\perp,2}(r,\xi)r_0(\xi)/3\,(1 - \Delta/(2r_0(\xi)))$ (r is chosen to be a small value near the axis), which is analogous to what we did for $m = 1$. In general, the agreement is not as good as the $m = 1$ case, where the details of the sheath do not directly appear in perturbed pseudopotential expression so a higher accuracy can be maintained. But we still find a moderate agreement with simulation for this first order approximation.

3.3 Summary

We have shown that by including all terms in the first order perturbation theory introduced by Huang et al. [88] and properly calculating the $m = 1$ plasma fields, we can more accurately predict the plasma channel centroid and therefore the beam hosing instability in the non-adiabatic, relativistic regime of interest to future experiments and applications.

We developed a formalism for calculating the fields for a general m mode, assuming a small radial perturbation to the sheath. For $m = 1$, this formalism gives the same result for the perturbed ψ to first order as the result derived from a rigid displacement of the channel.

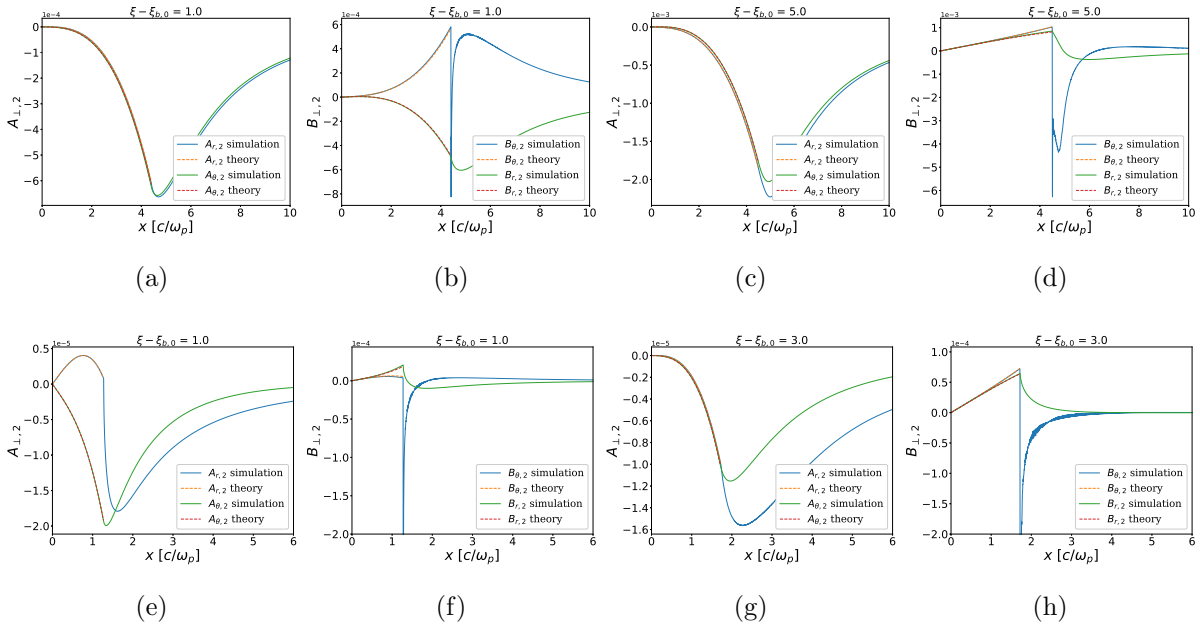

Figure 3.9: (a)-(d) $m = 2$ $A_\perp$ and $B_\perp$ fields (in normalized units) for case (b) in Table 3.1 except with an aspect ratio of 2 instead of a tilt. (a) $A_{\perp,2}$ and (b) $B_{\perp,2}$ at $k_p\xi = 1$ behind the head of the beam. (c) $A_{\perp,2}$ and (d) $B_{\perp,2}$ at $k_p\xi = 5$ behind the head of the beam. (e)-(h) $m = 2$ $A_\perp$ and $B_\perp$ fields (in normalized units) for case (d) in Table 3.1 except with an aspect ratio of 2 instead of a tilt. (e) $A_{\perp,2}$ and (f) $B_{\perp,2}$ at $k_p\xi = 1$ behind the head of the beam. (g) $A_{\perp,2}$ and (h) $B_{\perp,2}$ at $k_p\xi = 3$ behind the head of the beam. In all cases, the linear term gr or $\tilde{g}r$ is taken from the simulation.

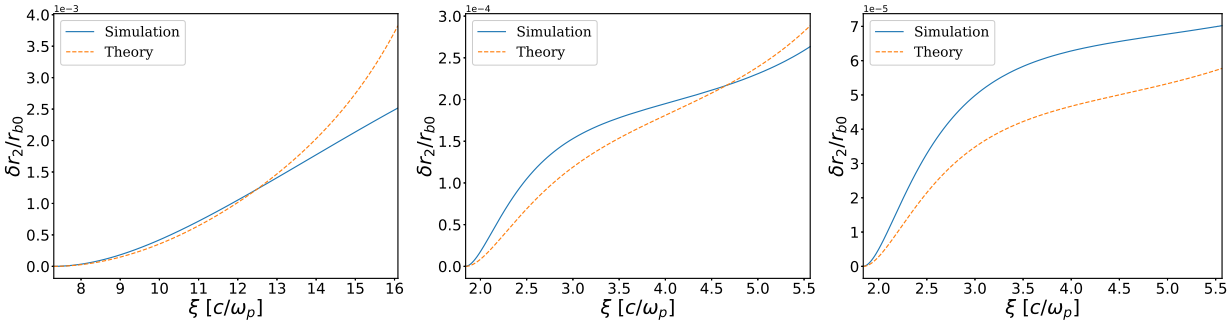

(a) (b) (c)

Figure 3.10: Perturbed wake shape comparison. (a) Case (b) in Table 3.1 but with the an aspect ratio of 2 instead of a tilt. $\Delta = 1.0$ was used. (b) Case (d) in Table 3.1 but with the an aspect ratio of 2 instead of a tilt. $\Delta = 0.8$ was used. (c) Case (d) with four times the beam density (both beams) and therefore twice the blowout radius. $\Delta = 1.0$ was used. The simulation line is measured using the slope of the $m = 2$ focusing force.

This was found to agree well with simulations. Knowing the perturbed pseudopotential, it was then possible to calculate the perturbed potentials and fields (up to an additive constant). These were also found to match simulations. Using these fields, we then rederived the equation for the channel displacement. We find this improved equation provides much more accurate results for a variety of different scenarios. There is still large discrepancy in some scenarios, where the blowout radius is very small and the sheath structure is more complicated.

We apply the same formalism to the $m = 2$ mode to describe wakes made by asymmetric beams. We calculate the pseudopotential and fields in the same way as $m = 1$. We can again use a perturbation theory on the symmetric blowout to predict the new wake shape. In this case, instead of the channel being displaced, it is widened in the direction of the larger spot size. The model for the perturbed wake shape was this was found to roughly agree with simulations. Once the perturbed wake shape is solved for, the wakefields caused by a given asymmetric beam can be calculated.

Finally, we discuss improvements one can make to the azimuthal mode model presented in this chapter. In the seminal work of Whittum et al. [86], an $m = 1$ like analysis of the channel was simple because there was assumed to be no electron sheath. In reality, blown out plasma wakes have finite-width electron sheaths, even in the long pulse limit. Self-consistently describing how the structure of the sheath is altered due to the perturbation by an offset beam is challenging. In this chapter, we showed if we assume a simple radial shift in the sheath, meaning its density and thickness are unchanged and do not vary in angle, θ, then an analogous result to Whittum et al. for ψ can be derived and used to calculate the plasma sheath fields. This gave the same result as a simple rigid displacement calculation to lowest order. We extended the result for the $m = 2$ case. However, this model does not rigorously conserve the source charge, S. In reality, the perturbed sheath density/thickness must vary in a way to conserve the charge. More detailed (and perhaps complicated) models may include perturbations that are not purely radial and may include the azimuthal current self-consistently in order to conserve the total source charge.

CHAPTER 4

Mitigation mechanisms for the hosing instability

In the previous chapter, we presented theoretical models for describing beam hosing and asymmetric wakes in plasma-based accelerators (PBAs). In this chapter, we show how the hosing instability can be mitigated, including by driving an asymmetric wake with an asymmetric drive beam. We first review the basic physics of mitigating hosing (called beam breakup by the accelerator community) in conventional accelerators. We will introduce the two-particle model which is useful for investigating mitigation conditions and timescales. Then, we will review the existing literature for mitigating hosing in PWFAs, including why the drive beam is inherently stable. We then show two ways of mitigating witness beam hosing. The first by using an initial energy chirp and the second by using an asymmetric drive beam. In the next chapter, we will discuss in detail how ion motion can not only mitigate hosing but even eliminate any misalignments.

4.1 Transverse instability overview

First, we provide some physics background based on conventional accelerators for the transverse or beam breakup instability, including how it was dealt with, and then discuss how these ideas can be applied to PBA and PWFA in particular. One method to mitigate beam breakup is to apply an energy chirp on the beam and it turns out the drive beam inherently acquires such an energy chirp. Thus, the necessary condition for stability of the drive beam can occur naturally during wake excitation and propagation through the plasma. The witness beam is more challenging to stabilize with these methods.

4.1.1 The BBU instability and BNS damping

We will briefly review the transverse physics in conventional accelerator physics because the same ideas will apply to PBAs, although the equations are more involved. One important tool for investigating the transverse dynamics of a beam is the two-particle model, where one macroparticle at the front of the beam drives the wake that the second macroparticle at the tail of the beam experiences. Of course this is not a realistic description, however, it captures the essential physics of the resonance condition between the transverse oscillations of two particles when they are offset from a defined axis. In RF cavities, when a beam is misaligned it will execute betatron oscillations and induce a dipole mode in the wakefield that the tail and subsequent bunches may experience. This acts to increase the transverse oscillations and eventually cause the beam to break up, hence the name beam breakup (BBU) instability (this is also called the hosing instability, which is more commonly used is the plasma context).

To introduce the two-particle model, we follow Ref. [96]. With the two-particle model, we can analyze a beam with initial offset $\hat{y}$. The head with oscillate with constant amplitude

$$y_1(s) = \hat{y} \cos k_\beta s, \tag{4.1}$$

where s is the propagation distance and k_β is the energy-dependent betatron wavenumber. In PBA, $k_\beta = k_p/\sqrt{2\gamma}$. The tail particle located a distance z behind the head then is deflected according to

$$y_2'' + k_\beta^2 y_2 = -\frac{N r_0 W_1(z)}{2\gamma L} \hat{y} \cos k_\beta s, \tag{4.2}$$

where γ is the Lorentz factor, r_0 is the classical electron radius, $W_1(z)$ is the transverse wake function for a cavity with a period L, and N is the number of particles in the bunch. The transverse wake function is essentially the Green's function for a beam with an $m = 1$ mode, which depends on the properties of the vacuum chamber environment. The solution is

$$y_2(s) = \hat{y} \left(\cos k_\beta s - \frac{N r_0 W_1(z)}{4 k_\beta \gamma L} s \, \sin k_\beta s \right), \tag{4.3}$$

where the second term represents the resonant response of the tail particle to the driving wakefield created by the head. The growth parameter can be defined as

$$\Upsilon \equiv -\frac{Nr_0W_1(z)L_0}{4k_\beta\gamma L}, \tag{4.4}$$

where L_0 is the linac length. A more involved analysis that includes acceleration shows the resonant term growths logarithmically with s instead of linearly [96]. The modified growth parameter in that case is

$$\Upsilon = -\frac{Nr_0W_1(z)L_0}{4k_\beta\gamma_f L}\ln\frac{\gamma_f}{\gamma_i}. \tag{4.5}$$

This growth is still quite severe, but as one might guess it is not hard to break this resonance. As long as the tail particle oscillates at a different frequency than the head, they will not be in resonance. This method of changing the beam betatron focusing along the bunch is known as BNS damping after Balakin, Novokhatsky, and Smirnov [97]. The solution to Eq. 4.2, assuming the tail particle oscillates at $k_\beta + \Delta k_\beta$, where $|\Delta k_\beta/k_\beta| \ll 1$, is

$$y_2(s) = \hat{y}\cos(k_\beta s + \Delta k_\beta s) + \frac{Nr_0W_1(z)}{4k_\beta\Delta k_\beta\gamma L}\hat{y}\left[\cos(k_\beta s + \Delta k_\beta s) - \cos k_\beta s\right]. \tag{4.6}$$

We notice that if

$$\frac{\Delta k_\beta}{k_\beta} = -\frac{Nr_0W_1(z)}{4k_\beta^2\gamma L} = \frac{\Upsilon}{k_\beta L_0}, \tag{4.7}$$

then the tail will oscillate uniformly with the exact same betatron oscillation as the head, i.e., the instability has been completely suppressed. This condition is referred to as the BNS condition. Conventionally, BNS damping as been applied either with a quadrupole whose strength changes as the bunch passes by or by positioning the bunch relative to the acceleration voltage such that the tail acquires a lower energy than the head, i.e., by using chromaticity. In the case of the SLAC linac, a typical energy deviation required by the BNS condition from head to tail would be around -5.5% [96].

4.1.2 BNS damping in a plasma

Next, we discuss how the idea of BNS damping has been applied to plasmas and the blowout regime. In the first paper to describe the hosing (or BBU) instability in a PBA, Whittum

et al. [86], several mitigation techniques were proposed. BNS damping was suspected to be ineffective due to the large betatron spread required because the wavenumber resonance is weak. However, because of the strong growth predicted in this seminal paper, i.e., the beam offset may exponentially grow from noise causing beam breakup, there has been much effort on studying this instability theoretically, computationally, and experimentally. Experimentally, no evidence of hosing was found unless specifically seeded [21]. This has been speculated to be due to BNS damping due to several different possible mechanisms [98]. This is the main topic of this chapter.

First, we review some of the theoretical advancements on the mitigation of hosing in PBAs. In the linear regime, hosing was found to be suppressed after a long proton bunch was self-modulated into a train of beamlets [99]. The suppression mechanism was a BNS-type mechanism because each beamlet resides in a different focusing region with the amplitude increasing for each beamlet. As long as the self-modulation instability grows faster than the hosing instability, the hosing would be suppressed after saturation. In the quasilinear regime of a PBA, the ions are not fully blown out and therefore the focusing force naturally varies longitudinally. This variation of focusing along the bunch was found to suppress hosing [100]. In the blowout regime, the drive beam was found to be intrinsically stable due to the energy variation that results from the decelerating field [98]. Ref. [98] also showed hosing would be suppressed for a beam with a correlated energy chirp or an uncorrelated energy spread. Drive beams with widths on the order of the blowout radius are also intrinsically stable due to the different focusing strengths along the beam [101].

Witness beam stability in the blowout regime is more challenging because we generally want the beams to be monoenergetic, which we achieve by properly beam loading. There is a relationship between the energy variation one can impose to suppress witness beam hosing and the efficiency of the acceleration process [102]. So directly applying a chirp has to be done carefully, as we will discuss in Sec. 4.2. Longitudinally varying focusing strengths to induce BNS damping will cause the accelerating field to vary transversely, as stated by

the Panofsky-Wenzel theorem [95], which causes growth in energy spread. This will be discussed in Sec. 4.3. Finally, the motion of ions can also introduce a density variation (both transversely and axially) which causes slightly nonlinear focusing forces and focusing variation along the bunch, which, as we have discussed, will suppress hosing [103, 104]. If the ion motion is severe, the hosing will be strongly damped owing to the nonlinear focusing forces created by the ions [104], or even completely eliminated. The next two chapters will discuss this in depth.

Next, we review the equations for the beam centroid when we consider energy effects, derived in Mehrling et al. [98]. The equation for a beam particle is

$$\ddot{x} + \frac{\dot{\gamma}}{\gamma}\dot{x} + k_\beta^2 x = k_\beta^2 x_c, \tag{4.8}$$

where x is the beam particle transverse position, $x_c(\xi, s)$ is the channel centroid, γ is the Lorentz factor, and the derivative is with respect to the propagation distance s. We assume the energy change is slow relative to a betatron oscillation, i.e., $\frac{\dot{\gamma}}{\gamma}\dot{x} \ll k_\beta^2 x$, and so we can solve this equation like the standard Hill-like equation and we can use the Green's function solution for the x_c term. We have

$$\begin{aligned} x(s) =& x_0 A(s)\cos\phi(s) + \frac{p_{x,0}}{\gamma_0 k_{\beta,0}} A(s)\sin\phi(s) \\ &+ k_{\beta,0}\int_0^s A(s)A(s')\sin[\phi(s)-\phi(s')]x_c(s')ds', \end{aligned} \tag{4.9}$$

where $A(s) = (\gamma_0/\gamma)^{1/4}$, x_0 is the initial x coordinate, $p_{x,0}$ is the initial momentum, and $\phi(s) = \int k_\beta ds$. The energy of a beam electron is given by $\gamma(s) = \overline{\gamma_0} - E_z s + \delta\gamma$, where the bar refers to the slice average. Note that all three terms may be slice dependent, i.e., a function of ξ. Expanding k_β for $\delta\gamma \ll 1$, leads to $k_\beta \approx \overline{k_\beta}(1 - \delta\gamma/2\overline{\gamma})$. The phase advance is then

$$\phi(s) = \overline{\phi}\left(1 - \frac{\delta\gamma}{2\overline{\gamma_0}}\frac{\overline{k_\beta}}{\overline{k_{\beta,0}}}\right), \tag{4.10}$$

where $\overline{\phi} = 2(\overline{k_{\beta,0}}/\overline{k_\beta} - 1)/\epsilon$ and $\epsilon \equiv E_z/(\overline{\gamma_0}\overline{k_{\beta,0}})$. This equation elucidates the phase mixing of particles with different energies. Finally, we can take the average over each slice to get the

beam centroid, $x_b = \int x f_0 dx_0 dp_{x,0} d\delta\gamma$, where f_0 is the normalized distribution. We assume the energy is separable and distributed as a Gaussian, $f_\gamma = \exp\left(-\delta\gamma^2/2\sigma_\gamma^2\right)/\sqrt{2\pi}\sigma_\gamma$. We define $\overline{\alpha} \equiv \overline{\phi k_\beta}/2\overline{k_{\beta,0}}$ and $\Delta\gamma \equiv \sigma_\gamma/\overline{\gamma_0}$. The integrals needed are of the form

$$\int \cos\left(\overline{\phi} - \overline{\alpha}\frac{\delta\gamma}{\overline{\gamma_0}}\right) \exp\left(-\delta\gamma^2/2\sigma_\gamma^2\right) d\delta\gamma = \exp\left(-\overline{\alpha}^2\Delta\gamma^2/2\right)\cos\overline{\phi}, \tag{4.11}$$

and we neglect the variation of $A(s)$ due to $\delta\gamma$, so upon averaging the first term of Eq. 4.9 one obtains

$$\int x_0 A(s)\cos\phi(s) f_0 dx_0 dp_{x,0} d\delta\gamma = x_{b,0}\overline{A}(s)\cos\overline{\phi}\exp\left(-\overline{\alpha}^2\Delta\gamma^2/2\right). \tag{4.12}$$

We repeat similar procedures for the other terms to arrive at the expression given in Mehrling et al. [98],

$$\begin{aligned} x_b(s) =& \overline{A}(s)\exp\left(-\overline{\alpha}^2\Delta\gamma^2/2\right)\Bigg[x_{b,0}\cos\overline{\phi} \\ &+ k_{\beta,0}\int_0^s ds'\, x_c(s')\overline{A}(s')\exp\left(\overline{\alpha}(s')^2\Delta\gamma^2/2\right)\sin\left(\overline{\phi}(s) - \overline{\phi}(s')\right)\Bigg], \end{aligned} \tag{4.13}$$

where we assume $\langle x_0 p_{x,0}\rangle = 0$. There are three main energy effects that can cause decoherence from plasma channel oscillation that are described in this equation. The decoherence times for these three effects can be calculated with the two-particle model in Ref. [105]. The first is the acceleration or deceleration of the beam that may be different for different slices ($\partial_\xi E_z \neq 0$). Hosing of the beam tail at ξ_2 will decohere from the head at ξ_1 after a time

$$\overline{k_{\beta,0}} s_{dc} = \sqrt{\frac{3\pi}{\Delta\epsilon}}, \tag{4.14}$$

where $\Delta\epsilon = |\epsilon(\xi_1) - \epsilon(\xi_2)|$ and $\epsilon \equiv -E_z\sqrt{2/\overline{\gamma_0}}$. This time was found to be generally shorter than that of pump depletion for most scenarios. This fact is why drive beams are intrinsically stable (as long as they are not shaped so that the deceleration field is flattened). However, the initial hosing growth before decoherence may be large and even small hosing growth of the drive beam may seed witness beam hosing. In this case, it may be useful to use a chirped drive beam so that the decoherence time is shorter. For a chirp $\chi \equiv \partial_\xi\overline{\gamma}/\gamma_b$, where γ_b is the

average over all beam electrons, the decoherence time is given by

$$k_{\beta,b}s_{dc} = \frac{2\pi}{|\chi|(\xi_2 - \xi_1)}. \tag{4.15}$$

Finally, for an uncorrelated energy spread $\Delta\gamma$, the decoherence time is

$$\overline{k_{\beta,0}}s_{dc} = \frac{2\Delta\gamma - \epsilon}{(\Delta\gamma - \epsilon)^2}. \tag{4.16}$$

These times given in Ref. [105] are for each isolated effect, but of course these effects generally occur together. Also it should be noted these predictions from the two-particle model are rough approximations, and there are important effects from continuous beams are not captured.

4.2 Witness beam energy chirp

To summarize the previous section, drive beam hosing should be mitigated as long as the drive beam is not shaped, due to the deceleration at different rates for different slices, or by a chirp or uncorrelated energy spread. However, any oscillation from the drive beam, even if stabilized, may seed the hosing of the witness beam. Thus, we also must ensure that the witness beam itself can be stabilized. However, all three energy effects that induce the BNS mechanism are undesirable for witness beams. For the witness beam, the beam quality is important, which makes hosing much more detrimental. Energy spread is undesirable because the beam becomes harder to focus outside the plasma with conventional optics at the final focus. Even if hosing is completely damped but the beam is still oscillating, if there is energy spread on the beam the phase space will fill in as it propagates leading to potentially large emittance growth. This section includes work published in Ref. [106].

4.2.1 QuickPIC simulation with FACET-II parameters

We start by describing the simulation setup we will refer to throughout this section. The parameters are similar to those anticipated at FACET-II, given in Table 4.1. Fig. 4.1 shows

$n_p = 4 \times 10^{16}$ cm^{-3} $\quad \Delta\xi = 150$ μm		
Parameter	Drive Beam	Witness Beam
E (GeV)	10	10
I_{peak} (kA)	15	9
$Q(nC)$	1.6	0.69
σ_r (μm)	3.65	3.65
σ_z (μm)	12.77	6.38
ϵ_N (μmrad)	50	50

Table 4.1: Simulation parameters for FACET-II

the setup - we use two Gaussian beams with the witness beam loaded in the back of the bubble. First, we run two simulations, one with both beams aligned on the axis of the wake and one with the witness beam rigidly offset one micron in the transverse direction from the axis. We show the hosing of the witness beam and the resulting emittance growth in Fig. 4.2. With no offset, we see stable acceleration with no growth in the beam centroid or emittance. With these parameters, the beam propagates through approximately 60 cm of plasma until pump depletion of the drive beam and the witness beam energy doubles. However, if the witness beam is misaligned by one micron, the hosing instability is strong and the emittance grows rapidly.

4.2.2 Simulation with an initial energy chirp on the witness beam

We apply an initial 10% head-to-tail linear energy chirp to the witness beam, while offsetting it one micron. By 10% energy chirp we mean there is a 10% energy difference between the head of the beam ($-\sigma_z$) and the tail ($+\sigma_z$) with respect to the average energy, i.e.,

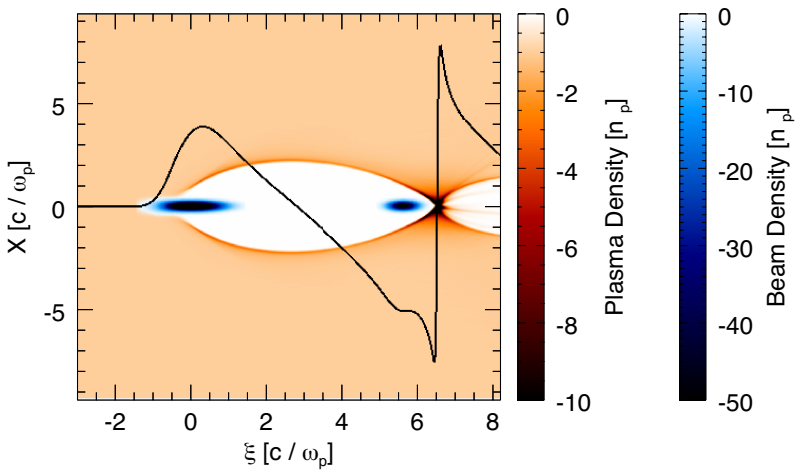

Figure 4.1: Beam and plasma electron density with the on-axis lineout of the accelerating field, for FACET-II parameters.

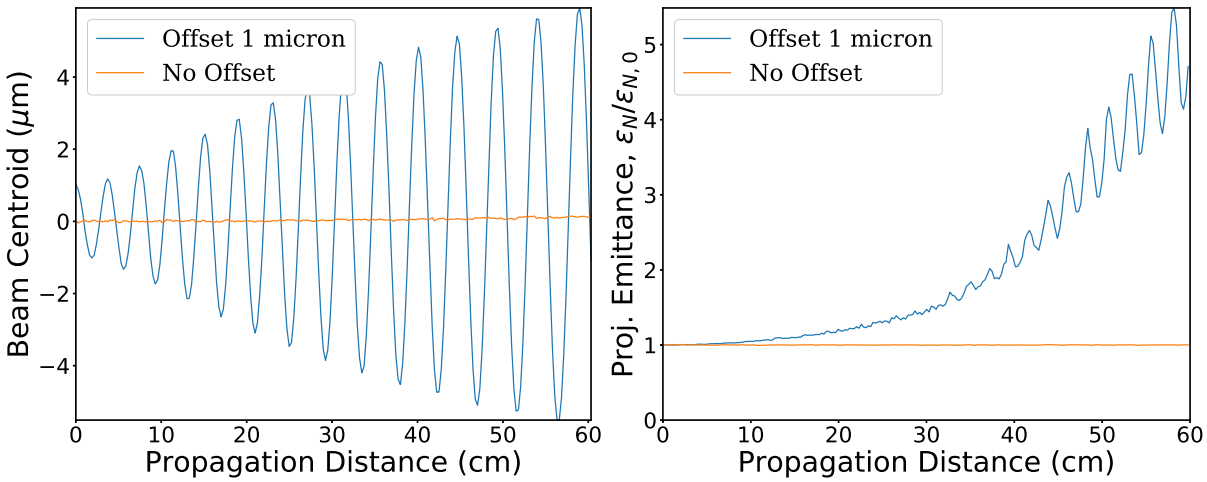

(a) (b)

Figure 4.2: Beam centroid (a) and emittance (b) evolution of an on-axis witness beam and one offset one micron. The centroid is measured at the tail, $\xi = +\sigma_z$. The large oscillations in the emittance is caused by some tail particles escaping the bubble because of the strong hosing.

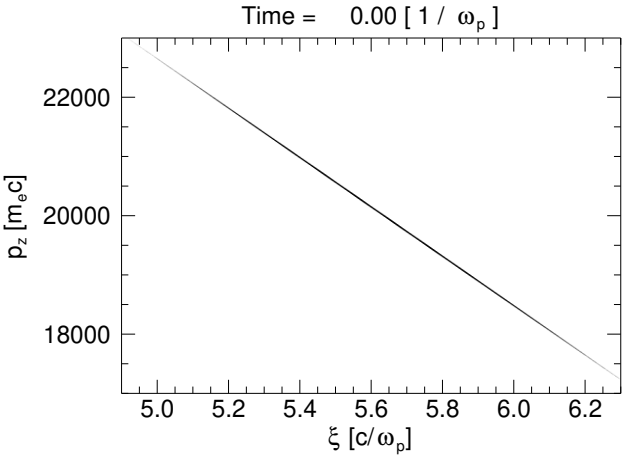

Figure 4.3: Initial longitudinal phase space of the witness beam, showing the 10% energy chirp.

$\Delta\gamma/\gamma_0 = 0.1$. This corresponds to an rms energy spread of 4.4%. Fig. 4.3 shows the initial chirp where the head is at a higher energy than the tail. Of course, this energy chirp is undesirable, so we need the beam to dechirp as it propagates through the plasma. We can do this by underloading the wake. Then the head of the beam will see the lower accelerating field and the tail will see the larger accelerating field, so the energy chirp will be corrected. There will still be some emittance growth in this process which places a tolerance on the beam parameters. We also show in this section that Gaussian beams naturally dechirp because of the way they load the wake.

Fig. 4.4 shows the suppression of the hosing instability when the witness beam has an energy chirp and therefore a smaller emittance growth. The decoherence time for this chirp is around 60 cm because the beam is short which takes longer to decohere. We see an initial hosing growth followed by the growth starting to saturate. The emittance growth is much smaller however, even though the centroid oscillation amplitude is only moderately smaller. Finally, of course we also need the witness beam energy spread to decrease as it propagates for this mitigation strategy to be useful.

Because we are using a Gaussian witness beam, there will not be perfect loading of the

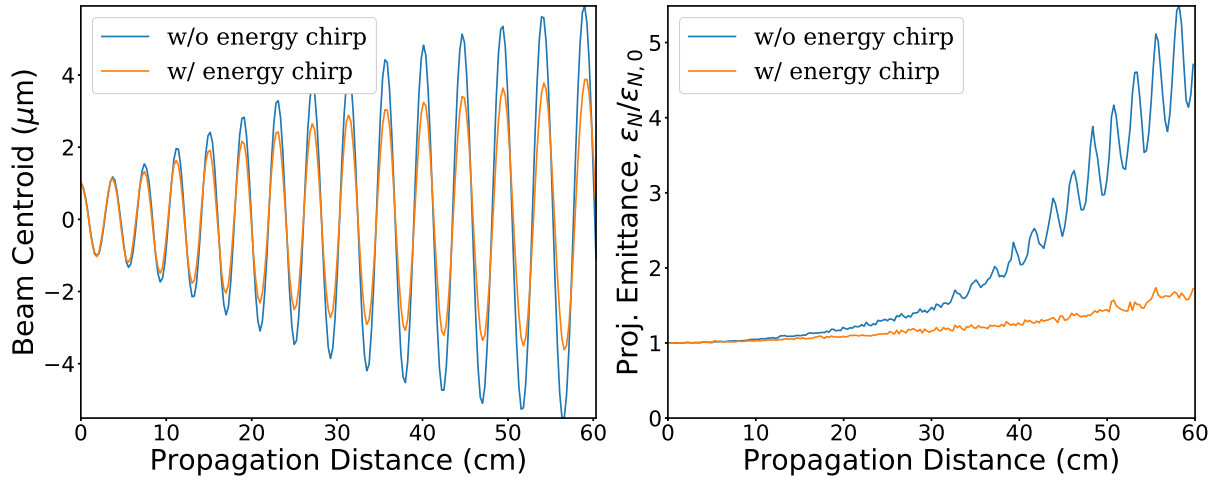

(a) (b)

Figure 4.4: Beam centroid (a) and emittance (b) evolution of a witness beam offset one micron with and without a 10% energy chirp. The centroid is measured at the tail, $\xi = +\sigma_z$.

head and tail of the beam. The head of the beam will see a slightly smaller acceleration field and the tail will see a slightly larger one, as can be seen in Fig. 4.1. So in the case without an energy chirp there will be about a one percent growth in energy spread due to this natural underloading. This is mostly independent of the hosing. But if we have a head-to-tail linear energy chirp, this loading of the witness beam will tend to cancel with the chirp, as illustrated in Fig. 4.5.

We compare the evolution of the projected energy spread of the beam in Fig. 4.6 for the two cases. From this figure, we can see the energy spread decrease to about one percent, less than that for the case with no initial chirp, after 60 cm of propagation. This is because the chirp corrects the imperfect loading of the Gaussian beam. In Fig. 4.5a, it can be seen that in the middle of the beam ($\xi = 5.5$ to 5.9), where the accelerating field is flat, that the initial chirp is mostly preserved.

In the case of a perfectly-loaded shaped bunch, the chirp would be preserved so that, even though hosing is mitigated, the beam would be left with an undesirable energy spread.

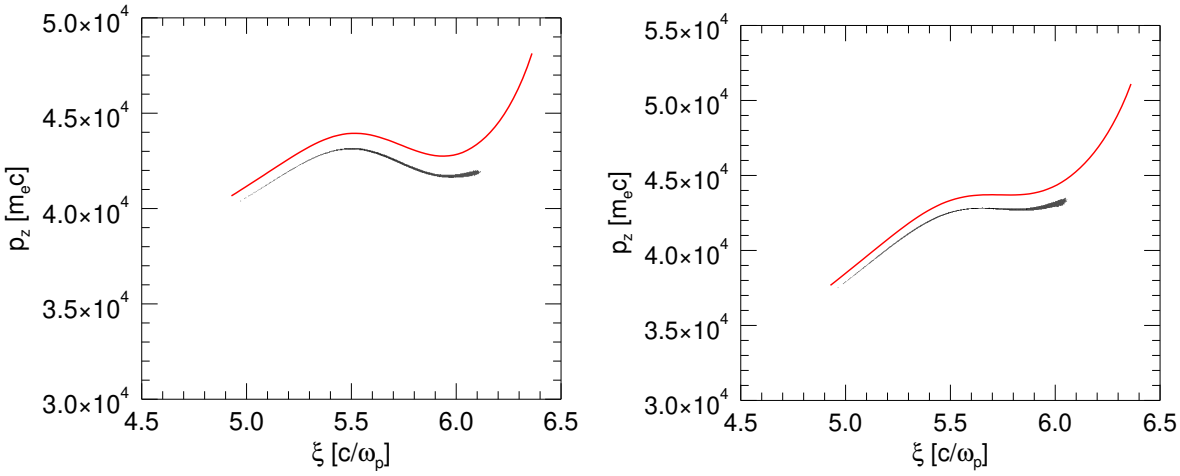

(a) (b)

Figure 4.5: Final longitudinal phase space of the beam with (a) and without (b) the 10% energy chirp. The red lines show the ideal acceleration using $\gamma(\xi, s) = \gamma(\xi, 0) - sE_z(\xi)$. In both cases, particles in the tail of the beam escape the bubble due to the strong hosing.

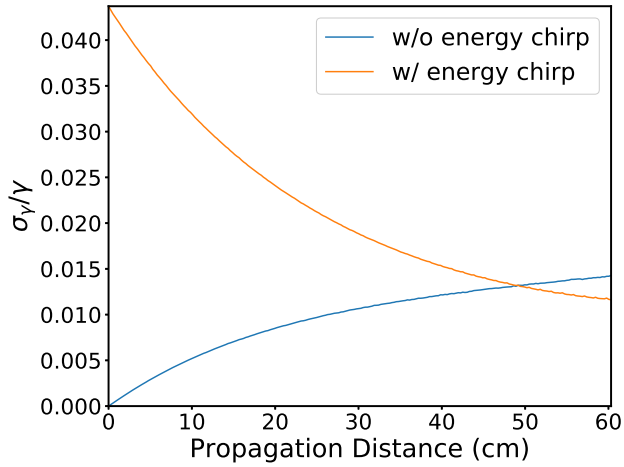

Figure 4.6: Evolution of the witness beam projected (95%) energy spread with and without the initial 10% energy chirp. Note by 10% energy chirp we are referring to the value of $\Delta\gamma/\gamma_0$ and by energy spread we are referring to the rms value of σ_γ/γ_0.

However, it is possible to design a shaped bunch using the beam loading theory from Ref. [29] that leads to a linearly decreasing E_z field (or any E_z needed to cancel a given initial chirp) that would exactly compensate the initial linear chirp over some propagation distance, s. This is shown in Appendix A. Conversely, one could attempt to design an initial chirp on the beam based on the loaded E_z field that results from its current profile, so that over a given distance the final energy spread would vanish. However, this is likely to be more difficult experimentally. A similar method was discussed in Ref. [105][1], except in this proposed scheme, the beam had no initial chirp, but the loaded wakefield had a linear E_z so that the beam develops a chirp during the propagation in the plasma. After exiting the plasma, the beam could potentially be transported with the chirp using optics with appropriate chromatic dependence. For collider designs and other applications this chirp could also possibly be removed using, e.g., a plasma-dechirper. Assuming it is straightforward to provide a linear chirp before the plasma section, the method proposed here would be preferable because the beam would be monoenergetic after leaving the plasma and would not need achromatic optics or dechirping. And the chirp is present at the beginning of acceleration, mitigating any initial hosing growth more strongly.

4.3 Asymmetric drive beams

Drive beams with differing transverse spot sizes (elliptical) will create an asymmetric bubble [71]. We discussed how to predict the resulting perturbation to the wake shape and therefore how to calculate the fields of an asymmetric bubble. The focusing force, and thus betatron oscillation, will vary along the direction of propagation. This axial variation of the betatron frequency along the beam will lead to BNS damping, similar to the previous section. Ref. [100] examined the saturation of the hosing instability due to this effect in the quasi-linear regime of PWFA, where longitudinally varying focusing forces occur naturally. This section

[1]This reference was published after the work presented in this section, published in the AAC 2018 proceedings [106]

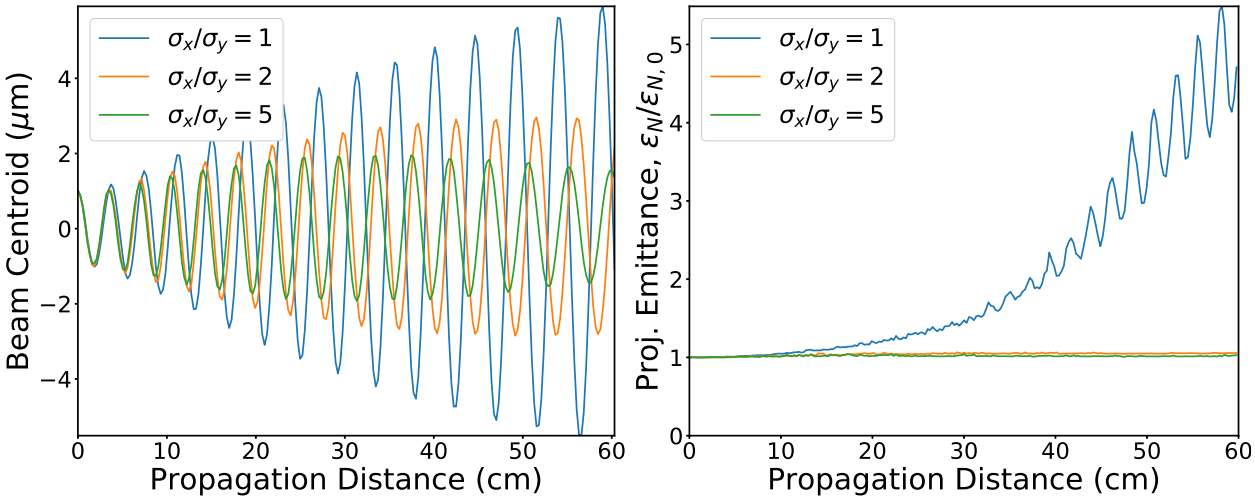

(a) (b)

Figure 4.7: Beam centroid (a) and emittance (b) evolution with drive beams of various spot size ratios, $\sigma_x/\sigma_y = 1, 2, 5$. The centroid is measured at the tail, $\xi = +\sigma_z$. The drive beam is initially matched in each direction.

includes work published in Ref. [106].

4.3.1 Mitigation of hosing due to asymmetric wakes

We rerun the simulation setup from Sec. 4.2.1, where now the drive beam is asymmetric. In Fig. 4.7, we plot the simulation results for a transverse spot size ratio of $\sigma_x/\sigma_y = 1, 2, 5$ (the drive beam charge is kept fixed) and the witness beam is offset by one micron in the x direction. In Fig. 4.7, we observe the damping of the centroid oscillations of the witness beam and emittance preservation.

A drawback to using asymmetric drive beams as a way to control hosing growth is that the accelerating field is no longer constant transversely in the bubble, i.e., the E_z now has a radial dependence, so there will be some slice energy spread growth in the witness beam. This is a consequence of the Panofsky-Wenzel theorem [95]. However, as shown in Fig. 4.8, this growth can be small for a range of drive beam parameters. For the parameters listed

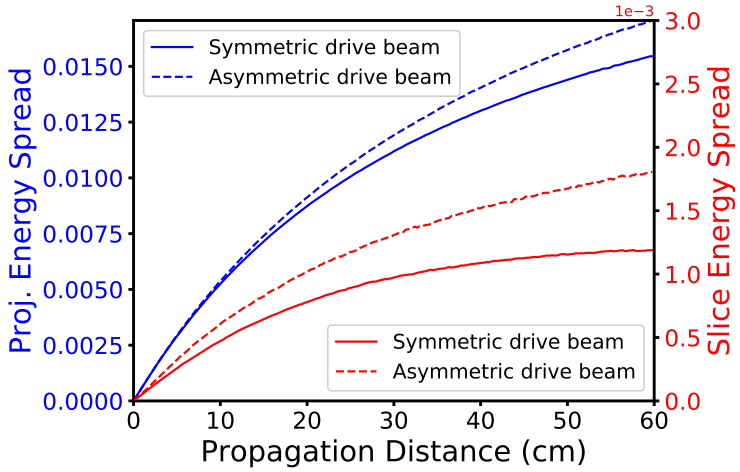

Figure 4.8: Projected (95%) and slice ($\xi = +\sigma_z$) energy spread growth in the witness beam, initially offset one micron, for a drive beam with $\sigma_x/\sigma_y = 2$ compared to the symmetric drive beam case with no hosing seed (hosing has negligible effect on energy spread except when particles escape the bubble).

in section 4.2.1, we have $< 0.5\%$ difference in growth after 60 cm using a drive beam with a spot size aspect ratio of 2. In this case, we start with no initial energy spread. However if we start with a small initial energy spread less than the final value (under 1% in this case) the final energy spread approaches the same value after 60 cm.

If the asymmetry of the drive beam is rotated by $\pi/2$, i.e., $\sigma_y > \sigma_x$ with the witness beam still offset in the x direction, the effect on hosing mitigation is similar. In this case, the focusing force perturbation will be negative, but the arguments are the same. As long as there is a change in the focusing force along the witness beam, the betatron oscillations in each slice will detune and the hosing will damp. This is also shown in Fig. 4.9 for the different drive beam aspect ratios. Unlike the previous plots, we do not consider the beam particles after they leave the bubble, so we no longer see the large emittance oscillations in the symmetric case. The emittance growth in these cases when the asymmetry is opposite of the offset direction is larger of course but still saturates with a lower projected emittance growth than the symmetric case after 60 cm.

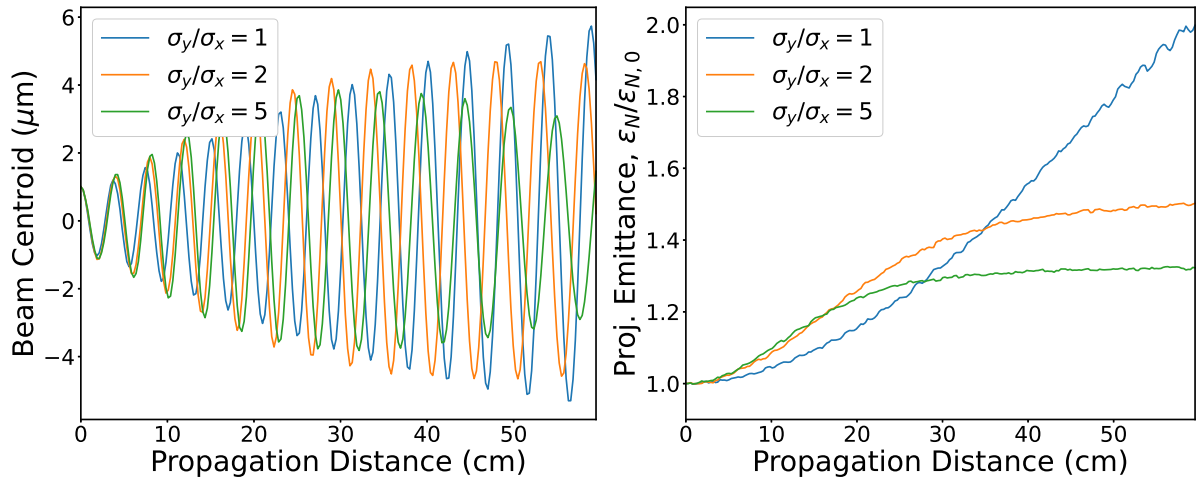

(a) (b)

Figure 4.9: Beam centroid (a) and emittance (b) evolution with drive beams of various spot size ratios, $\sigma_y/\sigma_x = 1, 2, 5$. The witness beam is still offset one micron in the x direction. The centroid is measured at the tail, $\xi = +\sigma_z$. The drive beam is initially matched in each direction. In this case, beam particles that leave the bubble are not considered when calculating the beam centroid and emittance.

Asymmetric witness beams generally do not perturb the fields enough to have an effect on themselves, because they are often short and narrow. For the parameter regime examined in this section, we found an asymmetric witness beam with a large spot size ratio has a negligible effect on its own hosing.

4.3.2 Asymmetric wake field scaling

Next, we explore how the field perturbations scale with drive beam spot size aspect ratio σ_x/σ_y and the absolute value of the spot size normalized to the blowout radius σ_x/r_m, where r_m is the maximum blowout radius (~ 2.2 in this case, as seen in Fig. 4.1). In Fig. 4.10, we see for this relatively narrow beam that for aspect ratios of $\sigma_x/\sigma_y > 4$, the field perturbations saturate. On the other hand, for larger spot sizes the fields are perturbed strongly. These results show that for a narrow beam ($\sigma_x/r_m = 0.0633$) and a modest aspect ratio of two there was drastically reduced emittance growth due to hosing. This is due to the large slope in the perturbed focusing force at the witness beam tail.

It is important to note that in the simulations over pump depletion distances the evolution of the drive beam is important and can lead to growth of the field perturbations as it propagates through the plasma. If we turn off drive beam evolution in the simulation, a substantial initial perturbation is needed in order to detune the resonance and damp the hosing. In simulations where the asymmetric drive beam is matched in both transverse directions, the zeroth order evolution of the beam is dominated by the head erosion, which tends to increase the projected spot size and cause larger field perturbations. Unmatched drive beams undergo spot size oscillations and have smaller overall projected spot sizes and therefore smaller field perturbations. Therefore, in this case the hosing would likely not be reduced much. One would need a wide drive beam in order to sufficiently perturb the focusing force.

These results should also apply to laser drivers. With laser drivers the perturbations should be larger because they are similar to wide particle beams and have smaller spot size

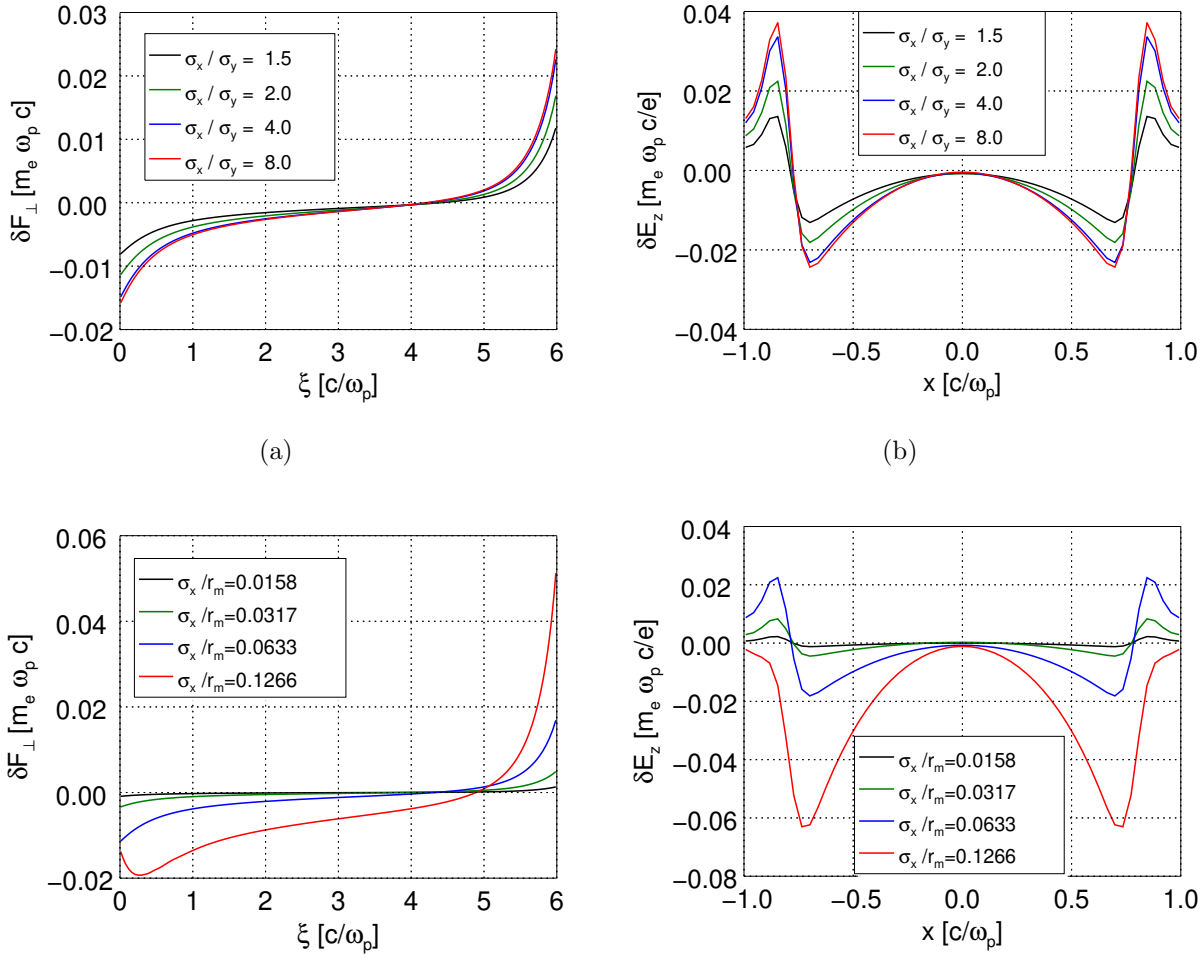

Figure 4.10: Scanning of field perturbations from one timestep QuickPIC simulations. The first row is a scan over the spot size ratio of the drive beam with σ_x held fixed at 3.65 μm, the second row is a scan of the absolute value of the spot size of the drive beam with the ratio fixed to $\sigma_x/\sigma_y = 2$. The first column shows the focusing force perturbation (the difference of the asymmetric and symmetric) lineout along 0.5 c/ω_p. The second column shows the accelerating field perturbation as a function of x taken at the tail of the witness beam $\xi = +\sigma_z$.

oscillations. As shown in Fig. 4.10, the field perturbations are large for wide beams. Of course this will also mean the slice energy spread growth will be larger.

In many early PWFA experiments (and still today), many beams had large spot size asymmetries. This fact along with the other mechanisms described in this section could explain why no hosing growth was seen in experiments where hosing was not seeded. Understanding the wakefields and instability mitigation of asymmetric wakes will continue to be important for current experimental campaigns.

4.4 Summary

In this chapter, we have discussed several methods to mitigate the hosing instability in plasma wakefield accelerators. These methods are all based on breaking the resonance of the hosing instability that couples the beam oscillations with the plasma channel oscillations. This is the same idea used in conventional accelerators, called BNS damping. By changing the energy or focusing along the beam, the dipole wakefield induced by the head or preceding bunch will no longer cause resonant oscillations. If the BNS condition is met, the oscillation at the tail will be the same as the head. The basic physics is often investigated using a two-particle model.

In a plasma, the equations are more complicated but the fundamental physics is the same. If each slice acquires a different betatron oscillation, the hosing resonance will be detuned and the centroid growth will be suppressed. Longitudinal variation of the focusing force is natural in the linear or quasi-linear regime of PWFA, where the plasma electrons are not fully blown out, so hosing is naturally suppressed. In the blowout regime, there are several mechanisms that can invoke BNS damping. These mostly require the beams to not be monoenergetic. For example, the drive beam energy loss for a Gaussian current profile is usually different at different longitudinal positions along the beam so it naturally has different betatron oscillations between slices, and so it is less susceptible to hosing.

Mitigating witness beam hosing is a little more challenging in that we generally want the beam to be monoenergetic. We presented a scheme where the beam is initially chirped in order to suppress the hosing, but is then dechirped naturally as it propagates by using an underloaded wake. This can be done naturally for a witness beam with a Gaussian current profile or, to keep the energy spread very low, one could design a witness beam profile that would exactly cancel the chirp after some propagation distance.

Finally, we discussed asymmetric drive beams that cause a perturbed bubble radius. This leads to focusing forces that vary along the beam. For the FACET-II case, modest drive beam aspect ratios were found to lead to significant focusing force variation at the tail of the witness beam that mitigated the hosing, while only leading to a slightly higher slice energy spread. The perturbed fields saturated after aspect ratios of around four, whereas perturbations were much larger for larger spot sizes.

These findings will be important in current and future experiments and potentially linear collider designs for controlling the beam stability in the plasma and minimizing emittance growth. However, as we will discuss in the next chapter, ion motion will be the dominant effect in linear colliders and has significant implications for beam hosing.

CHAPTER 5

Ion motion in plasma wakefield accelerators

In previous chapters, we described the hosing instability and ways to mitigate it assuming the plasma ions were immobile and therefore the focusing force is symmetric and linear. The witness beam spot size could be matched to the linear focusing force to preserve its emittance, in the absence of hosing, as discussed in Sec. 2.5.2. Matching in more general nonlinear forces will be discussed in this chapter. A matched beam with parameters in the LC regime has a large enough space charge force to pull plasma ions into the beam during its transit time. This ion collapse causes the focusing forces to become nonlinear.

In this chapter, we briefly review a few recent works addressing the consequences of ion motion in PBAs. We derive the ion density profile that arises from ion motion for a prescribed electron beam and quantify how this modifies the associated wakefields. Using this profile, we can then derive an approximately nonlinearly matched spot size for the beam such that the emittance growth is minimized. Moreover, we discuss how to calculate the exact slice-by-slice matching distribution. Next, we present a scheme to calculate the emittance growth when a beam is transversely misaligned in a given perturbed ion column, assuming the ion density remains fixed for the witness beam. This is the case when the drive beam causes ion motion and the witness beam is does not cause significant additional deflections to the ions. Finally, we consider the linear collider (LC) regime, where ion motion will be substantial. We show that drive beam induced ion motion (with an appropriate beam density) can damp the centroid oscillations of the witness beam. This chapter considers beams that are focused directly into a uniform plasma. In the next chapter, we will extend these ideas to beams

propagating in plasma density ramp matching sections. This chapter covers works to be published in Ref. [107].

5.1 The problem of ion motion in PWFA

In the LC regime, witness beams must have emittances on the order of hundreds of nanometers and around a nanocoulomb of charge in order to achieve luminosities of $L = fN^2/4\pi\sigma_x\sigma_y \sim 10^{-34}\,\mathrm{cm}^{-2}\mathrm{s}^{-1}$, where f is the frequency of collisions, N is the number of particles in each beam, and σ_x and σ_y are the transverse spot sizes of the beam at the interaction point [58]. High current, tightly focused beams required for LCs can cause the plasma ions to collapse within the transit time of the beam which can cause severe emittance growth. The possibility of ion motion in the blowout regime was first studied in Ref. [108]. The problem of severe emittance growth was pointed out in Ref. [109], where flat-top electron beams (transversely uniform) were assumed. Inside this flat-top beam, Gauss's Law can be used to derive the transverse electric field an ion will experience,

$$E_r = \frac{4\pi}{r}\int_0^r \rho_b r' dr' = -\frac{4\pi e n_b}{2} r, \tag{5.1}$$

where n_b is the beam density and n_p is the plasma density. We have

$$F_\perp = ZeE_r = -4\pi\frac{Ze^2}{2}n_b r = -\left(\frac{Z}{2}\frac{n_b}{n_p}r\right)m\omega_p^2, \tag{5.2}$$

where Z is the ion charge state. Thus, the equation of motion for an ion is

$$r'' + k_i^2 r = 0, \tag{5.3}$$

where $' \equiv \frac{d}{d\xi}$ and

$$k_i = \sqrt{\frac{Zn_b/n_p}{2M/m}}k_p, \tag{5.4}$$

M is the ion mass, and m is the electron mass. The self-force from the ions is assumed to be negligible. So the ions will move sinusoidally and they will collapse onto the same point

$k_i\xi = \pi/2$, leading to very large peaks in ion density that significantly alter the focusing force on a beam electron and thus can potentially cause large emittance growth. The phase advance of a plasma ion within the length of a beam is given by $\Phi = k_i L_b$, where L_b is the length of the beam. We note that if the beam does not have a longitudinal flat-top profile, then $k_i = k_i(\xi)$, and L_b will be an effective length based on the exact profile. Thus, when $\Phi \sim 1$, ion motion effects becomes important. Since the publication of Ref. [109], ion motion has been considered a major obstacle for PWFA-LCs and much research has been devoted to investigating and determining paths to overcome it.

The first work to quantify the emittance growth due to ion collapse was An et al. [110]. In this work, the ion collapse and resulting focusing forces were characterized using QuickPIC simulations. As mentioned in Chapter 1, the simulations in this regime are very computationally expensive. At the time Ref. [110] was published, it was not practical to simulate the entire simulation box with fine enough resolution to resolve the ion collapse and model the entire transverse dimensions of the wakefield. So instead, only a small region around the narrow witness beam was simulated with fine resolution throughout, where only the ions and witness beam particles were evolved. Such simulations only model how the witness beam modifies the focusing force but not the accelerating field. The plasma electrons were modeled as a thin, immobile, and neutralizing sheath at the edge of the simulation box. These results and conclusions have since been verified by simulations that model the entire domain and use a refined mesh near the witness beam. Furthermore, QPAD has allowed us to simulate this regime fully self-consistently with fine resolution throughout the domain while keeping a limited number of azimuthal modes. It is possible to use a much higher resolution in r as compared to the full $x - y$ plane and there is significant speed up so that the simulations are less computationally expensive.

In Ref. [110], theoretical analysis was presented assuming a Gaussian profile was assumed for the ion collapse, $\rho_i = Ae^{-r^2/2\sigma^2}$. Thus, the resulting (total) focusing force is

$$F_\perp = -\frac{r}{2} - \frac{A\sigma^2}{r}\left(1 - e^{-r^2/2\sigma^2}\right). \tag{5.5}$$

Using this model, it is possible to study the evolution of a beam slice. If the spot size of the beam and the ion collapse are of the same order in size, the emittance growth would scale as $\sqrt{A}$, which would be catastrophic. However, the width of the self-consistent ion collapse was found to be much smaller than the spot size of the witness beam. So instead of an order of magnitude emittance growth, QuickPIC simulations found the projected emittance growth for a tri-Gaussian witness beam with a spot size matched to the unperturbed focusing force to be around $\sim 80\%$, assuming no misalignments and a low density (non-evolving) driver. At the time, it was thought that once the beam achieved this steady state, it could possibly be transported to subsequent stages and therefore the emittance growth would only occur in the first stage. This work also mentions using asymmetric witness beams or overfocused witness beams to decrease this emittance growth. It also employed a 1D analytical model to predict this emittance growth, that agreed well with simulations.

5.2 Calculating the ion density

In this dissertation, we consider situations where the ion motion from both the drive and witness beam is important. In order to study the effects of ion motion on the wakefields and witness beams, we first calculate the trajectories of the ions and from these determine the ion density. We calculate the ion density collapse for a bi-Gaussian driver, $\rho_b(\xi) = \rho_{b,0}(\xi)e^{-r^2/2\sigma_r^2}$ (similar analysis can be done for other distributions). This is similar to the derivation in the previous section, but more general. The radial electric field on the ions from the beam can be derived from Gauss's Law as

$$\begin{aligned} E_{r,\text{beam}} &= \frac{4\pi\rho_{b,0}(\xi)}{r}\int_0^r e^{-r'^2/2\sigma_r^2} r'\, dr' \\ &= \frac{-4\pi e n_b(\xi)\sigma_r^2}{r}\left(1 - e^{-r^2/2\sigma_r^2}\right), \end{aligned} \tag{5.6}$$

as well as the self-force from other ions, given by

$$E_{r,\text{ion}} = \frac{2\pi Z e n_p r_0^2}{r}, \tag{5.7}$$

where r_0 is the initial radius of the ion and Z is the charge state. In this model, because of azimuthal symmetry, the ion trajectories represent rings of charge (as was done in Ref. [108]). Eq. 5.7 is valid as long as the rings do not cross. Therefore, if we neglect longitudinal ion motion, the total radial force on an ion is

$$\frac{F_r}{mc\omega_p} = -\frac{Z\Lambda(\xi)}{k_p r}\left(1 - e^{-r^2/2\sigma_r^2}\right) + \frac{Z^2(k_p r_0)^2}{2k_p r}, \tag{5.8}$$

where $\omega_p = ck_p$ is the plasma frequency and $\Lambda(\xi) = n_b(\xi)/n_p(k_p\sigma_r)^2$ is the normalized charge per unit length of the beam. We again normalize the force to $mc\omega_p$, lengths to k_p^{-1}, time to ω_p^{-1}, and densities to n_p. The radial equation of motion for an ion with mass M is then

$$r'' = -\frac{Z\Lambda(\xi)}{M/m}\frac{1 - e^{-r^2/2\sigma_r^2}}{r} + \frac{Z^2 r_0^2}{2(M/m)r}. \tag{5.9}$$

The second term is typically negligible because $\Lambda \gg r_0^2$ for any ion that will reach the axis by the time the witness beam arrives. In the limit $r \ll \sigma_r$, Eq. 5.9 reduces to that of a harmonic oscillator, assuming a constant Λ, as in Refs. [109] and [108]. The comparison between integrated trajectories from Eq. 5.9 and tracked particle trajectories from a PIC simulation is shown in Fig. 5.1.

Now that we know the trajectories, we can calculate the ion density using the ring model, where each ring (or sheet) represents a ring of ion particles. Each radial position on the ring follows the trajectory of an individual ion at the corresponding radius. Thus, as a ring converges, the density is proportional to $1/(r\Delta r)$, where r is the radius of the ring and Δr is the spacing between neighboring rings. Therefore, the density is given by $n = n_0 r_0 \Delta r_0/(r\Delta r)$. This same relationship can be obtained by viewing the plasma ions as a Lagrangian fluid element with charge density $\Delta\sigma = 2\pi n_0 r_0 \Delta r_0$, where r_0 is the initial radius, Δr_0 is the initial thickness, and n_0 is the initial density. As the boundaries of the fluid element change, the area of the element is compressed to $A = 2\pi r\Delta r$, where $r = r(r_0, \xi)$ is the ion ring trajectory and Δr is the ring thickness. Therefore, we have

$$\rho_i(r, \xi) = \frac{\Delta\sigma}{\Delta A} = \rho_{i,0}\frac{r_0 \Delta r_0}{r\Delta r}, \tag{5.10}$$

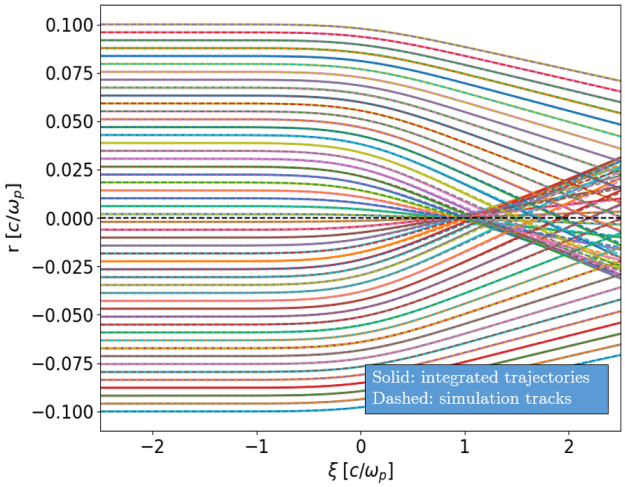

Figure 5.1: Comparison of numerical ion trajectories and tracked ion trajectories from QuickPIC for the case of FACET-II like parameters. This shows the region around the tri-Gaussian drive beam centered at $\xi = 0$ with one micron emittance. For reference, the transverse spot size of the beam is $\sigma_r \approx 0.02\, c/\omega_p$.

for each ring contribution. We sum over each ring to get the total ion density

$$\rho_i(r,\xi) = \rho_{i,0} \sum_k \frac{r_{k,0}\Delta r_0}{r_k \Delta r_k}, \tag{5.11}$$

where $\Delta r_k = r_k - r_{k-1}$. To calculate the ion density from this we need to introduce a grid in $r-\xi$ with transverse grid size Δ_r (not to be confused with the ring thickness Δr). The sum is then over ring trajectories within Δ_r of r, similar to a PIC charge deposit. The singularity at $r = 0$ and trajectory crossing can be dealt with by setting a cutoff $r_{\min}$, typically set to be around $r_{\min} \sim \Delta_r/4$. For the case of the uniform flat-top beam where the trajectories are harmonic, the density on axis would be $\rho_i(\xi) = 1/\cos^2(k_i\xi)$, where $k_i = \sqrt{\frac{Zn_{b,0}/n_p}{2M/m}}$. In the general case, the trajectories can be calculated by numerical integration of Eq. 5.9, then the charges can be deposited (with area weighting) onto a grid. This procedure somewhat surprisingly reproduces the self-consistent PIC simulation results even when there is strong ion motion and significant trajectory crossing. The cutoff acts like an effective zeroth order particle shape, so it gives similar results to the PIC codes when the ions reach the axis (the

density spikes are the same). Fig. 5.2 shows the comparison between this method and QPAD both for FACET-II like parameters with smaller emittances and LC parameters, as well as a comparison to the analytic result for a flat-top beam. The parameters are listed in Sec. 5.5.1 and Sec. 5.4.1, respectively. This method may be significantly faster than scanning the densities via a one 3D timestep PIC code, especially if one is only concerned with the on-axis density or a particular beam slice.

5.3 Calculating the transverse wakefield with ion motion

Next, we calculate the transverse wakefield (or focusing force, $F_\perp = -ZeW_\perp$) using the ion ring model described above. In Ref. [111] the transverse wakefield was calculated for weak ion motion ($\Phi \ll 1$) using an Eulerian fluid model. We can reproduce and extend this result using the ring model. Starting from Eq. 5.7, we can obtain an expression for $W_\perp$ at radial position r by replacing r_0 with $r + \delta r$,

$$W_{\perp,\mathrm{ion}}(r) = E_{r,\mathrm{ion}}(r) = \frac{2\pi Z e n_p (r+\delta r)^2}{r}, \tag{5.12}$$

where δr is the compression of the ion ring from r_0 to coordinate r (we define $\delta r > 0$ when the ring moves towards the axis) and we assume $B_\theta = 0$ due to azimuthal symmetry. This expression is fully nonlinear so long as the rings do not cross each other. Taking two derivatives with respect to ξ we arrive at

$$\frac{\partial^2 W_{\perp,\mathrm{ion}}}{\partial \xi^2} = \frac{4\pi Z e n_p}{r}\left[(r+\delta r)\frac{\partial^2 \delta r}{\partial \xi^2} + \left(\frac{\partial \delta r}{\partial \xi}\right)^2\right]. \tag{5.13}$$

To lowest order, we assume the velocity term $\frac{\partial \delta r}{\partial \xi}$ is small and that $r \gg \delta r$, which we note are equivalent to the weak ion motion assumption in Ref. [111]. Finally, we use the equation of motion

$$\frac{\partial^2 \delta r}{\partial \xi^2} = \frac{F_\perp}{Mc^2} = \frac{-ZeE_\perp}{Mc^2}, \tag{5.14}$$

to obtain

$$\frac{\partial^2 W_{\perp,\mathrm{ion}}}{\partial \xi^2} = -Z\frac{m}{M}k_p^2 E_\perp, \tag{5.15}$$

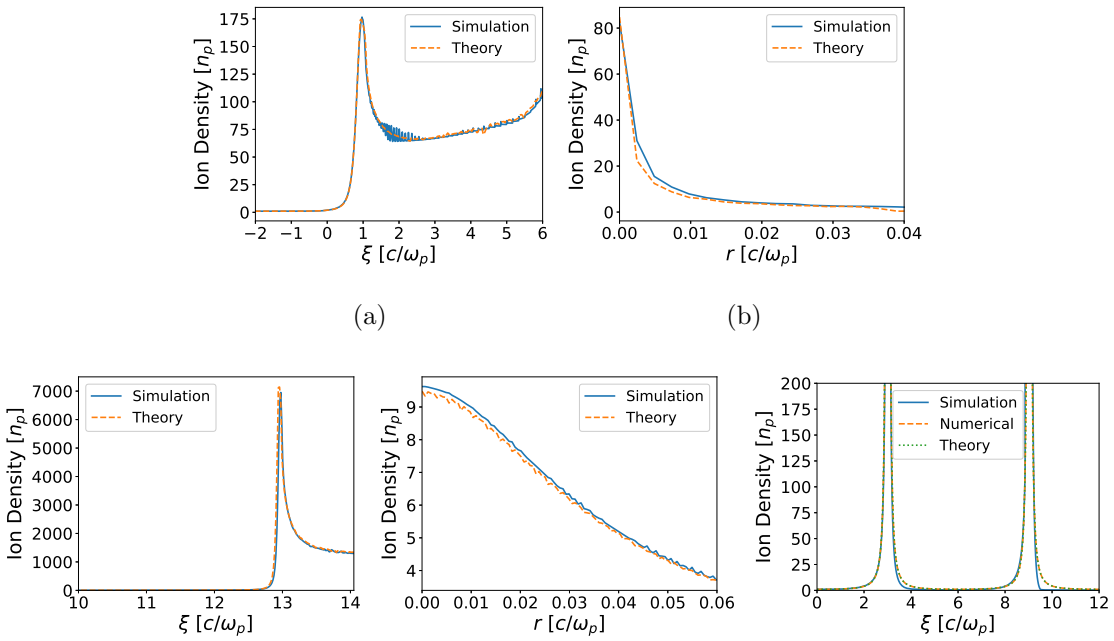

Figure 5.2: (a),(b) Ion density for FACET-II like parameters with 1 μm normalized emittances. The drive beam is centered at $\xi = 0$ and the witness beam at $\xi_{w,0} = 5.55$. (a) On axis ($r = 0$) density. (b) Transverse slice at the center of the witness beam, $\xi_{w,0} = 5.55$. (c),(d) Ion density for LC parameters with $n_{b,d} = 100$ and witness beam emittance of 0.0277 μm. The drive beam is centered at $\xi = 6.0$ and the witness beam is trapezoidal and starts at $\xi = 12.25$ and ends at $\xi = 14.05$. (a) On axis ($r = 0$) density. (b) Transverse slice at the head of the witness beam, $\xi = 12.25$. (e) Ion density in a uniform electron beam with $n_b = 1000$ (from $\xi = 0$ to $\xi = 12$ and radius $r = 5$). Numerical means the integrated theory like in the previous plots and theory means the analytic result $\rho_i(\xi) = 1/\cos^2(k_i\xi)$.

which is identical to an equation from Ref. [111]. Then, following Ref. [111], and normalizing quantities, we obtain

$$W_{\perp,\mathrm{ion}}(r,\xi) = \frac{r}{2} + Z\frac{m}{M}\int_0^{\xi} d\xi'(\xi-\xi')E_{\perp}(r,\xi'), \tag{5.16}$$

where the head of the bunch is at $\xi = 0$ and the contribution from the uniform background was added. For reasons given earlier, we assume the beam fields dominate so that $E_\perp$ is due solely to the beam. For a beam with a transverse distribution $g_\perp(r,\xi)$, longitudinal distribution $g_\parallel(\xi)$, and azimuthal symmetry, the wakefield with weak ion motion is given by

$$W_r = \frac{r}{2} - Z\frac{m}{M}\frac{n_b}{n_p}\frac{1}{r}\int_0^{\xi} d\xi'(\xi-\xi')g_\parallel(\xi')\int_0^{r} r'dr'g_\perp(r',\xi'). \tag{5.17}$$

Solutions to Eq. 5.16 for a longitudinally flat-top and Gaussian transverse beam are given in Ref. [111]:

$$W_r = \frac{r}{2}\left[1 + Z\frac{m}{M}\frac{n_b}{n_p}\frac{\xi^2}{2}H\left(\frac{r^2}{2\sigma_x^2}\right)\right], \tag{5.18}$$

where $H(x) \equiv (1-e^{-x})/x$. In Fig. 5.3, we reproduce Fig. 1 from Ref. [111] for this distribution using QPAD. We see the weak ion motion approximation breaks down for beams with densities $n_b > 2000$, where there is a strong perturbation to W_r around the beam core.

For higher density beams, we therefore go back to the original expression for the wake generated by the ion motion, Eq. 5.12, which is exact assuming ion ring trajectories do not cross. We can solve Eq. 5.9 to get $\delta r(\xi)$ (in general we need to solve this numerically). When ion rings do cross, we must calculate the wakefield by integrating (numerically) over the ion density obtained in the previous section using

$$W_{\perp,\mathrm{ion}}(\xi) = \frac{1}{r}\int_0^{r} dr'r'\rho_{\mathrm{ion}}(r',\xi). \tag{5.19}$$

Wakefields obtained through the ring model are compared to the fully nonlinear simulation result, with $n_b = 8000$ in Fig. 5.4. The ring model provides very accurate results when no crossing occurs, but of course this is not a closed solution, as the ion trajectory must be calculated first. When rings cross more numerical errors come in when computing Eq. 5.19, but the formalism still provides accurate results. This is expected because we found the ion density based on the ring model agrees well with simulation.

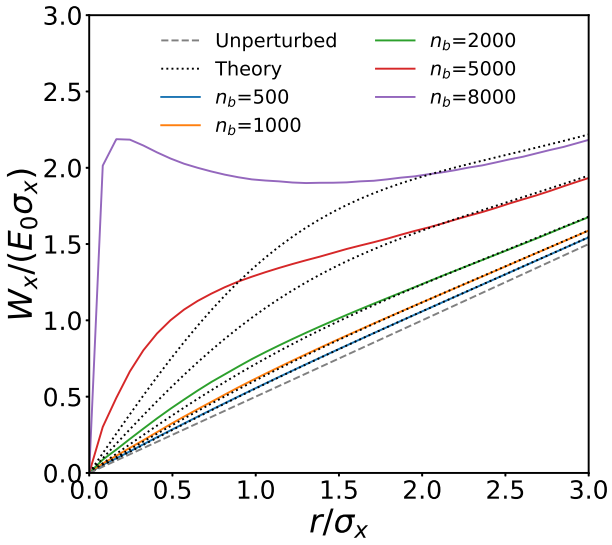

Figure 5.3: Transverse lineouts of the wakefield for a flat-top beam ($L = c/\omega_p$) with Gaussian transverse profile $\sigma = 0.0015\, c/\omega_p$ with a $n_p = 10^{17}$ cm^{-3} plasma. Lineouts are taken at $\xi = L$. Dotted lines represent the theoretical prediction from Eq. 5.18. This figure is a reproduction of Fig. 1 from Ref. [111].

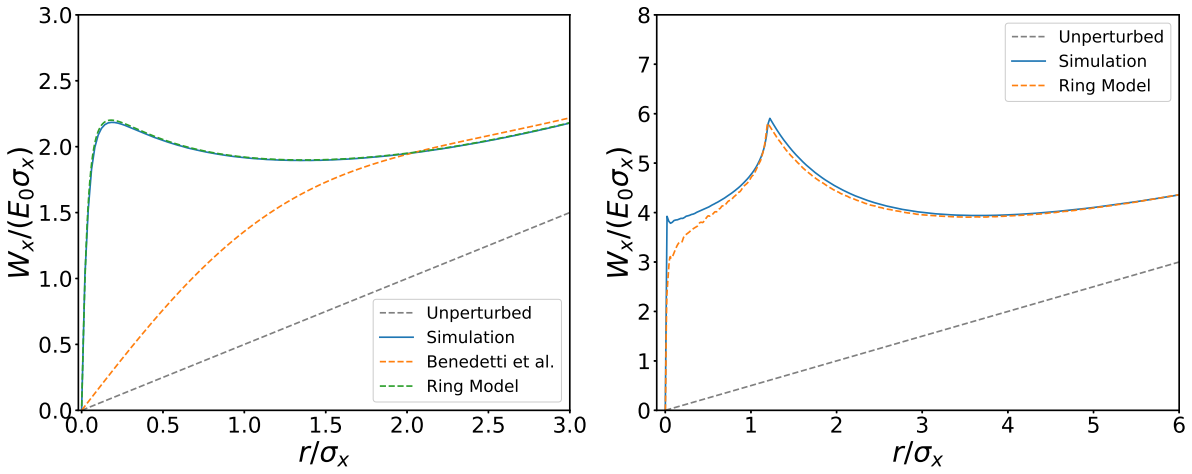

(a) (b)

Figure 5.4: Transverse lineouts of the wakefield for a flat-top beam ($L = 2\,c/\omega_p$) with Gaussian transverse profile $\sigma = 0.0015\,c/\omega_p$ with a $n_p = 10^{17}$ cm^{-3} plasma. (a) Lineout taken at $\xi = c/\omega_p$ before ion trajectory crossing occurs (same as Fig. 5.3). Benedetti et al. refers to the closed form solution, Eq. 5.18. (b) Lineout taken at $\xi = 2\,c/\omega_p$ after trajectory crossing occurs, therefore the ring model is computed using Eq. 5.19.

5.4 Beam matching in nonlinear focusing forces

The nonlinear forces created by the ion collapse will cause many of the ideal properties of the wake to no longer strictly hold, including matching the beam so that the spot size does not oscillate as it propagates and emittance is preserved. In this section, we will look at various methods to overcome this.

5.4.1 Modified envelope equation approach

In order to investigate the transverse beam dynamics when the wakefields are modified by ion collapse, we model the transverse ion density as a Gaussian, $\rho_i = Ae^{-r^2/2\sigma^2}$ (we will discuss other profiles later). The focusing force is then

$$F_\perp = -\frac{r}{2} - \frac{A\sigma^2}{r}\left(1 - e^{-r^2/2\sigma^2}\right), \tag{5.20}$$

and the pseudopotential is

$$\psi(r,\xi) = \psi(\xi=0) - \frac{r^2}{4} + \frac{A\sigma^2}{2}\left[\mathrm{Ei}\left(-\frac{r^2}{2\sigma^2}\right) - \ln\left(r^2\right) + \gamma - \ln\left(2\sigma^2\right)\right], \tag{5.21}$$

where $\mathrm{Ei}(x)$ is the exponential integral and $\gamma \approx 0.577$ is Euler's constant (not the relativistic factor).

The ion motion leads to a nonlinear perturbation to the focusing force so that the usual beam matching condition, $\sigma_m^2 = \epsilon/k_\beta$, where $k_\beta = k_p/\sqrt{2\gamma}$ and $\epsilon = \sqrt{\langle x^2\rangle\langle x'^2\rangle - \langle xx'\rangle^2}$, no longer holds. However, a nonlinear focusing force does not mean that a matching profile does not exist or that emittance cannot be preserved. To find equilibrium distributions for nonlinear focusing forces, we look for steady state solutions to the 2D Vlasov equation, assuming γ is constant,

$$\frac{\partial f}{\partial t} + \mathbf{v}\cdot\frac{\partial f}{\partial \mathbf{r}} + \frac{\mathbf{F}(\mathbf{r})}{\gamma m}\cdot\frac{\partial f}{\partial \mathbf{v}} = 0, \tag{5.22}$$

where $f = f(\mathbf{r},\mathbf{v};t)$ is the distribution function and $\mathbf{F}(\mathbf{r})$ is the focusing force [112]. We

assume separation of variables $f(\mathbf{r},\mathbf{v}) = R(\mathbf{r})V(\mathbf{v})$, leading to

$$\mathbf{v}\cdot\frac{\partial R(\mathbf{r})}{\partial \mathbf{r}}V(\mathbf{v}) + \frac{\mathbf{F}(\mathbf{r})}{\gamma m}\cdot\frac{\partial V(\mathbf{v})}{\partial \mathbf{v}}R(\mathbf{r}) = 0. \tag{5.23}$$

We use azimuthal symmetry to separate this to

$$\frac{1}{F_r(\mathbf{r})}\frac{R'}{R} = -\frac{1}{\gamma m v_r}\frac{V'}{V} = \alpha^2, \tag{5.24}$$

where α is a constant. Thus, we have

$$R(\mathbf{r}) = R_0\exp\left(\alpha^2\int F_r(\mathbf{r})\,dr\right) = R_0\exp\bigl(\alpha^2 e\psi(\mathbf{r})\bigr), \tag{5.25}$$

$$V(\mathbf{v}) = V_0\exp\bigl(-\alpha^2\gamma m v_r^2/2\bigr). \tag{5.26}$$

This result is consistent with Jeans's theorem, which states the steady state solutions to the Vlasov equations are functions of the constants of the particle motion. In this case, the constant of the motion is just the Hamiltonian for an electron moving in the potential ψ, which is $H = \frac{p_\perp^2}{2\gamma} - e\psi$. The matched distribution function in our case for a relativistic electron beam in the pseudopotential above will be of the form $e^{-\gamma\psi(r)/\sigma_p^2}$ assuming the momentum distribution is symmetric, i.e., $\sigma_{p_x} = \sigma_{p_y} = \sigma_p$. Beam matching for Gaussians is unique in that once the second moment is matched all higher order (even) moments will be matched too. In general, it is not straightforward to match other distributions. However, it is observed from self-consistent simulations that the deviation of the distribution function from Gaussian may be small depending on the ion profile parameters and beam spot size. Thus, we can derive a correction to the matched spot size for our nonlinear force assuming the distribution is still close to Gaussian.

We can derive an approximate matched spot size for a Gaussian beam as follows. We start with the standard derivation for the beam envelope equation in one transverse direction and later extend the analysis to both directions. The spot size is defined as

$$\sigma_x = \sqrt{\langle x^2\rangle}, \tag{5.27}$$

and we take two derivatives to get

$$\sigma_x'' = \frac{\langle x^2\rangle\left(\langle x'^2\rangle + \langle xx''\rangle\right) - \langle xx'\rangle^2}{\langle x^2\rangle^{3/2}} = \frac{\epsilon_x^2}{\sigma_x^3} + \frac{\langle xx''\rangle}{\sigma_x}, \tag{5.28}$$

where $\epsilon_x \equiv \sqrt{\langle x^2\rangle\langle x'^2\rangle - \langle xx'\rangle^2}$ (note this is the geometric emittance, $\epsilon = \epsilon_N/\gamma$). Next, instead of the linear focusing force we use the nonlinear force (Eq. 5.20) to obtain x'' in terms of x leading to

$$\langle xx''\rangle = -k_\beta^2\left(\sigma_x^2 + 2A\sigma^2\left(1 - \left\langle e^{-x^2/2\sigma^2}\right\rangle\right)\right), \tag{5.29}$$

where

$$\begin{aligned}\left\langle e^{-x^2/2\sigma^2}\right\rangle &= \frac{\int_{-\infty}^{\infty} e^{-x^2/2\sigma^2}e^{-x^2/2\sigma_x^2}\,dx}{\int_{-\infty}^{\infty} e^{-x^2/2\sigma_x^2}\,dx} \\ &= \frac{\sigma}{\sqrt{\sigma^2+\sigma_x^2}},\end{aligned} \tag{5.30}$$

and we assumed the beam's distribution is Gaussian. The envelope equation is therefore

$$\sigma_x'' = \frac{\epsilon_x^2}{\sigma_x^3} - k_\beta^2\left(\sigma_x + \frac{2A\sigma^2}{\sigma_x}\left(1 - \frac{\sigma}{\sqrt{\sigma^2+\sigma_x^2}}\right)\right). \tag{5.31}$$

We can find the matching condition by setting $\sigma_x'' = 0$ and using a root finding method to solve for σ_x, given an initial emittance ϵ_x. For the case $\sigma \ll \sigma_x$, the condition becomes a quadratic and we can solve to obtain $\sigma_{m,NL}^2 = \sqrt{A^2\sigma^4 + \epsilon_x^2/k_\beta^2} - A\sigma^2$.

Because the nonlinear focusing force couples the motion in the transverse planes, the above analysis can only be applied to a 2D beam slice if it is azimuthally symmetric (with $p_\theta = 0$). However, we can redo the analysis in 2D Cartesian in a similar way as follows:

$$\begin{aligned}\langle xx''\rangle &= -k_\beta^2\left[\sigma_x^2 + 2A\sigma^2\left\langle\frac{x^2}{x^2+y^2}\left(1 - e^{-(x^2+y^2)/2\sigma^2}\right)\right\rangle\right] \\ &= -k_\beta^2\left[\sigma_x^2 + \frac{2A\sigma^2}{2\pi\sigma_x\sigma_y}\int_{-\infty}^{\infty}\int_{-\infty}^{\infty} dxdy\, e^{-x^2/2\sigma_x^2}e^{-y^2/2\sigma_y^2}\frac{x^2}{x^2+y^2}\left(1 - e^{-(x^2+y^2)/2\sigma^2}\right)\right] \\ &= -k_\beta^2\left[\sigma_x^2 + \frac{2A\sigma^2\sigma_x^2}{\sigma^2+\sigma_x^2+\sqrt{\sigma^2+\sigma_x^2}\sqrt{\sigma^2+\sigma_y^2}}\right].\end{aligned} \tag{5.32}$$

Therefore, the beam envelope equation is

$$\sigma_x'' = \frac{\epsilon_x^2}{\sigma_x^3} - k_\beta^2 \sigma_x \left(1 + \frac{2A\sigma^2}{\sigma^2 + \sigma_x^2 + \sqrt{\sigma^2 + \sigma_x^2}\sqrt{\sigma^2 + \sigma_y^2}}\right) \tag{5.33}$$

$$= \frac{\epsilon_x^2}{\sigma_x^3} - k_\beta^2 \sigma_x \left(1 + \frac{A\sigma^2}{\sigma^2 + \sigma_x^2}\right) \text{ for } \sigma_x = \sigma_y, \tag{5.34}$$

and the analagous equation for σ_y'' with $\sigma_x \leftrightarrow \sigma_y$ and $\epsilon_x \to \epsilon_y$. In the case $\sigma_x = \sigma_y \gg \sigma$, like in 1D, we can find an expression for the matching σ_x by solving the resulting quadratic equation after setting $\sigma_x'' = 0$, resulting in $\sigma_{m,NL}^2 = \sqrt{A^2\sigma^4/4 + \epsilon_x^2/k_\beta^2} - A\sigma^2/2$.

In Fig. 5.5, we illustrate the effectiveness of using a nonlinearly matched beam based on the Gaussian assumption to mitigate the emittance growth. The results are from a 2D beam slice simulation with a fixed focusing force given by Eq. 5.20. We consider two cases. The first (Figs. 5.5a - 5.5d) considers FACET-II like parameters with 1 μm normalized emittances, plasma density of $n_p = 4.0 \times 10^{16}$ cm^{-3}, and $\gamma = 20,000$. For the focusing force, we set $A = 90$, $\sigma = 0.0045$. The second case (Figs. 5.5e - 5.5h) considers LC parameters with 465 nm normalized emittances, plasma density of 1.0×10^{17} cm^{-3}, and $\gamma = 48,925$. For the focusing force, we set $A = 2217$, $\sigma = 0.001$. In both Fig. 5.5a and Fig. 5.5e, it can be seen that the emittance growth is significantly reduced when the beam enters the plasma with a nonlinearly matched spot size compared to the linearly matched spot size. However, there is still some emittance growth which can be understood from Figs. 5.5c and Fig. 5.5g. These show the distribution in x deviates from a Gaussian and instead saturates to the equilibrium distribution. Figs. 5.5d and 5.5h show the momentum remains Gaussian. The deviation from Gaussian in larger for the LC case due to the much larger A, while the ratio σ/σ_m, where σ_m is the nonlinearly matched spot size, was only slightly smaller. To quantify the effect of this deviation from Gaussian on the emittance growth, we run a series of beam slice simulations with A kept fixed. We vary σ in the model, and calculate the corresponding σ_m for each case. The results are shown in Figs. 5.5b and 5.5f, where we see the emittance growth is small for the nonlinearly matched Gaussian beam when either $\sigma \ll \sigma_m$ or $\sigma \gg \sigma_m$. In the $\sigma \ll \sigma_m$ case, most beam particles see the $r/2$ focusing force and thus the profile

remains Gaussian, while in the $\sigma \gg \sigma_m$ case, the beam mostly sees the focusing force near the axis that goes like $(A+1)r/2$, so it also remains Gaussian. Therefore, larger A will only increase the error slightly in these limits, but it will increase the error more significantly when $\sigma \sim 0.5\sigma_m$. However, even in this case the emittance growth may be moderate if A is not large ($\sim 20\%$ emittance growth for the FACET-II case). It is worth noting that, even in the case when $\sigma \sim 0.5\sigma_m$, if the beam is initialized with the non-Gaussian equilibrium profile, the emittance would not grow.

We also tested nonlinear matching with full QPAD simulations. We considered a two-bunch LC scenario with a Gaussian current profile for the drive beam and a trapezoidal current profile for the witness beam that optimally loads the wake. The following is what we will refer to simply as LC parameters for the rest of the chapter. The plasma density is $n_0 = 10^{17}$ cm^{-3}. Both beams have energy $E = 25$ GeV and the head of the witness beam starts 105 μm behind the center of the drive beam. The drive beam has 4.8 nC of charge, normalized emittance $\epsilon_{N,d} = 59.1$ μm, and spot size $\sigma_{r,d} = 2.52$ μm, and length $\sigma_{z,d} = 30$ μm. The witness beam has 1.63 nC of charge, normalized emittance $\epsilon_{N,w} = 0.465$ μm and spot size $\sigma_{r,w} = 0.223$ μm. The beam current linearly decreases from $I_b = 27$ kA to $I_b = 5.4$ kA over $L_b = 30.24$ μm. The resolution is 10.3 nm $\times$ 241 nm and the 3D timestep is $\Delta t = 5\,\omega_p^{-1}$. A small timestep is needed to capture the beam dynamics in the large ion densities created when the drive beam seeds the ion motion. We only keep the $m = 0$ mode because we are considering round beams. The projected emittance growth is shown in Fig. 5.6. The emittance growth for a linearly matched beam is $\sim 200\%$ while for a nonlinearly matched beam it is $\sim 50\%$. Just as for the beam slice simulation presented in Fig. 5.5, the use of nonlinearly matched beams significantly reduces the emittance growth.

This concept of matching to the nonlinear focusing force created by the ions is what was alluded to in Ref. [110] when the beam was focused to a smaller spot size than the linearly matched spot size. It showed that the emittance growth was smaller when the beam was initialized with an initial emittance corresponding to the saturated value after it evolved in

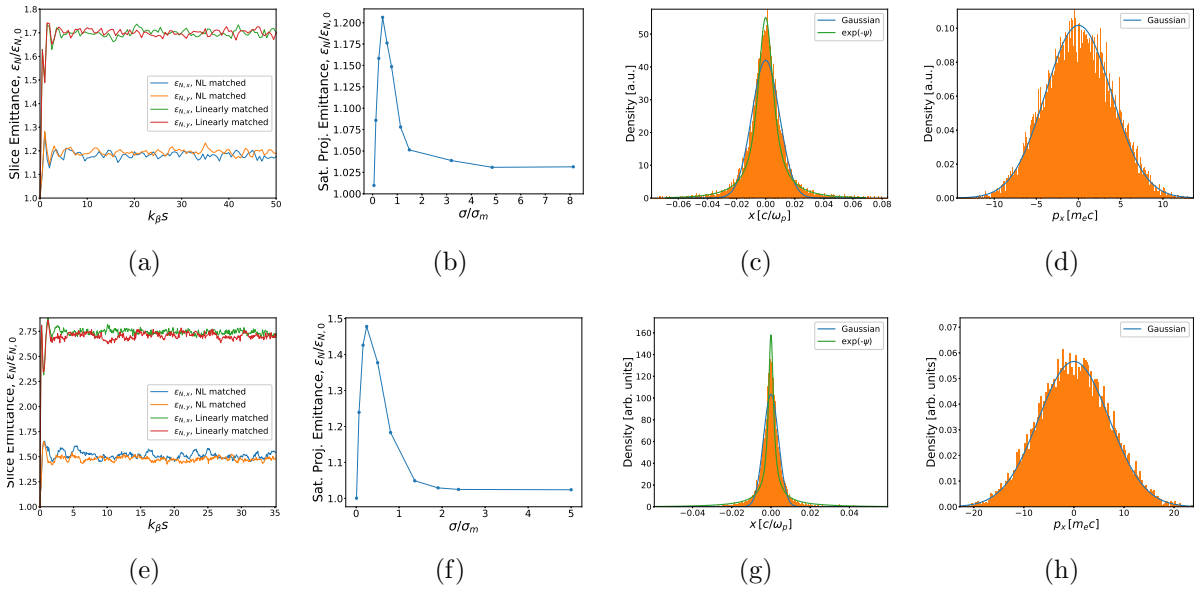

Figure 5.5: (a)-(d) Nonlinear matching for FACET-II like parameters with 1 μm normalized emittances using 2D round beam slice simulation in a fixed nonlinear focusing force. (a) Normalized emittance growth using $A = 90$, $\sigma = 0.0045$. The beam has $\gamma = 20,000$ and $\epsilon_{N,x} = 0.037$. The spot size matched to the linear focusing force is $\sigma_x = 0.01942$ and matched to the nonlinear focusing force is $\sigma_{N,x} = 0.00949$. (b) Scan over ion width with $A = 100$, showing the final emittance growth percentage, which is related to the deviation of the matched distribution from a Gaussian. (c) Spatial distribution for the case in (a) after saturation. (d) Momentum distribution for the case in (a) after saturation. (e)-(h) Nonlinear matching for LC parameters with 465 nm normalized emittance (with $n_{b,d} = 100$) using 2D round beam slice simulation in a fixed nonlinear focusing force. (e) Normalized emittance growth using $A = 2217$, $\sigma = 0.001$. The beam has $\gamma = 48,925$ and $\epsilon_{N,x} = 0.028$. The spot size matched to the linear focusing force is $\sigma_x = 0.0133$ and matched to the nonlinear focusing force is $\sigma_x = 0.00386$. (f) Scan over ion width with $A = 2000$, showing the final emittance growth percentage, which is related to the deviation of the matched distribution from a Gaussian. (g) Spatial distribution for the case in (e) after saturation. (h) Momentum distribution for the case in (e) after saturation.

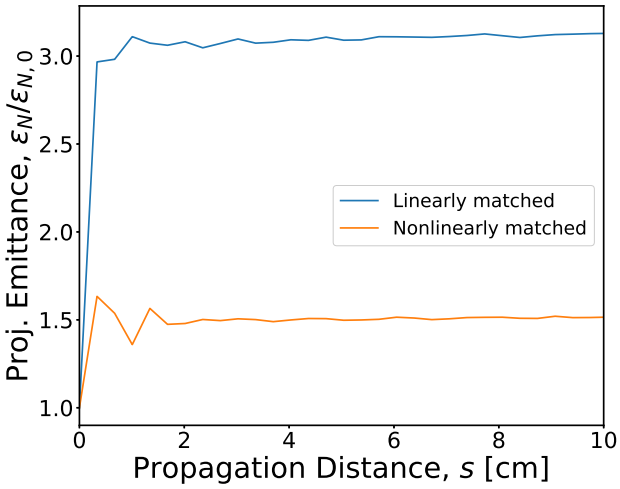

Figure 5.6: Full QPAD simulation showing approximate beam matching to the nonlinear focusing force, corresponding to the beam slice simulation in Fig. 5.5e.

the nonlinear force. This corresponds to a smaller initial spot size and a larger momentum spread.

5.4.2 Matching for different transverse ion profiles

For weak ion collapse, the transverse ion density profile looks close to Gaussian (see Fig. 5.2d), but for stronger collapse it looks more like an exponential profile (see Fig. 5.2b). We plot a couple of profiles in Fig. 5.7 for comparison to the strong ion collapse profile obtained from PIC simulations. Clearly the Gaussian profile is not the best fit, while both other profiles do a better job. The $1/(1+|x|)$ profile can capture the "fat tail" which is an important feature with respect to the emittance growth. It is possible to derive the modified envelope equation (using the Gaussian ansatz for the beam profile) in 1D for the exponential profile, $\rho_i = Ae^{-|x|/\sigma}$. The focusing force is

$$F_\perp = -k_p^2 \left[\frac{x}{2} + \frac{A\sigma}{x} \left(\sigma - e^{-|x|/\sigma} (|x| + \sigma) \right) \right]. \tag{5.35}$$

This can be used to obtain

$$\langle x x'' \rangle = -k_\beta^2 \left[\sigma_x^2 + 2A\sigma \left(\sigma - \left\langle e^{-|x|/\sigma} (|x| + \sigma) \right\rangle \right) \right], \tag{5.36}$$

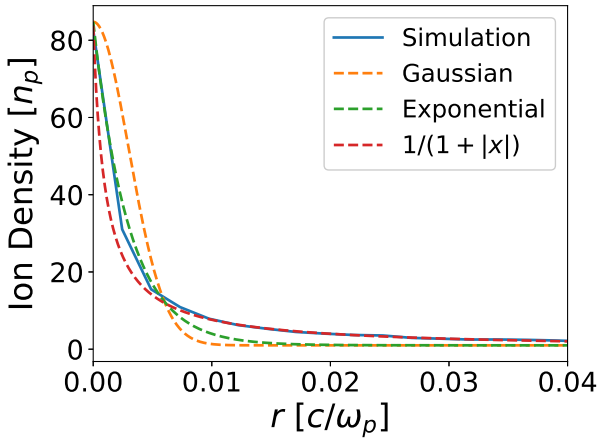

Figure 5.7: Various functions compared to the simulation data for the transverse ion profile: Gaussian - $e^{-x^2/2\sigma^2}$, exponential - $e^{-|x|/a}$, and $1/(1+|x|/b)$. $\sigma = a = 0.003$ and $b = 0.001$ were used.

where

$$\begin{aligned}\left\langle e^{-|x|/\sigma}(|x|+\sigma)\right\rangle &= \frac{1}{\sqrt{2\pi}\sigma_x}\int_{-\infty}^{\infty} dx\, e^{-x^2/2\sigma_x^2} e^{-|x|/\sigma}(\sigma - |x|) \\ &= \sqrt{2/\pi}\sigma_x + \frac{\sigma^2-\sigma_x^2}{\sigma}\, e^{\sigma_x^2/2\sigma^2}\mathrm{Erfc}\left(\frac{\sigma_x}{\sqrt{2}\sigma}\right). \end{aligned} \tag{5.37}$$

Thus, for the exponential profile, the envelope equation becomes

$$\sigma_x'' = \frac{\epsilon_x^2}{\sigma_x^3} - k_\beta^2\left[\sigma_x + \frac{2A\sigma}{\sigma_x}\left(\sigma - \sqrt{2/\pi}\sigma_x - \frac{\sigma^2-\sigma_x^2}{\sigma}\, e^{\sigma_x^2/2\sigma^2}\mathrm{Erfc}\left(\frac{\sigma_x}{\sqrt{2}\sigma}\right)\right)\right]. \tag{5.38}$$

These profiles cannot easily be integrated in 2D Cartesian however, which is necessary for the calculation of Eq. 5.33. While these other profiles may be useful in some cases, we generally use the Gaussian profile. It is possible to choose narrower Gaussian profiles to match the core ion density, but usually we use a wider profile to better match the integral (charge) over a small radius. This seems to better capture the emittance growth.

Because the ions strongly collapse to the axis, many ions reside within a single cell on axis in the simulations. This leads to a density spike whose amplitude depends on the resolution. Even with very fine resolution, the density on axis will still increase, seemingly unresolved.

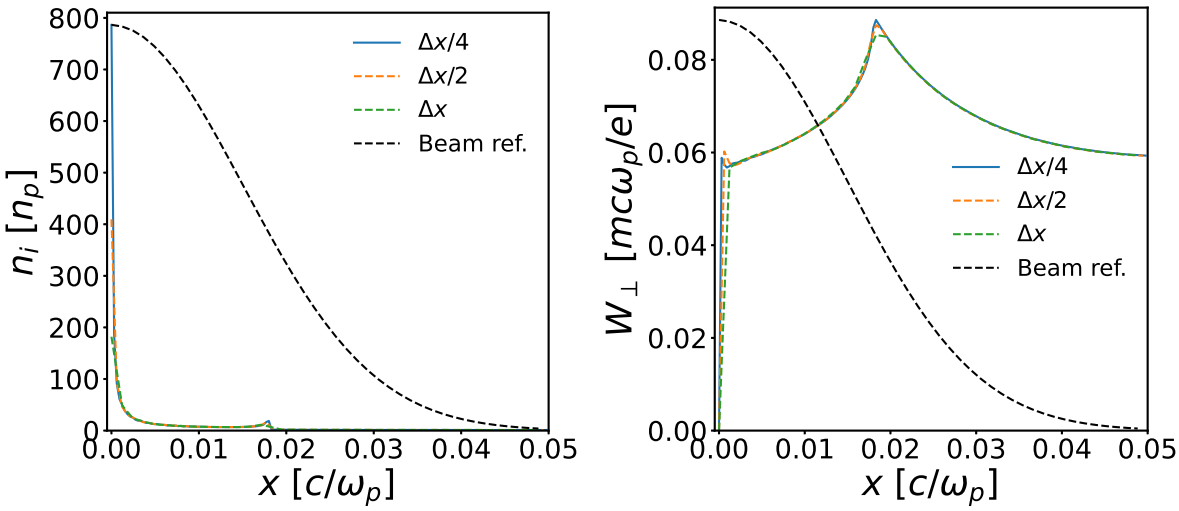

(a) (b)

Figure 5.8: Transverse lineouts of the (a) transverse wakefield and (b) ion density for different transverse resolutions. We use $\Delta x = 0.0012\, c/\omega_p$ as the largest cell size. We use a flat-top beam ($L = 2\, c/\omega_p$) with Gaussian transverse profile (the normalized profile is shown with the black dashed line) with $\sigma = 0.0015\, c/\omega_p$, $n_b = 8000$, and a $n_p = 10^{17}$ cm^{-3} plasma.

However, we have found that the use of very fine resolution with very large density spikes provides the same focusing force and emittance growth as the relatively lower resolution simulations, so long as the beam itself is properly resolved. This is due to the fact that the electric field due to these ions is unchanged for all beam electrons except those within the cell on axis. Fig. 5.8 shows an example of the ion density and resulting wakefields for three different resolutions. We can see the ion density on axis, A, changes dramatically with different resolutions but this has little effect on the transverse wakefields (or focusing force) within the beam, and therefore on the beam dynamics.

5.4.3 Exact longitudinally varying envelope approach

In general, the ion collapse will vary axially along the bunch, i.e., A and σ will be functions of ξ. So the matched beam distribution will be different for each slice. For example, if the ion density increases as you move further back in the beam, then the matched spot size will also gradually decrease with ξ, this is sometimes called a taper. Finding the matched distribution for each slice can be challenging because there is a feedback between this distribution and resulting ion density profile. In Ref. [111], a theory for obtaining this self-consistent matched distribution was developed. We will briefly review it in this section as it is relevant for the exact matching that occurs when we introduce plasma density ramps in a later section. We will use our notation so as to not cause confusion with different normalizations and definitions.

We start with the matched distribution from the previous section

$$f_\perp(r,\xi) = \frac{1}{N(\xi)} \exp\left(-\frac{\gamma}{\sigma_p(\xi)^2}\psi(r,\xi)\right), \tag{5.39}$$

where

$$N(\xi) = 2\pi \int_0^\infty r dr \exp\left(-\frac{\gamma}{\sigma_p(\xi)^2}\psi(r,\xi)\right) \tag{5.40}$$

is a normalization factor and we have assumed azimuthal symmetry and γ is constant. If we define the head of the beam to be at $\xi = 0$, then for $\xi > 0$ the beam's profile will be non-Gaussian and we can compute its second order spatial moment as

$$\begin{aligned}\langle x^2\rangle(\xi) &= \frac{1}{N(\xi)} \int_0^{2\pi}\int_0^\infty dr\, r^3 \cos^2\theta \exp\left(-\frac{\gamma}{\sigma_p(\xi)^2}\psi(r,\xi)\right) \\ &= \frac{\pi}{N(\xi)} \int_0^\infty dr\, r^3 \exp\left(-\frac{\gamma}{\sigma_p(\xi)^2}\psi(r,\xi)\right).\end{aligned} \tag{5.41}$$

The momentum distribution will remain Gaussian as we described previously. We now define a scaling parameter that relates the second order moment to the initial spot size at the beam head (which is Gaussian)

$$\eta(\xi) \equiv \frac{\langle x^2\rangle(\xi)}{\sigma_x^2}. \tag{5.42}$$

We look for solutions where the beam is perfectly matched, which means the slice emittance along the beam is conserved, i.e., at any point the emittance is equal to the initial emittance at the beam head, given by $\epsilon_{N,i} = \sqrt{\frac{\gamma}{2}}\sigma_x^2$. The emittance for all other slices is given by $\epsilon_N = \sqrt{\langle x^2 \rangle(\xi)}\sigma_p(\xi) = \epsilon_{N,i}$. Thus, we can relate the second order moments through

$$\sigma_p(\xi)^2 = \frac{\gamma}{2}\frac{\sigma_x^4}{\langle x^2 \rangle(\xi)} = \frac{\gamma}{2}\frac{\sigma_x^2}{\eta(\xi)}. \tag{5.43}$$

Now, we can solve for the value of $\eta(\xi)$ by equating Eq. 5.41 with $\langle x^2 \rangle(\xi) = \eta(\xi)\sigma_x^2$ and substitute the above equation into the distribution function to obtain

$$\frac{\int_0^\infty dr\, r^3 \exp\left(-\frac{2\eta(\xi)}{\sigma_x^2}\psi(r,\xi)\right)}{\int_0^\infty dr\, r \exp\left(-\frac{2\eta(\xi)}{\sigma_x^2}\psi(r,\xi)\right)} - 2\eta(\xi)\sigma_x^2 = 0. \tag{5.44}$$

This equation can be iterated numerically to find the value $\eta(\xi)$ and therefore the matching distribution along the beam, given an initial spot size at the head, emittance, and the self-consistent ion profile in order to calculate $\psi(r,\xi)$.

In practice, creating beams with these profiles is not currently possible using conventional beam optics. Ref. [111] also presented results showing an approximate Gaussian fit to the ideal distributions. That is each slice would be a Gaussian with the same RMS properties of the ideal matched distribution (essentially what is seen in Fig. 5.5c). The emittance growth of such a beam was much smaller (3%) compared to the standard linearly matched Gaussian bunch (20%). The beam initialized with the exact matching distribution showed no emittance growth as expected. However, even the approximate equilibrium beam may be hard to produce in practice (and has not been demonstrated for PWFA yet). It would require tailoring the beam spot size along the longitudinal direction.

In order to produce a beam with this profile, a plasma-based method is probably the best candidate, specifically an adiabatic (or quasi-adiabatic) matching method. Ref. [113] suggests an adiabatic matching technique where an initially untapered beam is injected into PWFA stage where the energy is low enough such that ion motion effects are small. Then as the beam is accelerated the ion motion will become stronger and the beam will adiabatically

find the matching distribution with little emittance growth. For example, it was found that an injected bunch with $\epsilon_{x,0} = 0.2\,\mu$m, $E = 50$ MeV, and $\Phi = 1.3$ ($\Phi = k_i L_b$ characterizes the amount of ion motion) adiabatically acquired the desired matching distribution as it is accelerated to 10 GeV, with a projected emittance growth of $\sim 15\%$. Higher initial injection energies or lower initial emittance would increase the emittance growth in this process.

One major issue with this approach is that, while it does create the matched beam within the first stage, this matched profile must be preserved into the later stages of a multi-stage PBA-LC. This would require an advanced beam transport system. Moreover, Ref. [113] did not consider plasma density ramps, which are useful for decreasing the beam spot size to the small values required for LC plasma stages. In Ref. [114], we proposed to use quasi-adiabatic plasma density ramps at the entrance and exit of each stage. In this scenario, the beam is focused to the ramp entrance with a spot size too large to trigger ion motion. The spot size then adiabatically decreases as it propagates in the upramp, causing the beam to gradually trigger ion motion. This allows the beam to gradually adjust itself to the nonlinear wakefields and acquire the desired slice-by-slice matching distribution with little emittance growth. This adiabatic triggering of ion motion is similar to Ref. [113]. The advantage to this approach is that the beam exits the plasma through the downramp where the beam will gradually expand and transition back to a Gaussian with a large spot size. This can then be transported to the next stage using conventional beam optics. We will present this method in detail in Sec. 6.2.

5.5 Drive beam induced ion motion

In all previous studies of ion motion in PWFA, such as in Ref. [110], low density drive beams were used to avoid additional ion motion induced by the drive beam. However, if allowed to evolve, these drive beams suffer significant head erosion and the wake deteriorates quickly, as shown in Fig. 5.9. This leads to the distortion of the accelerating field and thus

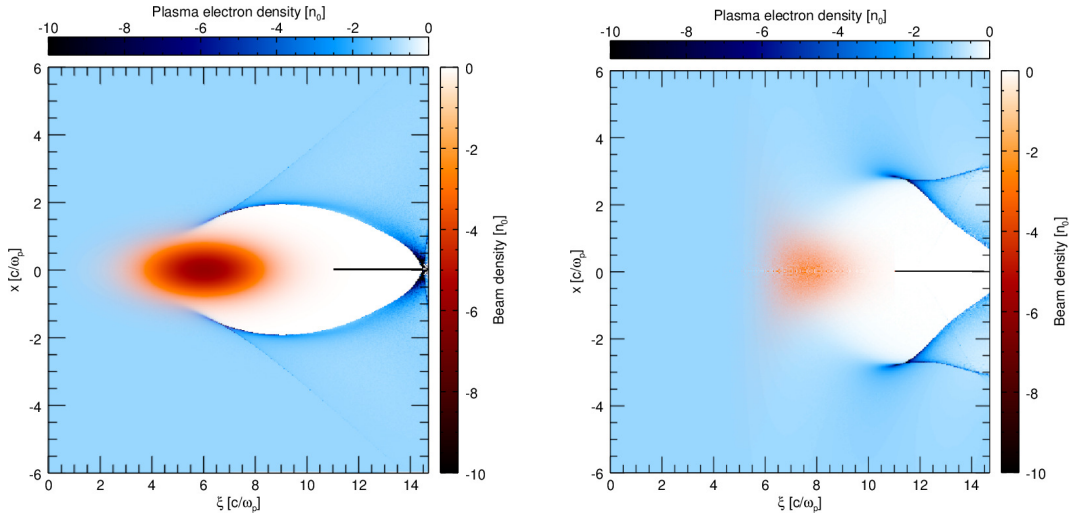

(a) (b)

Figure 5.9: (a) Initial nonlinear plasma wake from [110]. (b) Plasma wake after $t = 20{,}000$ $\omega_p^{-1} = 33.6$ cm.

a large increase in energy spread of the witness beam. One solution is to use a precursor beam to help ease the head erosion of the drive beam by blowing out the initial electrons and creating a focusing channel for the drive beam. With this approach one has to properly design the precursor such that it sufficiently suppresses the drive beam head erosion while not significantly altering the wake or inducing ion motion itself. Another solution is to use higher density drive beams that do not suffer this severe head erosion. In this case, the drive beam will cause ions to move to the axis at the location of the witness beam. We consider two general regimes. The first regime is drive beams with $\Phi \lesssim 1$, which only give the ions an impulse such that they do not reach the axis before the witness beam arrives. The ion motion is then amplified by the witness beam leading to a larger ion density than from the witness beam alone, and hence larger emittance growth. The other is drive beams with $\Phi \gtrsim 1$, where there is strong ion collapse before the witness beam arrives. We will quantify these two regimes in the next section.

5.5.1 Regime where ion motion is dominated by the drive beam

First, we examine the case where the drive beam ion motion is dominant so that even if the witness beam is offset, the ions will be centered on axis (defined by the drive beam). This will be true for beams with relatively small ion parameter, $\Phi \sim 1$, e.g., short beams or beams with less charge. The FACET-II parameters we have already mentioned fall into this regime. We carried out QPAD simulations for this regime with the following parameters: the plasma density is $4 \times 10^{16}\,\mathrm{cm}^{-3}$, each beam is 10 GeV and bi-Gaussian with a spot size $\sigma_r = 0.516\,\mu\mathrm{m} = 0.0194\,c/\omega_p$ and normalized emittances of 1 $\mu\mathrm{m} = 0.0376\,c/\omega_p$. The drive beam has a peak density $n_b/n_p = 4651.4$ and length $\sigma_z = 12.77\,\mu\mathrm{m} = 0.481\,c/\omega_p$, while the witness beam has a peak density $n_b/n_p = 2790.84$ and length $\sigma_z = 6.38\,\mu\mathrm{m} = 0.24\,c/\omega_p$. The beam centers are separated by $\Delta\xi = 150\,\mu\mathrm{m} = 5.65\,c/\omega_p$. We used an $r - z$ grid with resolution 63.6×221.5 nm and up to $m = 3$ azimuthal modes.

There is essentially one parameter we can vary to control the amount of driver induced ion motion, assuming a fixed beam current, Λ, and a matched spot size. By increasing the density of the beam, the matched spot size (and emittance) decreases, leading to a larger ion parameter. However, another important parameter is the location of the focus of the ions with respect to the location of the witness beam. For relatively large drive beam densities ($\Phi \gtrsim 1$), the ions that begin within the beam will focus before the witness beam and then overshoot. So the ion density the witness beam sees will include ions that start at large radii compared to the beam spot size and arrive at the axis within the witness beam. In the limit of very high drive beam density, the ions will focus immediately and the on-axis ion density behind the drive beam will grow roughly linearly in ξ because each ion ring that subsequently arrives carries a larger charge. However, in this case many ions overshoot the axis and move away from it before the witness beam, so there is not a large enhancement to the ion density from the witness beam. Fig. 5.10 shows the results of a scan over the drive beam spot size and the resulting ion density (which can be predicted as shown in Fig. 5.2a). We can see that for relatively larger spot sizes, we get larger ion densities. This is because

the ions are focusing on top of the witness beam, which amplifies the density.

We can derive a simple scaling law for the location of the first ion peak if we assume the drive beam focuses the ions as a thin lens, which will be the case as long as the drive beam is relatively short, which is typical in two bunch scenarios. We consider an ion that starts at the drive beam spot size, $r = \sigma_{r,d}$. This ion will pick up an impulse from the drive beam

$$p_r = F_r \Delta t = F_r k_p L_b / c, \tag{5.45}$$

directed towards the axis, where L_b is the drive beam length. The force from the drive beam is

$$F_r(r = \sigma_r) = \frac{\Lambda}{k_p \sigma_r} \left(1 - e^{-1/2}\right) mc\omega_p. \tag{5.46}$$

We can now calculate the location where this ion will reach the axis,

$$k_p(\xi_{\text{peak}} - \xi_{d,0}) = \frac{M k_p \sigma_r}{p_r} = \frac{M/m}{\Lambda} \frac{1}{k_p L_b} \frac{\sigma_r^2}{1 - e^{-1/2}} = \frac{M/m}{n_b/n_p} \frac{1}{k_p L_b} \frac{1}{1 - e^{-1/2}}, \tag{5.47}$$

where $\xi_{d,0}$ is the center of the drive beam. For a longitudinally Gaussian beam, $L_b \cong \sqrt{2\pi}\sigma_z$. This scaling can be useful to find the location of the first ion peak to ensure it lies either before or after the witness beam.

5.5.2 Drive beam ion motion in the LC regime

In the LC regime, the witness beams have more charge and lower emittance. Thus, they have a higher density, smaller matched spot size, and are typically longer. We will consider a trapezoidally shaped witness beam that optimally loads the wake. In this regime, $\Phi \gg 1$ for the witness beam, thus it will dramatically impact ion motion.

As with the previous regime, the location where the drive beam focuses the ions is essential. We want the ions to focus either before or after the witness beam. If the focus is on top of the beam, the ion density will be greatly amplified and this generally leads to larger emittance growth. We can thus identify two separate regimes of drive beam induced ion motion. First, the underfocused regime, shown in Fig. 5.11b, where the ions do not reach

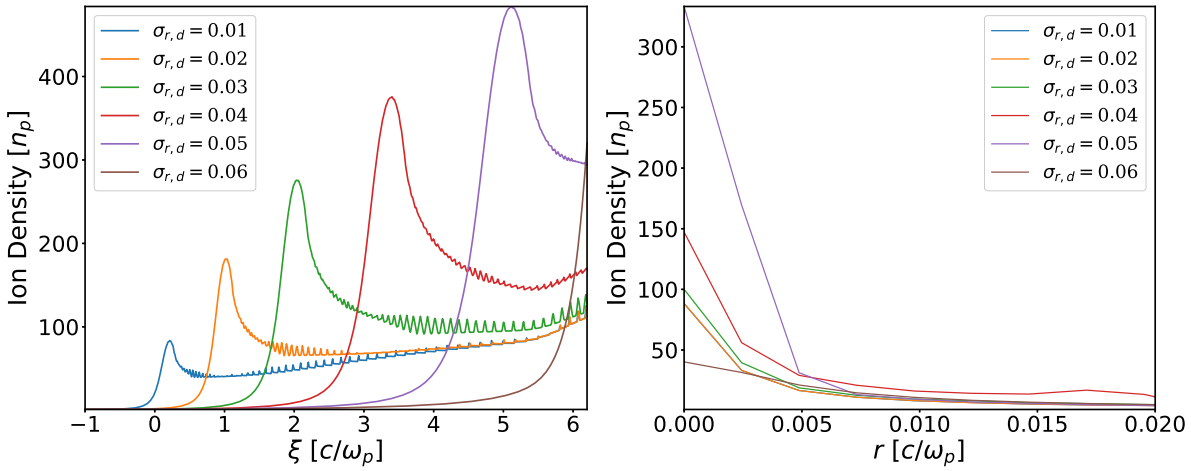

(a) (b)

Figure 5.10: Ion density for FACET-II like parameters with 1 μm normalized emittances. The drive beam is centered at $k_p\xi = 0$ and the witness beam at $k_p\xi_{w,0} = 5.55$. (a) On axis and (b) transverse ($\xi = \xi_{w,0}$) ion density from a parameter scan over transverse drive beam spot size, $k_p\sigma_{r,d}$, with the drive beam current, Λ, held fixed.

the axis until well after the witness beam arrives. The ions will still move toward the axis and the witness beam will finally pull them to the axis, thus the density will be amplified in the witness beam region. Second, the overfocused regime, shown in Fig. 5.11c, where the drive beam drives the ions to the axis, thus creating a spike in ion density, before the witness beam arrives. We can define the overfocused (underfocused) regime by $\xi_{\text{peak}} \ll \xi_{w,0}$ ($\xi_{\text{peak}} \gg \xi_{w,0}$), where $\xi_{w,0}$ is the center of the witness beam.

We consider matched drive beams, as unmatched drive beams have spot size oscillations that may lead to complicated ion motion that is hard to predict. Moreover, we use hydrogen plasmas, but in principle higher ion masses will experience less ion motion and in general have smaller density amplification in the witness region. They will also be less susceptible to being pulled off axis by an offset witness beam, which may be beneficial in the overfocused regime. However, the ionization of higher levels by the witness beam may pose a significant problem. We will talk about heavier ion species and ionization in Sec. 6.4.3.

5.6 Elimination of hosing and witness beam realignment

Although ion collapse can be detrimental to beam emittance, it can help control transverse instabilities. For example, Ref. [98] showed the inherent stability of the drive beam due to energy variation along the beam and Ref. [104] showed the witness beam hosing can be suppressed in the LC regime and argued this was due to a BNS-type mechanism induced by the ion collapse. In the latter case, ion motion from the drive beam was ignored. In this section, we will show drive beam induced ion motion not only suppresses hosing but it can realign the witness beam with the drive beam. However, this occurs at the cost of large emittance growth for FACET-II like parameters.

In this case, where the drive beam ion motion dominates, the witness beam centroid will execute betatron oscillations but will not perturb the focusing force too much. In other words, the witness beam will experience the nonlinear focusing force created by the drive beam ion

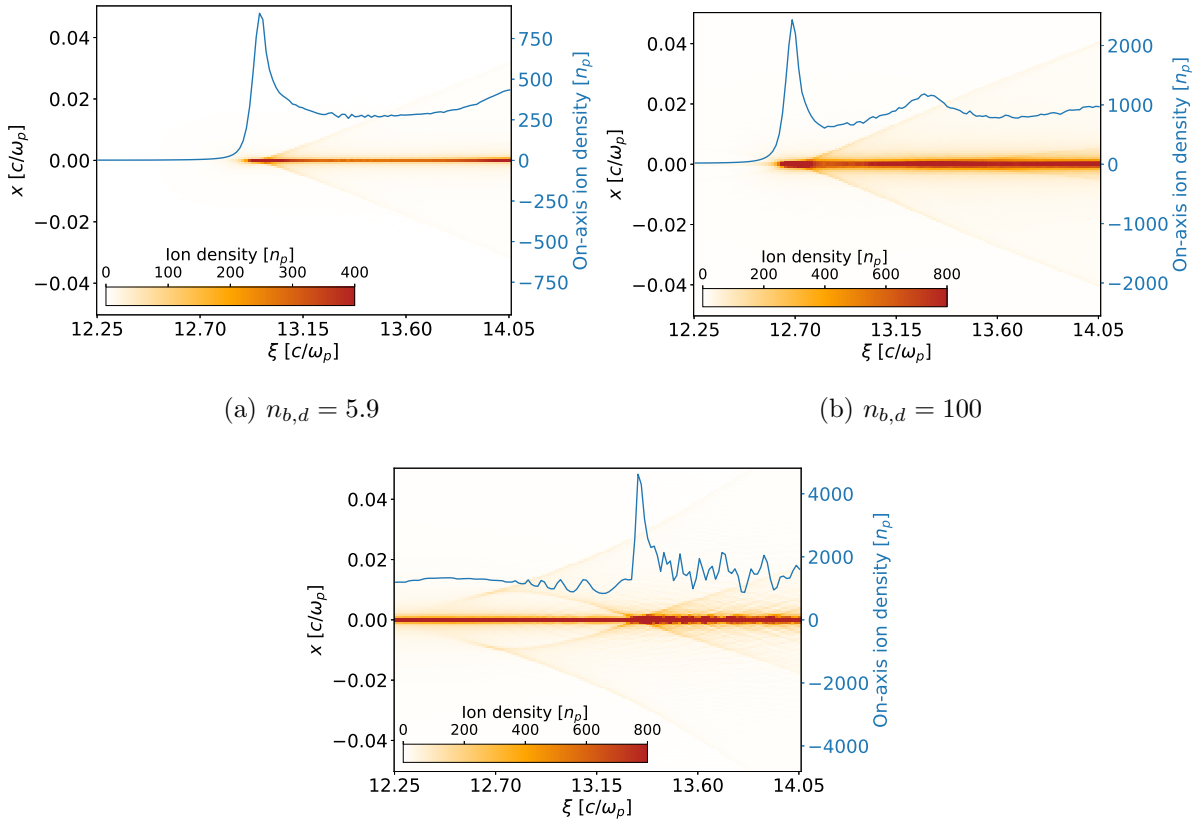

(a) $n_{b,d} = 5.9$

(b) $n_{b,d} = 100$

(c) $n_{b,d} = 570$

Figure 5.11: Ion density in the witness beam region for various drive beam densities after it reaches steady state. (a) Low density drive beam so as to not perturb the ions before the witness beam. (b) The underfocused regime which has similar features to (a) but with an amplified magnitude. (c) The overfocused regime, which has a more complicated transverse structure and large on-axis density.

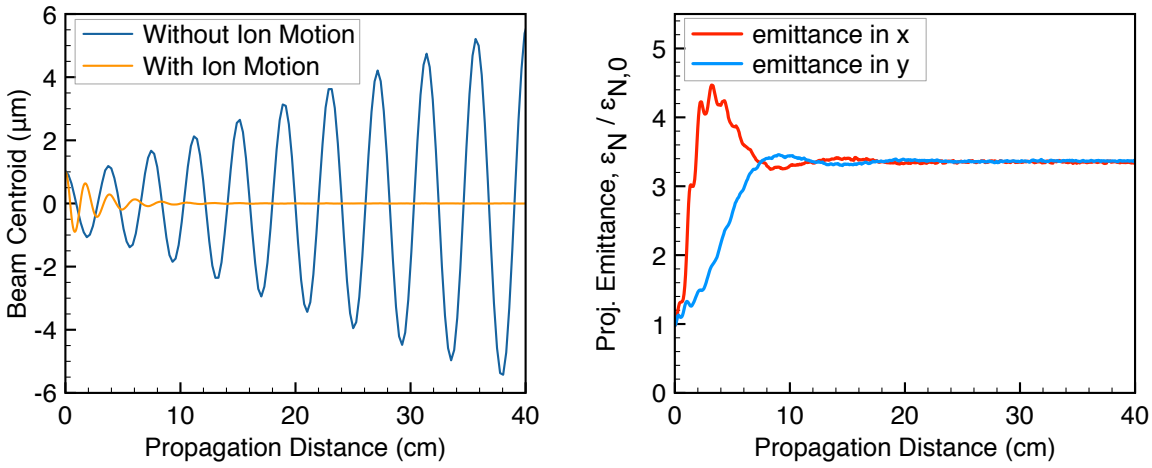

Figure 5.12: Ion motion with FACET-II parameters with a one micron offset. (a) Beam centroid evolution with and without ion motion. (b) Projected emittance evolution in transverse directions with ion motion. The centroid is measured at the tail, $\xi = +\sigma_z$.

motion which is centered on axis. As its centroid oscillates, the witness beam will phase mix in this nonlinear focusing force, thus filling up phase space until the centroid vanishes at the cost of emittance growth. The final spot size, and hence the emittance, will scale with the initial witness beam centroid. We first present a proof of principle QuickPIC simulation with the FACET-II parameters that were given in Sec. 5.5.1 and an initial witness beam offset of $x_{b,0} = 1\,\mu\text{m} = 0.0376\,c/\omega_p$. We see in Fig. 5.12 that the witness beam is quickly realigned with the drive beam axis over several betatron periods, but at the cost of the emittance growing by 200% from 1 to $3\,\mu$m.

In Fig. 5.13, we present results from two QPAD simulations with FACET-II parameters using two different drive beam spot sizes: the spot size listed above and double that value ($\sigma_{r,d} = 1.03\,\mu\text{m} = 0.0388\,c/\omega_p$). The larger spot size causes a larger ion density peak in the witness beam region and therefore larger emittance growth as seen in Fig. 5.13a, but faster damping of the centroid as seen in Fig. 5.13b. This suggests that there is an optimum drive beam spot size that damps the centroid within a certain propagation distance that causes

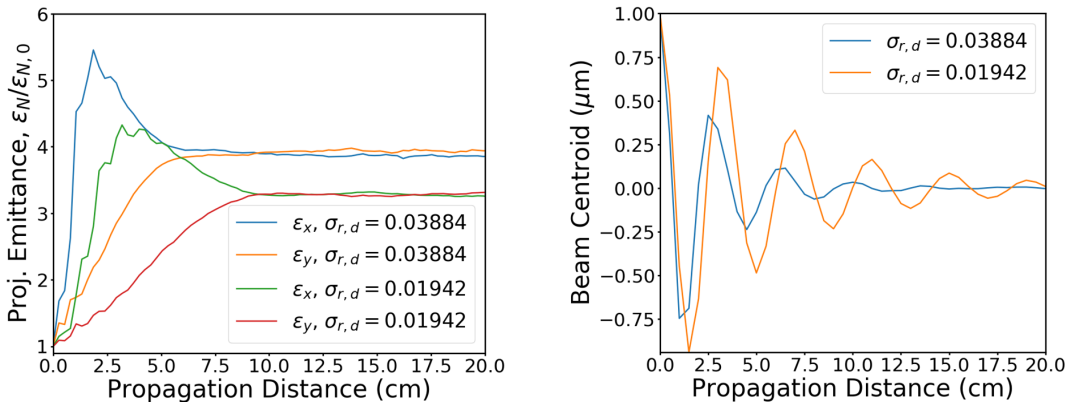

(a) (b)

Figure 5.13: (a) Projected emittance growth and (b) beam centroid for two different drive beam spot sizes with FACET-II like parameters. The witness beam starts $\Delta x = 1\,\mu$m off axis.

minimal emittance growth of the witness beam. We note that this conclusion will be slightly altered when we consider plasma density ramps in the next chapter.

When the beam is not offset, the emittance growth is mostly due to the larger spread in momentum, σ_p. As explained in Ref. [110], the max p_{x0} will increase approximately by a factor of $\sqrt{A}$, because the slope of the focusing force is enhanced by A near the beam center. However, the full emittance will not scale as $\sqrt{A}$, depending on the size of the ion collapse σ. When the beam is offset, it spreads out in the offset direction but also in the momentum. The phase space density for these scenarios can be seen in Fig. 5.14.

We can also examine how the emittance growth scales with the offset magnitude using 2D beam slice simulations, the results are shown in Fig. 5.15. These simulations evolve particles in a beam slice using a prescribed (fixed) focusing force. These are much faster than full PIC simulations if one is just investigating transverse dynamics. We find that for large offsets the centroid takes longer to damp, as expected, and that the emittance growth scales roughly as $x_{b,0}^2/\sigma_{x,0}^2$. In the next section, we will show how we can predict this growth for many different sets of initial beam parameters.

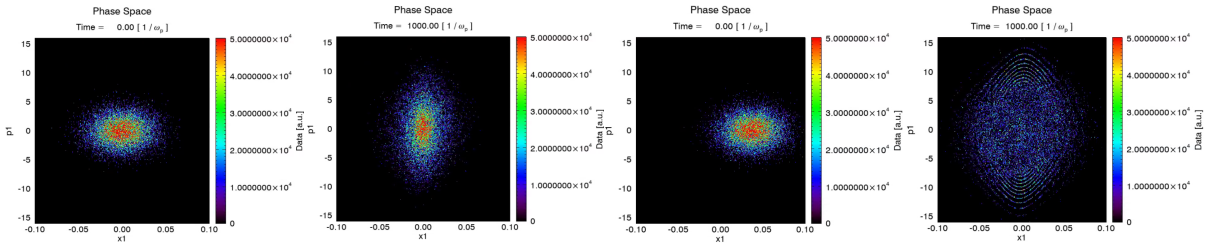

(a) (b) (c) (d)

Figure 5.14: Witness beam $x - p_x$ phase space density evolution for FACET-II parameters. (a) Initial phase space with no offset. (b) Saturated phase space with no offset. (c) Initial phase space with an offset. (d) Saturated phase space with an offset.

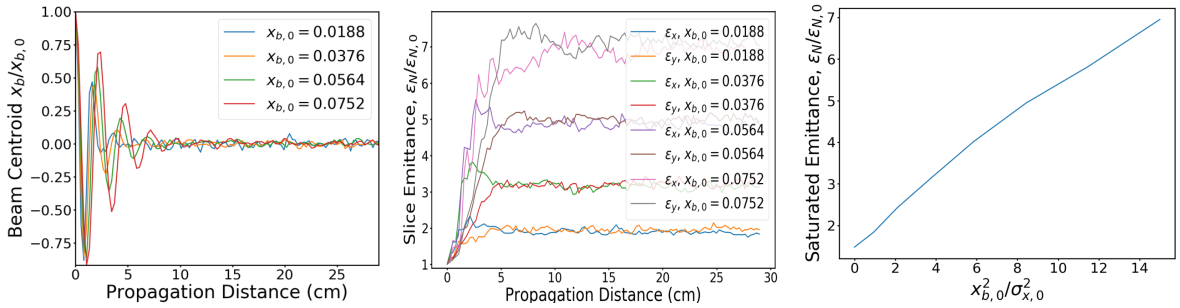

(a) (b) (c)

Figure 5.15: (a) Beam centroid and (b) emittance evolution for various beam offsets using a beam slice (fixed focusing force) simulation. (c) Scaling of the saturated emittance with initial offset.

5.7 Predicting the emittance growth of asymmetric or offset witness beams

In the regime where the drive beam ion motion dominates, i.e., the nonlinear focusing force is centered on axis, the emittance growth can be predicted. First, it is important to describe the salient features of the physics that can be inferred from the simulations described in the previous section. We find that the emittance initially grows in the offset direction x, and then it subsequently grows in the other transverse direction. Eventually, an equilibrium is reached where the final emittances and spot sizes reach the same value in both directions. This is due to the ion density being symmetric about the drive beam axis and the focusing forces being nonlinear. This leads to coupling between the two planes that acts to make the witness beam symmetric about the drive beam axis.

As we mentioned in Chapter 1, future PWFA-LCs may require asymmetric beams to avoid strong beamstrahlung radiation. It may be possible to use an asymmetric drive beam to cause an asymmetric ion collapse and therefore the saturated witness beam emittance would be asymmetric. However, this requires very large aspect ratios and therefore QPAD is not suitable. Future studies of this using QuickPIC with mesh refinement are underway, including designs for a final focus that will make a high energy symmetric witness beam asymmetric before the interaction point. We note that some recent work [68] indicates that the use of symmetric beams at the interaction point may be permissible in some cases.

5.7.1 Asymmetric witness beam evolution

As just described, when a witness beam with an offset oscillates in a fixed nonlinear focusing force it will rapidly become asymmetric about the drive beam axis and subsequently equilibrate between the two planes, leading to a symmetric saturated emittance. Thus, we study asymmetric witness beam evolution in these nonlinear forces. Asymmetric beams are also worth studying in their own right, as many times the beams produced in experiment are

asymmetric. In this analysis, we consider beams with no energy spread.

The evolution of the spot size of an asymmetric witness beam is governed by Eq. 5.33 (coupled to the corresponding equation for σ_y). We typically do not know the evolution in s of the geometric emittance terms, ϵ_x and ϵ_y, in these two equations. Thus, there is currently no self-consistent description. Instead, we use beam slice simulations to identify several conserved quantities. Fig. 5.16 shows the results of four such simulations with the results showing that the spot size and momentum spread in each plane roughly converge to the root mean square (RMS) of their initial values in x and y, i.e., $\sigma_x^2 = \sigma_y^2 \cong \frac{1}{2}\left(\sigma_{x,0}^2 + \sigma_{y,0}^2\right) \equiv \sigma_{\rm sat}^2$ and $\sigma_{p_x}^2 = \sigma_{p_y}^2 \cong \frac{1}{2}\left(\sigma_{p_x,0}^2 + \sigma_{p_y,0}^2\right) \equiv \sigma_{\rm p,sat}^2$. As of yet, we do not have a first principles argument for why they are conserved. The closer the beam remains to Gaussian (see Fig. 5.5) the less error between the actual saturated value and the RMS result. The saturated normalized emittance can then be calculated as $\epsilon_{N,\rm sat} = \sigma_{\rm sat}\sigma_{p,\rm sat}$. This value is very close to the average of the initial emittance in each direction, i.e., $\epsilon_{N,\rm sat} \simeq \frac{1}{2}(\epsilon_{x,0} + \epsilon_{y,0})$ for the parameters studied. So in summary, beam slice simulations have shown if both directions start matched to the nonlinear focusing force, i.e., $\sigma_{x,0}'' = \sigma_{y,0}'' = 0$, then $\sigma_x^2 + \sigma_y^2$, $\sigma_{p_x}^2 + \sigma_{p_y}^2$, and $\epsilon_x + \epsilon_y$ are conserved assuming the beams stay close to Gaussian in x and y. We note these findings only strictly apply for parameters similar to those considered in this section, and have not been tested rigorously for other regimes, although the general principles should still apply.

5.7.2 Offset witness beam evolution

A witness beam that starts with a centroid offset in a fixed nonlinear force will rapidly phase mix and the centroid will vanish typically within a couple betatron oscillations. In other words, the witness beam will become realigned to the drive beam through the ions, however, this comes at the cost of emittance growth of the witness beam. The smearing out in the offset direction leaves the beam asymmetric and therefore it will evolve to become symmetric as we have described above. In reality, this is a continuous process, however, the

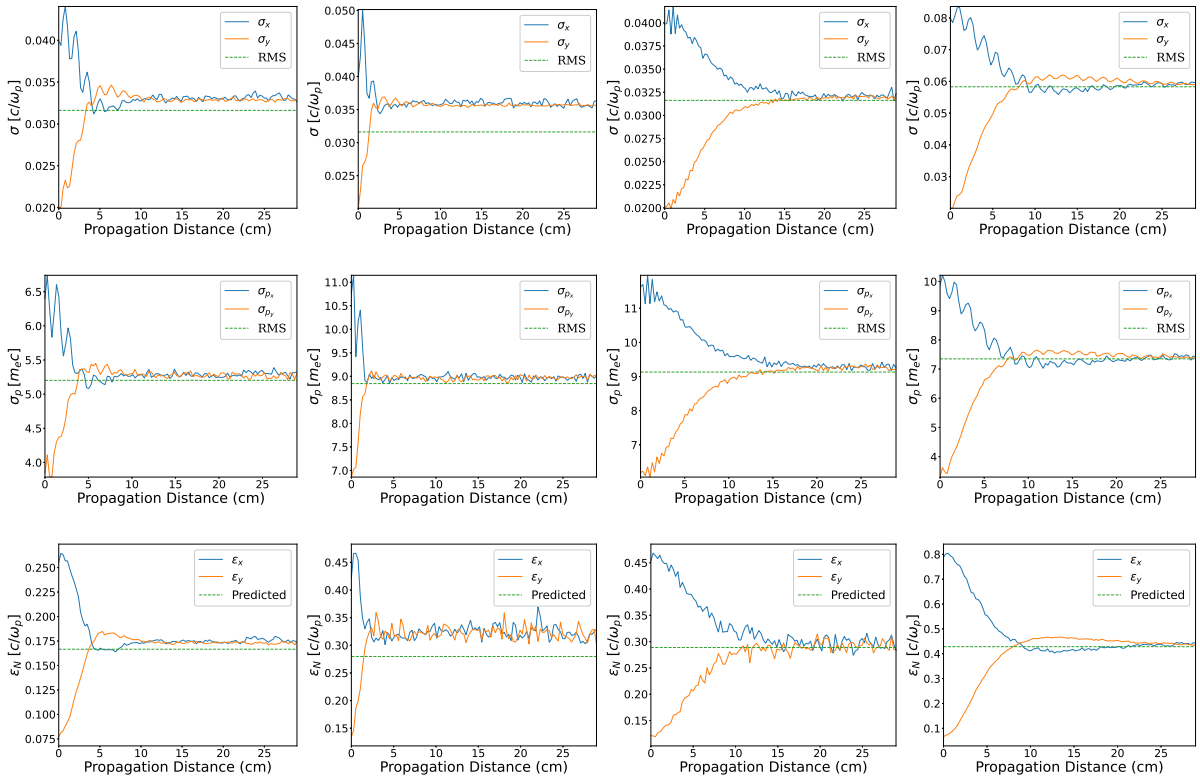

Figure 5.16: Simulations of an asymmetric beam slice in a fixed nonlinear focusing force. Each direction starts matched to this focusing force. The first row is the beam spot size, the second row is the momentum spread, and the last row is the slice emittance ϵ_N. The first column uses a beam with $k_p\sigma_x = 0.04$ and $k_p\sigma_y = 0.02$ and ion profile with $A = 10$ and $\sigma = 0.015$ (ion width, not to be confused with the beam spot size). The second column uses the same beam but with $A = 40$. The third column uses the same beam but with $\sigma = 0.06$. The fourth column uses the ion profile $A = 10$ and $\sigma = 0.015$ but with $k_p\sigma_x = 0.8$, i.e. the aspect ratio is increased from 2 to 4. The slice emittance is predicted through $\epsilon_{N,\text{sat}} = \sigma_{\text{sat}}\sigma_{p,\text{sat}}$. Using $\epsilon_{N,\text{sat}} \simeq \frac{1}{2}(\epsilon_{x,0} + \epsilon_{y,0})$ gave results that were about 1-2% less than this for all cases.

phase mixing of the centroid oscillations generally occurs within the first couple betatron oscillations, while the coupling between the transverse planes occurs over a much longer timescale. Thus, we treat this as a two step process. In the first step, taking x to be the offset direction, the beam smears out to a new σ_x predicted by 1D theory from [110], and we typically assume the y direction is unchanged. However, for sufficiently small offsets, the y direction can also change significantly and must be estimated using the 1D theory as well. Along with the beam smearing out in x, it also rapidly reaches the matched σ_{p_x} and σ_{p_y} values predicted by Eq. 5.33. The second step will then be the symmetrization of the beams transverse spot sizes, equivalent to the matched asymmetric beam described above.

5.7.2.1 Calculating the 1D beam phase space with an offset

As discussed earlier, in a uniform plasma, the emittance of an nonlinearly unmatched beam in a nonlinear force saturates quickly and reaches a steady state where $\epsilon = \sigma_x \sigma_{p_x}$. Even if the beam is asymmetric or offset, it will still eventually reach a symmetric steady state as described above. In Ref. [110], a method for calculating the saturated emittance in 1D was provided. This same method can be straightforwardly modified to calculate the saturated spot size and emittance when the beam has an offset so we will breifly review this calculation. Because the beam is in steady state, we can calculate the time average of x^2 of a beam particle orbit as

$$X^2_{\text{ave}} \equiv \frac{\int_{osc} x^2 dt}{T_{osc}} = \frac{\int_0^{x_0} \frac{dx}{v_x} x^2}{\int_0^{x_0} \frac{dx}{v_x}} = \frac{\int_0^{x_0} dx\, x^2 / \sqrt{\psi(x,\xi) - \psi(x_0,\xi)}}{\int_0^{x_0} dx / \sqrt{\psi(x,\xi) - \psi(x_0,\xi)}}, \tag{5.48}$$

where x_0 is the maximum value of x, and $v_x = \sqrt{2(\psi(x,\xi) - \psi(x_0,\xi))/\gamma}$ was used, where $\psi(x,\xi)$ is given by Eq. 5.21, and lastly we assumed γ can be taken out of the integrals because the energy does not change much during the saturation process. We can calculate the saturated spot size by integrating over all particles in phase space as follows

$$\sigma_{x,f} = \frac{1}{N} \int_0^\infty dx_0\, N_{x_0} X^2_{\text{ave}}, \tag{5.49}$$

where N_{x_0} is given by

$$N_{x_0} = 2\int_{-x_0}^{x_0} f_0(x, p_x)\frac{dp_x}{dx_0}dx, \tag{5.50}$$

where $f_0(x, p_x)$ is the initial distribution function of the beam. We have integrated over the positive side of the $x - p_x$ plane and multiplied by two to capture the negative side, which is needed where there is an offset (Ref. [110] only used one quadrant and multiplied by 4). Using the expression for v_x given above we can calculate

$$\frac{dp_x}{dx_0} = \frac{\sqrt{\gamma}F_\perp(x_0)}{\sqrt{2(\psi(x) - \psi(x_0))}}, \tag{5.51}$$

where we used $F_\perp = -\partial\psi/\partial_x$. We now have all the pieces required to calculate the final saturated spot size $\sigma_{x,f}$, given an initial beam slice distribution $f_0(x, p_x)$ and Gaussian ion profile parameterized by A and σ. Of course, it is straightforward to do the same calculation for σ_{p_x} so that you can calculate the saturated emittance. However, this 1D based derivation only works when there is no offset, as this does not take into account the transverse plane coupling, and therefore does not capture the symmetrization discussed in the previous section. Instead, as we laid out before, we can use this approach to calculate the maximum spot size achieved when the beam oscillates and expands in the x direction, before the beam symmetrizes.

5.7.3 Calculating the emittance growth of an offset beam

We are now ready to put these approaches together. In Fig. 5.17, we show the validation of this two step approximation using beam slice simulations for FACET-II parameters with a witness beam offset of $x_{b,0} = 1\,\mu\text{m} = 0.0376\,c/\omega_p$ and ion profile parameterized by $A = 90$ and $\sigma = 0.0045$. We consider the special case where the beam spreads out to $\sigma_x^2 \to \sigma_{x,0}^2 + x_{b,0}^2$, which corresponds to the beam starting with the matched σ_p after it has undergone the initial phase mixing in the offset direction x. The matched σ_p in each direction is calculated with the nonlinear matching condition from Eq. 5.33 with $\sigma_x'' = 0$ and $\epsilon_x = \sigma_x\sigma_{p_x}/\gamma$ (and analogous condition for the y direction). It then symmetrizes to $\sigma_{\text{sat}}^2 = \frac{1}{2}\left(\sigma_{x,0}^2 + x_{b,0}^2 + \sigma_{y,0}^2\right)$

and therefore reaches a final emittance of $\epsilon_{\rm sat} = \frac{1}{2}\sqrt{(\sigma_{x,0}^2 + x_{b,0}^2 + \sigma_{y,0}^2)(\sigma_{p_x,0}^2 + \sigma_{p_y,0}^2)}$. We compare the offset beam slice simulation with another beam slice simulation initialized with an asymmetric beam (with no offset) with spot sizes $\sigma_{x,\rm asym} = \sqrt{\sigma_{x,0}^2 + x_{b,0}^2}$ and $\sigma_{y,\rm asym} = \sigma_{y,0}$, which corresponds to the offset beam after phase mixing (beginning of the second step). The agreement between these two simulations verifies the two step method is a good approximation for this parameter regime. In the general case, there may be some discrepancy between the offset initialization and asymmetric initialization in the spot sizes, while for the momentum, the disagreement is usually very small - within $\sim$5% for parameters considered here. Finally, we use this model to predict the emittance growth in the case from Fig. 5.12, where the beam is offset with a linearly matched spot size when it enters the plasma. The results are shown in Fig. 5.18, where we compare the two step method prediction with a beam slice simulation and a fully self-consistent QPAD simulation (which was presented in Sec. 5.6). We see the saturated projected emittance from QPAD is close to the predicted emittance value. Because we have only considered the effect of the ion collapse on the beam emittance, these results validate our assumption that, in this regime, the transverse beam dynamics in the fixed ion column dominate and hosing has little effect.

5.8 Suppression and elimination of hosing in a uniform plasma in the LC regime

In Sec. 5.6, we showed drive beam induced ion motion can realign the witness beam with the drive beam at the cost of emittance growth for FACET-II like parameters. In this section, we will expand on this idea for the LC regime and show we can minimize emittance growth of a misaligned witness beam by choosing an appropriate drive beam density to cause a minimal amount of ion motion at the witness beam head, while still damping its centroid oscillations. Subsequently, the rest of the beam will realign behind the beam head.

Ref. [104] showed the witness beam hosing can be suppressed in the LC regime via a

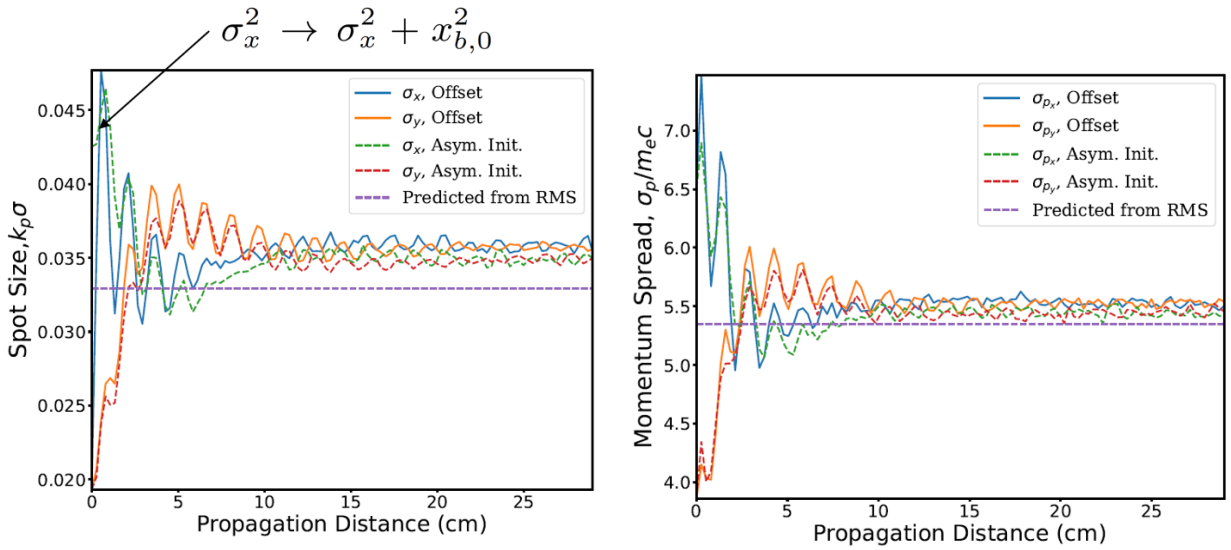

(a) (b)

Figure 5.17: Verification of the two step method for calculating the saturated (a) σ_r and (b) σ_p values for a beam slice with FACET-II parameters and a 1 μm offset in the x direction. The solid lines represent the evolution with the initialization with the beam offset and the green and red dashed lines represent an initialization with an asymmetric beam slice equivalent to the offset beam after the spot size expansion $\sigma_x^2 \rightarrow \sigma_x^2 + x_{b,0}^2$ and the violet dashed line is the predicted saturated values. The error in the spot size is mostly due to the beams matched distributions deviation from Gaussian.

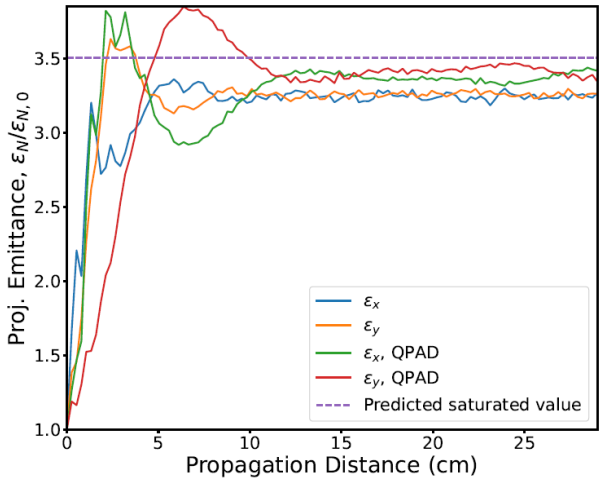

Figure 5.18: Comparison of the emittance from the FACET-II parameter simulation shown in Fig. 5.12 (both QuickPIC and QPAD with up to $m = 3$) to the predicted emittance from the two step method. The beam is initially linearly matched to the plasma.

BNS-type mechanism induced by the ion collapse of the witness beam itself. This work also derived an equation for the average wakefield (the wakefield is defined as $\mathbf{W}_\perp = \mathbf{E}_\perp + \hat{z} \times \mathbf{B}_\perp$, so $\mathbf{F}_\perp = -Ze\mathbf{W}_\perp$) experienced by a beam in the weak ion motion regime ($\Phi \lessapprox 1$) and incorporated it into their model for the plasma channel centroid to predict the mitigation of hosing in this regime. The expression for the average wakefield is

$$\langle W_x \rangle = \frac{x_b(\xi) - x_p(\xi)}{2} + Z_i \frac{m}{M} \frac{I_b}{I_A} \int_\infty^\xi d\xi' \, (\xi - \xi') g_\parallel(\xi') \frac{x_b(\xi) - x_b(\xi')}{\sigma_x^2(\xi) + \sigma_x^2(\xi')}, \tag{5.52}$$

where I_b is the beam current, $I_A \approx 17$ kA is the Alfvén current, x_b is the beam centroid, x_p is the channel centroid, and $g_\parallel$ is the longitudinal beam profile. This does not strictly apply to the strong ion collapse regime that we are interested in, but can provide some physical insight into the beam and ion dynamics. Namely this equation highlights the longitudinal variation to the wakefield induced from ion motion. For straight beams ($x_b(\xi) = x_b(\xi')$), the average wakefield will be $\langle W_x \rangle = (x_b - x_p)/2$ (this applies to strong collapse because the ions will oscillate on top of and in phase with the beam). However, if slices become misaligned with respect to the head of the beam, they will experience different average wakefields. This

variation along the beam induces the BNS mechanism and detunes the hosing resonance.

We now consider the dynamics of misaligned witness beams in the presence of ion motion in the LC regime ($\Phi \gg 1$). Ref. [104] studied a uniform offset witness beam in the LC regime using a low density (non-evolving) drive beam that causes no ion motion and showed that the witness beam hosing growth is completely suppressed, i.e., the beam oscillates with constant amplitude. In this case, the ions collapse directly on top of the witness beam and oscillate in phase with it, so the emittance growth will be very close to the non-offset case (assuming no energy spread). To further study this regime, we carry out two QPAD simulations of tilted beams. The simulations highlight the physics of ion motion suppressing the beam hosing in the LC regime. We consider a two-bunch LC scenario with a Gaussian current profile for the drive beam and a trapezoidal current profile for the witness beam that optimally loads the wake. The plasma density is $n_0 = 10^{17}$ cm^{-3}. Both beams are 25 GeV with no energy spread and the head of the witness beam starts 105 μm behind the center of the drive beam. The drive beam has 4.8 nC of charge, normalized emittance $\epsilon_{N,d} = 1$ mm and spot sizes $\sigma_{r,d} = 10.37$ μm, $\sigma_{z,d} = 30$ μm. The witness beam has 1.63 nC of charge, normalized emittance $\epsilon_{N,w} = 0.465$ μm and spot size $\sigma_{r,w} = 0.223$ μm. The beam current linearly decreases from $I_b = 27$ kA to $I_b = 5.4$ kA over $L_b = 30.24$ μm. The resolution is 10.3 nm $\times$ 241 nm and the 3D timestep is $\Delta t = 5\,\omega_p^{-1}$. A small timestep is needed to capture the beam dynamics in the large ion densities created when the drive beam seeds the ion motion. We use up to $m = 5$ to capture the witness beam hosing.

The results from the simulations are shown in Fig. 5.19. In Fig. 5.19a, it can be seen that when the entire beam has a uniform offset it oscillates as a rigid body, with no hosing growth. In Fig. 5.19b, results for the case of a beam tilted about its head so that its head is on axis ($r = 0$) are shown. In this case, the head of the beam will pull the ions towards the axis. The perturbed focusing force that the subsequent beam slice sees will tend to eventually pull it towards the axis. This argument holds for each subsequent beam slice to the beam tail such that eventually the beam will be aligned to the drive beam axis, as we

can see in Fig. 5.19b. We also consider a beam tilted about its center so its head is not aligned with the axis. In the same way as the previous scenario, the ion collapse will align behind the location of the head and oscillate with it. Each subsequent beam slice will then align with the head as can be seen in Fig. 5.19c. Thus, in the case of strong ion collapse from the witness beam, an arbitrary offset will eventually become uniform, i.e., the beam will become straight, and oscillate at constant amplitude corresponding to the initial offset of the head of the beam. Therefore, the key parameter is the offset of the head of the witness beam relative to the drive beam.

In order to achieve realignment, we thus only need to realign the head of the witness beam using the ion collapse from the drive beam. The ion density in the witness beam region, which is a function of the drive beam density, should be high enough to realign the beam but not too high to cause extra emittance growth. Such an ion density at the location of the head of the witness beam can be created by a drive beam with a moderate Φ. A drive beam with a density of $n_{b,d} = 100$ (corresponding to a spot size of $2.52\,\mu$m and $\Phi = 1.4$ at the witness beam head) that causes an on-axis ion density at the witness beam head of $A_0 \approx 10$ was found to work well. Fig. 5.11b shows the saturated ion density for this simulation. The damping of the centroid oscillations of the head is due to the phase mixing in the nonlinear focusing force, as shown in Fig. 5.20, which is different of course from the BNS-type mechanism responsible for the suppression of hosing when the ions are oscillating with the beam. Once the head of the witness beam completely phase mixes, its centroid fully aligns with the drive beam. The rest of slices become aligned with the head so that the entire beam is realigned, as shown in Fig. 5.19d.

In Fig. 5.21 we show the how the focusing force damps the beam oscillation because the zero point of the focusing force (and the ion center) is between the beam centroid and the axis, due in part to the drive beam ion motion, so the average wakefield it will experience will tend to damp the oscillation. We also note that there is a significant perturbation of the focusing force compared to the unperturbed one, due to the large ion collapse, which has a

significant effect on the dynamics. We can see the results in Fig. 5.19d show that the beam is realigned but at the cost of large emittance growth. This realignment scheme will work for general positional offsets as well as initial velocity angles as long as there is a sufficient ion collapse at the beam head.

A method to approximately determine the appropriate drive beam density required to damp the witness beam head oscillation is as follows. Given the drive and witness beam parameters, we calculate the ion density using the ring model from Sec. 5.2. Alternatively, you could run a single 3D timestep (quasi-static) PIC simulation and extract the ion density. The ion density profile can then be fit to a Gaussian transverse profile (obtain A and σ) and use this to obtain the corresponding focusing force for a particular slice. This focusing force can be prescribed in a beam slice simulation to study how this beam slice centroid will damp in this fixed focusing force. For cases where Φ of the witness beam is large, this procedure only works for slices near the head as the evolution of the witness beam will change the focusing force. It is possible to directly import a focusing force profile into a beam slice simulation, but usually this degree of accuracy is not necessary. We can use this workflow either in a uniform plasma or a plasma ramp, as we will show in the next chapter.

5.9 Summary

In this chapter, we reviewed the basic physics of ion motion in PWFA. Usually, PWFA theory neglects ion motion because it is weak for typical beam parameters. However, with more intense, tightly focused beams that will soon be used in experiments and will be necessary for future applications, such as a plasma-based linear collider design, ion motion will be a fundamental challenge that must be addressed.

We reviewed previous work that characterized the basic problem of ion motion and identified the basic physics associated with ion collapse and how aligned witness beams evolve in the nonlinear focusing forces created by this collapse. We then calculated the ion density

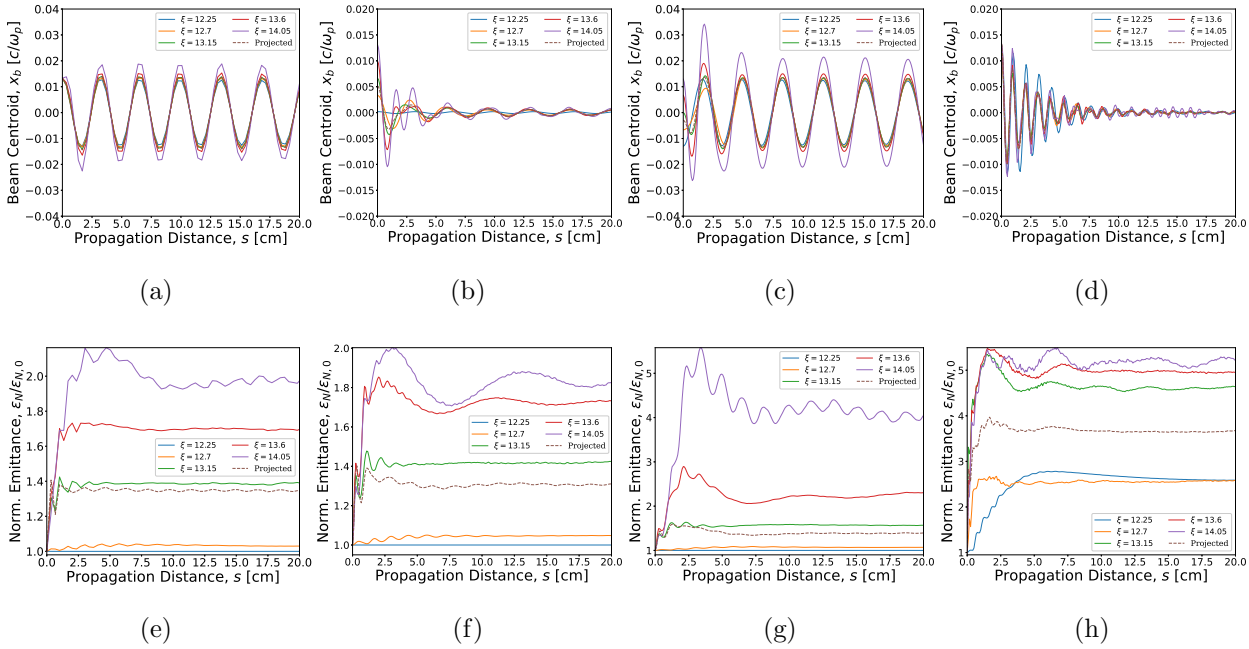

Figure 5.19: The first three columns show beam centroid and emittance evolution for a low density ($n_{b,d} = 5.9$) drive beam. The first column is similar to Ref. [104], that uses a uniform beam offset $\Delta x = \sigma_{x,0}$. The second column has a witness beam with a linear tilt about the head, with $\theta = 0.00739$ rad so that the tail is $x = \sigma_{x,0}$ above the axis. The second column has a witness beam with a linear tilt about the the center, with $\theta = 0.0148$ rad so that the tail is $x = \sigma_{x,0}$ above the axis. The fourth column uses a higher density ($n_{b,d} = 100$) drive beam with a uniform witness beam offset, $\Delta x = \sigma_{x,0}$. The final projected emittance growths are 35%, 40%, 31%, and 268%, respectively.

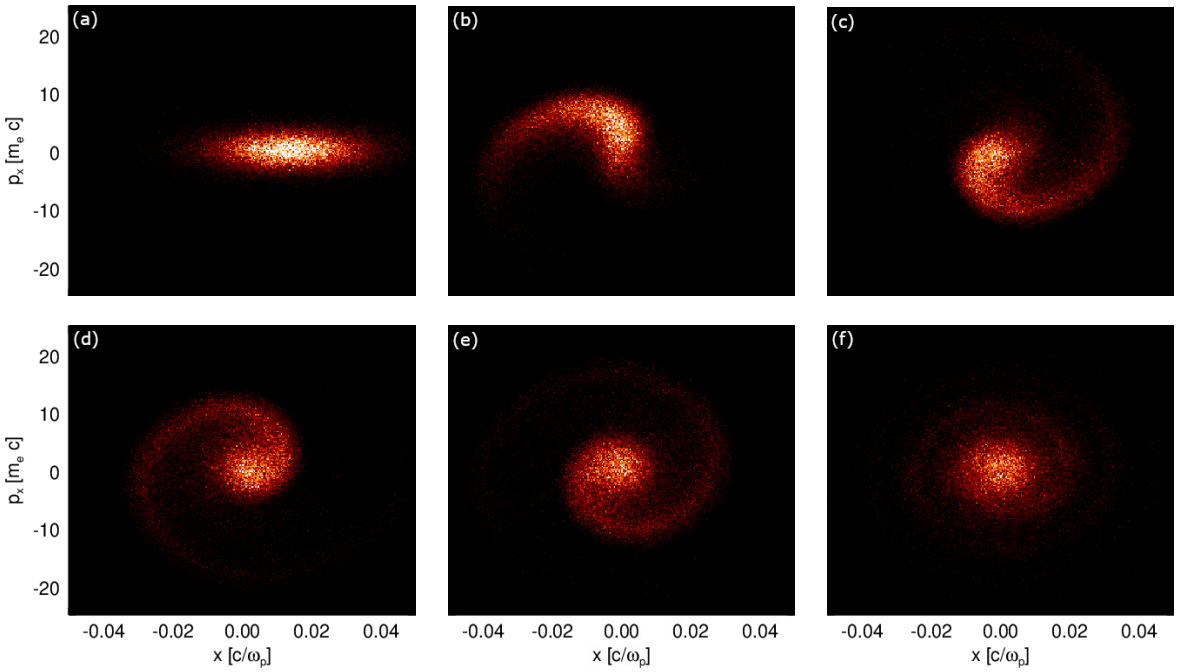

Figure 5.20: Phase space density evolution of the head of the witness beam, $\xi = 12.25$ through $\xi = 12.35$, from Fig. 5.19d. $s = 0, 1.68, 3.36, 5.04, 6.72, 20$ cm, respectively.

created by Gaussian electron beams using a ring model. We found we can reproduce the ion density from simulations even when trajectories cross by using a small cutoff value. This ion density can then be integrated to calculate the resulting focusing force. When ion motion is weak, we can use the ring model to calculate the wake analytically assuming a flat-top longitudinal and Gaussian transverse beam profile.

We reviewed how beam matching is altered when there is strong ion motion. In general, the beam distribution becomes non-Gaussian, but we found that we can calculate a correction to the standard envelope equation and therefore matching condition if we assume the transverse profile remains Gaussian. Beams matched using this nonlinear matching condition still have a small emittance growth, but it is much reduced from than linear matching. In general, the beams need to be slice-by-slice matched due to the variation in ion density along the beam. An iterative procedure for finding the slice-by-slice matching was reviewed. We noted that this can be achieved using adiabatic matching schemes.

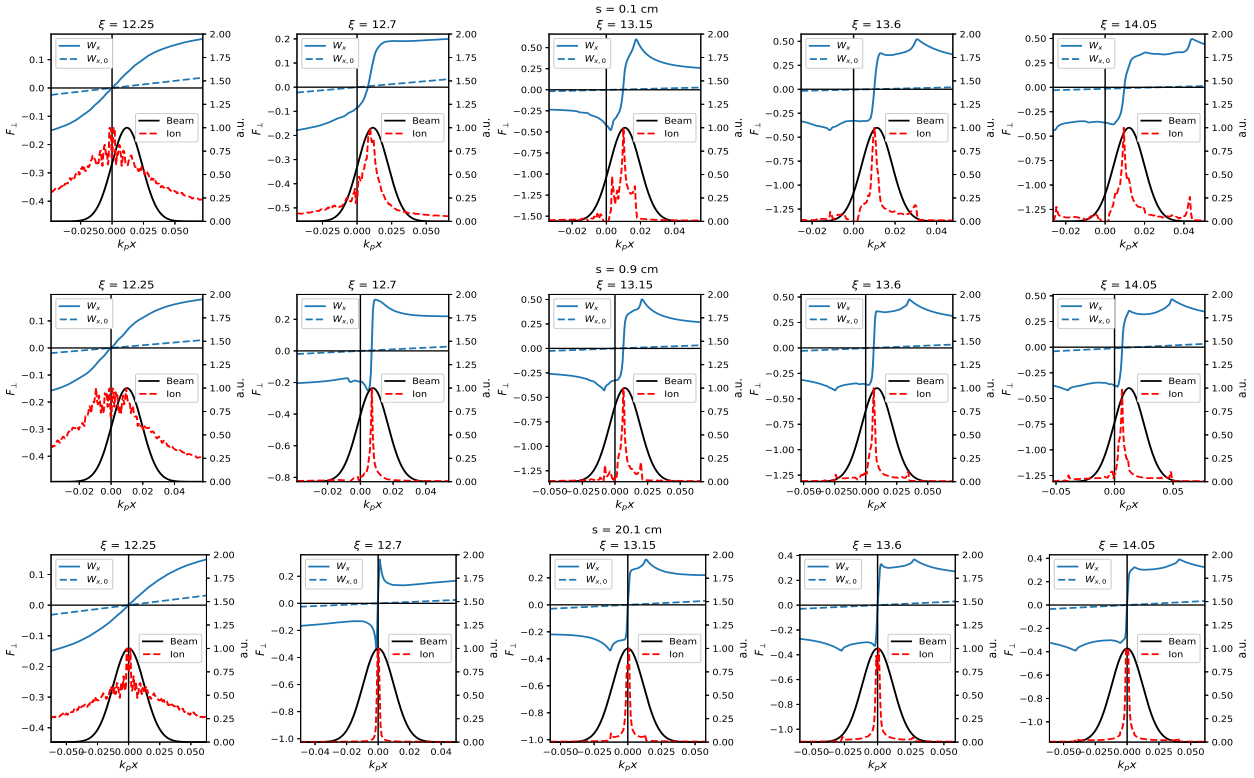

Figure 5.21: Demonstration of centroid damping for the case with drive beam ion motion, shown in Fig. 5.19d. The first row is the first 3D timestep, the second row is after one betatron oscillation, and the third row is the final timestep (after saturation). The left axis of each plot shows the focusing force in normalized units. The dashed line represents the unperturbed wakefield and its zero-crossing is the center of the plasma channel. The right axis shows the beam and ion densities. Their max values are normalized to one and the beam densities are fitted to a Gaussian.

We discussed how the physics changes when one considers drive beam ion motion. This issue has not been addressed previously, likely because it is more complicated and it leads to larger ion density compression. However, in reality large spot size beams that do not cause ion motion suffer significant head erosion causing wake deterioration. We found that using narrower drive beams to prevent head erosion causes ion motion in front of the witness beam and can actually have a stabilizing effect on head-to-tail instabilities. The on-axis focusing force created by drive beam ion collapse realigns the witness beam by causing it to phase mix. This comes at the cost of large emittance growth. In the LC regime, where the witness beam has $\Phi \gtrsim 1$, we find that we can realign the head of the beam, using a minimal ion density. When the head of the beam is on axis, the rest of the beam will realign behind it.

Finally, we presented a scheme for predicting the emittance growth for asymmetric and offset witness beams in the case when the focusing force is on-axis. A symmetric drive beam causes a symmetric ion collapse. The symmetric, nonlinear force will tend to make the witness beam symmetric. When the witness beam is offset, it will quickly become asymmetric and then symmetrize in a two step process. The scaling of this emittance growth was found to agree well with simulations.

CHAPTER 6

Beam realignment via drive beam induced ion motion in quasi-adiabatic matching sections

In this chapter, we combine the ideas from previous chapters to study a full stage for the electron arm of a plasma wakefield accelerator linear collider (PWFA-LC) with quasi-adiabatic plasma matching sections. We start by discussing the importance of matching sections in the electron arm of a PWFA-LC and the development of plasma density ramps to match intense electron beams into the plasma, including the basic notation and equations such as Courant-Snyder parameters. We will discuss how these ramps in the LC regime, in the absence of any initial beam misalignment, can match beams in and out of a single stage with essentially no emittance growth. We extend this idea to situations where the drive beam causes ion motion. We then discuss how the matching section can suppress beam centroid oscillations. We put this all together and present a scheme where drive beam induced ion motion realigns a witness beam in the LC regime within one stage, with minimal emittance growth through the use of quasi-adiabatic matching sections. This stage provides a high transformer ratio and the witness beam is loaded such that the energy spread remains small. This is a significant advance in LC designs that may allow the stable transport and acceleration of electron beams over many stages. Finally, we discuss some other scenarios for realignment and how higher levels of ionization may be an issue when using heavier ion species such as lithium. This chapter covers works to be published in Ref. [107].

6.1 Matching sections without ion motion

We begin by reviewing the physics of matching sections in the absence of ion motion. It was recognized that when particle beams with any energy spread enter a plasma with an unmatched spot size, there is a large normalized emittance growth. Furthermore, when a tightly-focused beam exits a plasma, there is a large normalized emittance growth when the beam drifts and expands in vacuum. Thus, matching the beam into and out of the plasma is a critical. Plasma wakes in the blowout regime provide focusing forces much stronger than conventional optics. Moreover, in experiments, plasmas naturally will have some density ramps at the entrance and exits. Therefore, it makes sense to design and tailor the plasma ramps as matching sections to transition beams from a large (small) spot size to a small (large) spot size at the entrance (exit) of the uniform plateau section of the plasma. There has been much recent work on this front [32, 33, 35, 36, 115, 37].

Recall that the envelope equation for the spot size evolution of a beam in a linear focusing force is

$$\sigma_x'' + \frac{\epsilon^2}{\sigma_x^3}\left(1 - k_\beta^2 \frac{\sigma_x^4}{\epsilon^2}\right) = 0, \tag{6.1}$$

where $k_\beta = k_p/\sqrt{2\gamma}$ and ϵ is the geometric emittance. Setting σ_x'' gives the matched spot size

$$\sigma_m = \sqrt{\frac{\epsilon}{k_\beta}}. \tag{6.2}$$

Now for a plasma matching section, the plasma density will vary as a function of propagation distance, z. So we can define the local matched spot size as

$$\sigma_m(z) = \left(\frac{2}{\gamma(z)} \frac{\epsilon_N(z)^2}{k_{p0}^2} \frac{n_0}{n(z)}\right)^{\frac{1}{4}}, \tag{6.3}$$

where $\epsilon_N = \gamma\epsilon$ is the normalized emittance, n_0 is the reference density, and $n(z)$ is the local plasma density. From this, we can see that if we have a plasma upramp where $n(z)$ increases, the spot size will correspondingly decrease.

For a beam with energy spread that is not properly matched, chromatic effects will cause

particles of different energies to rotate at different angular frequencies in phase space, leading to a larger slice and projected normalized emittance.

6.1.1 Courant-Snyder parameters

The beam phase space is typically described in terms of the Courant-Snyder (CS) parameters [116] (also known as Twiss parameters). Here, we briefly review how these arise from studying single particle motion and how they are useful for defining matching. The equation of motion for a beam particle in a linear focusing force is

$$x'' + \frac{\gamma'}{\gamma}x' + k_\beta^2 x = 0. \tag{6.4}$$

If we use the substitution $x = \sqrt{\gamma(z_0)/\gamma(z)}\,\tilde{x}$, and assume no phase slippage, i.e., $\gamma''/\gamma \ll k_\beta^2$, and adiabatic acceleration, i.e., $\gamma'/\gamma \ll k_\beta$, we arrive at a Hill like [117, 84] equation

$$\tilde{x}'' + k_\beta^2 \tilde{x} = 0. \tag{6.5}$$

This has an exact solution [116]

$$\tilde{x}(z) = a\sqrt{\frac{\beta}{\beta_0}}\cos\left(\int_{z_0}^{z}\frac{dz'}{\beta(z')} + \phi_0\right), \tag{6.6}$$

where a and ϕ_0 are constants and $\beta(z)$ is a function that satisfies the differential equation

$$\frac{1}{2}\beta\beta'' - \frac{1}{4}\beta'^2 + k_\beta^2\beta^2 = 1. \tag{6.7}$$

Moreover, we can define a constant of motion for the Hill like equation [116]

$$\gamma_{cs}x^2 + 2\alpha x x' + \beta x'^2 = a^2/\beta_0, \tag{6.8}$$

where $\alpha \equiv -\beta'/2$ and $\gamma_{cs} \equiv (1+\alpha^2)/\beta$. α, γ_{cs}, and β are called the Courant-Snyder parameters (for a single particle). We have also dropped the tilde, so we are tacitly assuming the γ remains constant. It is straightforward to modify Eq. 6.8 for cases where γ is changing, but this is not generally necessary for plasma density ramps. Jeans's theorem states that

any function of the constant of the motion of a given potential is a solution to the steady state Vlasov equation. Therefore, we can use this constant of motion for a single particle to obtain a distribution function

$$f(x,x') = \frac{1}{2\pi\epsilon}\exp\left(-\frac{\gamma_{cs}x^2 + 2\alpha xx' + \beta x'^2}{2\epsilon}\right), \tag{6.9}$$

that will be a solution of the steady-state Vlasov equation. We emphasize that this is not a unique solution, so it is essentially a Gaussian ansatz. Using this distribution function, we can calculate the moments of this distribution to obtain $\langle x^2\rangle = \beta\epsilon$, $\langle xx'\rangle = -\alpha\epsilon$, and $\langle x'^2\rangle = \gamma_{cs}\epsilon$. These can be rearranged as

$$\beta = \frac{\langle x^2\rangle}{\epsilon} \tag{6.10}$$

$$\alpha = -\frac{\langle xx'\rangle}{\epsilon} \tag{6.11}$$

$$\gamma_{cs} = \frac{\langle x'^2\rangle}{\epsilon}, \tag{6.12}$$

which are the well-known CS parameters for a beam. These CS parameters for a beam are the same relationships that define the CS parameters for a single particle. So the matching condition in a uniform plasma is

$$\beta = \beta_m = \frac{\sigma_m^2}{\epsilon} = \frac{1}{k_\beta} \tag{6.13}$$

$$\alpha = 0. \tag{6.14}$$

6.1.2 Matching with an adiabatic density ramp

In a ramp, the matching condition is slightly modified to

$$\beta = \beta_m \tag{6.15}$$

$$\alpha = \alpha_m, \tag{6.16}$$

where now the matched CS parameters are

$$\beta_m(z) = \sqrt{2\gamma}c/\omega_p(z) \tag{6.17}$$

and

$$\alpha_m(z) = -\frac{1}{2}\beta'_m(z). \tag{6.18}$$

In an adiabatic ramp, the density (and therefore k_β) changes slowly so that the beam can continuously remain matched as it propagates up or down the ramp. In other words, the betatron frequency changes little in one betatron wavelength. Based on Eq. 6.7, the adiabatic conditions are $\beta''/(k_\beta^2\beta) \ll 1$ and $\beta'/(k_\beta\beta) \ll 1$, from which it follows that $\beta \approx 1/k_\beta$. We can therefore define an adiabaticity parameter $\mathcal{A} \equiv |\alpha_m|$. For the ramp to be strictly adiabatic, we require $\mathcal{A} \ll 1$ [36]. Adiabatic density ramps have shown to preserve emittance well even when there is energy spread [32, 37, 118]. Recently, it has been shown that quasi-adiabatic ramps where $\mathcal{A} \lesssim 1$ (or, in some cases, even $\mathcal{A} \lesssim 5$) can also preserve the emittance well [114].

6.2 Matching in the presence of ion motion

In this section, we will cover the work done with Yujian Zhao in Ref. [114] on adiabatic plasma ramps in the presence of ion motion. This work only considers ion motion from the witness beam. We later extend these ideas to the case where the drive beam also causes ion motion. This will set the stage for the next section, where we will show these ramps can also help drastically reduce the emittance growth while realigning the witness beam via drive beam induced ion motion.

The first idea to match a beam in the presence of ion motion was to use a plasma section with decreasing ion masses so that the ion motion would gradually (adiabatically) increase as the ions in the plasma became less massive [112]. This would result in the beam being adiabatically matched to the nonlinear focusing force from the ions (as we have discussed before). Of course, such a plasma section would be very hard to create in practice even with a small number of discrete steps. Additionally, this work did not consider the effects of multiple ionization (something we will discuss in Sec. 6.4.3). However, this was the first

work to recognize that adiabatic matching is a solution to the nonlinear forces created by ion collapse.

Instead, we can use adiabatic plasma density ramps to achieve the same effect. Namely, when the density is low the matched spot size will be very large, and thus the ion motion will be small. While the spot size decreases, the ion motion will be gradually triggered and the beam will find the matching distribution. This will work even for large ion collapse as long as the ramp is adiabatic because the beam can find the ideal matching distribution and the emittance will not grow, as described in Sec. 5.4.3.

As we discussed in Sec. 5.4.3, there was recently another idea for an adiabatic matching section proposed [113] that injects a beam into a uniform plasma at low energy. As the beam accelerates, the spot size adiabatically decreases and the ion motion is gradually triggered, allowing the beam find the matching distribution. However, this concept if only viable for the first stage, and this work did not consider plasma density ramps, which are important to preserve the emittance, as we have discussed.

6.2.1 Adiabatic ramp design

One can imagine many different adiabatic ramp designs. In this dissertation, we will mainly use a simple design where the α_m linearly decreases to zero in the upramp so that the beam is matched when it enters the plateau. If L is the length of the upramp and α_{mi} is the initial value, we have

$$\alpha_m(z) = -\alpha_{mi}\frac{z-L}{L}. \tag{6.19}$$

Using the definition of α_m, it follows that

$$\beta_m(z) = \beta_{m0} + \alpha_{mi}\frac{(z-L)^2}{L}. \tag{6.20}$$

In the upramp, the acceleration is negligible and so we assume γ is constant. Thus, the density profile can be written as

$$\frac{n(z)}{n_0} = \frac{\omega_p(z)^2}{\omega_{p0}^2} = \frac{\beta_{m0}^2}{\beta_m(z)^2} = \frac{1}{\left(1 + \frac{\alpha_{mi}(z-L)^2}{\beta_{m0}L}\right)^2}. \tag{6.21}$$

Evaluating this expression at the entrance of the plasma ($z = 0$) we have

$$\frac{n(0)}{n_0} = \frac{1}{\left(1 + \frac{\alpha_{mi}}{\beta_{m0}}L\right)^2}. \tag{6.22}$$

We have two free parameters between $n(0)$, α_{mi}, and L. The above constraint implies several trade-offs. We want to make $n(0)$ small so that the initial ion motion is as small as possible. The α_{mi} should be small so that the ramp is adiabatic and emittance growth is limited. And ideally we want L to be short so that we preserve a high effective acceleration gradient per stage. In practice, we have to make sacrifices somewhere with these three parameters.

For simplicity, we often mirror the upramp profile for the downramp. However, when the beam has gained energy in the density plateau, the ideal downramp profile should be slightly longer to account for this, but this may not be practical in reality. In the next section, we show a comparison between two profiles from Ref. [114].

6.2.2 An adiabatic ramp stage with PWFA-LC parameters

In Ref. [114], it was shown quasi-adiabatic ramps (at both the entrance and exit) can limit emittance growth to $\sim 2\%$, when using a low density (non-evolving) drive beam and on-axis witness beam with LC parameters. Fig. 6.1 shows results from a self-consistent QPAD simulation. The parameters for the simulation are as follows: the hydrogen plasma is pre-formed with a density $n_0 = 10^{17}$ cm^{-3} in the plateau. Each beam has an energy of 25 GeV and they are separated by 105.2 μm (from center of the drive beam to head of the witness beam). The drive beam is bi-Gaussian (in r and ξ) with a charge of $Q = 4.8$ nC, normalized emittance $\epsilon_N = 1$ mm, density $n_b = 5.89$, and spot size $\sigma_r = 10.4\,\mu$m, and length $\sigma_z = 30\,\mu$m

(note these are the parameters the beam is designed to have when it gets to the plateau). The drive beam is non-evolving to isolate the witness beam physics. The witness beam is transversely Gaussian but has a trapezoidal current profile to optimally load the wake (using the multisheath beam loading model [31]). It has a charge of $Q = 1.6$ nC, normalized emittance $\epsilon_N = 100$ nm, and spot size $\sigma_r = 100$ nm. The beam current decreases from $I_b = 25.26$ kA to $I_b = 6.42$ kA over a length of 30.3 μm. The loaded accelerating field is nearly constant at $E_z = -1.2$ in normalized units. The beams are initialized with no energy spread. The $r-\xi$ simulation box size has dimensions $201.6 \times 252\,\mu$m with resolution 8.4×168 nm. The ramp is of the form in the previous section where α linearly decreases to zero in the upramp so that the beam is matched when it enters the plateau. The ramps have length $3 \times 10^4\, c/\omega_{p0}$ and the plateau has length $4 \times 10^4\, c/\omega_{p0}$. A small density of $n(0) = 10^{-4}$ is used to so that the ion motion is essentially negligible at the entrance. However, this corresponds to $\alpha_{mi} \approx 1$, which strictly speaking is not adiabatic (we refer to it as quasi-adiabatic). However, α_{mi} will decrease by the time the ions start significantly modifying the focusing force. This ramp was found to preserve the emittance well. Of course it would be possible to make the ramp longer and therefore more adiabatic, but the emittance growth by the end of the plasma is already very small, so this is not necessary for these parameters, and it would decrease the average acceleration gradient. Because the beams are axisymmetric, we use only the $m = 0$ azimuthal mode, making this simulation computationally inexpensive for the LC regime. A simulation with modes $m = 0, 1, 2$ was also done to test if any asymmetry (e.g., hosing) grows from noise, and no significant growth of the $m = 1, 2$ modes was observed. Another ($m = 0$) simulation with a longer downramp designed to account for the energy doubling of the witness beam was performed, and a slightly lower emittance growth was achieved.

It was found that the projected emittance increases by $\sim 15\%$ in the plateau. This is due to the slices in the witness beam no longer overlapping in phase space due to slice-dependent nonlinear focusing forces and matched phase space distributions. However, as

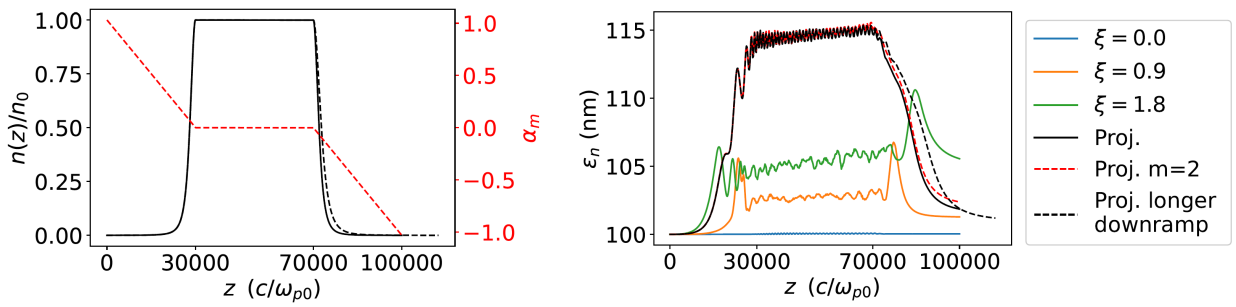

(a) (b)

Figure 6.1: (a) The resulting adiabatic plasma density profile (solid black) based on a linear ramp for α_m. The profile assumes the witness beam energy remains constant, so the downramp is symmetric to the upramp. The black dashed downramp takes into account the energy doubling of the witness beam, thus it is $\sqrt{2}$ times as long as the solid black downramp. (b) Evolution of the projected emittance (solid black) and selected slice emittances. The witness beam's head and tail are located at $\xi = 0$, $1.8\,k_{p0}^{-1}$ respectively. The red dashed curve shows the evolution of the projected emittance when three azimuthal modes, $m = 0, 1, 2$, are kept in a QPAD simulation. The black dashed curve shows the evolution of the projected emittance for the case where the black dashed downramp in (a) is used. Reproduced from [114].

the beam propagates in the downramp, the focusing forces gradually revert back to being linear and therefore the phase space ellipses of each slice unwind to overlap with each other again causing the projected emittance to decrease. The slice emittance (and therefore the final projected emittance growth) grows slightly due to imperfect matching to the nonlinear focusing forces. This slice emittance growth is stronger for the larger ion densities at the tail of the beam, however, it is still very modest.

6.2.3 An adiabatic ramp stage with drive beam induced ion motion

As we mentioned before, in reality the drive beams such as the one used in Ref. [114], described above, will not be straightforward to use because of head erosion. Two possible solutions to head erosion are a precursor (which we discuss in Sec. 6.3.3) and using a narrower (higher density, lower emittance) drive beam. The latter solution leads to a larger Φ for the drive beam and hence substantially larger ion densities in the witness beam region. This can lead to larger emittance growth as $A\sigma^2$ will be larger because many more ions have been pulled closer to the axis. However, if we can still adiabatically match the witness beam to the focusing force created by the ion collapse, we may still expect a tolerable emittance growth. We performed another axisymmetric ($m = 0$) QPAD simulation to test this. The parameters are similar to the ones in the previous section. However, for reasons that will become clear later, we use a higher emittance witness beam, but this is still in the range of interest of many LC designs [59, 58]. In addition, the beam loading will be slightly different due to the drive beam spot size and evolution. The plasma density is $n_0 = 10^{17}$ cm^{-3}. Both beams are 25 GeV and the head of the witness beam starts 105 μm behind the center of the drive beam. The drive beam has 4.8 nC of charge, normalized emittance $\epsilon_{N,d} = 59.1$ μm, density $n_b, d = 100$, spot size $\sigma_{r,d} = 2.52$ μm, and length $\sigma_{z,d} = 30$ μm. The witness beam has 1.63 nC of charge, normalized emittance $\epsilon_{N,w} = 0.465$ μm, and spot size $\sigma_{r,w} = 0.223$ μm. The witness beam current linearly decreases from $I_b = 27$ kA to $I_b = 5.4$ kA over $L_b = 30.24$ μm. The resolution is 10.3 nm $\times$ 241 nm and the 3D timestep is $\Delta t = 5\,\omega_p^{-1}$. A small timestep

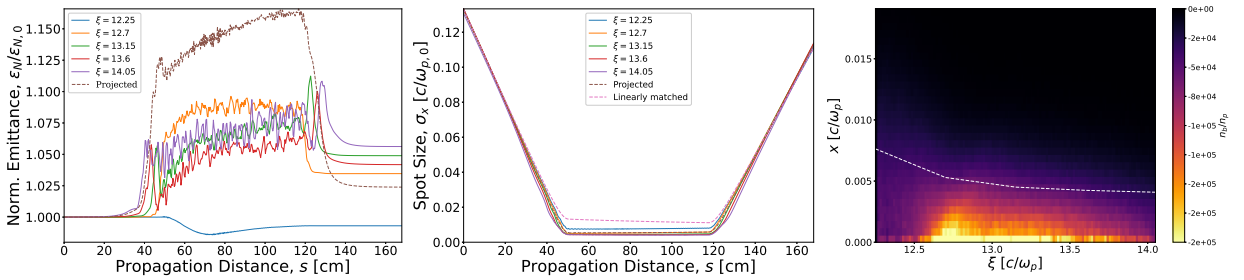

(a) (b) (c)

Figure 6.2: Adiabatic plasma ramp stage with a higher density drive beam, $n_b = 100$. (a) Slice and projected emittance growth evolution (the head slice emittance decreases in x because it is transferred to y). (b) Spot size, σ_x, evolution including the designed linearly matched value. The final value decreases due to energy gain. (c) Witness beam density in the center of the plateau ($s = 84$ cm). The dashed white line shows the spot size, σ_x (or technically the second order moment because the distribution is non-Gaussian) with the expected tapering in ξ.

is needed to capture the beam dynamics in the large ion densities created when the drive beam seeds the ion motion. The ramp is the same as the one used in the previous section, with α_m linearly decreasing from one to zero in the upramp. In this simulation, both the drive beam and witness beam are matched to the plasma using this ramp. The results are shown in Fig. 6.2. We can see we still see a very small emittance growth of $\sim 2\%$, even with stronger ion collapse. See Fig. 5.2c for the one timestep ion density.

6.3 Witness beam realignment via drive beam ion motion in an adiabatic density ramp

We have previously shown that ion motion caused by witness beams in the LC regime can suppress the hosing instability by a BNS-type mechanism, and moreover, witness beams will always align themselves behind the head and oscillate more or less rigidly with an

amplitude equal to the initial offset of the head. We have also shown that drive beam induced ion motion can fully realign the witness beam with the drive beam. However, in a uniform plasma, realignment came at the cost of large emittance growth due to the beam oscillating through very nonlinear focusing forces caused by large ion motion and eventual phase mixing. In this section, we will show that the adiabatic ramps used in the previous sections can drastically limit this emittance growth by matching the beams into the plasma density plateau as they oscillate and adjust to the focusing forces simultaneously.

6.3.1 Centroid suppression due to the density upramp

Plasma density upramps will greatly reduce the hosing seed (centroid oscillation amplitude). However, this is not a free lunch (except potentially as a plasma-based lens for the final focus), because the opposite process occurs in the downramp. In the absence of drive beam ion motion and, for example, a uniform offset witness beam, the centroid will be reduced in the upramp, remain constant (hosing is suppressed) in the plateau, but return to the same oscillation amplitude by the end of the downramp.

Refs. [98, 105] explore the reduction of the hosing seed for different density ramp lengths using full PIC simulations and Ref. [105] provides some analytic analysis including investigating the asymptotic behavior for long ramps. The basic equation for the beam centroid, when energy spread, acceleration, and channel displacement are neglected, is

$$\frac{d^2 X_b}{dz^2} + k_\beta(z)^2 X_b = 0, \tag{6.23}$$

which is a harmonic oscillator equation with varying frequency (non-conservative system). For a plasma density ramp, $k_\beta(z)^2 = k_{\beta 0}^2 n(z)/n_0$ is the local betatron wavenumber (we use frequency and wavenumber interchangeably). As the density increases, the frequency will increase and the amplitude of oscillation will decrease.

First, we show we can use energy arguments similar to those used in Ref. [105] when the ramp is adiabatic ($|\alpha_m| \ll 1$) to calculate the oscillation amplitude suppression. Later,

we will show a more robust analysis for quasi-adiabatic ramps ($|\alpha_m| \lesssim 1$). The energy of a harmonic oscillator is

$$E = \frac{1}{2}X_b'^2 + \frac{1}{2}k_\beta^2 X_b^2. \tag{6.24}$$

If we assume there is no initial velocity then we have

$$\frac{E}{E_i} = \frac{k_{\beta 0}^2 X_{b0}^2}{k_{\beta i}^2 X_{bi}^2}, \tag{6.25}$$

where E_i is the initial energy, X_{bi} is the initial offset, and X_{b0} is the amplitude of oscillation in the plateau. Now the adiabatic invariant of a harmonic oscillator is $I = E/k_\beta$, so for an adiabatic ramp we have

$$\frac{E}{E_i} = \frac{k_{\beta 0}}{k_{\beta i}}. \tag{6.26}$$

Thus, equating Eq. 6.25 and 6.26, we have

$$\frac{X_{b0}^2}{X_{bi}^2} = \frac{k_{\beta i}}{k_{\beta 0}} = \sqrt{\frac{n_i}{n_0}} = \frac{1}{1 + \alpha_{mi} k_{\beta 0} L}, \tag{6.27}$$

where n_i is the density at the plasma entrance. So the suppression of the amplitude of centroid oscillations is

$$\frac{X_{b0}}{X_{bi}} = \frac{1}{\sqrt{1 + \alpha_{mi} k_{\beta 0} L}}. \tag{6.28}$$

For general ramps, where α_m is arbitrary, we instead start with the exact single particle solution to the Hill-like equation, Eq. 6.6. This can be expressed using the initial conditions at $z = 0$ as [84]

$$x(z) = \sqrt{\frac{\gamma_0}{\gamma}}\Bigg[x(0)\sqrt{\frac{\beta_m(z)}{\beta_m(0)}}\cos[\phi(z)] + \sqrt{\beta_m(z)\beta_m(0)}\left(x'(0) + \frac{\left(\alpha_m(0) + \frac{\gamma_0'\beta_0}{2\gamma_0}\right)}{\beta_m(0)}x(0)\right)\sin[\phi(z)]\Bigg], \tag{6.29}$$

where $\phi(z) = \int_0^z dz'/\beta(z')$. If we assume there is no acceleration in the ramp, we arrive at

$$x(z) = x(0)\sqrt{\frac{\beta_m(z)}{\beta_m(0)}}\cos[\phi(z)] + \sqrt{\beta_m(z)\beta_m(0)}\left(x'(0) + \frac{\alpha_m(0)}{\beta_m(0)}x(0)\right)\sin[\phi(z)]. \tag{6.30}$$

We assume the initial positions are independent of energy, $\langle x'(0)\rangle = 0$, and there is no energy spread, so all particles will have the same ϕ. We take an ensemble average to obtain

$$\langle x(z)\rangle = \langle x(0)\rangle \sqrt{\frac{\beta_m(z)}{\beta_m(0)}} \left(\cos[\phi(z)] + \alpha_m(0)\sin[\phi(z)]\right). \tag{6.31}$$

Thus, the maximum oscillation amplitude is calculated by taking the maximum of

$$f(z) \equiv \cos[\phi(z)] + \alpha_m(0)\sin[\phi(z)]. \tag{6.32}$$

The maximum occurs when $\phi(z) = \arctan(\alpha_m(0))$ and so the maximum of $f(z)$ is

$$\max(f(z)) = \cos(\arctan[\alpha_m(0)]) + \alpha_m(0)\sin(\arctan[\alpha_m(0)]) = \sqrt{1+\alpha_m(0)^2}. \tag{6.33}$$

Reverting to our previous notation, the suppression of the amplitude of oscillation for a general ramp is

$$\frac{X_{b0}}{X_{bi}} = \sqrt{\frac{\beta_{m0}}{\beta_{mi}}}\sqrt{1+\alpha_{mi}^2}. \tag{6.34}$$

For a general ramp, the β_{mi} can be solved for by integrating Eq. 6.7 backward along the upramp to achieve the desired β_{m0} when it enters the density plateau [114]. For an adiabatic (or quasi-adiabatic) ramp, where

$$\frac{|k'_\beta(z)|2\pi}{k_\beta^2(z)} \ll 1, \tag{6.35}$$

$\beta(z) = 1/k_\beta(z)$, and therefore Eq. 6.34 reduces to

$$\frac{X_{b0}}{X_{bi}} = \left(\frac{n_i}{n_0}\right)^{\frac{1}{4}} \sqrt{1+\alpha_{mi}^2}. \tag{6.36}$$

For the adiabatic ramp design we discussed in previous sections, with α_m linearly decreasing from one to zero in the upramp, we have

$$\frac{X_{b0}}{X_{bi}} = \sqrt{\frac{1+\alpha_{mi}^2}{1+\alpha_{mi}k_{\beta 0}L}}, \tag{6.37}$$

where L is the length of the ramp. For small $\alpha_m(0)$, when the ramp is strictly adiabatic, this reduces to the previous result using energy and adiabatic invariant arguments. The ramp

we consider in this chapter is quasi-adiabatic as it starts with $\alpha_{mi} = 1$. For this ramp, we have

$$\frac{X_{b0}}{X_{bi}} = \sqrt{\frac{2}{1 + k_{\beta 0} L}} \approx \sqrt{\frac{2}{k_{\beta 0} L}}, \tag{6.38}$$

which is compared (the first equality) to numerical integration results in Fig. 6.3c.

Adiabatic ramps may be hard to realize experimentally, such as the one we have described where $\alpha_m(z)$ decreases linearly. In general, real plasma density ramps tend to be smoother and have regions where $\alpha > 1$ at low plasma density. Therefore, we study a more realistic ramp profile provided in Ref. [114] that uses a 5th order polynomial profile given by

$$\frac{n(z)}{n_0} = 6\left(\frac{z}{L}\right)^5 - 15\left(\frac{z}{L}\right)^4 + 10\left(\frac{z}{L}\right)^3, \tag{6.39}$$

defined for $0 \leq z \leq L$. Because this ramp starts at zero density, the CS parameters diverge at the plasma entrance, so this ramp is not adiabatic. However, Ref. [114] determined this ramp still does a good job at matching LC beams in the presence of ion motion. As we discussed above, the initial CS parameters at $z = 0$: β_{mi}, α_{mi}, can be obtained by numerically integrating the differential equation for β (Eq. 6.7) backwards from the plateau with the desired matching CS parameters at $z = L$: $\beta_{m0} = \sqrt{2\gamma} k_{p0}^{-1}$, $\alpha_{m0} = 0$ (in the absence of ion motion). Then, the amplitude suppression in this ramp can be predicted using Eq. 6.34.

We show the results for integrating Eq. 6.23 with this ramp profile and the adiabatic ramp profile in Fig. 6.3. In these plots, we can see the centroid actually gets magnified in the downramp to a larger offset than it started with. This oscillation depends on its phase when it enters the downramp. However, this does not change amplitude of oscillation in the next stage. If we import this offset and velocity (actually we must flip the velocity) to the second stage, we get the same amplitude in the plateau of the second stage and at the end of the second stage the offset comes back to its initial value. Finally, in Fig. 6.3c, we compare the oscillation amplitude suppression as a function of ramp length from the numerical solutions to Eq. 6.23 to the predicted scaling from Eq. 6.37 for the adiabatic ramps, and Eq. 6.34 for the polynomial ramp.

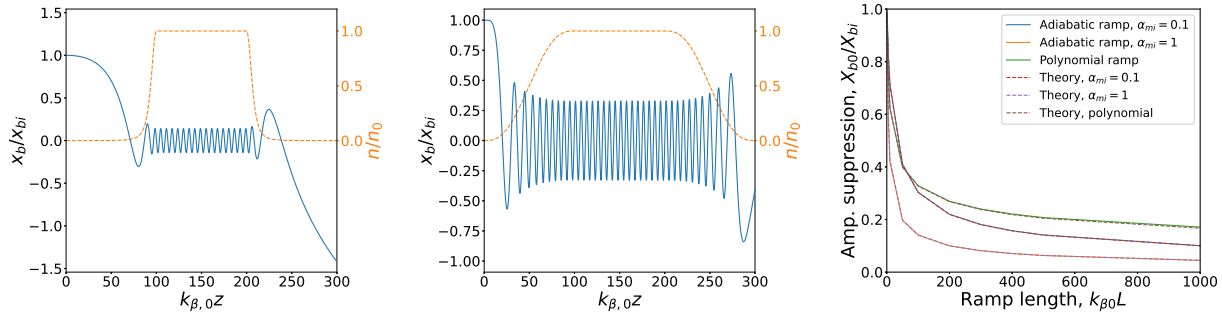

(a) (b) (c)

Figure 6.3: Numerical integration of the beam centroid equation, Eq. 6.23, with (a) the adiabatic density ramp, Eq. 6.21, and (b) the polynomial density ramp, Eq. 6.39. The lengths are normalized to $k_{\beta 0}$ and $\alpha_{mi} = 1$. The ramp lengths are $k_{\beta 0}L = 100$ and the plateau length is $k_{\beta 0}L = 100$. (c) Scan over the length of the upramp, measuring the amplitude of oscillation in the density plateau, using the polynomial ramp and adiabatic ramp with $\alpha_{mi} = 0.1$ and $\alpha_{mi} = 1$. Note that using a smaller α_{mi} will require a longer ramp to keep the initial density the same, which is important to control ion motion.

6.3.2 Centroid damping in an adiabatic ramp due to energy spread

We now take a brief digression to explore the effects of energy spread on the offset in adiabatic density ramps. This was first studied in Ref. [118], where analytic solutions to the single particle motion with adiabatic density ramps were derived along with beam moments and emittance expressions.

We start with Eq. 6.31, which describes the centroid evolution in a general density ramp, except we keep the average over the ϕ terms, i.e.,

$$\langle x(z)\rangle = \langle x(0)\rangle \sqrt{\frac{\beta_m(z)}{\beta_m(0)}} \left(\langle \cos[\phi(z)]\rangle + \alpha_m(0)\langle \sin[\phi(z)]\rangle\right). \tag{6.40}$$

We have assumed there is no acceleration, the only energy dependence is contained in ϕ, and the initial positions are uncorrelated with energy. We assume the energy is normally distributed, i.e., $f_\gamma = \frac{1}{\sqrt{2\pi}\sigma_\gamma} e^{-(\gamma-\bar{\gamma})^2/2\sigma_\gamma^2}$ and assume the energy spread is small such that $\phi \sim \frac{1}{\sqrt{\gamma}} \approx \frac{1}{\sqrt{\bar{\gamma}}}\left(1 - \frac{1}{2}\frac{\delta\gamma}{\bar{\gamma}}\right)$, where $\delta\gamma = \gamma - \bar{\gamma}$. Therefore, we can calculate the averages

$$\langle \cos[\phi(z)]\rangle = \exp\left(-\sigma_\phi^2/2\right)\cos\bar{\phi} \tag{6.41}$$

$$\langle \sin[\phi(z)]\rangle = \exp\left(-\sigma_\phi^2/2\right)\sin\bar{\phi}, \tag{6.42}$$

where $\sigma_\phi = \frac{\bar{\phi}}{2}\frac{\sigma_\gamma}{\bar{\gamma}}$. If we make the adiabatic approximation, we have $\beta = k_p^{-1} \sim n^{-1/2}$ and then the centroid evolution is given by

$$\langle x(z)\rangle = \langle x(0)\rangle \left(\frac{n(0)}{n(z)}\right)^{\frac{1}{4}} \left(\cos\bar{\phi} + \alpha_m(0)\sin\bar{\phi}\right) \exp\left(-\frac{\bar{\phi}^2\sigma_\gamma^2}{8\bar{\gamma}^2}\right). \tag{6.43}$$

A more general expression for the beam centroid moment is given in Ref. [118].

The saturated emittance can be calculated using the moments derived from the transport matrix based on the solution to the Hill like equation [84]. This results in the geometric emittance in terms of the initial distributions for x and x' and the initial CS parameters,

$$\epsilon = \frac{1}{2}\left(\gamma_{mi}\langle x_i^2\rangle + \beta_{mi}\langle x_i'^2\rangle + 2\alpha_{mi}\langle x_i x_i'\rangle\right). \tag{6.44}$$

If we include offsets $x_i = \tilde{x}_i + \Delta x$ and $x_i' = \tilde{x}_i' + \Delta x'$, where $\tilde{x}_i$ and $\tilde{x}_i'$ have normal distributions with zero mean. Upon substituting these into the above equation, we get the expression (details in Ref. [84])

$$\frac{\epsilon_{\rm sat}}{\epsilon_i} = \frac{1}{2}\left(\gamma_{mi}\beta_i + \beta_{mi}\gamma_i - 2\alpha_{mi}\alpha_i\right) + \frac{1}{2\epsilon_i}\left(\gamma_{mi}\Delta x^2 + \beta_{mi}\Delta x'^2 + 2\alpha_{mi}\Delta x\Delta x'\right), \tag{6.45}$$

where the first term is due to mismatch and the second is due to the offsets. This is similar to the expression derived in Ref. [118]. We now consider the case where the beam starts matched to the plasma ($\alpha_{mi} = 0$) and has only a positional offset, i.e., $\Delta x' = 0$. In this case, the emittance growth comes only from one term,

$$\frac{\epsilon_{\rm sat}}{\epsilon_i} = 1 + \frac{\Delta x^2}{2\sigma_{mi}^2}, \tag{6.46}$$

where σ_{mi} is the matched spot size at the plasma entrance. If we neglect acceleration, then $\epsilon_N = \gamma\epsilon$ and thus the ratio $\epsilon_{\rm sat}/\epsilon_i = \epsilon_{N,{\rm sat}}/\epsilon_{N,i}$. This can be applied to an adiabatic ramp that is carefully designed so that the beam starts matched at the plasma entrance and is also matched when it reaches the plateau, i.e., $\alpha_m(z) \sim \sin(\pi z/L)$. We show the results in Fig. 6.4. We see the projected centroid vanishes due to the amplitude suppression of the ramp and the phase mixing caused by energy spread, and the normalized emittance saturates to the predicted value. Thus, an adiabatic ramp can reduce the offset and preserve the emittance if the beam is matched and has a small energy spread.

This chromatic phase mixing of the beam leading to the vanishing of its centroid may seem very useful to control the hosing instability and indeed it is for controlling hosing of the drive beam as explained in Ref. [98]. But in order to align a witness beam in the LC regime in a single stage, a moderate to large energy spread would be needed. However, in many applications, including a LC, having a moderate or large energy spread on the witness beam to damp the projected beam centroid and mitigating hosing can be problematic. Low energy spreads are required to suppress chromatic effects in conventional beam lines between stages and at the final focus. For this reason, we need to properly load the beams so that the energy spread remains below a percent. We thus propose to take advantage of ion motion

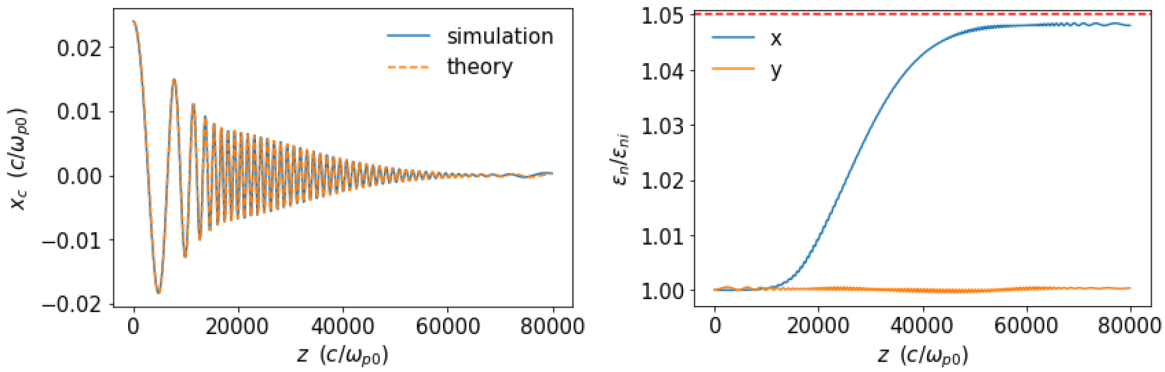

(a) (b)

Figure 6.4: (a) Beam centroid evolution and (b) slice emittance growth (dashed line is the predicted saturated value) in beam slice simulations with a sinusoidal adiabatic density ramp and FACET-II like beams. The witness beam is offset $\Delta x = \sigma_m$ and has initial energy spread $\sigma_\gamma/\bar{\gamma} = 2\%$. The ramp length is $2 \times 10^4\, k_{p0}^{-1}$ and the plateau length is $4 \times 10^4\, k_{p0}^{-1}$. Plots made by Yujian Zhao [93].

induced by the drive beam to control hosing of the witness beam as discussed earlier in this chapter.

However, one interesting idea would be to use a LC class witness beam with a finite uncorrelated energy spread only at the head of the beam. The drive beam would be low density so as to not cause ion motion. Then, in the plateau, the witness beam head would realign due to the phase mixing caused by its energy spread. The beam would then self-align behind the head as described previously. In Fig. 6.5, we show a beam slice simulation using the quasi-adiabatic ramp from Sec. 6.2.1. This shows the head slice of the witness beam with parameters from Sec. 6.2.3, and offset of the linearly matched spot size in the plateau $x_{bi} = \sigma_{m,0}$, and an uncorrelated energy spread, $\sigma_\gamma/\bar{\gamma}$, of 3% and 5%. We see the oscillation is damped within the plateau in both cases. We describe these beam slice simulations with ramps in greater detail in Sec. 6.5. This idea may be studied in the future with full QPAD simulations and compared to the scheme with drive beam ion motion as the realignment

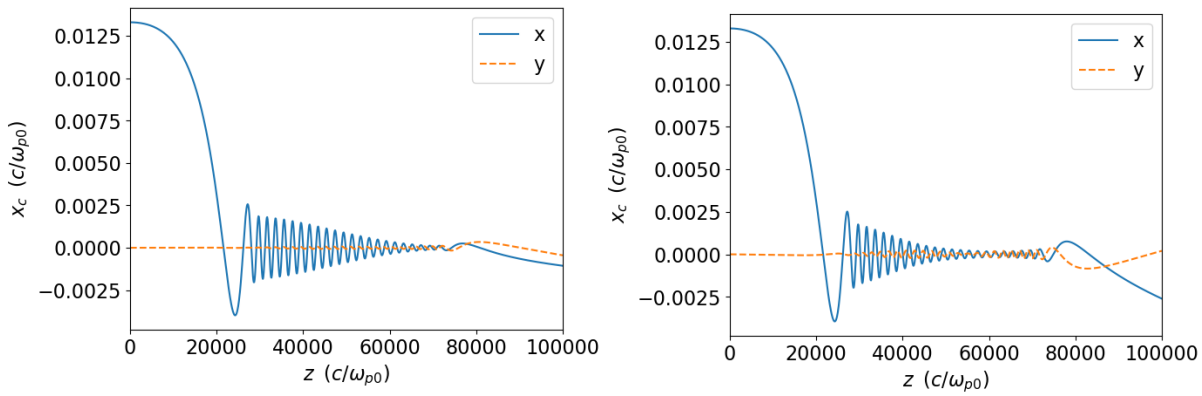

(a) (b)

Figure 6.5: Beam slice simulations using a quasi-adiabatic ramp with $\alpha_{mi} = 1$ and a beam slice with LC parameters, an initial offset of $x_{bi} = \sigma_{m,0}$ and uncorrelated energy spreads of (a) $\sigma_\gamma/\bar{\gamma} = 0.03$ and (b) $\sigma_\gamma/\bar{\gamma} = 0.05$. The focusing force is unperturbed (linear).

mechanism we present later. However, these witness beams with energy spreads at the head slice only may be difficult to create in reality.

6.3.3 Linear collider stage with a precursor

A precursor beam placed in front of the drive beam could limit drive beam head erosion, potentially allowing us to use low density drive beams for many of the stages in a PWFA-LC design. In this case, when the witness beam is misaligned and there is ion motion, it will oscillate in the plateau with constant amplitude (the initial offset will be decreased by the ramp and hosing will be suppressed). However, in the downramp this amplitude would be amplified. In theory, one could propagate these oscillating beams through all the plasma stages until the final one, where a higher density drive beam could be used for realignment. However, a major challenge would be propagating these beams with offsets between stages and aligning them with the drive beams of the next stages. It should be noted that the transverse momentum needs to be reversed between each stage with the adiabatic ramp design because it starts with $\alpha = 1$ and ends with (approximately) $\alpha_m = -1$. If the

propagation of misaligned beams can be done effectively between stages then this design may be preferred.

Another potential concern is the betatron radiation emitted by the oscillating beam. We can approximate the power radiated from an oscillating beam using the relativistic Larmor formula

$$P = \frac{2e^2\gamma^4}{3c^3}a_\perp^2, \tag{6.47}$$

where $a_\perp$ is the transverse acceleration. We assume the beam is oscillating at a fixed frequency k_β and amplitude X_b, so we have

$$a_\perp = -k_\beta^2 X_b \cos(k_\beta s). \tag{6.48}$$

The average acceleration over a period is

$$\langle a_\perp^2 \rangle = -k_\beta^4 X_b^2 \langle \cos^2 k_\beta s \rangle = \frac{1}{2}k_\beta^4 X_b^2, \tag{6.49}$$

so we have

$$\langle P \rangle = \frac{e^2\gamma^4 k_\beta^4 X_b^2}{3c^3} = \frac{r_e mc^3 \gamma^2 k_p^2 (k_p X_b)^2}{12}, \tag{6.50}$$

where r_e is the classic electron radius. To calculate the rate of energy loss, we simply divide by the speed of light to obtain

$$\frac{\mathrm{d}W_{\mathrm{loss}}}{\mathrm{d}z} = \frac{r_e mc^2 \gamma^2 k_p^2 (k_p X_b)^2}{12} = 4.25 \times 10^{-13} \gamma^2 (k_p x_\beta)^2 n[10^{14}\ \mathrm{cm}^{-3}]\ \mathrm{GeV/m}. \tag{6.51}$$

We can now compare this to the engineering formula for the maximum energy gain in a nonlinear wake (Eq. 1.3)

$$\frac{\mathrm{d}W_{\mathrm{gain}}}{\mathrm{d}z} = 0.96\sqrt{n[10^{14}\ \mathrm{cm}^{-3}]}\ \mathrm{GeV/m}, \tag{6.52}$$

to obtain

$$\frac{\mathrm{d}W_{\mathrm{loss}}}{\mathrm{d}W_{\mathrm{gain}}} = 4.43 \times 10^{-13} \gamma^2 (k_p X_b)^2 \sqrt{n[10^{14}\ \mathrm{cm}^{-3}]}. \tag{6.53}$$

Assuming a plasma density of $n_p = 10^{17}$ cm^{-3}, a beam energy of 1 TeV, an offset of $X_b = \sigma_{x,0} = 0.0133\ c/\omega_p$, the rate of energy loss to gain is $dW_{\rm loss}/dW_{\rm gain} \sim 1\%$. So this will not be a major concern for PWFA-LCs until the beam energy approaches $\gtrsim 5$ TeV.

We carry out a simulation using the same quasi-adiabatic plasma ramp and beam parameters from Sec. 6.2.2, namely a witness beam with $\epsilon_N = 100$ nm and a low density drive beam, however we use a lithium plasma (we will discuss higher mass ions in Sec. 6.4.3) with density $n_0 = 10^{17}$ cm^{-3}. The precursor beam is designed to blowout the initial plasma electrons, while not significantly altering the wake or causing ion motion. The precursor has an energy of 25 GeV and it is located 67.2 μm in front of the drive beam center. It has charge $Q = 0.13$ nC, spot size $\sigma_r = 2.52\,\mu$m, length $\sigma_z = 8.4\,\mu$m, and normalized emittance $\epsilon_N = 59.1\,\mu$m in the plasma density plateau. The precursor is also matched to the plasma entrance. The witness beam has a uniform offset $\Delta x = \sigma_{m,0} = 223$ nm, where $\sigma_{m,0}$ is the linearly matched spot size in the density plateau. The results are shown in Fig. 6.6. We can see similar dynamics to the idealized beam slice case shown in Fig. 6.3a. Specifically, the amplitude is suppressed by the upramp, remains constant in the plateau, but then grows again in the downramp. Recall in the beam slice case, the offset and the offset velocity by the end of the first stage depend on the phase of the oscillation as it enters the downramp. However, the offset returns to its initial value (with no velocity) by the end of the second stage.

6.3.4 Witness beam realignment stage

We are now in a position to put all the pieces together. We can use quasi-adiabatic density ramps to match LC class beams to the plasma in the presence of ion motion, while significantly compressing the initial witness beam offset. In the upramp, the ion motion will be gradually triggered and the focusing forces will gradually become nonlinear. As described in Sec. 5.5.2, the ions driven to the axis by the drive beam will cause an on-axis nonlinear focusing force at the witness beam head and therefore the head of the witness beam will

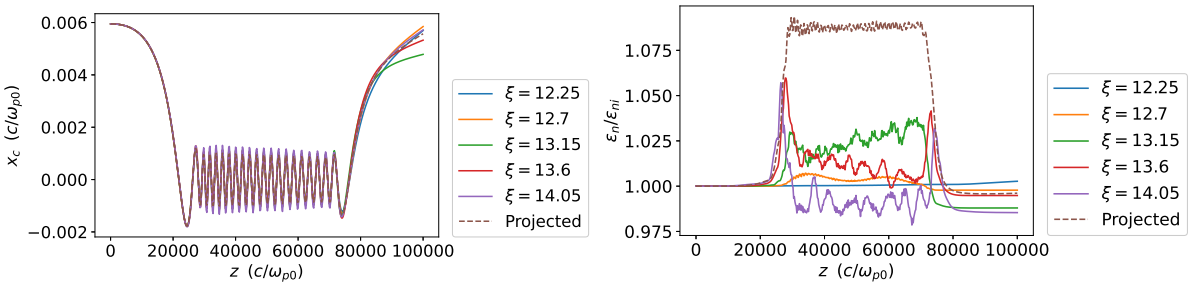

(a) (b)

Figure 6.6: Adiabatic ramp simulation with a precursor beam and a low density driver. (a) Beam centroid evolution (b) Normalized emittance evolution. The emittance decreases because it is transferred to the y direction which has around $\sim 2\%$ emittance growth.

slowly phase mix and become realigned with the drive beam (with no energy spread). The subsequent beam slices will be realigned due to the focusing force center being located between the beam center and the axis, i.e., the average focusing force tends to bring the beam to the axis. This process starts in the adiabatic upramp where the beam slowly adjusts itself to the evolving nonlinear forces while its oscillation damps. The remaining centroid oscillation will damp in the plateau.

We carry out the same simulation as in Sec. 6.2.3, but with a uniform initial witness beam offset, $\Delta x = \sigma_{m,0} = 223$ nm $= 0.0133\ c/\omega_{p0}$, where $\sigma_{m,0}$ is the linearly matched spot size in the density plateau. The evolution of the witness beam spot size, centroid, and emittance are shown in Figs. 6.7b, 6.7c, and 6.7d, respectively. It can be seen that the witness beam centroid is reduced by 95% by the beginning of the plateau. The final projected centroid at the end of the downramp is $|x_b/\sigma_m| = 0.01$. The beam tail centroid is amplified in the downramp to $|x_{b,\mathrm{tail}}/\sigma_m| = 0.09$. The tail oscillations are mostly due to the halo particles, not from within the beam core. This small downramp amplification of the tail may be mitigated by using a smoother (non-adiabatic) downramp, as will be demonstrated in Sec. 6.5. We correspondingly see a much larger slice emittance growth in the tail slice,

although this tail slice represents a small fraction of the total beam charge. The projected emittance growth in the upramp arises because the phase space distributions in each slice become non-Gaussian and their phase space ellipses do not overlap. Some of this growth can therefore be reversed in the downramp as the slices revert back to Gaussian and therefore overlap again [114]. The projected emittance growth by the end of the stage is 4.4%. Due to the trapezoidal current profile of the witness beam, the energy spread is limited to $< 1\%$ and the drive-to-witness energy transfer efficiency is $\sim 50\%$.

This realignment stage is an important tool that we can use to control the stability of the beam transport in multi-stage PWFA-LC designs, with minimal emittance growth while maintaining low energy spread and high energy transfer efficiency. Because the emittance growth is still very modest for this stage, it may be preferable to use these stages for every stage instead of using precursor stages. This would depend on the emittance growth in stages with even lower emittance witness beams, which we will discuss in the next section.

6.4 Other witness beam realignment scenarios

We have described the physics of beam matching and realignment in the LC regime. In this section, we will review different parameter regimes including even smaller emittance witness beams, drive beam densities, and higher mass ion species. As we will show, these scenarios generally have higher emittance growth compared to the previous section, but may be required if smaller emittance or higher energy beams are desired, which will be a topic for future studies. First, we discuss witness beam realignment in the more forgiving FACET-II regime (with 1 μm emittances), where the witness beam does not have as strong of an affect on the ion motion. In other words, the nonlinear focusing forces will primarily remain centered on-axis. This regime is where near future experiments may operate. At the end of this chapter, we discuss the implications of the ionization of higher charge states by intense LC beams and we present beam slice simulation scans to explore the effects of different ramp

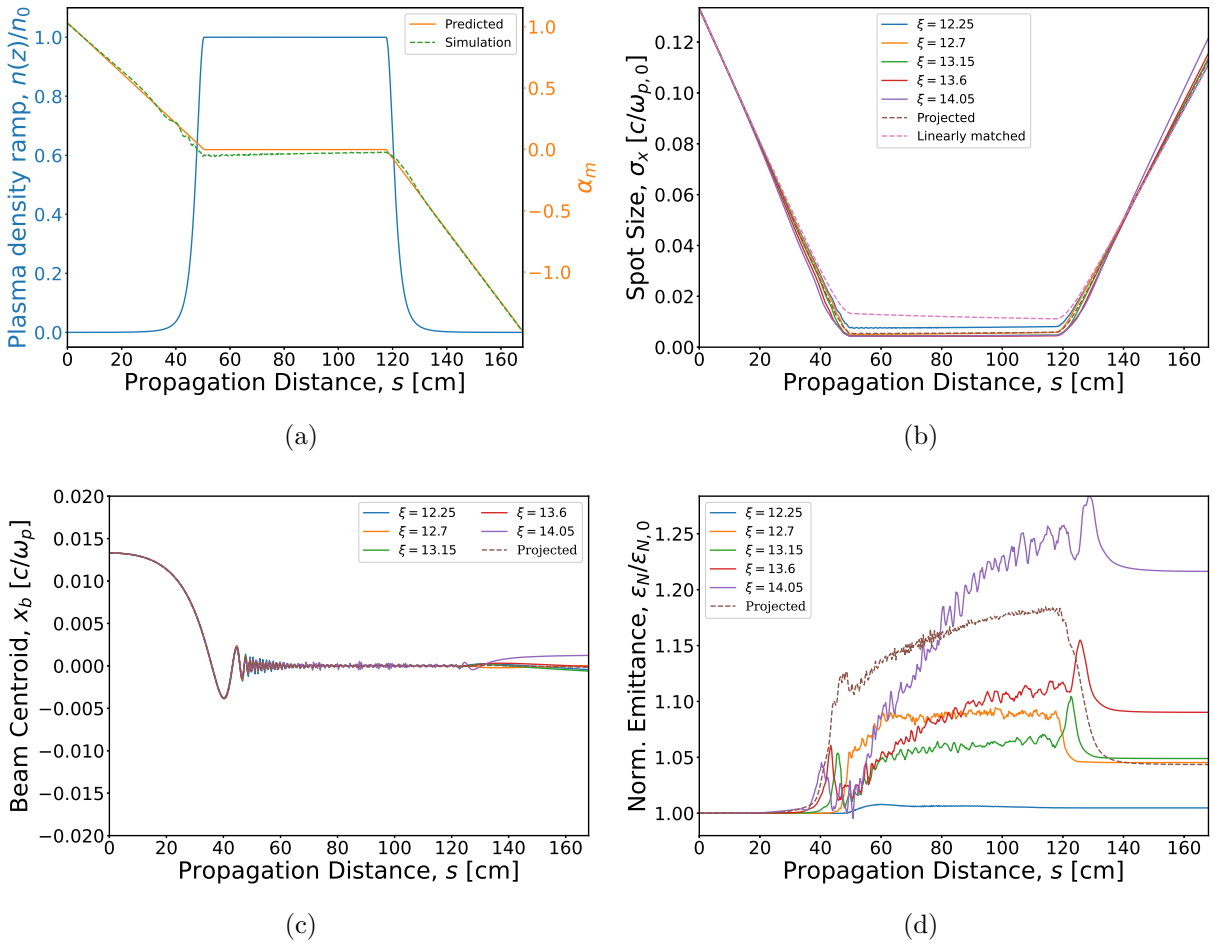

Figure 6.7: (a) Adiabatic plasma density ramp with the expected and simulated adiabatic parameter, α_m. The expected α_m is calculated using $\alpha_m = -\frac{1}{2}\frac{d}{dz}\beta_m(z)$ and $\beta_m(z) = \sqrt{2\gamma}c/\omega_p(z)$, where γ is taken from simulation. (b) Witness beam spot size evolution. The linearly matched spot size uses γ from the simulation and assumes constant emittance. The actual spot size is smaller than this because of ion motion. (c) Witness beam centroid evolution. (d) Projected normalized emittance growth.

profiles and beam misalignments.

6.4.1 FACET-II like parameters with adiabatic matching sections

In Sec. 5.5.1, we discussed the FACET-II regime with 1 μm normalized emittances (close to LC regime), where the drive beam ion motion is weakly perturbed by the witness beam. The parameters for this regime are listed in Sec. 5.5.1 (the witness beam is offset $\Delta x = 1\,\mu$m). In a uniform hydrogen plasma (with no matching section), the witness beam is quickly realigned but with over 200% emittance growth, which we could roughly predict. We now demonstrate the effect of an adiabatic matching section for this scenario.

In this case, we assume the beam starts matched to the plasma entrance and reaches the plateau matched to the plasma, so we choose to model α_m in the upramp with a sine, namely

$$\alpha_m = A\sin(\pi z/L), \tag{6.54}$$

where A is the peak value and should be less than one. The corresponding plasma density is

$$\frac{n(z)}{n_0} = \frac{1}{\left(1 + \dfrac{2AL}{\pi\beta_{m0}}\left(1+\cos(\pi z/L)\right)\right)^2}. \tag{6.55}$$

Evaluating the expression at the plasma entrance and solving for A, we get

$$A = \frac{\pi\beta_{m0}}{4L}\left(\frac{1}{\sqrt{n_i/n_0}} - 1\right). \tag{6.56}$$

The drive and witness beams start at 10 GeV, so $\beta_{m0} = 200$, and choosing $n_i/n_0 = 0.01$ and $L_{\rm ramp} = 15,000$, we get $A = 0.094$. The plateau length is $L_{\rm plateau} = 10,000$ (this can be longer for acceleration to pump depletion, but the physics we are demonstrating isn't affected). This beam ramp was designed for these beam parameters by Yujian Zhao [93].

The results of this simulation are shown in Fig. 6.8. The emittance growth is dramatically reduced from the uniform plasma case, as expected. We see the centroid is completely eliminated in this regime. With these parameters, we decided to use the overfocused regime,

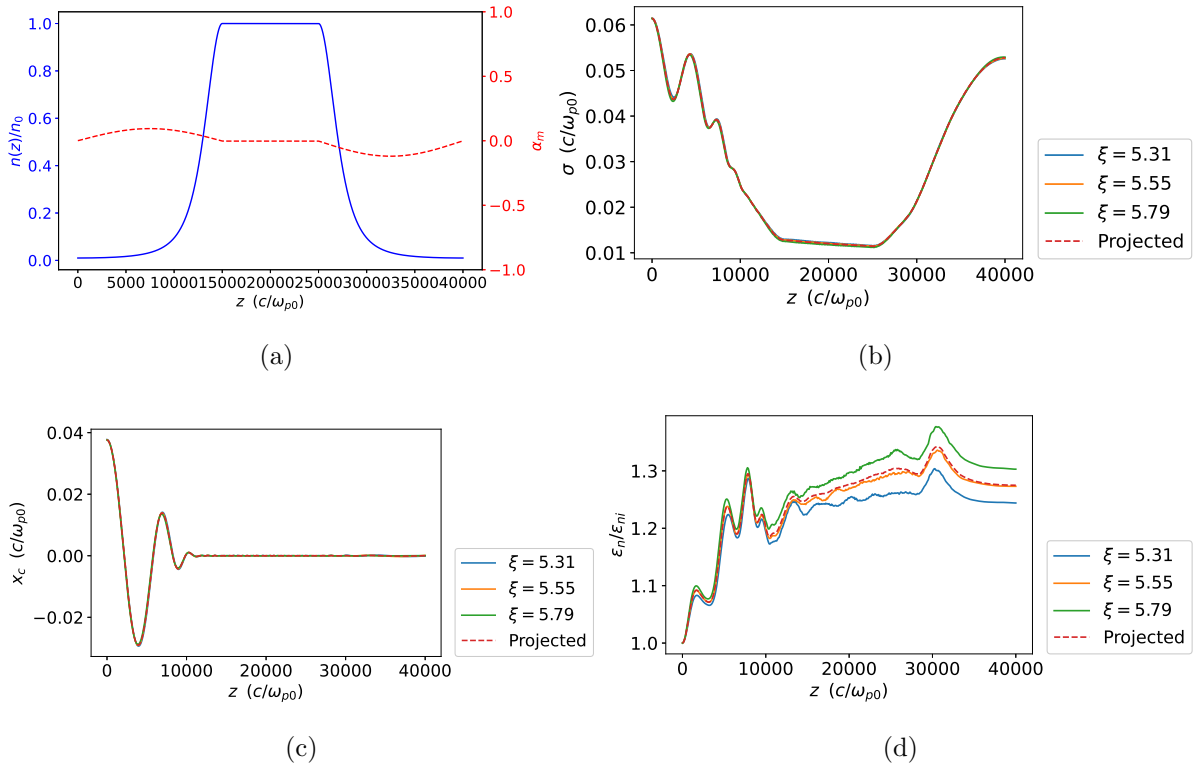

Figure 6.8: Witness beam realignment stage for FACET-II like parameters with a one micron initial emittance. (a) Adiabatic plasma density ramp and α_m design. Witness beam (b) spot size (c) centroid and (d) normalized emittance evolution.

where the drive beam first focuses the ions to the axis before the witness beam. The ion density remains roughly constant (and on-axis) along the witness beam. We found that the longer and higher current witness beams needed in the LC regime are able to move the ions off axis. We found it was more natural to work in the underfocused regime for hydrogen plasmas. We explore this further in the next sections.

6.4.2 Smaller drive beam density

In the previous section, we found a drive beam density of $n_{b,d} = 100$ create an ion density peak value of $A_0 \approx 10$ at the witness beam head, which damp its oscillation early in the

density plateau. Here, we present a simulation with a lower drive beam density of $n_{b,d} = 70$ (all other parameters the same as the previous section) to examine if we can reduce the ion density and therefore the nonlinearlity in the focusing force the witness beam experiences and thus its emittance growth further. In this case, the ion density at the witness beam head is around $A_0 \approx 4$. The results are shown in Fig. 6.9. Although the emittance growth is small, the centroid is not damped and we can see it grows to almost the initial value at the end of the second stage, similar to what we saw in the precursor simulation. Evidently, the ion density at the witness beam was not large enough to phase mix the head slice. It may be possible to use a density between $n_{b,d} = 70 - 100$ to damp the beam slowly over the plateau and reduce the emittance growth. We have not undertaken these simulations due to their large computational costs. We leave more parameter scans and optimization for future work.

6.4.3 Plasmas with higher ion mass

Thus far, we have mostly focused on hydrogen plasmas. Using plasmas with higher ion masses will reduce the ion motion caused by a given beam, and generally lead to lower ion densities. In Ref. [110], lithium plasmas were shown to reduce the emittance growth dramatically, all else being equal, for ion motion caused by only the witness beam (ionization of higher levels of lithium was not explored). For drive beam induced ion motion with a misaligned witness beam, the conclusion is not as straightforward. As we discussed before, the ion motion caused by the drive beam can be focused in front of or behind the witness beam. The higher ion mass simply changes the density and spot size we must use to achieve either of these regimes. The biggest difference between hydrogen and higher ion mass species is in how the witness beam perturbs the ion density. In hydrogen, intense witness beams can quite easily pull the ions that are on the axis to its centroid, sometimes causing overshooting and complex dynamics which can cause large emittance growth. This is why we needed to utilize the underfocused regime, where a minimum amount of drive beam ion motion was provided

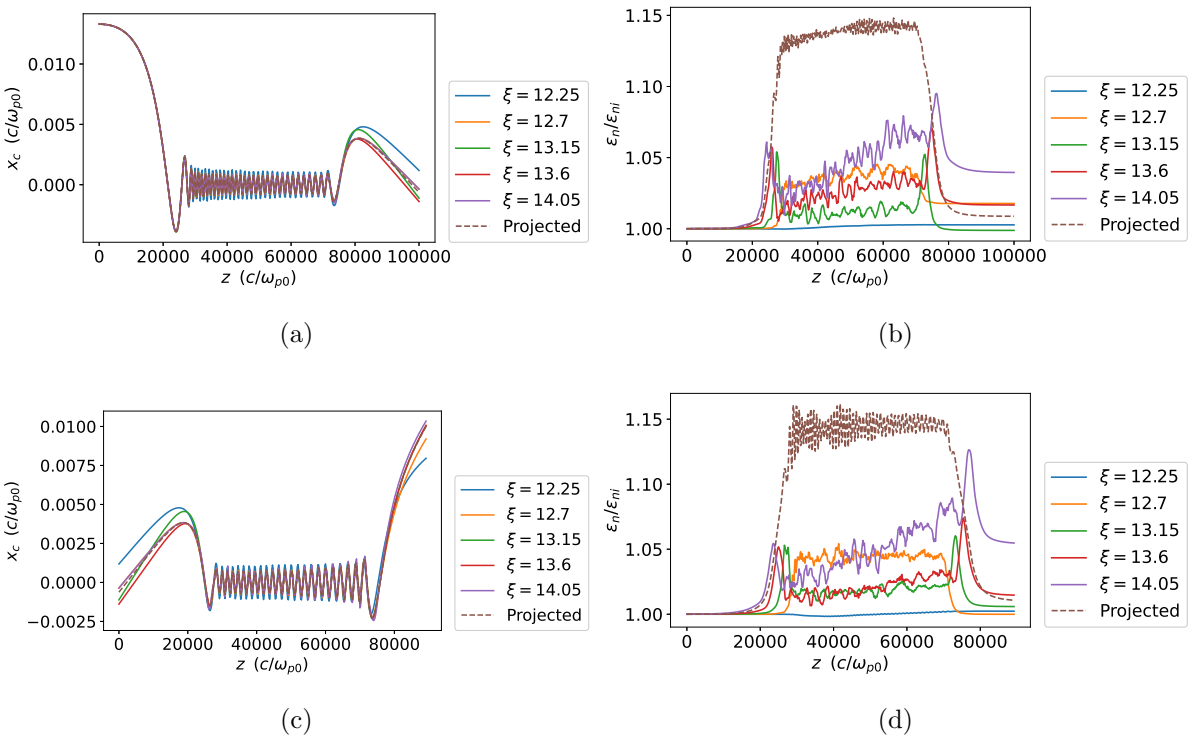

Figure 6.9: LC stage with drive beam density $n_{b,d} = 70$. (a) Centroid evolution and (b) normalized emittance growth in the first stage. We import the witness beam from the end of the first stage to the second stage and reverse the transverse momentum. (c) Centroid evolution and (d) Normalized emittance growth in the second stage.

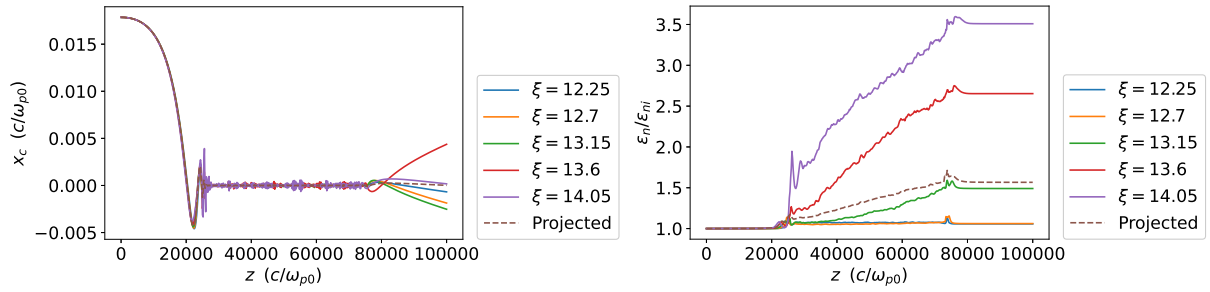

(a) (b)

Figure 6.10: Witness beam realignment stage with lithium plasma and 100 nm emittance witness beam with an initial offset of $\Delta x = 3\sigma_{m,0}$, and drive beam with density $n_{b,d} = 4000$. (a) Centroid and (b) normalized emittance evolution.

only to damp the head, and the rest of the beam aligns itself behind the head. However, in the FACET-II case, where the witness beam does not pull the ions off axis, we can use the overfocused case. With higher ion masses, it is possible to again use the overfocused regime because these ions will not be pulled off axis by the witness beam.

We consider a lithium plasma where the ions are approximately seven times as massive as hydrogen. The beam charges, energy, and profiles as well as the ramp parameters are the same as Sec. 6.2.3. But now the drive beam density is $n_{b,d} = 4000$ and the witness beam has spot size and normalized emittance of 100 nm and initial offset of $\Delta x = 3\sigma_{m,0}$. These beam parameters are much more extreme than Sec. 6.3.4. We can see in Fig. 6.10, the emittance growth ($\sim 50\%$) is much higher than the case from Sec. 6.3.4. The slice emittance growth is still very high for the tail slices, which may be a problem, if they continue to grow in later stages. We also see the centroid amplification effect of the downramp because there is some jitter of the tail slices in the plateau. This effect needs to be investigated further.

Next, we simulate a lithium plasma in the underfocused regime. The drive beam density is $n_{b,d} = 561$. At this density, the witness beam is not fully realigned in the first stage, as demonstrated in Fig. 6.11. Therefore, we import this beam to the second stage (reversing the

transverse momentum). We increase the length of the ramp, corresponding to the increase in energy (both the upramp and downramp, kept symmetric). By the end of the second stage, the beam is realigned. In the first stage, we see only a couple percent projected emittance growth, but in the second stage, we see emittance growth of a little over 20%. Thus, this scheme is preferable to the overfocused case, assuming the beam can be transported between stages in the prescribed fashion. Unless the oscillation after the first stage is very small, it may be difficult to align the drive beam for the second stage to the witness beam, as we have discussed previously. Thus, instead of slowing damping the beam centroid over many stages, in reality, more misalignments may be introduced in each stage defeating the purpose. The fact that the emittance growth is much smaller in the first stage implies that it may be advantageous to only use these stages every several stages as misalignments build up in order to keep them under a certain threshold. The final stages could include several of these stages back-to-back, similar to what we have shown here, to fully realign the beam before the final focus. Of course these designs would be constrained by the experimental tolerances and the beam transport systems between stages.

There is still a lot of room for optimization with higher mass ion species. Each scenario must be investigated separately because of the interplay between many different physical mechanisms we described in this chapter. It may be possible in the future to run these simulations much faster and more efficiently to scan parameters and minimize the emittance growth. For example, these speedups could be achieved by adding mesh refinement into QPAD and/or porting it to run on GPUs. It will be important to investigate the accumulation of emittance over several stages for these different schemes.

6.4.4 Ionization of higher charge states

In many recent studies of ion motion that considers higher ion mass plasmas, the potential further ionization of the plasma ions is not considered, as we have done in this section. But in reality, the witness beams required for LCs can easily ionize all levels lithium, as we can

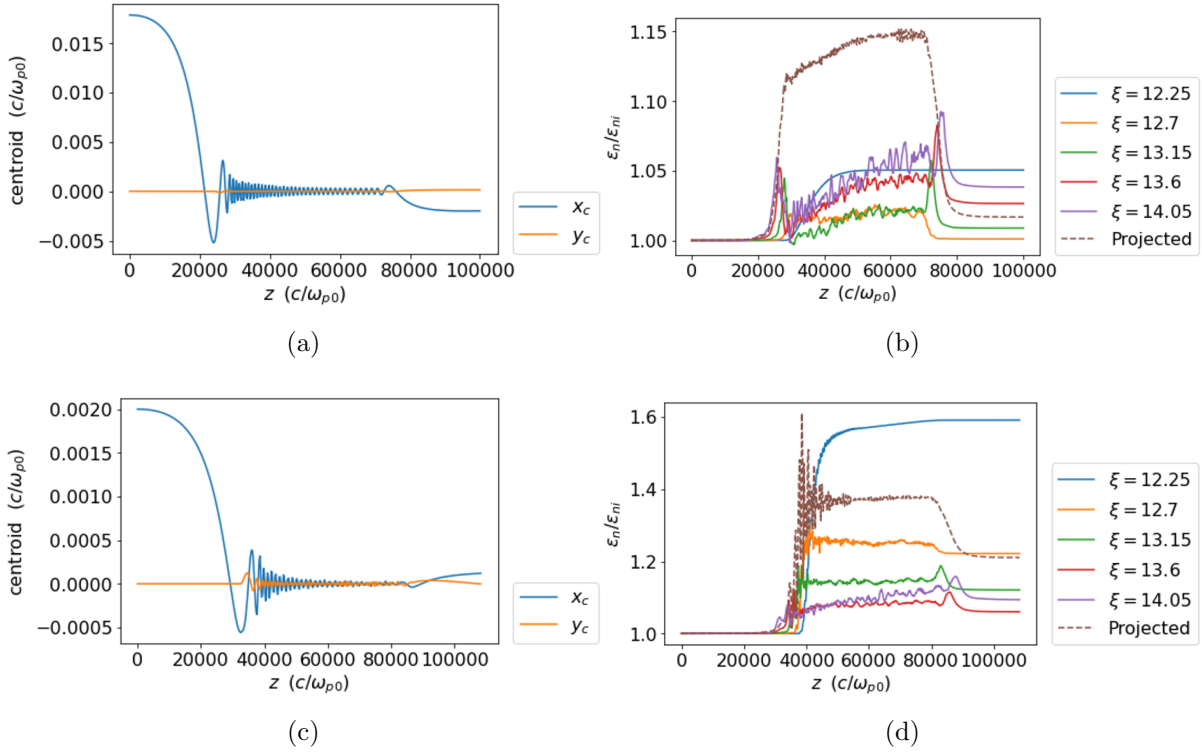

Figure 6.11: Two stage witness beam realignment scheme with lithium plasma with 100 nm emittance witness beam with initial offset $\Delta x = 3\sigma_{m,0}$, and drive beam with density $n_{b,d} = 561$. (a) Centroid and (b) normalized emittance evolution for the first stage. (c) Centroid (note the change of scale) and (d) normalized emittance evolution for the second stage.

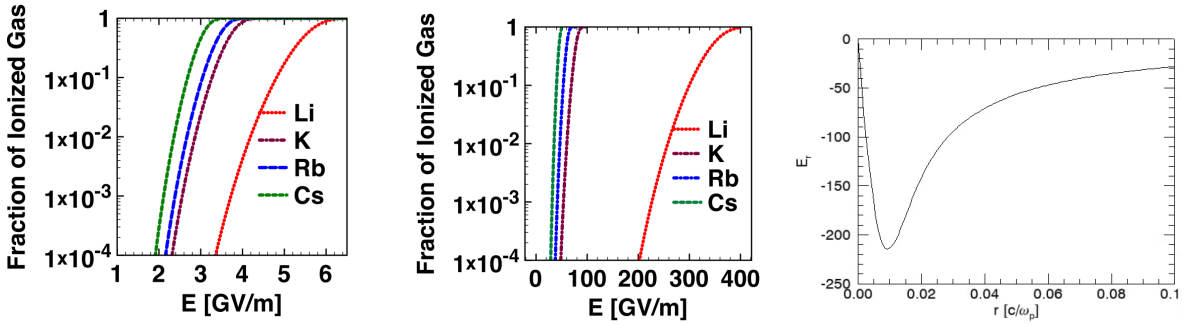

(a) 1st ionization (b) 2nd ionization (c)

Figure 6.12: (a), (b) Fraction of ionized gas vs electric field (assumed to be constant for 50 fs). Reproduced from [119]. (c) Radial electric field at the head of the 100 nm emittance witness beam (normalized units).

see in Fig. 6.12, noting the units of E_r are $mc\omega_p/e \approx 10\sqrt{n_p/10^{16}\ [\mathrm{cm}^{-3}]}$ [GeV/m] ≈ 31.6 GeV/m for $n_p = 10^{17}$ cm^{-3}.

If we wish to utilize these plasmas in future studies, it is crucial we study the effect of higher ionization of the plasma ions on the wakefields. Thus, we carry out single 3D timestep QPAD simulations with the parameters used in the previous section with the a lithium gas. We use a particle-based ionization method and allow all three levels of lithium to be ionized.

The preliminary results shown in Fig. 6.13 reveal a high ion density due to the extra ionization and a more complex transverse structure. Moreover, we see a large electron density in the witness beam region as a result of the ionization by the witness beam. These have a dramatic impact on the accelerating field experienced by the witness beam. This problem must be addressed in future studies.

Of course we can also use helium instead of lithium. It may also be possible to ionize both levels of helium using powerful lasers, so that the higher ionization by the witness beam is not an issue. This may be the most immediate area for future realignment stage designs for witness beams with $\epsilon_N \lesssim 500$ nm[1]. Many current designs and experiments are

[1]We have done a few simulations with helium but these show large emittance growth because the drive

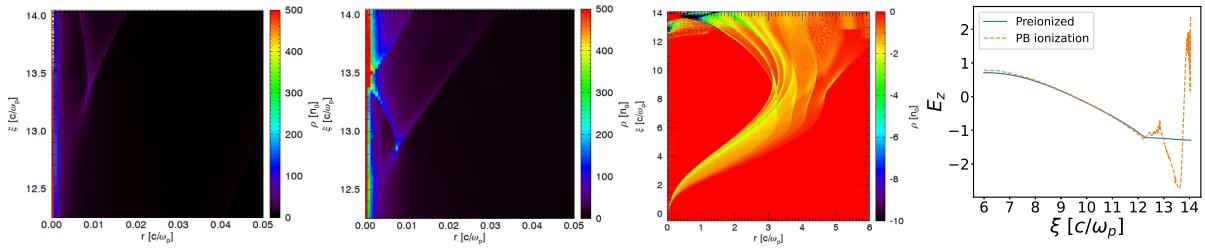

(a) (b) (c) (d)

Figure 6.13: (a) Preionized (1st level only) lithium plasma ion density in the witness beam region. (b) Particle-based ionization (all levels) of lithium gas - total ion density in the witness beam region. (c) Beam-ionized plasma wake. (d) Accelerating field for the preionized and the particle-based beam ionization cases.

considering lithium, but if these effects are substantial and unavoidable, it may be required to use helium or hydrogen instead for realignment stages. Finally, we note that this further ionization might be an approach for focusing positron beams in the ion channel.

6.5 Beam slice simulations with a prescribed focusing force

Full stage QPAD simulations with up to $m = 5$ azimuthal modes can be very computationally expensive, costing on the order of 10^5 core hours (around 3×10^4 core hours with no azimuthal modes). In the case with no beam offset, the dynamics are dominated by the beams evolution in the nonlinear focusing force. Therefore, much can be learned by evolving beam particles in the prescribed focusing force, as described earlier, to capture the transverse dynamics of a beam slice in a very simple and fast code. To model the evolution in a plasma density ramp, we can simply scale the ion density by the local plasma density, as done in Ref. [84]. Assuming the Gaussian model for the transverse ion profile we have,

$$n_{\rm ion}(r,z)/n_0 = n(z)/n_0 + A(z)\exp\left(-r^2/2\sigma_{\rm ion}\right), \tag{6.57}$$

beam density wasn't properly chosen.

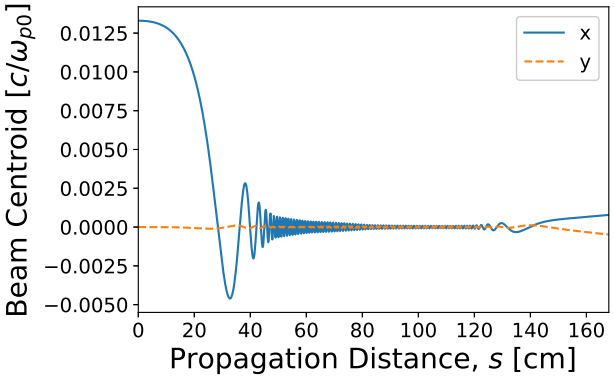

Figure 6.14: Centroid evolution for a beam slice in a prescribed focusing force corresponding to the ion density from Fig. 5.2d.

where

$$A(z) = A_0 \frac{n(z) - n(0)}{n_0 - n(0)}, \tag{6.58}$$

such that $A(0) = 0$. The focusing force is then

$$F_\perp(r, z) = -\frac{r}{2}\frac{n(z)}{n_0} - A(z)\sigma_{\text{ion}}^2 \frac{1 - e^{\frac{-r^2}{2\sigma_{\text{ion}}^2}}}{r}. \tag{6.59}$$

First, we can use this beam slice simulation to help predict the appropriate drive beam density for the underfocused regime in hydrogen. Recall that the head of the witness beam experiences the on-axis focusing force caused only by the drive beam ion motion, thus we can simulate the damping of the head slice with the beam slice simulation. With the beam parameters we presented in Sec. 6.3.4, we find $A_0 \approx 10$ to work well. Fig. 6.14 shows the centroid is suppressed in the upramp and then damps in the plateau. Of course to really capture the full physics of the realignment and resulting emittance growth one must run the full simulation, but this can be used for parameter scans to find feasible sets of parameters.

We can also use these beam slice simulations for the overfocused regime with lithium because the focusing force is mostly fixed on-axis. The simulations are very fast (typically a couple of minutes) so they lend themselves to parameter scans for testing various ramps and beam parameters. Thus, we scan the witness beam offset, initial centroid velocity, and

ramp length. The witness beam offset scan is shown in Fig. 6.15. The beam slice is aligned in the upramp even for very large offsets. The final emittance growth still scales roughly as $(\Delta x/\sigma_{mi})^2$, but with a small prefactor, so the emittance growth is relatively small even for large offsets. In Fig. 6.16, we see that if we instead initialize the beam slice with an initial average velocity, we still get realignment by the plateau with moderate emittance growth. Finally, Fig. 6.17 shows that the longer ramp, and therefore smaller α_{mi}, sees less emittance growth as expected, but there is not much effect on the realignment. Even very short ramps can realign in this regime. Long downramps can cause the beam oscillation amplitude to grow larger from the small oscillations in the plateau. Therefore, we present an additional simulation with a smoother downramp to see if this mitigates the issue. We use the 5th order polynomial ramp, given by Eq. 6.39, for the downramp and the adiabatic ramp with $\alpha_{mi} = 1$ for the upramp. In Fig 6.18, we see that the centroid growth in the downramp is suppressed, while the emittance growth is only marginally higher than the adiabatic downramp.

6.6 Summary

We have reviewed the design of plasma matching sections that use density ramps at the entrance and exit of the plasma to match the beam to the plasma so that it does not undergo spot size oscillations. In the ideal case with no ion motion or misalignment, the emittance will be preserved. We reviewed the solution to the Hill equation for single particle motion with varying k_β and the Courant-Snyder parameters used to characterized the beam distribution and phase space.

We reviewed the recent work [114] that showed quasi-adiabatic density ramps can match the beams (without offsets) to the plasma in the presence of strong ion motion with small emittance growth. This is due to the beam slowly adjusting itself to the nonlinear forces that become stronger as the beam propagates in the upramp. The beam can then be accelerated in the density plateau with minimal emittance growth and finally the beam will return to

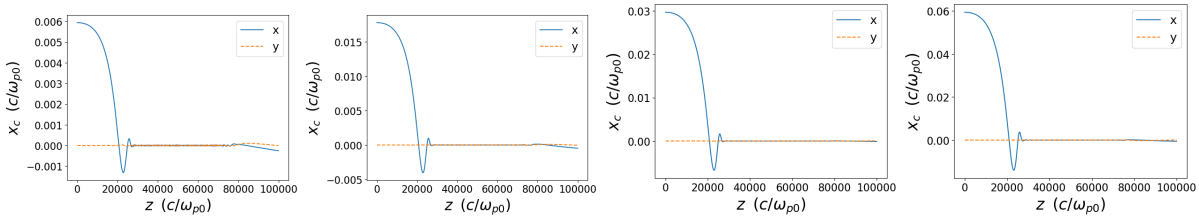

(a) $\Delta x = \sigma_m$ (b) $\Delta x = 3\sigma_m$ (c) $\Delta x = 5\sigma_m$ (d) $\Delta x = 10\sigma_m$

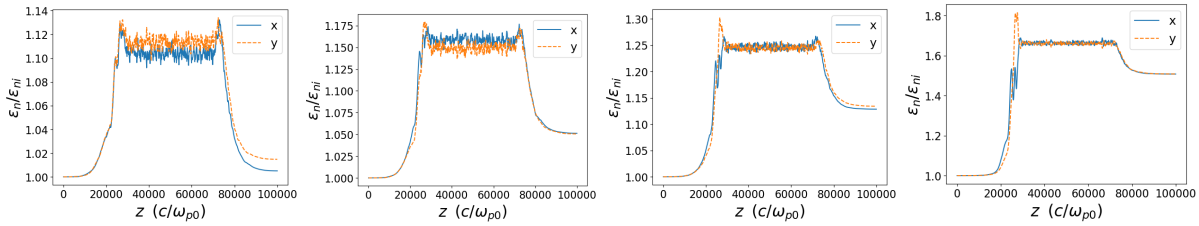

(e) $\Delta x = \sigma_m$ (f) $\Delta x = 3\sigma_m$ (g) $\Delta x = 5\sigma_m$ (h) $\Delta x = 10\sigma_m$

Figure 6.15: Beam slice simulation scan over witness beam offset for the lithium realignment simulation in Fig. 6.10. The ion model parameters are $A_0 = 332$, $\sigma_{\text{ion}} = 0.001$. (a)-(d) Centroid and (e)-(h) normalized emittance evolution.

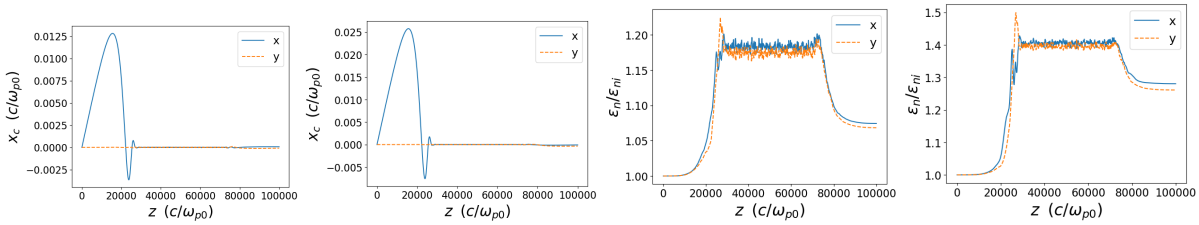

(a) $\Delta p_x = 0.05$ (b) $\Delta p_x = 0.1$ (c) $\Delta p_x = 0.05$ (d) $\Delta p_x = 0.1$

Figure 6.16: Beam slice simulations with initial average beam velocity for the lithium realignment simulation in Fig. 6.10. The ion model parameters are $A_0 = 332$, $\sigma_{\text{ion}} = 0.001$. (a)-(b) Centroid and (c)-(d) normalized emittance evolution.

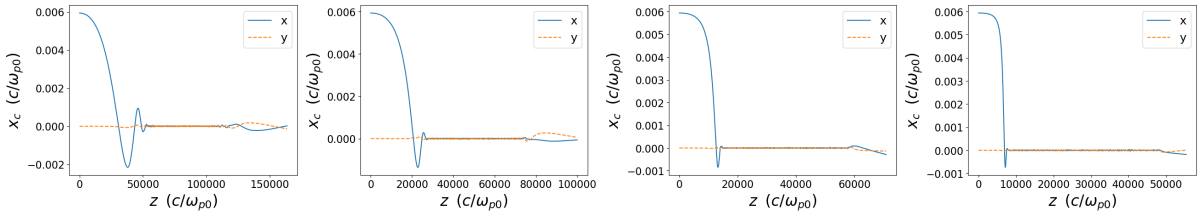

(a) $k_pL = 6 \times 10^4$ (b) $k_pL = 3 \times 10^4$ (c) $k_pL = 15 \times 10^3$ (d) $k_pL = 7.5 \times 10^3$

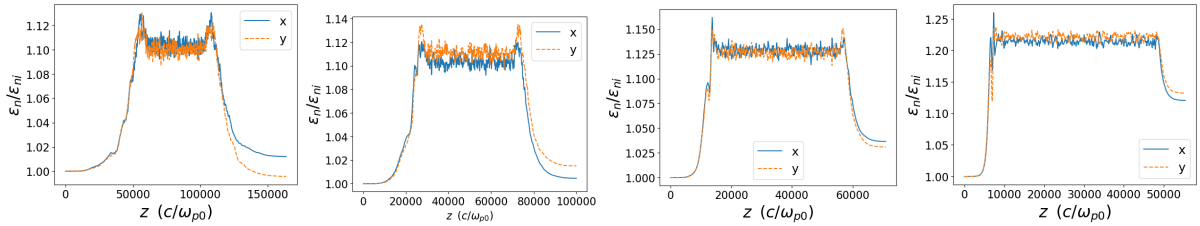

(e) $k_pL = 6 \times 10^4$ (f) $k_pL = 3 \times 10^4$ (g) $k_pL = 15 \times 10^3$ (h) $k_pL = 7.5 \times 10^3$

Figure 6.17: Beam slice simulation scan over ramp length for the lithium realignment simulation in Fig. 6.10. The α_{mi} is adjusted so that the n_i/n_0 is the same. $\alpha_{mi} = 0.5$, 1, 2, 4 for $k_pL = 6 \times 10^4$, 3×10^4, 15×10^3, 7.5×10^3, respectively. The ion model parameters are $A_0 = 332$, $\sigma_{\text{ion}} = 0.001$. (a)-(d) Centroid and (e)-(h) normalized emittance evolution.

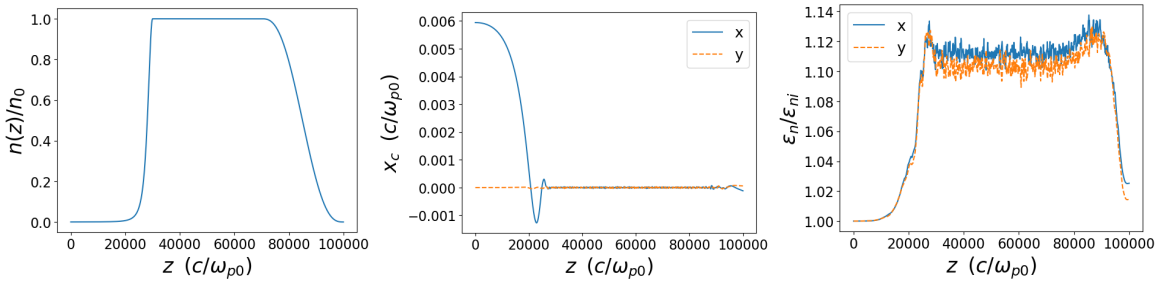

(a) (b) (c)

Figure 6.18: Beam slice simulation with polynomial downramp ($k_pL = 3{\times}10^4$) for the lithium realignment simulation in Fig. 6.10. The ion model parameters are $A_0 = 332$, $\sigma_{\text{ion}} = 0.001$. (a) Plasma density profile and (b) centroid and (c) normalized emittance evolution.

Gaussian in the density downramp. These ramps will be required for PWFA-LCs because conventional optics cannot transport the beams without large emittance growth.

We showed that with an evolving, higher density drive beam, these quasi-adiabatic ramps can still match the beams with small emittance growth $\sim 2\%$. We then showed how plasma density ramps will suppress the amplitude of beam centroid oscillations. We calculated the scaling of this suppression with ramp length for adiabatic ramps. This effect is reversed in the downramp if additional damping is not imparted. This suppression effect combined with the realignment due to the drive beam ion motion allows us to realign witness beams with very small emittance growth in the first stage of a PWFA-LC. With an offset of one matched spot size (in the plateau), we achieved an emittance growth of $\sim 4\%$ with witness beam realignment, for ~ 500 nm emittance beams. This stage provides an energy transfer efficiency of $\sim 50\%$, an average acceleration gradient (including the matching sections) of 15.8 GeV/m, while keeping the witness beam energy spread $< 1\%$. There is still room for optimization of this realignment stage. In later stages, this emittance growth will be larger if realignment is required, such as before the final focus. It may be possible to use these ideas in the design of a plasma-based final focus.

We presented other scenarios of witness beam realignment including FACET-II like parameters, a precursor with low density drive beam, and scenarios using a lithium plasma. We discussed the possibility of using heavier ion plasma species, which cause smaller ion densities but further complications. These may be necessary for realigning very small emittance beams. Finally, we discussed the issues with higher ionization by the witness beam and presented some single particle simulation parameter scans.

CHAPTER 7

Conclusion

This dissertation has explored several topics in the theory and simulation of plasma-based accelerators that will play an important role in understanding the nonlinear physics of the beam and plasma interactions in future experiments and applications such as plasma-based linear collider designs. Much of this research was enabled by advances in particle-in-cell codes that allow us to simulate extreme regimes over full plasma stages by using reduced models. The quasi-static approximation based PIC code, QPAD [80], was used extensively due to its very large speedups over full 3D PIC codes. Theoretical advancements were also inspired by the azimuthal decomposition used in QPAD. These reduced models will continue to be crucial in simulating and modeling the complex plasma physics in PWFA experiments at SLAC and in the design of PWFA-LCs.

In Chapter 2, we described the initial theoretical descriptions for nonlinear plasma wakefields given in Lu et al. [27, 28]. This phenomenological model describes the innermost plasma electron trajectory (blowout radius) by modeling the plasma electron sheath and calculating the pseudopotential ψ, which fully characterizes the wakefields. Using this theory for the blowout regime, both a beam loading theory [29, 30] and hosing theory [88] have been developed to describe two very important aspects of PWFA. Properly beam loading the wake is crucial to limit energy spread and increase energy transfer efficiency. The hosing instability must be understood and controlled because it is arguably the most devastating instability for PWFA, as it can cause beam loss, emittance growth, and alignment issues.

In Chapter 3, we expand on this theory of hosing in the blowout regime to more ac-

curately describe the instability in non-adiabatic, highly-relativistic regimes of interest to future experiments and LC applications. We found the $m = 1$ plasma sheath fields were crucial in understanding the plasma channel motion. However, a full, self-consistent description of $B_{\theta,1}$ (which appears explicitly in the plasma channel equation) was not found due to the need for a description of the perturbed plasma fields outside the bubble. In the future it may be possible to describe these fields using a perturbed current description, which will allow one to solve for the additive constant needed for $B_{\theta,1}$ at the blowout radius. For regimes with more complicated sheath structures in the back of the wake, it may be required to use a more accurate description such as Ref. [31] which allows for $\psi < 0$, as seen in simulations. We also described the structure of asymmetric wakes using an analogous theory but including $m = 2$ perturbations. In general, this was slightly less accurate than the results for hosing, but it is the first description of asymmetric wake structure which will be important for describing PWFA experiments and LC design where asymmetric beams may be used to avoid beamstrahlung at the final focus.

In Chapter 4, we discussed ways to mitigate the hosing instability. We discussed BNS damping in PWFA via direct energy variations in the beam and by variations of the focusing force along the beam. Although, the drive beams may be inherently stable, they can seed hosing of the witness beam. Witness beam stability can be controlled by direct energy chirps only if the chirp can be eliminated by underloading the wake or by dechirping after the stage. It is possible to design a witness beam profile to perfectly cancel the initial chirp for a given propagation distance. Although we have derived the profile for this scheme, it was not implemented into PIC simulations. This should be straightforward to study for different misalignments and initial chirps. Next, we looked at asymmetric drive beams as a way to mitigate witness beam hosing. This seems to be more effective for the parameters we studied. Although we were able to describe and explain the wake structure and mitigation mechanism, the details of drive beam evolution and optimal focusing variation was not rigorously explored. These different mitigation methods could be used together and full

plasma stages can be simulated to test offset tolerances. The main reason we did not pursue some of these research routes was the realization that in regimes with high current, tightly focused beams ion motion will dominate the transverse beam dynamics. Of course these mitigation methods will still be very useful for other regimes and applications, especially for current PWFA experiments that have large asymmetries and misalignments.

In Chapter 5, we discuss the basic physics of ion motion in PWFA. The possibility of ions moving within the transit time of a matched beam was first explored in Ref. [108] and the possibility that this would lead to significant emittance growth was described in Ref. [109]. The ion collapse and the emittance growth of the witness beam was quantified using theory and simulation in Ref. [110]. We first described the ion density collapse for a given electron beam and the resulting wakefields using a ring model. In the weak ion motion regime, our results reduce to the analytic model in Ref. [111], and in the regime of strong ion collapse where trajectories cross, the ring model becomes a reduced numerical model that can accurately reproduce PIC simulation results. We then expand on the theory of Ref. [110] to cases where the offset beam oscillates in a fixed nonlinear focusing force, which is the case when the drive beam causes ion motion. We showed how the witness beam phase space saturates to be centered on-axis (no centroid offset) with symmetric distributions in transverse phase space. However, this realignment and coupling between the two planes leads to emittance growth. Although the rough scalings were explained, a closed-form model including derivation of the conserved quantities is an area for future work.

In Chapter 6, we first discussed the concept of using quasi-adiabatic plasma density ramps to match LC class beams to the plasma with minimal emittance growth [114]. We then described how these matching sections can also reduce the offset between the drive and witness beam. Analytic expressions for the reduction in oscillation amplitude when the beam is propagating in the upramp were presented. If there is full suppression of hosing due to ion motion [104] in the density plateau (but not realignment), then for an anti-symmetric downramp at the exit, the misalignments will re-emerge. Therefore, it is necessary that

hosing not only be suppressed but that the witness beam aligns itself behind the drive beam in the plateau. Thus, we presented a scheme for witness beam realignment using drive beam ion motion. A drive beam density can be chosen such that a minimal amount of ion density at the witness beam head will eliminate its oscillations and subsequently the witness beam will self-align behind the head. We found that after the witness beam offset amplitude was decreased by $\sim$ 95% in the upramp, the ion motion could realign the beam with a very low final emittance growth by the end of the stage ($\sim$ 4% compared to almost 250% in a uniform plasma). This result shows the main two issues of PWFA-LCs can be overcome by combining drive beam ion motion and density ramps leading to a stable design for a single plasma stage. These ideas may also be used in the design of a plasma-based final focus. Moreover, we have assumed round beams in these simulations, but flat (very asymmetric) beams may be needed to avoid beamstrahlung. Studying how to produce very asymmetric beams would require using QuickPIC with mesh refinement [81] to provide enough speedup for full stage simulations. The realignment scheme we have suggested is a novel concept and so there is much room to explore. We have discussed the problems with higher ion mass species, but this may be overcome in the future. With more advancements in PIC codes and machine learning techniques, it will be possible to explore more parameters and optimize the beam parameters for smaller witness beam emittances.

This dissertation has focused on the electron arm of a PWFA-LC design. This may enable experiments with extreme beam parameters so that QED effects may be explored, potentially though beam-beam interactions [62] or via a $\gamma - \gamma$ collider [66, 68]. In order to explore the Higgs Boson, supersymmetry, and dark matter/energy, it is desirable to collide electrons and positrons. There are still many challenges associated with the positron arm of a PWFA-LC, however, recently there have been extensive research efforts exploring how to focus and accelerate positron beams in nonlinear blowout wakes [48, 49, 50, 51, 52, 53, 54, 55, 56]. These innovative ideas will soon be explored in experiments at SLAC and elsewhere. Experiments are underway to show emittance preservation in two-bunch PWFA scenarios to prove the

theoretical understanding amassed in the last couple decades. Soon, real beams will have high enough current to see ion motion in experiments and the work in this dissertation can be tested. The strong ties between theoretical models, high-fidelity PIC simulations, and experiments is what has led to the successes of plasma-based acceleration and will continue to do so in the future.

APPENDIX A

Beam loading theory to achieve a linear E_z

In this appendix, we calculate the beam longitudinal profile that results in a linear E_z for the witness beam using the theory from Tzoufras et al. [29]. This could be used to cancel a linear energy chirp in order to achieve a monoenergetic beam after some propagation distance, while invoking the BNS mechanism to mitigate beam hosing. More accurate profiles can be found using the improved beam loading theory of Dalichaouch et al. [31], but for our purposes the theory of Tzoufras et al. suffices.

In the witness beam region we want the accelerating field to have the form

$$E_z = -E_s - m(\xi - \xi_s), \tag{A.1}$$

where $m \equiv |\partial_\xi E_z|$, and the s subscript refers to the start of the witness beam. Using the ultra-relativistic blowout assumption, we have $E_z = r_b r_b'/2$. Setting this equal to the above equation and integrating both sides we obtain

$$r_b^2 = r_s^2 - 4E_s(\xi - \xi_s) - 2m(\xi - \xi_s)^2. \tag{A.2}$$

From the standard beam loading theory, we have

$$\frac{r_s^2}{4} = \sqrt{E_s^4 + \frac{R_b^4}{2^4}} - E_s^2, \tag{A.3}$$

where R_b is the maximum blowout radius. We also have

$$r_b r_b'' = -r_b'^2 - 2m, \tag{A.4}$$

and after substituting this into the differential equation for the blowout radius and rearranging terms, we obtain

$$\lambda(\xi) = \frac{r_b^2}{4}(1 + r_b'^2 - 2m). \tag{A.5}$$

We can substitute in the expressions for r_b and r_b' in terms of r_s and E_s into the above equation, yielding

$$\begin{aligned}\lambda(\xi) = \frac{r_s^2}{4}(1-2m) + E_s^2 + (2mE_s - E_s(1-2m))(\xi - \xi_s) \\ + (m^2 - (1-2m)m/2)(\xi - \xi_s)^2.\end{aligned} \tag{A.6}$$

Finally, upon using the expression for r_s and then simplifying, we obtain

$$\begin{aligned}\lambda(\xi) = (1-2m)\sqrt{E_s^4 + \frac{R_b^4}{2^4}} + 2mE_s^2 + (4m-1)E_s(\xi - \xi_s) \\ + \frac{m}{2}(4m-1)(\xi - \xi_s)^2.\end{aligned} \tag{A.7}$$

This is the beam profile that will result in the accelerating field having a negative slope m. We can immediately notice an interesting case: when $m = 1/4$, the beam current profile is a flat-top. Of course we recover the standard beam loading result when $m = 0$. The amount of charge that can be accelerated is

$$Q_s = 2\pi \int_0^{\hat{\xi}_f} d\hat{\xi}\, \lambda(\hat{\xi}) \tag{A.8}$$

$$= 2\pi \int_0^{\hat{\xi}_f} d\hat{\xi} \left[(1-2m)\sqrt{E_s^4 + \frac{R_b^4}{2^4}} + 2mE_s^2 + (4m-1)E_s\hat{\xi} + \frac{m}{2}(4m-1)\hat{\xi}^2\right] \tag{A.9}$$

$$= 2\pi \left[\left((1-2m)\sqrt{E_s^4 + \frac{R_b^4}{2^4}} + 2mE_s^2\right)\hat{\xi}_f + \frac{1}{2}(4m-1)E_s\hat{\xi}_f^2 + \frac{m}{6}(4m-1)\hat{\xi}_f^3\right], \tag{A.10}$$

where $\hat{\xi} \equiv \xi - \xi_s$ and

$$\hat{\xi}_f = \frac{1}{m}\left(\sqrt{E_s^2 + 2m\left(\sqrt{E_s^4 + R_b^4/2^4} - E_s^2\right)} - E_s\right), \tag{A.11}$$

for $m \neq 0$, which corresponds to the ξ where $r_b \to 0$. We plot the normalized profiles in Fig. A.1. We can see these profiles are very close to trapezoids, thus they can be approximated as such when trying to create these beams in practice.

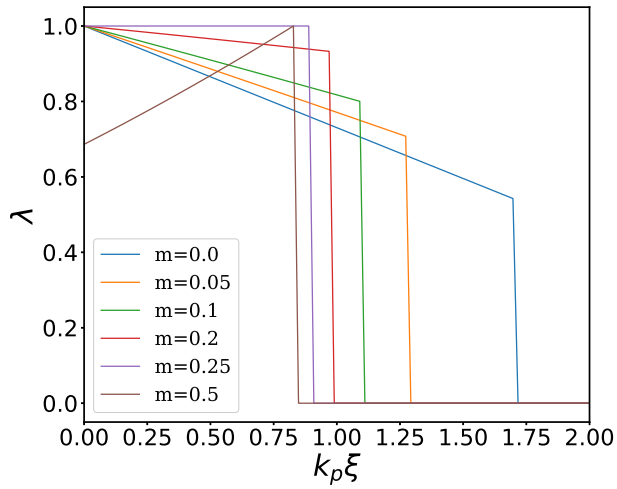

Figure A.1: Normalized profiles for beam loading that acquire different slopes $m \equiv \partial_\xi E_z$, over the beam region. $E_s = 2$ and $R_b = 5$ are used, ξ_s is set to zero.

A given chirp can be eliminated over some propagation distance, $k_p s$, as follows. The initial energy is

$$\gamma_0(\xi) = \gamma_{s,0} - m_\gamma(\xi - \xi_s), \tag{A.12}$$

where $m_\gamma \equiv \frac{(\Delta\gamma/\gamma_b)\gamma_b}{k_p L_b}$, $\Delta\gamma/\gamma_b$ defines the chirp (0.1 corresponds to a 10% chirp), and L_b is the beam length. The energy evolves according to

$$\gamma(\xi, s) = \gamma_{s,0} + E_s k_p s - (m_\gamma - m k_p s)(\xi - \xi_s), \tag{A.13}$$

where $m = \frac{(\Delta E/E_s)E_s}{k_p L_b}$. In order for the beam to remain monoenergetic, we want $m_\gamma - m k_p s = 0$, so the chirp will be eliminated after $k_p s = m_\gamma/m$. If, for example, we want the beam to be uniform longitudinally, we choose $m = 1/4$, and thus $k_p s = 4m_\gamma$. For a 10 GeV beam with a 10% chirp and length $k_p L_b = 1$, the chirp would be eliminated after $k_p s = 8000$. For a plasma density of $n_p = 4 \times 10^{16}$ cm^{-3}, this corresponds to about 20 cm. For $m = 0.1$, the chirp would be eliminated after about half a meter. Usually, the propagation distance is set by the pump depletion of the driver, so one could instead design the witness beam shape to remove the chirp needed to suppress hosing. For a propagation of one meter, the slope of E_z would need to be $m = 0.053$ for the beam parameters above.

REFERENCES

[1] https://home.cern/science/accelerators/large-hadron-collider.

[2] https://linearcollider.org.

[3] https://muoncollider.web.cern.ch.

[4] https://home.cern/science/accelerators/future-circular-collider.

[5] S. Dobert. RF-Breakdown in high-frequency accelerators. In *2004 IEEE Power Modulator Conference and 26th Power Modulator Symposium and 2004 High Voltage Workshop (PMC 2004)*, 5 2004.

[6] T. Tajima and J. M. Dawson. Laser electron accelerator. *Phys. Rev. Lett.*, 43:267–270, Jul 1979.

[7] P. Chen, J. M. Dawson, R. W. Huff, and T. Katsouleas. Acceleration of electrons by the interaction of a bunched electron beam with a plasma. *Phys. Rev. Lett.*, 54:693–696, Feb 1985.

[8] D. Strickland and G. Mourou. Compression of amplified chirped optical pulses. *Optics Communications*, 56(3):219–221, 1985.

[9] F. Amiranoff, S. Baton, D. Bernard, B. Cros, D. Descamps, F. Dorchies, F. Jacquet, V. Malka, J. R. Marquès, G. Matthieussent, P. Miné, A. Modena, P. Mora, J. Morillo, and Z. Najmudin. Observation of laser wakefield acceleration of electrons. *Phys. Rev. Lett.*, 81:995–998, Aug 1998.

[10] S. P. D. Mangles, C. D. Murphy, Z. Najmudin, A. G. R. Thomas, J. L. Collier, A. E. Dangor, E. J. Divall, P. S. Foster, J. G. Gallacher, C. J. Hooker, D. A. Jaroszynski, A. J. Langley, W. B. Mori, P. A. Norreys, F. S. Tsung, R. Viskup, B. R. Walton, and K. Krushelnick. Monoenergetic beams of relativistic electrons from intense laser-plasma interactions. *Nature*, 431(7008):535–538, Sep 2004.

[11] J. Faure, Y. Glinec, A. Pukhov, S. Kiselev, S. Gordienko, E. Lefebvre, J.-P. Rousseau, F. Burgy, and V. Malka. A laser-plasma accelerator producing monoenergetic electron beams. *Nature*, 431(7008):541–544, Sep 2004.

[12] C. G. R. Geddes, Cs. Toth, J. van Tilborg, E. Esarey, C. B. Schroeder, D. Bruhwiler, C. Nieter, J. Cary, and W. P. Leemans. High-quality electron beams from a laser wakefield accelerator using plasma-channel guiding. *Nature*, 431(7008):538–541, Sep 2004.

[13] W. P. Leemans, B. Nagler, A. J. Gonsalves, Cs. Tóth, K. Nakamura, C. G. R. Geddes, E. Esarey, C. B. Schroeder, and S. M. Hooker. Gev electron beams from a centimetre-scale accelerator. *Nature Physics*, 2(10):696–699, Oct 2006.

[14] N. A. M. Hafz, T. M. Jeong, I. W. Choi, S. K. Lee, K. H. Pae, V. V. Kulagin, J. H. Sung, T. J. Yu, K.-H. Hong, T. Hosokai, J. R. Cary, D.-K. Ko, and J. Lee. Stable generation of gev-class electron beams from self-guided laser-plasma channels. *Nature Photonics*, 2(9):571–577, Sep 2008.

[15] X. Wang, R. Zgadzaj, N. Fazel, Z. Li, S. A. Yi, X. Zhang, W. Henderson, Y.-Y. Chang, R. Korzekwa, H.-E. Tsai, C.-H. Pai, H. Quevedo, G. Dyer, E. Gaul, M. Martinez, A. C. Bernstein, T. Borger, M. Spinks, M. Donovan, V. Khudik, G. Shvets, T. Ditmire, and M. C. Downer. Quasi-monoenergetic laser-plasma acceleration of electrons to 2 gev. *Nature Communications*, 4(1):1988, Jun 2013.

[16] M. J. Hogan, R. Assmann, F.-J. Decker, R. Iverson, P. Raimondi, S. Rokni, R. H. Siemann, D. Walz, D. Whittum, B. Blue, C. E. Clayton, E. Dodd, R. Hemker, C. Joshi, K. A. Marsh, W. B. Mori, S. Wang, T. Katsouleas, S. Lee, P. Muggli, P. Catravas, S. Chattopadhyay, E. Esarey, and W. P. Leemans. E-157: A 1.4-m-long plasma wake field acceleration experiment using a 30 GeV electron beam from the Stanford Linear Accelerator Center Linac. *Physics of Plasmas*, 7(5):2241–2248, 05 2000.

[17] C. E. Clayton, B. E. Blue, E. S. Dodd, C. Joshi, K. A. Marsh, W. B. Mori, S. Wang, P. Catravas, S. Chattopadhyay, E. Esarey, W. P. Leemans, R. Assmann, F. J. Decker, M. J. Hogan, R. Iverson, P. Raimondi, R. H. Siemann, D. Walz, T. Katsouleas, S. Lee, and P. Muggli. Transverse envelope dynamics of a 28.5-gev electron beam in a long plasma. *Phys. Rev. Lett.*, 88:154801, Apr 2002.

[18] B. E. Blue, C. E. Clayton, C. L. O'Connell, F.-J. Decker, M. J. Hogan, C. Huang, R. Iverson, C. Joshi, T. C. Katsouleas, W. Lu, K. A. Marsh, W. B. Mori, P. Muggli, R. Siemann, and D. Walz. Plasma-wakefield acceleration of an intense positron beam. *Phys. Rev. Lett.*, 90:214801, May 2003.

[19] P. Muggli, B. E. Blue, C. E. Clayton, S. Deng, F.-J. Decker, M. J. Hogan, C. Huang, R. Iverson, C. Joshi, T. C. Katsouleas, S. Lee, W. Lu, K. A. Marsh, W. B. Mori, C. L. O'Connell, P. Raimondi, R. Siemann, and D. Walz. Meter-scale plasma-wakefield accelerator driven by a matched electron beam. *Phys. Rev. Lett.*, 93:014802, Jun 2004.

[20] M. J. Hogan, C. D. Barnes, C. E. Clayton, F. J. Decker, S. Deng, P. Emma, C. Huang, R. H. Iverson, D. K. Johnson, C. Joshi, T. Katsouleas, P. Krejcik, W. Lu, K. A. Marsh, W. B. Mori, P. Muggli, C. L. O'Connell, E. Oz, R. H. Siemann, and D. Walz. Multi-gev energy gain in a plasma-wakefield accelerator. *Phys. Rev. Lett.*, 95:054802, Jul 2005.

[21] I. Blumenfeld, C. E. Clayton, F.J. Decker, M.J. Hogan, C. Huang, R. Ischebeck, R. Iverson, C. Joshi, T. Katsouleas, N. Kirby, W. Lu, K. A. Marsh, W. B. Mori,

P. Muggli, E. Oz, R. H. Siemann, D. Walz, and M. Zhou. Energy doubling of 42 gev electrons in a metre-scale plasma wakefield accelerator. *Nature*, 445:741 EP –, Feb 2007.

[22] M. Litos, E. Adli, W. An, C. I. Clarke, C. E. Clayton, S. Corde, J. P. Delahaye, R. J. England, A. S. Fisher, J. Frederico, S. Gessner, S. Z. Green, M. J. Hogan, C. Joshi, W. Lu, K. A. Marsh, W. B. Mori, P. Muggli, N. Vafaei-Najafabadi, D. Walz, G. White, Z. Wu, V. Yakimenko, and G. Yocky. High-efficiency acceleration of an electron beam in a plasma wakefield accelerator. *Nature*, 515:92 EP –, Nov 2014.

[23] P. Chen, J. J. Su, T. Katsouleas, S. Wilks, and J. M. Dawson. Plasma focusing for high-energy beams. *IEEE Transactions on Plasma Science*, 15(2):218–225, 1987.

[24] T. C. Katsouleas, S. Wilks, P. Chen, J. M. Dawson, and J. J. Su. Beam loading in plasma accelerators. *Part. Accel.*, 22:81–99, 1987.

[25] J. B. Rosenzweig, B. Breizman, T. Katsouleas, and J. J. Su. Acceleration and focusing of electrons in two-dimensional nonlinear plasma wake fields. *Phys. Rev. A*, 44:R6189–R6192, Nov 1991.

[26] W. Lu, C. Huang, M. M. Zhou, W. B. Mori, and T. Katsouleas. Limits of linear plasma wakefield theory for electron or positron beams. *Physics of Plasmas*, 12(6):063101, 05 2005.

[27] W. Lu, C. Huang, M. Zhou, W. B. Mori, and T. Katsouleas. Nonlinear theory for relativistic plasma wakefields in the blowout regime. *Phys. Rev. Lett.*, 96:165002, Apr 2006.

[28] W. Lu, C. Huang, M. Zhou, M. Tzoufras, F. S. Tsung, W. B. Mori, and T. Katsouleas. A nonlinear theory for multidimensional relativistic plasma wave wakefields. *Physics of Plasmas*, 13(5):056709, 2006.

[29] M. Tzoufras, W. Lu, F. S. Tsung, C. Huang, W. B. Mori, T. Katsouleas, J. Vieira, R. A. Fonseca, and L. O. Silva. Beam loading in the nonlinear regime of plasma-based acceleration. *Phys. Rev. Lett.*, 101:145002, Sep 2008.

[30] M. Tzoufras, W. Lu, F. S. Tsung, C. Huang, W. B. Mori, T. Katsouleas, J. Vieira, R. A. Fonseca, and L. O. Silva. Beam loading by electrons in nonlinear plasma wakesa). *Physics of Plasmas*, 16(5):056705, 05 2009.

[31] T. N. Dalichaouch, X. L. Xu, A. Tableman, F. Li, F. S. Tsung, and W. B. Mori. A multi-sheath model for highly nonlinear plasma wakefields. *Physics of Plasmas*, 28(6):063103, 06 2021.

[32] K. Floettmann. Adiabatic matching section for plasma accelerated beams. *Phys. Rev. ST Accel. Beams*, 17:054402, May 2014.

[33] I. Dornmair, K. Floettmann, and A. R. Maier. Emittance conservation by tailored focusing profiles in a plasma accelerator. *Phys. Rev. ST Accel. Beams*, 18:041302, Apr 2015.

[34] Xiangkun Li, Antoine Chancé, and Phu Anh Phi Nghiem. Preserving emittance by matching out and matching in plasma wakefield acceleration stage. *Phys. Rev. Accel. Beams*, 22:021304, Feb 2019.

[35] X. L. Xu, J. F. Hua, Y. P. Wu, C. J. Zhang, F. Li, Y. Wan, C.-H. Pai, W. Lu, W. An, P. Yu, M. J. Hogan, C. Joshi, and W. B. Mori. Physics of phase space matching for staging plasma and traditional accelerator components using longitudinally tailored plasma profiles. *Phys. Rev. Lett.*, 116:124801, Mar 2016.

[36] R. Ariniello, C. E. Doss, K. Hunt-Stone, J. R. Cary, and M. D. Litos. Transverse beam dynamics in a plasma density ramp. *Phys. Rev. Accel. Beams*, 22:041304, Apr 2019.

[37] Y. Zhao, W. An, X. Xu, F. Li, L. Hildebrand, M. J. Hogan, V. Yakimenko, C. Joshi, and W. B. Mori. Emittance preservation through density ramp matching sections in a plasma wakefield accelerator. *Phys. Rev. Accel. Beams*, 23:011302, Jan 2020.

[38] C. A. Lindstrøm and M. Thévenet. Emittance preservation in advanced accelerators. *Journal of Instrumentation*, 17(05):P05016, may 2022.

[39] M. Chen, Z.-M. Sheng, Y.-Y. Ma, and J. Zhang. Electron injection and trapping in a laser wakefield by field ionization to high-charge states of gases. *Journal of Applied Physics*, 99(5):056109, 03 2006.

[40] E. Oz, S. Deng, T. Katsouleas, P. Muggli, C. D. Barnes, I. Blumenfeld, F. J. Decker, P. Emma, M. J. Hogan, R. Ischebeck, R. H. Iverson, N. Kirby, P. Krejcik, C. O'Connell, R. H. Siemann, D. Walz, D. Auerbach, C. E. Clayton, C. Huang, D. K. Johnson, C. Joshi, W. Lu, K. A. Marsh, W. B. Mori, and M. Zhou. Ionization-induced electron trapping in ultrarelativistic plasma wakes. *Phys. Rev. Lett.*, 98:084801, Feb 2007.

[41] A. Pak, K. A. Marsh, S. F. Martins, W. Lu, W. B. Mori, and C. Joshi. Injection and trapping of tunnel-ionized electrons into laser-produced wakes. *Phys. Rev. Lett.*, 104:025003, Jan 2010.

[42] S. Bulanov, N. Naumova, F. Pegoraro, and J. Sakai. Particle injection into the wave acceleration phase due to nonlinear wake wave breaking. *Phys. Rev. E*, 58:R5257–R5260, Nov 1998.

[43] H. Suk, N. Barov, J. B. Rosenzweig, and E. Esarey. Plasma electron trapping and acceleration in a plasma wake field using a density transition. *Phys. Rev. Lett.*, 86:1011–1014, Feb 2001.

[44] X. L. Xu, F. Li, W. An, T. N. Dalichaouch, P. Yu, W. Lu, C. Joshi, and W. B. Mori. High quality electron bunch generation using a longitudinal density-tailored plasma-based accelerator in the three-dimensional blowout regime. *Phys. Rev. Accel. Beams*, 20:111303, Nov 2017.

[45] A. Martinez de la Ossa, Z. Hu, M. J. V. Streeter, T. J. Mehrling, O. Kononenko, B. Sheeran, and J. Osterhoff. Optimizing density down-ramp injection for beam-driven plasma wakefield accelerators. *Phys. Rev. Accel. Beams*, 20:091301, Sep 2017.

[46] https://facet-ii.slac.stanford.edu.

[47] C. Joshi, E. Adli, W. An, C. E. Clayton, S. Corde, S. Gessner, M. J. Hogan, M. Litos, W. Lu, K. A. Marsh, W. B. Mori, N. Vafaei-Najafabadi, B. O'shea, X. Xu, G. White, and V. Yakimenko. Plasma wakefield acceleration experiments at facet ii. *Plasma Physics and Controlled Fusion*, 60(3):034001, 2018.

[48] S. Corde, E. Adli, J. M. Allen, W. An, C. I. Clarke, C. E. Clayton, J. P. Delahaye, J. Frederico, S. Gessner, S. Z. Green, M. J. Hogan, C. Joshi, N. Lipkowitz, M. Litos, W. Lu, K. A. Marsh, W. B. Mori, M. Schmeltz, N. Vafaei-Najafabadi, D. Walz, V. Yakimenko, and G. Yocky. Multi-gigaelectronvolt acceleration of positrons in a self-loaded plasma wakefield. *Nature*, 524(7566):442–445, Aug 2015.

[49] S. Gessner, E. Adli, J. M. Allen, W. An, C. I. Clarke, C. E. Clayton, S. Corde, J. P. Delahaye, J. Frederico, S. Z. Green, C. Hast, M. J. Hogan, C. Joshi, C. A. Lindstrøm, N. Lipkowitz, . Litos, W. Lu, K. A. Marsh, W. B. Mori, B. O'Shea, N. Vafaei-Najafabadi, D. Walz, V. Yakimenko, and G. Yocky. Demonstration of a positron beam-driven hollow channel plasma wakefield accelerator. *Nature Communications*, 7(1):11785, Jun 2016.

[50] A. Doche, C. Beekman, S. Corde, J. M. Allen, C. I. Clarke, J. Frederico, S. J. Gessner, S. Z. Green, M. J. Hogan, B. O'Shea, V. Yakimenko, W. An, C. E. Clayton, C. Joshi, K. A. Marsh, W. B. Mori, N. Vafaei-Najafabadi, M. D. Litos, E. Adli, C. A. Lindstrøm, and W. Lu. Acceleration of a trailing positron bunch in a plasma wakefield accelerator. *Scientific Reports*, 7(1):14180, Oct 2017.

[51] C. A. Lindstrøm, E. Adli, J. M. Allen, W. An, C. Beekman, C. I. Clarke, C. E. Clayton, S. Corde, A. Doche, J. Frederico, S. J. Gessner, S. Z. Green, M. J. Hogan, C. Joshi, M. Litos, W. Lu, K. A. Marsh, W. B. Mori, B. D. O'Shea, N. Vafaei-Najafabadi, and V. Yakimenko. Measurement of transverse wakefields induced by a misaligned positron bunch in a hollow channel plasma accelerator. *Phys. Rev. Lett.*, 120:124802, Mar 2018.

[52] S. Diederichs, T. J. Mehrling, C. Benedetti, C. B. Schroeder, A. Knetsch, E. Esarey, and J. Osterhoff. Positron transport and acceleration in beam-driven plasma wakefield accelerators using plasma columns. *Phys. Rev. Accel. Beams*, 22:081301, Aug 2019.

[53] S. Diederichs, C. Benedetti, E. Esarey, J. Osterhoff, and C. B. Schroeder. High-quality positron acceleration in beam-driven plasma accelerators. *Phys. Rev. Accel. Beams*, 23:121301, Dec 2020.

[54] S. Diederichs, C. Benedetti, M. Thévenet, E. Esarey, J. Osterhoff, and C. B. Schroeder. Self-stabilizing positron acceleration in a plasma column. *Phys. Rev. Accel. Beams*, 25:091304, Sep 2022.

[55] S. Zhou, J. Hua, W. An, W. B. Mori, C. Joshi, J. Gao, and W. Lu. High efficiency uniform wakefield acceleration of a positron beam using stable asymmetric mode in a hollow channel plasma. *Phys. Rev. Lett.*, 127:174801, Oct 2021.

[56] S. Zhou, J. Hua, W. Lu, W. An, Q. Su, W. B. Mori, and C. Joshi. High efficiency uniform positron beam loading in a hollow channel plasma wakefield accelerator. *Phys. Rev. Accel. Beams*, 25:091303, Sep 2022.

[57] W. Leemans and E. Esarey. Laser-driven plasma-wave electron accelerators. *Physics Today*, 62(3):44–49, 2009.

[58] A. Seryi, M.J. Hogan, S. Pei, T. Raubenheimer, P. Tenenbaum, T. Katsouleas, C. Huang, C. Joshi, W. Mori, and P. Muggli. In *Proceedings of the 23rd PAC Conference, Vancouver, Canada, 2009*.

[59] E. Adli, J.P. Delahaye, S.J. Gessner, M.J. Hogan, T. Raubenheimer, W. An, C. Joshi, and W.B. Mori. A beam driven plasma-wakefield linear collider: From higgs factory to multi-tev. In *Proceedings, 2013 Coummunity Summer Study on the Future of U.S. Particle Physics (CSS2013): Minneapolis, 2013*.

[60] P. Chen. *Handbook of Accelerator Physics and Engineering*, chapter Beam-beam effects in linear colliders, pages 140–144. World Scientific, 1999.

[61] V. I. Ritus. Quantum effects of the interaction of elementary particles with an intense electromagnetic field. *Journal of Soviet Laser Research*, 6(5):497–617, Sep 1985.

[62] V. Yakimenko, S. Meuren, F. Del Gaudio, C. Baumann, A. Fedotov, F. Fiuza, T. Grismayer, M. J. Hogan, A. Pukhov, L. O. Silva, and G. White. Prospect of studying nonperturbative qed with beam-beam collisions. *Phys. Rev. Lett.*, 122:190404, May 2019.

[63] A. W. Chao, K. H. Mess, M. Tigner, and F. Zimmermann. *Handbook of Accelerator Physics and Engineering*. World Scientific, 2012.

[64] F. Del Gaudio, T. Grismayer, R. A. Fonseca, W. B. Mori, and L. O. Silva. Bright γ rays source and nonlinear breit-wheeler pairs in the collision of high density particle beams. *Phys. Rev. Accel. Beams*, 22:023402, Feb 2019.

[65] D. Schulte. Beam-beam effects in linear colliders. In *Proceedings of the CAS-CERN Accelerator School: Intensity Limitations in Particle Beams, Geneva, Switzerland, 2–11 November 2015*.

[66] E. Adli. Towards a pwfa linear collider — opportunities and challenges. *Journal of Instrumentation*, 17(05), May 2022.

[67] V. I. Telnov. Gamma-gamma collider with w$\gamma\gamma \leq$ 12 gev based on the 17.5 gev sc linac of the european xfel. *Journal of Instrumentation*, 15(10):P10028, oct 2020.

[68] T. Barklow, S. Gessner, M. Hogan, C.K. Ng, M. Peskin, T. Raubenheimer, G. White, E. Adli, G. J. Cao, C. A. Lindstrom, K. Sjobak, S. Barber, C. Geddes, A. Formenti, R. Lehe, C. Schroeder, D. Terzani, J. van Tilborg, J.-L. Vay, E. Zoni, C. Doss, M. Litos, I. Lobach, J. Power, M. Swiatlowski, L. Fedeli, H. Vincenti, T. Grismayer, M. Vranic, and W. Zhang. Beam delivery and beamstrahlung considerations for ultra-high energy linear colliders, 2023.

[69] J. M. Dawson. Particle simulation of plasmas. *Rev. Mod. Phys.*, 55:403–447, Apr 1983.

[70] C. K. Birdsall and A. B. Langdon. *Plasma Physics Via Computer Simulation*. Adam Hilger series on plasma physics. McGraw-Hill, 1985.

[71] R. G. Hemker. *Particle-In-Cell Modeling of Plasma-Based Accelerators in Two and Three Dimensions*. PhD thesis, University of California, Los Angeles, 2000.

[72] R. A. Fonseca, L. O. Silva, F. S. Tsung, V. K. Decyk, W. Lu, C. Ren, W. B. Mori, S. Deng, S. Lee, T. Katsouleas, and J. C. Adam. Osiris: A three-dimensional, fully relativistic particle in cell code for modeling plasma based accelerators. In *Computational Science*, pages 342–351, Berlin, Heidelberg, 2002. Springer Berlin Heidelberg.

[73] P. Sprangle, E. Esarey, and A. Ting. Nonlinear theory of intense laser-plasma interactions. *Phys. Rev. Lett.*, 64:2011–2014, Apr 1990.

[74] P. Mora and T. M. Antonsen Jr. Kinetic modeling of intense, short laser pulses propagating in tenuous plasmas. *Physics of Plasmas*, 4(1):217–229, 1997.

[75] C. Huang, V. K. Decyk, C. Ren, M. Zhou, W. Lu, W. B. Mori, J. H. Cooley, T. M. Antonsen Jr., and T. Katsouleas. Quickpic: A highly efficient particle-in-cell code for modeling wakefield acceleration in plasmas. *J. Comput. Phys.*, 217:658–679, Sep 2006.

[76] W. An, V. K. Decyk, W. B. Mori, and T. M. Antonsen Jr. An improved iteration loop for the three dimensional quasi-static particle-in-cell algorithm: Quickpic. *J. Comput. Phys.*, 250:165–177, Oct 2013.

[77] B. Feng, C Huang, V. Decyk, W. B. Mori, P. Muggli, and T. Katsouleas. Enhancing parallel quasi-static particle-in-cell simulations with a pipelining algorithm. *Journal of Computational Physics*, 228(15):5340–5348, 2009.

[78] A. F. Lifschitz, X. Davoine, E. Lefebvre, J. Faure, C. Rechatin, and V. Malka. Particle-in-cell modelling of laser-plasma interaction using fourier decomposition. *J. Comput. Phys.*, 228(5):1803–1814, mar 2009.

[79] A. Davidson, A. Tableman, W. An, F.S. Tsung, W. Lu, J. Vieira, R. A. Fonseca, L. O. Silva, and W. B. Mori. Implementation of a hybrid particle code with a pic description in r–z and a gridless description in ϕ into osiris. *Journal of Computational Physics*, 281:1063–1077, 2015.

[80] F. Li, W. An, V. K. Decyk, X. Xu, M. J. Hogan, and W. B. Mori. A quasi-static particle-in-cell algorithm based on an azimuthal fourier decomposition for highly efficient simulations of plasma-based acceleration: Qpad. *Computer Physics Communications*, 261:107784, 2021.

[81] Q. Su, F. Li, W. An, V. Decyk, Y. Zhao, L. Hildebrand, T. N. Dalichaouch, S. Zhou, E. P. Alves, A. S. Almgren, and W. B. Mori. Implementation of a mesh refinement algorithm into the quasi-static pic code quickpic. *Submitted to the Journal of Computational Physics*, 2024.

[82] D. H. Whittum. Transverse two-stream instability of a beam with a Bennett profile. *Physics of Plasmas*, 4(4):1154–1159, 04 1997.

[83] S. A. Yi, V. Khudik, C. Siemon, and G. Shvets. Analytic model of electromagnetic fields around a plasma bubble in the blow-out regime. *Physics of Plasmas*, 20(1):013108, 2013.

[84] Y. Zhao. *Emittance preservation in a plasma wakefield accelerator*. Ph.D. thesis, University of California, Los Angeles, 2023.

[85] T. Mehrling, J. Grebenyuk, F. S. Tsung, K. Floettmann, and J. Osterhoff. Transverse emittance growth in staged laser-wakefield acceleration. *Phys. Rev. ST Accel. Beams*, 15:111303, Nov 2012.

[86] D. H. Whittum, W. M. Sharp, S. S. Yu, M. Lampe, and G. Joyce. Electron-hose instability in the ion-focused regime. *Phys. Rev. Lett.*, 67:991–994, Aug 1991.

[87] A. A. Geraci and D. H. Whittum. Transverse dynamics of a relativistic electron beam in an underdense plasma channel. *Physics of Plasmas*, 7(8):3431–3440, 2000.

[88] C. Huang, W. Lu, M. Zhou, C. E. Clayton, C. Joshi, W. B. Mori, P. Muggli, S. Deng, E. Oz, T. Katsouleas, M. J. Hogan, I. Blumenfeld, F. J. Decker, R. Ischebeck, R. H. Iverson, N. A. Kirby, and D. Walz. Hosing instability in the blow-out regime for plasma-wakefield acceleration. *Phys. Rev. Lett.*, 99:255001, Dec 2007.

[89] C. Huang. *Quasi-static Modeling of Beam-Plasma and Laser-Plasma Interactions*. PhD thesis, University of California, Los Angeles, 2005.

[90] T. J. Mehrling, C. Benedetti, C. B. Schroeder, A. Martinez de la Ossa, J. Osterhoff, E. Esarey, and W. P. Leemans. Accurate modeling of the hose instability in plasma wakefield accelerators. *Physics of Plasmas*, 25(5):056703, 2018.

[91] X. Xu. The plasma wakefield with high-order azimuthal modes in the blowout regime. 2017.

[92] Wolfram Research, Inc. Mathematica, Version 14.0. Champaign, IL, 2024.

[93] Private communications with Yujian Zhao.

[94] D. J. Griffiths. *Introduction to Electrodynamics, 4th ed.* Pearson, Boston, MA, 2013.

[95] W. K. H. Panofsky and W. A. Wenzel. Some considerations concerning the transverse deflection of charged particles in radio-frequency fields. *Review of Scientific Instruments*, 27(11):967–967, 1956.

[96] A. W. Chao. *Physics of Collective Beam Instabilities in High Energy Accelerators*, chapter Instabilities in Linear Accelerators, pages 136–153. Wiley Series in Beam Physics and Accelerator Technology. Wiley-VCH, 1993.

[97] V. E. Balakin, A. V. Novokhatsky, and V. P. Smirnov. Vleep: Transverse Beam Dynamics. *Conf. Proc.*, C830811, 1983.

[98] T. J. Mehrling, R. A. Fonseca, A. Martinez de la Ossa, and J. Vieira. Mitigation of the hose instability in plasma-wakefield accelerators. *Phys. Rev. Lett.*, 118:174801, Apr 2017.

[99] J. Vieira, W. B. Mori, and P. Muggli. Hosing instability suppression in self-modulated plasma wakefields. *Phys. Rev. Lett.*, 112:205001, May 2014.

[100] R. Lehe, C. B. Schroeder, J.-L. Vay, E. Esarey, and W. P. Leemans. Saturation of the hosing instability in quasilinear plasma accelerators. *Phys. Rev. Lett.*, 119:244801, Dec 2017.

[101] A. Martinez de la Ossa, T. J. Mehrling, and J. Osterhoff. Intrinsic stabilization of the drive beam in plasma-wakefield accelerators. *Phys. Rev. Lett.*, 121:064803, Aug 2018.

[102] V. Lebedev, A. Burov, and S. Nagaitsev. Efficiency versus instability in plasma accelerators. *Phys. Rev. Accel. Beams*, 20:121301, Dec 2017.

[103] A. Burov, S. Nagaitsev, and V. Lebedev. Beam breakup mitigation by ion mobility in plasma acceleration, 2018.

[104] T. J. Mehrling, C. Benedetti, C. B. Schroeder, E. Esarey, and W. P. Leemans. Suppression of beam hosing in plasma accelerators with ion motion. *Phys. Rev. Lett.*, 121:264802, Dec 2018.

[105] T. J. Mehrling, R. A. Fonseca, A. Martinez de la Ossa, and J. Vieira. Mechanisms for the mitigation of the hose instability in plasma-wakefield accelerators. *Phys. Rev. Accel. Beams*, 22:031302, Mar 2019.

[106] L. Hildebrand, W. An, X. L. Xu, F. Li, Y. Zhao, M. J. Hogan, V. Yakimenko, S. S. Nagaitsev, E. Adli, C. Joshi, and W. B. Mori. Mitigation techniques for witness beam hosing in plasma - based acceleration. In *2018 IEEE Advanced Accelerator Concepts Workshop (AAC)*, pages 1–5, 2018.

[107] L. Hildebrand, Y. Zhao, W. An, F. Li, Q. Su, X. Xu, C. Joshi, and W. B. Mori. Beam realignment with emittance preservation in a plasma wakefield accelerator stage. *Submitted to Physical Review Letters*, 2024.

[108] S. Lee and T. Katsouleas. Wakefield accelerators in the blowout regime with mobile ions. *AIP Conference Proceedings*, 472(1):524–533, 1999.

[109] J. B. Rosenzweig, A. M. Cook, A. Scott, M. C. Thompson, and R. B. Yoder. Effects of ion motion in intense beam-driven plasma wakefield accelerators. *Phys. Rev. Lett.*, 95:195002, Oct 2005.

[110] W. An, W. Lu, C. Huang, X. Xu, M. J. Hogan, C. Joshi, and W. B. Mori. Ion motion induced emittance growth of matched electron beams in plasma wakefields. *Phys. Rev. Lett.*, 118:244801, Jun 2017.

[111] C. Benedetti, C. B. Schroeder, E. Esarey, and W. P. Leemans. Emittance preservation in plasma-based accelerators with ion motion. *Phys. Rev. Accel. Beams*, 20:111301, Nov 2017.

[112] R. Gholizadeh, T. Katsouleas, P. Muggli, and W. B. Mori. Preservation of Ultra Low Emittances Using Adiabatic Matching in Future Plasma Wakefield-based Colliders. *AIP Conference Proceedings*, 1086(1):575–579, 01 2009.

[113] C. Benedetti, T. J. Mehrling, C. B. Schroeder, C. G. R. Geddes, and E. Esarey. Adiabatic matching of particle bunches in a plasma-based accelerator in the presence of ion motion. *Physics of Plasmas*, 28(5):053102, 05 2021.

[114] Y. Zhao, L. Hildebrand, W. An, X. Xu, F. Li, T. N. Dalichaouch, Q. Su, C. Joshi, and W. B. Mori. Emittance preservation in the presence of ion motion for low-to-high energy stages of a plasma based accelerator. *Phys. Rev. Accel. Beams*, 26:121301, Dec 2023.

[115] M. D. Litos, R. Ariniello, C. E. Doss, K. Hunt-Stone, and J. R. Cary. Beam emittance preservation using gaussian density ramps in a beam-driven plasma wakefield accelerator. *Philosophical Transactions of the Royal Society A: Mathematical, Physical and Engineering Sciences*, 377(2151):20180181, 2019.

[116] E. D. Courant and H. S. Snyder. Theory of the alternating-gradient synchrotron. *Annals of Physics*, 3(1):1–48, 1958.

[117] C. Bender. Mathematical physics, lecture 2, 2011.

[118] R. Ariniello, C. E. Doss, V. Lee, C. Hansel, J. R. Cary, and M. D. Litos. Chromatic transverse dynamics in a nonlinear plasma accelerator. *Phys. Rev. Res.*, 4:043120, Nov 2022.

[119] W. An, M. Zhou, N. Vafaei-Najafabadi, K. A. Marsh, C. E. Clayton, C. Joshi, W. B. Mori, W. Lu, E. Adli, S. Corde, M. Litos, S. Li, S. Gessner, J. Frederico, M. J. Hogan, D. Walz, J. England, J. P. Delahaye, and P. Muggli. Strategies for mitigating the ionization-induced beam head erosion problem in an electron-beam-driven plasma wakefield accelerator. *Phys. Rev. ST Accel. Beams*, 16:101301, Oct 2013.